Politecnico di Torino

Academic year
A.y. 2021/2022
Graduation session October 2022

Construction of a dynamic test rig for damping investigations of helicopter tailplane components in carbon-flax hybrid design

Supervisors:
Prof. Andrea De Martin
M.Sc. Jonas John

Candidate:
Marco Somà

Alla mia famiglia
ed ai miei amici

Statement of Authorship

I, Marco Somà, confirm that the work presented in this thesis has been performed and interpreted solely by myself except where explicitly identified to the contrary. All verbatim extracts have been distinguished by quotation marks, and all sources of information have been specifically acknowledged.

I confirm that this work has not been submitted elsewhere in any other form for the fulfillment of any other degree or qualification.

Garching bei München, 10 October 2022

Marco Somà

Abstract

Vibrations play a crucial role in the design of helicopter structures where, in many cases, due to the complexity of the systems, dynamic interactions and excitations can only be determined in flight tests causing structural changes in the late development phase. Often, especially for unconventional designs for which practical experience is limited, such as eVTOLs, structural dynamic simulations can only make inaccurate predictions. Therefore, one possible solution to minimize the risk in design is increasing the damping of the helicopter structure. Recent studies showed that natural fibers can offer a promising approach increasing the damping of the aerospace structures. In detail, the horizontal tailplane, due to its location and mounting, undergoes aero-elastic phenomena whose effects could be limited by the outstanding damping properties of flax.

This thesis aims at developing a dynamic test rig for damping investigations of helicopter tailplane components tested with boundary conditions and excitations coincident to the real functioning. It contributes to clarify the gap in the literature where these parts are tested mainly in free-free conditions, missing the apport of the mounting and the material's effect when included in a 3D structure.

The test bench has been designed including the measuring transducers and exciter to provide the optimal FRF to extract damping factors of the specimen over the frequency range. The structure has been refined according to the FE structural dynamic simulation. Finally, experimental modal analysis has been carried out to verify the functionality of the test rig according to the considered helicopter's operation.

After the successful validation of the test rig, I-beams specimens, precursors of the tailplane, have been tested to highlight the differences between carbon and flax, obtaining damping factors according to the theoretical expectations. In the next stages of the project, the test bench will be used to test the tailplanes, providing improvements to obtain the best-hybridized solution. Then, in the future, thanks to its versatility, the test rig could be re-adapted and used for dynamic tests of other components.

Acknowledgements

Al termine di questi cinque anni di Università che mi hanno dato la possibilità di svolgere due interessanti esperienze all'estero negli Stati Uniti ed in Germania mi sento di porgere alcuni ringraziamenti.

Ringrazio innanzitutto la mia Famiglia, specialmente mio Papà e mia Mamma, per il sostegno e per aver sempre creduto in me. Ringrazio per l'educazione che hanno saputo darmi, per la loro semplicità e per assecondarmi in ogni idea.

Ringrazio i miei grandi Amici di Volpiano e Cavour: porto sicuro durante questi anni di Politecnico. Grazie per aver alleggerito le mie giornate di studio e per non avermi mai lasciato da parte nonostante mi trovassi all'estero. In particolare, ringrazio Luca Faudalet per avermi sempre incluso nei suoi lavori dandomi tanti momenti di spensieratezza e distrazione durante lo studio in remoto.

Ringrazio il gruppo "Gnoc" e la "Casa dell'amicizia" per ogni singolo momento, per tutte le avventure trascorse insieme e per quelle che verranno. Inoltre, ringrazio il "Comitato Amici di Babano" per avermi accolto e dato la possibilità di trascorrere delle vacanze bellissime per rifocillarsi dopo un anno di lavoro.

Ringrazio Andrea per la sua Amicizia e Sostegno in ogni situazione. Sono contento di aver percorso una buona parte del cammino scolastico insieme coltivando interessi e passioni comuni. Grazie per le chiamate quotidiane, per i progetti svolti insieme, per coinvolgermi sempre e per i consigli preziosi. Un grazie anche alla famiglia, sicuramente i miei successi scolastici sono anche merito vostro.

Ringrazio i Professori dell'Istituto Tecnico Industriale "Edoardo Agnelli", specialmente i Prof. Bosco e Gamba, per avermi indirizzato in questo bellissimo settore che è la meccanica e per avermi stimolato a proseguire gli studi. Sono grato dei loro consigli e pareri che, nonostante non sia più un loro studente, continuano a proferirmi con grande esperienza e professionalità.

Un grazie va infine al mio Relatore di Tesi Professore Andrea De Martin per il supporto e per avermi seguito in quest'ultima sfida universitaria all'estero. Thank you very much to the other supervisor M.Sc. Jonas John for guiding and helping me at TUM during the thesis project.

Concludo ringraziando il Politecnico di Torino, per la formazione e l'interesse che ha saputo trasmettermi in questi anni. Per aver amplificato il mio bagaglio culturale e per aver ampliato i miei orizzonti di crescita personale e professionale.

List of Contents

List of Figures

List of Tables

List of Abbreviations

Abbreviation	Description
NFRP	Natural Fiber Reinforced Polymers
CFRP	Carbon Fiber Reinforced Polymers
FRF	Frequency Response Function
FE	Finite Element
EMA	Experimental Modal Analysis
DMA	Dynamic Mechanical Analysis
GFRE	Glass Fiber Reinforced Epoxy
CFRE	Carbon Fiber Reinforced Epoxy
FFRE	Flax Fiber Reinforced Epoxy
GVT	Ground Vibration Testing
DUT	Device Under Testing
ASTM	American Society for Testing and Materials
FBS	Frequency Based Sub-structuring
VP	Virtual Point
VPT	Virtual Point Transformation
DOF	Degree of Freedom

List of Units

Symbol	SI Unit	Name of the variable
η	[%]	Damping factor
f	[Hz]	Frequency
m	[kg]	Mass
l	[m]	Length
v	[m/s]	Velocity

1 Introduction

1.1 Tailplane's hybridization: damping properties of bio-composites

Vibrations are a constant challenge in helicopter development and a frequent cause of delays in development time [1]. According to Stupar [2], vibrations in helicopters arise mainly from the sources such as the rotor system, the tail rotor, the engine, and the transmission. Moreover, as introduced by Datta [1], apart from mechanical sources, there are further aerodynamic causes, particularly the rotor and cell wake interactions with the tail boom or empennage. Aerodynamic interference by the rotor and fuselage wake and the tail boom and empennage causes vibrations, especially at low speeds and fast forward flight [1]. The components mentioned above influence each other and are strongly coupled.

In addition to the human discomfort [2], generally an increase of vibration level is a form of warning before the helicopter's failure. Surprisingly, vibration reduction efforts during the original design of most helicopters were not significant until the 1990s [2]. Too often it remained for later and costly flight-test programs causing structural changes in the late development phase, resulting in high costs and delays in development times [3, 4]. Nowadays, despite of the evolution of Finite Elements simulation software, due to the complexity of the systems, often dynamic interactions and excitations can only be determined in flight tests because structural dynamic simulations can only make inaccurate estimations.

According to John [5], to control these vibration mechanisms, the structure must be damped as much as possible to keep load amplitudes and the general vibration level of the cabin low. Possible solutions are using elastomer layer damper [6]. Other approaches in composite design consists of adding visco-elastic materials into the laminate [7]. A further alternative proposed in this project is to increase the damping of the fiber composite structure of the tailplane by using natural fibers. These are characterized by high inherent damping and lower density with respect to carbon. Therefore, by being hybridized with carbon fiber to obtain a trade-off of the mechanical properties, they can contribute to the damping of the overall component [8]. Thus, this solution offers a unique potential for future helicopter and aeronautical structures [5]. In addition to their damping performance, according to Choi [9], in the last few years, there has been significant interest in bio-composite motivated by their potential benefits of lower commodity prices and ecological advantages of using renewable resources.

In detail, a component of the helicopter that is consistently affected by dynamic excitations due to its location and mounting is the horizontal tailplane. From the aerodynamic point of view, its location is critical since it is placed above the tail rotor (T-tail) and in proximity to the main rotor. Therefore, according to Datta [1], especially at low speeds and fast forward flight, the rotor and fuselage wake and the tail boom and empennage aerodynamically interfere causing vibrations to the tailplane. Moreover, numerous components of the helicopter, due to their interaction, are involved in vibration generation and propagation affecting the performance of the tailplane. For example, main rotor vibrations are mechanically transmitted to the airframe, and airframe vibrations, in turn, excite the rotor dynamics [1]. The so-called "tail-shake" phenomenon or

“Flutter” are some of the possible consequences [10, 11]. This high level of vibrations often requires additional vibration reduction measures in the form of isolation systems [12] and vibration absorbers [13]. Interactions of the blade tip vortices and the rotor wake can lead to vibrations of the tail units [14, 15], which have to be reduced by unique tuning or dynamic isolation of the fuselage structure and the tail. In addition, considering the shape of the tailplane, it is a tridimensional component with the length prevalent with respect to the other dimensions and it is fixed to the tale in the middle on a concentrated region. Thus, this configuration causes the two free arms vibrating freely under the above-mentioned dynamic excitations.

Therefore, the excellent damping properties of flax fiber provide the opportunity to improve energy dissipation without increasing the weight and depleting the mechanical resistance of the current design of the part. Despite of flax fibers have already been used in other industries, such as automotive industry [16], according to John [5], they are still at the research stage in aerospace applications. For this reason, this thesis is inserted into a wider project called eVolve which aims at clarifying the gap present it the literature related to damping of hybrids applied to aerospace structures, principally the helicopter’s tailplane. The thesis itself, satisfies the need of testing the tailplane and its preliminary specimens according to the working conditions of real life of the helicopter. It is characterized by the realization of a dynamic test rig for damping characterizations of helicopter tailplane. This provides the basis for comparing specimens made up of different stacking sequencies, materials and orientations to define the best hybridized tailplane.

1.2 State of the art

Despite of flax fibers have already been used in other industries, such as the automotive industry [16], according to John [5], they are still at the research stage in aerospace applications. In the area of stiffness and failure criteria of flax materials, significant progress has been made recently, as it has been shown that competitive helicopter components like tail units can be designed [17, 8]. However, the prediction and optimization of the damping properties, especially when integrated in Carbon Fiber Reinforced Polymers (CFRP), is still largely unresolved. For example, Henschel [17] was able to determine higher damping during the production of a flax-carbon hybrid tailplane compared to a reference carbon tailplane. A faster decay of the accelerations and higher damping ratios were observed for the hybrid tailplane investigated. The damping ratio was more than three times higher. However, her design and investigations did not have damping as an optimization goal, but rather structural stiffness and a high organic content. The influence of flax hybrid design specifically on the damping behavior was not yet part of the study. By investigating the influencing factors of the design, it is possible that the damping can be even further improved. Therefore, for a target-oriented use of flax fibers in aerospace structures, specifically for damping enhancement, it is necessary to gather further knowledge and predictive capabilities about the properties of flax-carbon hybrids.

For this reason, the project adopts a built-up procedure based on a gradual approach starting from carbon, flax, and carbon-flax material properties investigation at the material level. Then, it extends to the structural level considering the behavior in a tridimensional structure and finally, it concerns the final tailplane. The first step has already been performed by John [5] and consists of the evaluation of the damping properties of carbon coupons by flax fiber hybridization. It is defined **1 D phase**, because the laminates are characterized prevalently by their length, while the other dimensions are negligible, represented in *Figure 1.1:*

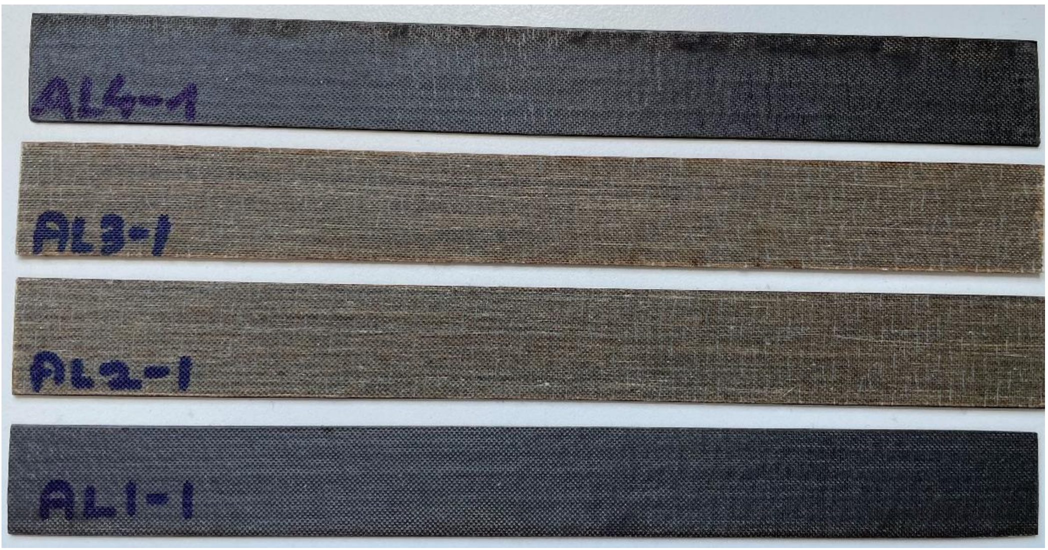

Figure 1.1 - 1 D Coupons

John's paper [5] presents new experimental data about the damping properties of flax and flax-carbon hybrid composite laminates over a wide range of fiber orientations, stacking sequences and their relations regarding the mechanical properties. In order to limit the investigation to the material level the specimens are produced with coupon shape characterized by a single dimension. There were previous studies about damping properties of flax and flax-carbon hybrid composites like in Ameur [18], Duc [19], Fairlie [20] or Assarar [21, 22], but 1 D study focuses not only on the investigation of unidirectional fiber composites but also on the promising combination of different fiber orientations in the hybridization.

1 D provides the basis for extending the study to the structural level, considering two coupons spaced by a central web. The obtained cross section is a double T profile, which extruded along the third directions originates an I-beam, represented in *Figure 1.2*:

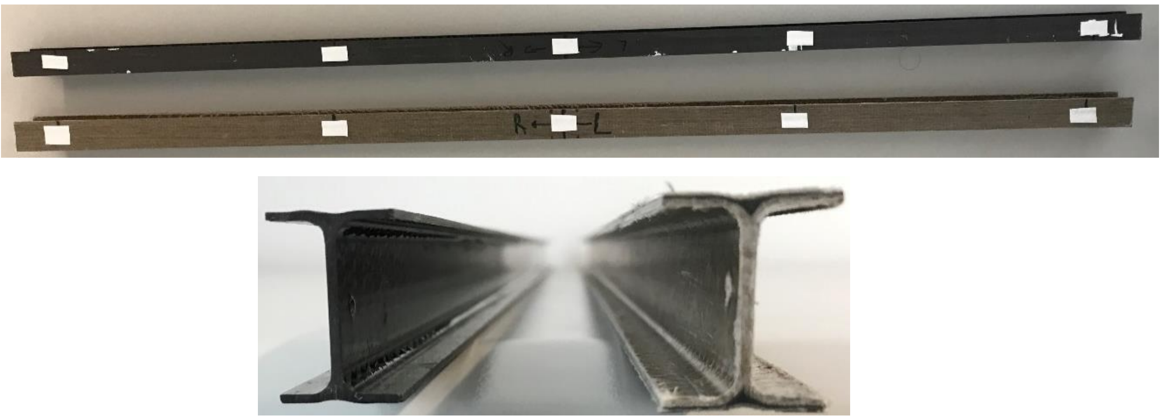

Figure 1.2 - 2 D I-beams

This step is defined **2 D phase**, because, in addition to the length of the part, there is a second dimension included in the analysis: the displacement of the flanges. By introducing a new dimension, it is possible to conduce new considerations compared to the 1 D. According to the results obtained by Benedikt Scheffler [23] in his master thesis, who investigated the damping properties of carbon-flax hybrid I-beams, the effect of the different layering solutions is attenuated in the 2 D with respect to the 1 D. In 1 D phase layering of the coupons plays the major role: flax fiber in the outer layers provides high damping properties, but at the same time, due to flax's characteristics, stiffness decreases. On the contrary, by structuring the composite with flax in the central layers and carbon outside, the stiffness of the coupon increases, and damping is reduced. According to Scheffler's results [23], in 2 D phase layup is not that relevant as in 1 D. Therefore, the effect of different stacking sequences of the flanges is less influent than in coupons. Moreover, it is important to study the I-beam since it is also introduced as reinforcement in the actual design of the tailplane.

In addition to the structural aspects, it is important extend the damping investigations to a tridimensional component, introducing also other aspects such the position of the hybridization spots and the presence of real mounting interfaces. Therefore, this step is called **3 D phase**, and it is currently missing in the literature.

The component studied in 3 D phase is the tailplane of the Coax2D helicopter, represented in *Figure 1.3*:

Figure 1.3 – 3 D Tailplane

Especially regarding the boundary conditions, due to their configurations, 1 D coupons and 2 D I-beams have been tested either in free-free or clamped-free conditions to investigate the effect of the material itself, and the material in the structure. Up to now, the contribution to the damping of the mounting and the position of the constraint region in the component have not been considered. On the contrary, with respect to the previous phases, as it can be observed in *Figure 1.3*, due to its geometry and interface it is not possible to clamp the tailplane similarly to a cantilever beam.

In addition to the necessity of testing the tailplane with the real boundary conditions, before the validation of the part, it arises the necessity of analyzing the behavior of the component undergoing to the real excitation applied by the helicopter. Thus, in order to save money from flight test and avoiding structural modifications in the late development phase, it has been decided to cater for a dynamic test rig for damping investigations of carbon-flax hybrid design tailplane components. According to the literature, Peumans [24] performed a realistic measurement on the tailplane of a glider to understand the advantages and disadvantages of its theoretical estimations. The system under test was the tailplane of a glider which was connected to a wall via its central mounting points. The tailplane was excited by two mini-shakers and the responses were measured at different locations using impedance heads. In this configuration the effect of the central mounting as boundary conditions deeply influences the FRF and consecutively the damping of the component. But, in this case, opposite to the study of Assarar [25] and John [5], the goal is not limited to the material point of view, it is extended to the component level. The test rig object of this thesis, in addition to the actual literature, in order to provide a better estimation of the damping properties aims at including in the experiment also the vertical tailplane where the horizontal tailplane is mounted on the top. The motivation is related to the excitation applied to the tailplane, because among its dynamic excitations, it is also shaked by the tale of the helicopter inducing moment excitations to the part, which is responsible for the asymmetric deformed configuration. Therefore, by using impact testing or shaker to excite the tailplane constrained according to Assarar [25] it would not be possible to include this excitation into the study.

1.3 Scope of the thesis

The procedure adopted to evaluate the damping properties of carbon-flax hybrid tailplane components provides the basis for developing a detailed material model for damping simulation and understanding the application in more complex aerospace structures such as spars and wing profiles up to complete tail structures. By increasing the global damping in the helicopter structure, it will be possible to compensate eventual lacks related to dynamic interactions and excitations which are currently not predicted by structural dynamic Finite Elements simulations, minimizing the risk in design, and reducing eventual modifications in the late development phase.

The purpose of this gradual procedure is to start from a simple component easy to simulate and test, analyzing the effect of different hybridization solutions and evaluating the obtained results from static and dynamic tests. Then, these results will be applied to the hybridization of more complex components with a higher similarity to the final tailplane.

In order to expand the knowledges related to the design and integration of hybrid structures in the helicopter, is necessary to focus on the refinement of the dynamic testing of the tailplane including realistic boundary conditions and all the excitations generated by aeroelastic phenomena and coupling from different sub-groups of the helicopter. For this motivation, it is important to design a dynamic test rig that also includes the vertical tailplane to induce moment excitation to the horizontal tailplane. In detail, this thesis aims at clarifying the actual gap present in literature related to the experimental test of carbon-flax hybrid tailplanes.

After its validation, the test bench will be used to determine the Frequency Response Function of the I-beams (2 D) and later of the tailplane (3 D) over the frequency range of interest. Next, the FRF will be used to compute the damping ratios of the different hybridized solutions that will be compared to the current traditional full carbon design to reach the best hybrid version of the component. Regarding the I-beams, the purpose of the test rig is to evaluate the damping properties of the parts constrained according to how it will be mounted inside the tailplane as reinforcement and excited in the same way of the operational life. Moreover, the purpose is to determine the optimal I-beam to apply to reinforce inside the horizontal tailplane. Regarding the tailplane, the dynamic test rig will play an important role for its damping investigation properties also considering the effect of the location of the hybridization spots and the influence of the constraint. In conclusion, by obtaining a precise characterization of the damping properties of hybrid structures in aerospace structure, it will be possible to refine the models and improve the reliability of the predictions obtained from the simulations, reducing the amount of changes in late development phase.

The thesis is structured in different chapters starting from *Chapter 1* which provides a introductory overview of the topic. Then, *Chapter 2* is related to the the theoretical knowledges which constitute the basis of Experimental Modal Analysis (EMA), set up of the test rig, sensors and exciters. The design and simulation of the test rig are presented in *Chapter 3*. The Experimental validation of the test rig, where the sub-groups and the complete test rig are tested to verify the correspondance with the simulations is also included in *Chapter 3* (Methods). Finally, the conclusions are contained in *Chapter 4*.

2 Chapter 2: Theory

2.1 Flax fiber

According to Alexander [26], flax (Linum usitatissimum L.) is the oldest textile fiber known to mankind and it has been primarily grown in Europe but also in other temperate regions. The fibers are extracted from the stem (*Figure 2.1*) by a multistage process: planting, harvesting, drying/rotting, scutching, hackling and partly by spinning and weaving:

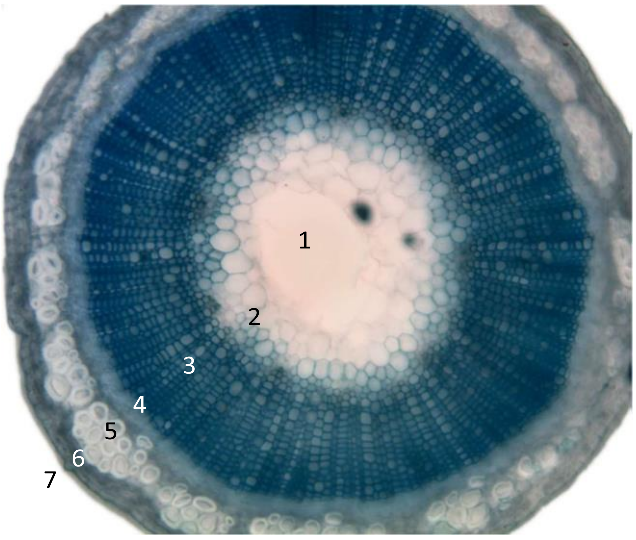

Legend:

1. Pith
2. Protoxylem
3. Xylem II
4. Phloem I
5. Sclerenchyma (Bast Fiber)
6. Cortex
7. Epidermis

Figure 2.1 - Cross section view of flax stem [49]

As evidenced by Bos [27], flax fibers, unlike man-made fibers, are not a continuous fiber but in fact a composite by itself. *Figure 2.2* depicts the schematic structure of the flax fiber, from stem to microfibril:

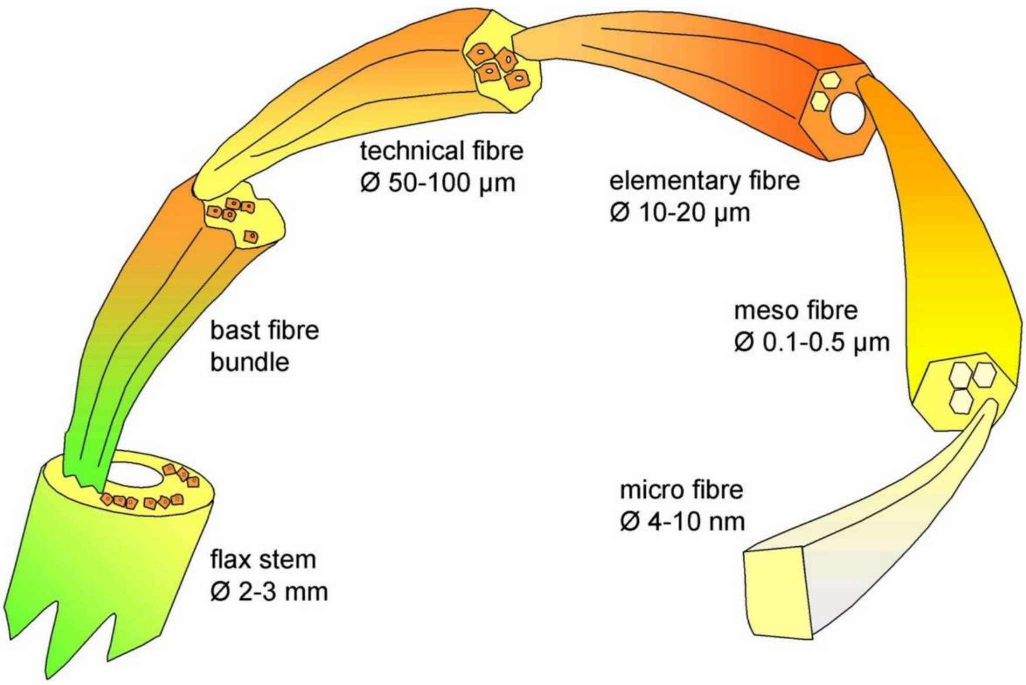

Figure 2.2 - Fiber classification in the flax stem [78]

According to Yan [28], the extracted fibers have an average diameter of 19 µm and a length of 25–120 cm. *Figure 2.3 a)* depicts a flax plant after harvesting a tuft off the field, and *Figure 2.3 b)* twill weave made from flax fibers extracted. Because the fibers are not synthetic and are not infinite, the weaving process necessitates yarning by spinning, whereas UD reinforced mats can be aligned without yarning. In smaller scales, today's woven fabrics are limited to a real density of about 100 g/m^2:

Figure 2.3 - Photographic Images of Flax, a) Harvested Plant [78] b) Flax Woven Fabric [77]

The political and environmental benefits of greener aviation support the use of NFRP. Soutis [29] mentioned that supporting arguments include weight-saving potential, a lower carbon footprint, and higher energy efficiency while manufacturing when compared to carbon. Moreover, Franck [30] found that in comparison to other natural fibers, flax fiber has previously been found to be the most promising natural fiber for applications requiring high specific strength and stiffness. The material selection for structures in aviation is frequently influenced by high specific mechanical properties, which include material density. Regarding flax fibers, Rinberg [31] discovered that they have a lower density than conventional fibers (such as glass and carbon); combined with a stiffness comparable to glass fiber composites and a strength in the same range as aluminum alloys, flax has a lightweight potential.

2.2 Composite vs Bio-composite

According to Mahmoudi [32], over the last decades, the use of composite materials has significantly increased. They have gradually replaced the metal materials in various industrial fields. As an example, in the aeronautical domain, this exponential use of composite materials is evidenced nowadays in the composition of the AIRBUS A350 XWB and the Boeing 787 Dreamliner where respective composite material weights amount to 53% and 50% of the total weight [32]. This is due to numerous beneficial properties of composites compared to traditional materials: weight reduction with high strength and rigidity, corrosion resistance, thermal properties, resistance to fatigue, wear, and energy dissipation. Weight reduction also decreases carbon dioxide emissions and generates significant energy savings. This is a key-issue in a context where energy prices keep increasing and finite resources are gradually depleting [32].

Among all the above-mentioned properties, this project relies on the interesting dissipative capacity of composites. As denoted by [32], energy dissipation in composites results mainly from the damping capacity of the constituent materials (matrix and fiber). Indeed, similarly to other mechanical properties, damping depends on the composite parameters such as constituent properties, fiber volume fraction and fiber orientation. For the polymeric matrix, Chung [33] showed that thermoplastic polymers are more dissipative than thermosets which are more widely used for their better elastic properties. Ni [33] and Haddad [34] investigated the effect of fiber volume fraction in synthetic composites through several research works. They confirm that damping decreases with respect to the fiber volume fraction. Similarly, according to Hadi, Suarez, Rahman [34, 35, 36], the influence of fiber orientation on dissipative capacity is studied in the context to optimize composites regarding both mechanical and damping properties.

According to Henschel [17], CFRP are beneficial in many ways for aerospace application, but there are drawbacks in terms of brittleness, dynamic behavior, cost, and environmental pollution. Bernadette [37] showed that carbon and glass composites fail, due to their inherent brittle failure of the fibers, often catastrophically, without prior indication for the operator. Additionally, the use of CFRP in helicopters raised new issues in structural dynamics, as rivets were highly contributing to structural damping in metallic joints. Furthermore, according to Jun [38] and Liddel [39], the cost for the production of carbon fibers is high, which is due to and along with a high energy consumption in production, but regarding the weight savings due to tremendously high specific strength and stiffness, it is still superior to metallic structural parts; as thereby, in the overall life-cycle of the aviation systems, costs and energy consumption can be reduced.

This is the reason why, as introduced by Saheb and Wambua [40, 41], in the last few years, there has been significant interest in natural fibers motivated by their potential benefits of lower commodity prices, ecological advantages of using renewable resources. Furthermore, they proof to have significantly higher damping potential by their damping performance. Later, natural fibers lost much of their interest due to the use of other more durable materials such as metals and synthetic composites [32]. This was explained by Drzal [42] by the fact that natural fibers exhibit poorer mechanical properties and, moreover, Le [43] mentioned the greater variability of these characteristics compared to synthetic fibers. However, Shanks [44] mentioned recently developed treatments have considerably improved these properties for the Flax Fiber Reinforced Polymer composites (FFRP). In addition to the common source of damping in composites such as the viscoelastic behavior of the matrix and/or fibers, Charlet [45] found that energy dissipation in FFRP is enhanced through the friction within flax fiber bundles.

Damping characterization of FFRP was the subject of several experimental investigations. Using the Dynamic Mechanical Analysis (DMA), the damping of Glass Fiber Reinforced Epoxy (GFRE) was compared to Flax Fiber Reinforced Epoxy (FFRE) by Wielage et al. [46]. They showed that FFRE are characterized by a higher loss factor and the recycling processing has a negligible effect on mechanical properties. Prabhakaran et al. [47] have shown that the FFRE can improve the damping coefficient by more than 50% while enabling a weight reduction of 33% compared to GFRE plates with the same thickness.

Duc et al. [48] have tested various composites made of glass, carbon and flax fibers associated with various thermosets and thermoplastic matrices. They have shown that the use of unidirectional FFRE increases the loss factor by 200% and 133% compared to unidirectional Carbon Fiber Reinforced Epoxy (CFRE) and GFRE, respectively. In addition, their results, according to Duc's results [19], show that the use of thermoplastic matrices makes it possible to further increase the damping composite properties. El Hafidi et al. [49] found that the damping property of FFRE can be 5 times higher than for unidirectional CFRE and 2 times higher than for GFRE. In order to improve the damping of FFRE, Bourbon [50] and Le Guen [51] investigated the effect of the impregnation quality, the fiber/matrix adhesion, the fiber quality, the twist angle of the flax yarns, the crimp in the flax fabrics and fiber treatment. It is observed that the fiber twist and crimp and the fiber treatment via polyol additions enhance the loss factor of FFRE significantly. Thus, composites reinforced with natural fibers generate higher vibration damping properties. As a result, numerous studies have been carried out on hybrid composites [47, 25], for example mixing carbon fibers and flax fibers to achieve better compromise between mechanical and damping performances. From the results obtained by the study of Cadou [32], the principal remarks that can be pointed out are:

- The damping properties of the FFRE structure depend on the fiber orientation
- The complex constant representation of the mechanical properties is not sufficient
- The stiffness and the damping of the FFRE seem to be frequency dependent.

For natural fiber composites, some researchers have already analyzed experimentally damping performances [46, 48]. For example, Wielage et al. [48] studied the dynamic properties of flax, hemp and glass fibers reinforced polypropylene composites using the Dynamic Mechanical Analysis (DMA). They found that, for the same conditions, the loss factors of flax and hemp composites are significantly higher than the glass ones. Recently, Duc et al. [50] analyzed the effect of several parameters on the damping properties of flax fiber reinforced composites such as the impregnation quality, the fiber–matrix adhesion, the twist angle of yarns and crimp in flax fabrics. They particularly observed an increase in the damping properties with fiber twist and crimp showing the important friction mechanisms which are induced. In another work, Le Guen et al. [52] analyzed the effect of fiber treatment with polyols on the damping of flax fiber reinforced epoxy composites. They observed a higher damping behavior of treated flax fiber composites compared with the non-treated ones. This could be attributed to the formation of hydrogen bonds between the polyols and flax micro fibrils within the lamellae as explained by Staiger [52]. Duc et al. [19, 48] compared the damping properties of carbon, glass and flax fibers composites by considering the DMA and vibration beam testing. In particular, they showed that flax fiber reinforced composites present a relatively higher damping behavior with respect to the other composites which could be attributed to the different friction mechanisms intrinsic to flax fibers.

According to [17], recent research studies state that bio-composites could reduce the environmental footprint of parts due to the significantly lower energy input in the production process. According to Nilmini, Gangarao and Madsen [53, 54, 55], the energy consumption for the production of flax sliver can be estimated between 10 – 60 MJ/kg and for a yarn by 86 MJ/kg, while Ashby and Vernet [56, 57] proved that CFRP production consumes 450 – 770 MJ/kg. Additionally, it is expected that a preferably high bio-based mass content would conclude to a better recyclability of the part. Recent studies also highlight the mechanical and lightweight potential of flax fiber reinforcements in modern composite structures [27, 58]. According to Karus [59], the purposeful application of modern flax composites is already demonstrated in the automotive industry. Here the applications focus on door panels and boot liners as the acoustic and vibratory insulation properties are considered superior. According to Alkbir, Meredith, Sarasini and Yan [60, 61, 62, 63], the good energy dissipating properties of FFRP are emphasized in different sources, including very good vibrational damping, crash absorbing and impact resistance properties.

According to [17], to give a short overview of energy consumption in the whole life cycle of a sport and leisure aviation technology, in detail an helicopter, with an assumed life cycle of 20 000 h, the break even in terms of embodied energy would be reached when the hybrid cabin is approximatively 5 % heavier than the reference. Eventually, the high energy demand in the operational life is strongly influencing the overall ecoefficiency, but minor drawbacks in weight (between 1–2 %) could still be beneficial when significant reductions of the embodied energy in the primary production can be achieved. Furthermore, the costs of flax are only 2 % of the costs of carbon, when comparing the raw fibers' primary production in [56]. This enormous difference can lead to significant cost savings in the system manufacturing. If we consider processed prepreg materials with epoxy coating, the prices will converge, but a remaining benefit is expected.

Table 2.1 shows the selected properties of the currently used aviation composites applied fibers (glassand carbon) in comparison with the flax fibers:

Property (Unit)	Glass	Carbon	Flax
Density (g cm^{-3})	2.55 - 2.60	1.80 - 1.84	1.42-1.52
Tensile strength (N mm^{-2})	1900 - 2050	4400 - 4800	750-940
Tensile Modulus (N mm^{-2})	72000-85000	225000 - 260000	75000-90000
Specific Strength (kN m kg^{-1})	731-804	2391-2667	493-662
Specific Stiffness (kN m kg^{-1})	27692-33333	122282-144444	49342-63380
Damping Ratio (%)*	0.15	0.81	1.47
Costs (USD kg^{-1})	1.63-3.26	124-166	2.10-4.20

*Value not related to the pure fiber, but to the cured fiber-reinforced laminate

Table 2.1 - Glass, Carbon, Flax properties *[56]*

From the table is possible to notice that the density is significantly lower for the flax composites, but in specific strength and stiffness, the carbon fiber is showing the best properties. Nevertheless, flax fibers show higher specific stiffness than glass fibers and as the design of some aviation structures, such as aerodynamic surfaces, is typically stiffness constrained, this is considered a supportive property. Additionally, Vanfleteren, Ramakrishan, Lebaupin, Kling and Bensadoun [64, 65, 66, 67, 68] proved that a superior energy dissipation of FFRP compared to CFRP and GFRP is emphasized in different sources, observing very good vibrational damping, crash absorbing, and impact resistance properties.

Another significant difference can be seen when comparing embodied energy and embodied CO_2. Flax fibers need only a small fraction of the primary production embodied energy values of the conventional fibers. On the other hand, when comparing water usage, but also area or space requirements, flax fibers are superior to conventional synthesized fibers. In terms of costs, flax fibers are also sharply inferior to carbon fibers. But, according to [17], the composites differ less in energy consumption and costs as the added epoxy also requires resources and further manufacturing steps add up equally to both fiber types and thereby reduce the relative discrepancy. The actually paid prices per square meter differs in approximatively 30%, still a significant benefit. As flax prepregs are not very common yet and production batches are small, it is expected that costs of flax prepregs will decrease as soon as they become more popular in industrial sectors.

2.3 Damping properties of flax-carbon hybrids

According to what was anticipated in the introduction, among the advantages of flax-carbon hybrid parts, the project is focused on the increase of damping properties by mean of hybridization of carbon with flax.

According to Berthelot [69] and El Mahi [70] et al., this energy dissipation depends on the constitution of the material such as the viscoelastic behavior of fiber and matrix, layer orientation, stacking sequence, etc. Le Guen et al. [71] reported the relationship between the Young's modulus and damping in carbon-flax hybrid composite laminates. They showed that the damping coefficient of composite structures was increased by increasing the proportion of flax fiber.

According to Fairlie [72], as previously mentioned, effective aspects are the stacking sequence and the fiber orientation. He produced different hybrid carbon-flax fiber reinforced composites using epoxy resin as the matrix using vacuum-assisted resin infusion molding technique. Each composite material was then tested for tensile properties using a universal testing machine, and the damping experiment was conducted using an impulse hammer and a Laser Doppler Vibrometer. The tensile study found out that adding a flax layer to the external layers of carbon fiber laminate reduced Young's modulus by 28% for one layer and 45% for two layers. It was noted that when the fiber orientation of the internal layer of $[C/F_2/C]_s$ was replaced with two ±45° layers, this had a very little effect on Young's modulus but reduced the ultimate tensile strength by 61%. This experimental study also showed that the most important layer when it comes to damping properties is the external layers, while the decrease in damping is attributed to the replacement of the internal layers by carbon layers. By adding an external flax layer into an epoxy/carbon fiber-reinforced composite considerably enhanced its damping ratio by 53.6% and by adding two layers increased it by 94%.

Regarding the orientation of the fibers, Ameur [73] tested hybrid laminates with four different stacking sequences prepared from six plies of the unidirectional materials with nominal width of 25 mm and nominal thickness. Ameur [73] investigated the variation of loss factor as a function of fiber orientation for different frequencies. The results of the study were that for each laminate the damping coefficient curves have the same shape varying the fiber orientation for the different frequencies; then, for any given type of laminates, transverse damping (90°) is higher than longitudinal damping (0°). In the case of unidirectional flax fiber laminates and hybrid laminates with external flax layers, damping is maximum for the 75° fiber direction. In the case of unidirectional carbon fiber laminates and hybrid laminates with external carbon layers, damping is maximum for the 45° direction.

2.4 Modal Analysis

Modal Analysis, according to “Experimental Vibration Analysis – Lecture Script Version 0.9” [74], is one of the most important tools to analyze the dynamic behavior of mechanical structures. With respect to Single Degree of Freedom (SDOF) systems, modal analysis goes one step further and uses multiple responses of systems with multiple degrees of freedom to include amplitude, frequency and location information into one model. According to [75], modal analysis is heavily used to analyze and validate designs like aircraft frame parts, wind or gas turbine blades, vehicle chassis, and any critical structure that is exposed to forces that might induce harmful or even destructive resonant frequencies without damping. At resonance frequencies with critically low damping, an object can react/vibrate strongly from even small amounts of input force or energy. Modal Analysis can give the user an overview of the object's natural frequencies, damping parameters, and structural mode shapes. This knowledge allows engineers to modify and optimize the object’s design to be less sensitive to applied forces. It is also used to correlate Finite Elements analytical models with real-life prototypes by using the damping characteristics, discovered by the empirical testing.

Figure 2.4 shows the measurement of multiple FRFs with the same input and multiple outputs along a tuning fork:

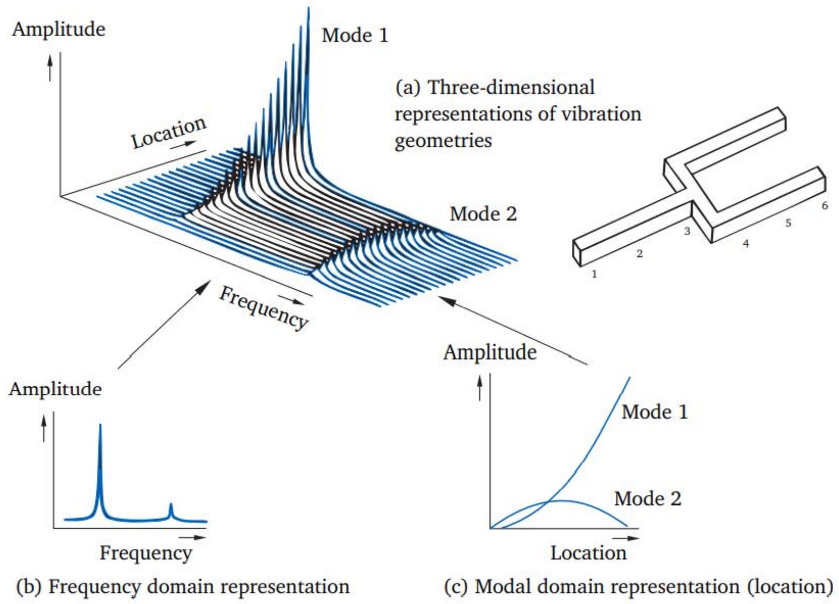

Figure 2.4 - Measurement of multiple FRFs at different locations at a tuning fork

Figure 2.4 (b) represents the amplitude of the response of the system measured at one location of the fork as function of the frequency of excitation. *Figure 2.4 (c)* represents the amplitude of the response of the system measured in all the points of interest as function of their position from the reference point. From these two figures emerges the presence of two eigenfrequencies in the frequency range considered in the experiment. It is possible to use multiple measurements as the one represented in *Figure 2.4 (b)* along the tuning fork and line them up in a three-dimensional diagram, *Figure 2.4 (a)*. This reveals that the amplitude from the response of the same input to these different outputs change along the location, while the frequencies stay the same. This already gives a hint that there are certain amplitude shapes associated with every eigenfrequency of a mechanical structure, which are called mode shapes. By means of linear superposition of these mode shapes is possible to describe the entire vibration behavior of a mechanical structure with any number of degrees of freedom. Modal Analysis has its roots in the Finite Element Method (FEM), which discretizes a continues structure using many discrete points and describes the interrelation between these points with a mass M, damping C and stiffness K matrix. This results in a big set of equations which take a long time to solve since usually a lot of degrees of freedoms show up in the same equations. Modal Analysis is a way to decouple these equations and describe the dynamic behavior of the system using the modal parameters:

- The eigenfrequencies
- The damping ratios
- The mode shapes associated with the eigenfrequencies.

As shown in *Figure 2.4*, these are quantities that can also be measured on a test structure using Experimental Modal Analysis. This provides a very good way to evaluate the results of a FE model by computing the expected modal parameters and comparing them to measured experiments.

Modal Analysis is generally possible for linear and time-invariant systems. The goal is to describe the dynamics of a mechanical structure with a set of n degrees of freedom x using the differential equation (*Equation 2.1*):

$$[M]\{\ddot{x}\} + [C]\{\dot{x}\} + [K]\{x\} = \{f\} \tag{2.1}$$

Where: $\{x\}$ is the vector that describes the displacements of the discretized points of the structure. $\{f\}$ includes all forces acting on the discretized points in the corresponding degree of freedom. The mass matrix $[M]$ is symmetric and positive definite. The damping matrix $[C]$ is symmetric. The stiffness matrix $[K]$ is symmetric and positive semi-definite. *Equation 2.1* is a system of n coupled ODE's, which makes solving and interpreting this system relatively complicated. A good way to simplify this system of ODE's is a modal transformation. With the assumption of proportional damping and assuming a synchronous solution in time domain, the resulting equation (*Equation 2.2*) is:

$$([K] - \omega^2[M]) = [0] \tag{2.2}$$

The solution of *Equation 2.2* consists to the eigenvalue problem that provides as output the eigenfrequencies ω_i with the corresponding eigenvectors (or modal shapes) $\{\psi_i\}$. With $[\Psi] = [\psi_1, \dots, \psi_n]$ being the modal matrix and $\{\omega\} = \{\omega_1, \dots, \omega_n\}$ being the eigenfrequencies with the characteristic properties of mass and stiffness orthogonality, *Equations 2.3* and *2.4*:

$$[\Psi]^T[M][\Psi] = [M_m] \tag{2.3}$$

$$[\Psi]^T[K][\Psi] = [K_m] \tag{2.4}$$

Where $[M_m]$ and $[K_m]$ are two diagonals $n\ x\ n$ matrixes. By exploiting this intermediate step, modal transformation (*Equation 2.5*) and the expansion theorem (*Equation 2.6*) are required to solve the coupled equations:

$$\{x\} = [\Psi]\{\eta\} \tag{2.5}$$

$$\{x\} = \sum_{i=1}^{n}\{\psi_i\}\eta_i \tag{2.6}$$

Where η is defined as modal coordinate. The final result consists of a system of n uncoupled ODEs which fulfills the requisites to be solved. Therefore, by solving the resulting system is possible to determine the equation of motion of each degree of freedom. Moreover, by means of the abovementioned equations, is possible to determine the FRF of the system with damping (*Equation 2.7*) and the simplified without damping (*Equation 2.8*):

$$\alpha(\omega)_{j,k} = \frac{x(\omega)_j}{f(\omega)_k} = \sum_{i=1}^{n}\frac{\psi_{j,r}\cdot\psi_{k,r}}{(K_r-\omega^2M_r+i\omega C_r)} = \sum_{i=1}^{n}\frac{\phi_{j,r}\cdot\phi_{k,r}}{(\omega_r^2-\omega^2+2i\omega\omega_r\xi_r)} \tag{2.7}$$

$$\alpha(\omega)_{j,k} = \frac{x(\omega)_j}{f(\omega)_k} = \sum_{i=1}^{n}\frac{\psi_{j,r}\cdot\psi_{k,r}}{(K_r-\omega^2M_r)} = \sum_{i=1}^{n}\frac{\phi_{j,r}\cdot\phi_{k,r}}{(\omega_r^2-\omega^2)} \tag{2.8}$$

2.5 Experimental modal analysis

According to Peumans [24], most mechanical structures such as buildings, bridges, airplanes are very susceptible to resonant behavior. Mechanical resonances can be induced by proper application of small forces which in turn result in excessive oscillatory motions of the structure [76]. As reported by Ewins and Bendat [76, 77], the FRF is a fundamental quantity which heavily facilitates the study of the dynamic behavior of these mechanical structures. According to PCB Inc. and Berninger [78, 79], by correctly measuring the non-parametric FRF and its corresponding uncertainty, a parametric model can be estimated which enables the extraction of modal parameters such as resonance frequencies and damping ratios. Through knowledge of these modal parameters is crucial to deduce whether a mechanical structure will exhibit oscillatory motion when taken into operation. In addition, these parameters allow engineers to counteract or control this possibly destructive behavior. For this reason, a proper equipment, schematized in *Figure 2.5*, is needed to carry out the experiment for the measurement of the FRF:

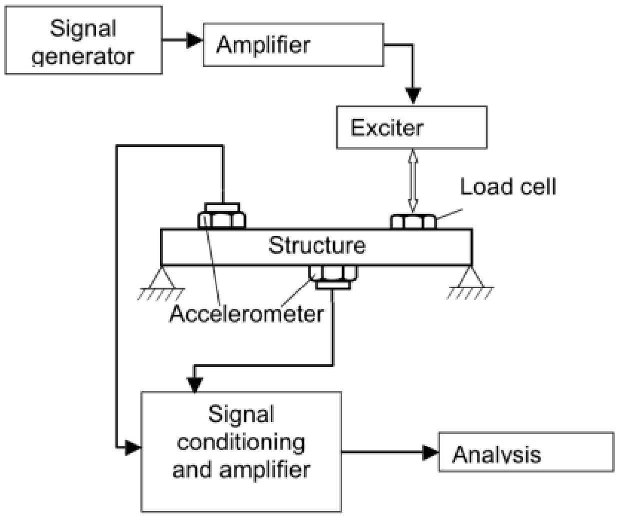

Figure 2.5 – Experiment set up

The test equipment is generally composed by:

- <u>Structure under testing</u>, it is the component or system that has to be tested. It is important to impose proper boundary conditions according to the purpose of the experiment because they have a strong influence on the FRF, modal shapes and eigenfrequencies. Usually, the component is constrained in free-free conditions when the purpose is to characterize only the part itself, or in the same way that is mounted in its real application when the purpose is to determine the behavior in its real functioning considering material and structural effects
- <u>Exciter</u>, it is the device that applies the excitation to the system. There are several types of exciters for example shakers or impact hammer that are recommended for different applications. Important factors that affect the decision of the type of exciter are: frequency range of excitation, type of component to excite, location of the exciter, purpose of the experiment. In addition, according to the type of exciter, is important to determine the interface connection between the exciter and the part, for example, a

shaker requires a stinger. And, between the exciter and the part, a load cell has to be placed to measure the force exchanged because, as it has been proved in the previous chapter, to compute the FRF is necessary to divide the displacement over the force applied. It is important to place the exciter in a position where the component is properly excited

- Measuring transducers, are the devices that measure the output and the input of the experiment. The input consists on the excitation, which is the force, and the output is the displacement of the system. There are different types of transducers with different characteristics but the most used are the accelerometers. According to its name, the accelerometer measures the acceleration of a point, then, in frequency domain it is possible to move from acceleration to displacement without integrating. After signal processing, this signal will be used to compute the FRF by dividing itself over the force signal, both converted in frequency domain. It is important to define the amount and their location of accelerometers along the structure to test
- Signal conditioning and amplifier, receives the signal measured by the force load cell and by the accelerometers or other transducers, processes them in term of filtering, adjusting the mean value and amplifying. In addition, measurement functions such as windowing, averaging and Fast Fourier Transforms (FFT) computation are usually processed within the analyzer.

After a general presentation of the equipment required for the execution of the dynamic experiment, some important aspects that influenced the decision of the final design of the test rig will be deeply investigated in the next paragraphs.

2.5.1 Mounting of the test structure

When performing modal testing the DUT (Device Under Test) must be able to vibrate dynamically in ways that will reveal all natural frequencies and mode shapes of the structure in the frequency range of interest. To pursue free vibration patterns, or similar vibration patterns as expected when the structure is operating in real life, materials like rubber bands, elastic wires, foam pads, and other materials providing a soft elastic system are often used to hang or place the structure avoiding adding extra stiffness.

While, on the other side, rigid body motions are vibrations of the whole DUT as a rigid object and do not provide information of the structural dynamic properties of the DUT (the flexible modes). Such rigid body modes are related to the selected support configuration. Depending on how the DUT is mounted the rigid body modes might affect the flexible modes of the structure in an unacceptable manner. The impact of the rigid modes on the flexible modes depends on how close in frequency the rigid modes are to some flexible modes, and on what is determined to be an acceptable accuracy of the measurements.

2.5.2 Type of input excitation and exciters

The next step in the measurement process involves selecting an excitation function (e.g. random noise) along with an excitation system (e.g. a shaker) that best suits the application. The choice of excitation can make the difference between a good measurement and a poor one. Excitation selection should be approached from both the type of function desired and the type of excitation system available because they are interrelated. The excitation function is the mathematical signal used for the input. The excitation system is the physical mechanism used to apply the signal. Generally, the choice of the excitation function dictates the choice of the excitation system. Different input excitation types can be selected for EMA testing. Which type to choose depends on the user scenario. For example:

- Impact excitation with a modal hammer is often the best solution for smaller homogeneous structures and for field measurements since it is fast, portable, and requires no fixturing
- Sine sweeps, random noise, and other excitation types from a modal shaker/exciter are often the best solution for larger complex structures, where more in-depth analysis is required. Its characteristics compared to an impact test are: provides a high Signal/Noise ratio, the nonlinear response can be minimized for modal extraction, wide frequency band with the possibility to control it, more accurate control of force input direction and location
- For complex structures, multiple shakers might be required if no excitation locations (reference DOFs) can be found where all the modes have sufficiently high participation for proper modal model extraction. Furthermore, with modal shakers, the force level can be precisely controlled

After a list with the input excitation follows a description of the most common exciters: **hammer** for an impact test and **shaker** for a shaker modal test. The hammer (*Figure 2.6*) is used for hammer impact tests and is typically carried out on a simple structure or is used as a quick survey before the more complex modal shaker test. It involves relatively less equipment, namely a sensor without the attachment of the shaker to the structure. In general, it takes little time to set up and carry out the modal test where a smaller amount of measurement points is sufficient. Modal hammers have different sizes and specifications depending on the types of structures they are designed to excite.

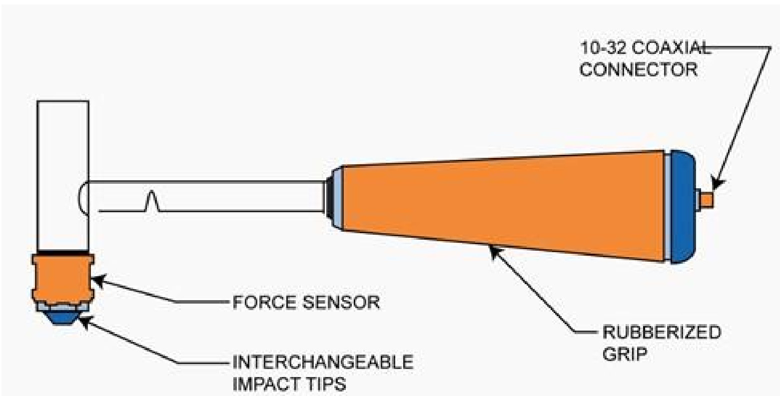

Figure 2.6 – The components of modal impact hammer

The hammer allows to excite only a limited range of frequency compared to the shaker. In order to extend the frequency range of the modal test, the hammer tip plays an important role. A harder tip material provides a larger frequency range, but it can also make it more difficult to avoid double hits and damages on the surface of the component.

A softer hammer tip gives a longer impact time which will give a better energy transfer to the structure at lower frequencies, but the frequency span in the modal test will be smaller (*Figure 2.7*):

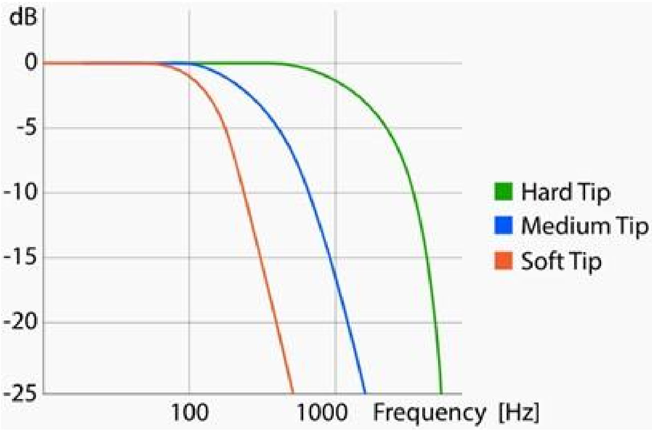

Figure 2.7 – Influence of the tip on the frequency range

The shaker is used to excite large or complex structures and to achieve high-quality modal data. In comparison to modal hammers, modal shakers can excite the structure in a broader frequency range, and with many different signal types, best suited for different structures and ideal for accurate test results. Also, modal shakers can be controlled to excite the structures with certain user-defined excitation levels, which can be used to gain a flat or shaped excitation curve with reference to the excitation frequencies. By controlling the shaker excitation level, the structure can be protected from critically high amplitude deflections, and different levels can be tested to analyze non-linear effects. Multiple shakers can be used together with and without controlled amplitude and/or phase patterns. Using multiple shakers on complex structures gives a more realistic force excitation and better investigation of all mode shapes. There are different types of shakers:

- Permanent magnet shaker, is a general-purpose type that allows the DUT to be fixed directly to the shaker armature, and the vibrating surface area can be enlarged by using a head expander to accommodate larger objects
- Inertial shaker (*Figure 2.8*) is used for structures requiring excitation in lower frequency bands. This shaker is directly connected to the structure, and the inertia motion of the shaker mass provides the necessary force to the structure. Inertial shakers are well-suited primarily for the same application as modal shakers: modal testing as well as a variety of general vibration testing applications. Depending on the dimensions of the structure and the desired excitation frequencies and levels required, either modal shakers or inertial shakers can be used

Figure 2.8 – Inertial shakers with different mass, output force and frequency range

- Modal shaker (*Figure 2.9*) has some advantages over normal vibration shakers when performing modal testing. For instance, instead of fixing the DUT to the shaker armature, a modal shaker is attached to the DUT via a connection rod called a "stinger." Modal shakers are designed with a through-hole armature for the stinger, such that the stinger can be adjusted with the required length to the DUT without moving the shaker, which simplifies the setup:

Figure 2.9 - Modal shakers with different displacement, output force and frequency range

The stinger, *Figure 2.10*, is a thin flexible rod that improves the accuracy of the modal test by mainly transmitting force in the axial direction to the force sensor or impedance head. The lateral flexibility also protects both the DUT and the modal shaker from critical forces.

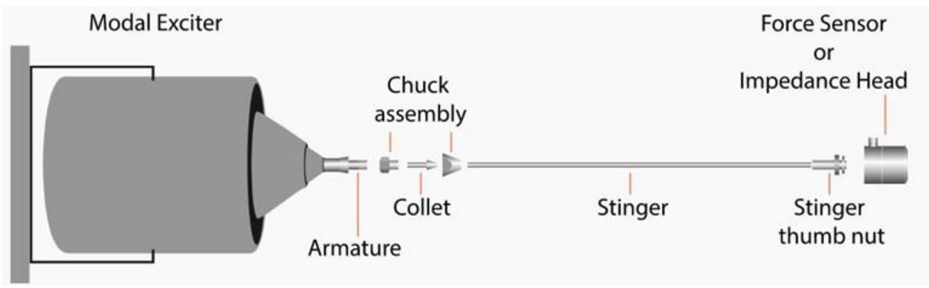

Figure 2.10 – Sketch of a stinger connection between a modal shaker and a force sensor

In order to summarize:

Impulse hammer		**Shaker**	
PROS	*CONS*	*PROS*	*CONS*
• Simple, quick • Various configuration • Accessibility • Price	• Repeatability • Possible damage of the structure • Limited to impulse excitation • Frequency band and resolution	• Repetitive • Various excitation functions • Frequency band and resolution	• Stinger mass and stiffness effects • Repositioning is time consuming • Location accessibility • Price

2.5.3 Set-up important aspects

Shaker mounting and alignment

According to [80], proper force excitation requires the thrust axis of the modal shaker to be aligned with the force sensor mounted on the structure under test. Failure to do so may result in unmeasured forces transmitted to the structure due to the side loading of the sensor and/or possible mechanical or electrical shaker damage due to forcing and rubbing of the armature coil. Alignment issues cause difficulty in any modal test. Care must be taken to provide the best alignment possible to attain the best possible measurements. Modal shakers can be bolted to the floor or any suitable base by using the holes located in the base of the shaker trunnion. According to [81], most times the shaker force levels used are very low in amplitude with no need to bolt the shaker to the floor or another mounting arrangement. However, there may still be some vibration that transmits back through the base to the floor. In these cases, friction against the floor alone may not be enough to stabilize the shaker and it should be firmly affixed to the floor. For low levels of force, hot glue around the base is typically adequate. In instances where hot glue is not sufficient the shaker may be attached with bolts or a clamping arrangement to the floor. Then, by loosening the shaker trunnion body, the modal shaker's angular position can be adjusted by rotating it in the trunnion base.

One way to align the shaker when setting up a test is to use the stinger. In setting up a shaker test, typically the stinger is slid into the shaker's through-hole armature with the force transducer or impedance head attached to the end of the stinger. With the shaker collet loosened, the stinger can be extended in and out of the armature to obtain the desired length. Once this is done, the force gage or impedance head mounting pad can be affixed to the structure. If the alignment is correct, the shaker stinger will easily unthread from the force transducer or impedance head and also thread right back in without any binding or difficulty whatsoever. This should be accomplished without the stinger putting side load onto the shaker armature, sliding easily within the chuck and collet assembly, which assures that the shaker and stinger are properly aligned. At times there may be a threaded mating hole in the structure for mounting the force gage or impedance head and attaching the shaker. Alignment in these situations is much more difficult, requiring that the shaker and/or the test article be moved in such a way that the fixed threaded hole places the stinger exactly in the correct position. The main point is that the shaker must be aligned so that the stinger can be very easily threaded into the force gage or impedance head with no difficulty or binding at all.

On the other way, if the excitation point on the structure requires suspending the shaker, an appropriate fixture that allows adjustments in vertical and longitudinal directions needs to be employed. In a suspended configuration, at very low frequencies below 10 Hz or 5 Hz, the inertia provided by the shaker body may not be sufficient and the shaker may exceed its stroke limits way before it exceeds its force capability. To minimize this issue, often heavy metal block masses are attached (bolted) to the base of the shaker trunnion to enhance the performance, providing more (double or triple) inertia to push against the structure. A typical representation of suspended shaker installation used to laterally excite an automobile for a modal test of a body-in-white car frame is represented in *Figure 2.11*. The stand allows for coarse adjustment of the shaker's vertical and longitudinal positions.

A set of 4-turnbuckles used to hang the shaker to the stand allows for fine adjustment of the shaker position and alignment angle to the structure driving point:

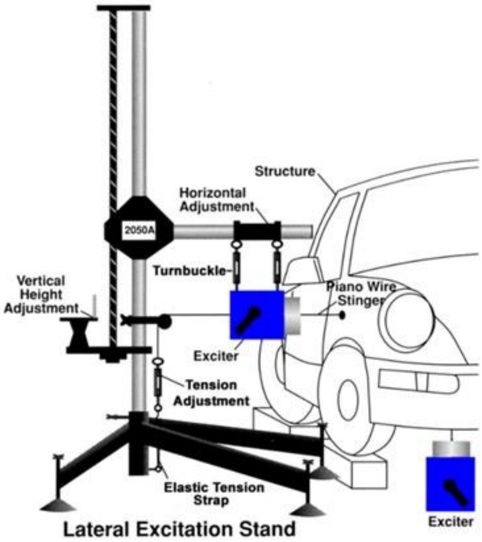

Figure 2.11 – Lateral shaker stand

<u>*Stinger*</u>

As mentioned earlier, a stinger is used on the interface between the shaker and the structure. The primary reason for the use of an exciter stinger is to prevent lateral constraint forces and moments [4]. By design, an exciter applies axial force to the test article with high fidelity. Its armature is designed to not have the freedom to move in a lateral direction, perpendicular to the force axis. The test article, on the other hand, may have lateral motion at the forcing point. This may be due to the geometry of the test article, or due to a lateral mode of vibration. This is especially true if the test article has a soft suspension.

If one were to connect the exciter directly to the forcing point, the exciter will constrain the article's tendency to move laterally. This resistance, even if it is only a small effect, can cause two problems. The first is that the force transducer will have a lateral force and moment that will not be measured accurately, since it senses properly only along its principal axis. The second is that the article feels the combined effect of the intended axial force and the unintended lateral force and moment. As a result, the test article would be excited with forces that are not measured at all. These effects will show up as errors in the force or frequency response measurements.

An exciter stinger has a lateral (bending) stiffness that is much smaller than its axial (compression or tension) stiffness. This means that, when the exciter's armature is stationary, a small lateral movement of the test article causes a small lateral force at the exciter, while a small movement in the axial direction causes a much larger axial force. In other words, axial forces through the stinger are accompanied by little relative axial motion, but lateral forces are accompanied by much larger relative lateral motion. The lateral force and moment generated by lateral motion of the test article are therefore reduced. An additional advantage of the use of a stinger is that a flexible stinger is more forgiving with positioning and aligning the exciter at the forcing point. Without a stinger, you may need to have the mounting centers of the exciter and force transducer within 0.5 mm or closer, in order to get a proper bolted connection. This is difficult to do if you must move the entire exciter and its support. A stinger can tolerate a misalignment of nearly ten times this amount, especially if the stinger is long. This reduces your setup time. Furthermore, the use of a coupling nut makes attachment and removal easy compared to other connection methods.

Another advantage of the use of a stinger is the isolation of the test article from the exciter. If a catastrophe should occur, either by failure of the test suspension or by a transient voltage into the power amplifier, a large force would be created at the connection between exciter and test article. The stinger acts as a mechanical fuse as the weakest link absorbing the damage. As a result, the inexpensive stinger is sacrificed to save the much more expensive exciter and test article.

Mounting technique for force transducers

A very important consideration when mounting force transducers is recognition that force transducers are "directional". This means that force transducers are designed to accurately measure force on only one of its two mounting faces, for example labeled "TOP" and "BASE" on the PCB model 208 series. This is shown in *Figure 2.12*, showing a 208 series force transducer mounted to a 2155G12 rod style stinger. Note that for this model force transducer the "TOP" of the unit is the designed sensing surface and should be mounted directly to the test article. This is because the force transducer itself has mass and stiffness. They are designed and calibrated to read force accurately on one of its mounting faces, and thus need to be installed accordingly.

Figure 2.12 – PCB 208 force transducer

Another important consideration is that the force transducer should always be mounted directly to the test structure, between it and the stinger and shaker assembly. If the force gage is mounted on the exciter side, then the dynamics of the stinger become part of the measured function, and this is not accepted.

Boundary conditions

According to [82], the first step in setting up a structure for frequency response measurements is to consider the fixturing mechanism necessary to obtain the desired constraints (boundary conditions). This is a key step in the process as it affects the overall structural characteristics, particularly for subsequent analyses such as structural modification, finite element correlation and substructure coupling.

Analytically, boundary conditions can be specified in a completely free or completely constrained sense. In testing practice, however, it is generally not possible to fully achieve these conditions. The free condition means that the structure is, in effect, floating in space with no attachments to ground and exhibits rigid body behavior at zero frequency. Physically, this is not realizable, so the structure must be supported in some manner. The constrained condition implies that the motion, displacements/rotations is set to zero. However, most structures exhibit some degree of flexibility at the grounded connections.

In order to approximate the free system, the structure can be suspended from very soft elastic cords or placed on a very soft cushion. By doing this, the structure will be constrained to a degree and the rigid body modes will no longer have zero frequency. However, if a sufficiently soft support system is used, the rigid body frequencies will be much lower than the frequencies of the flexible modes and thus have negligible effect. The rule of thumb for free supports is that the highest rigid body mode frequency must be less than one tenth that of the first flexible mode. If this criterion is met, rigid body modes will have negligible effect on flexible modes.

The implementation of a constrained system is much more difficult to achieve in a test environment. To begin with, the base to which the structure is attached will tend to have some motion of its own. Therefore, it is not going to be purely grounded. Also, the attachment points will have some degree of flexibility due to the bolted, riveted, or welded connections. One possible remedy for these problems is to measure the frequency response of the base at the attachment points over the frequency range of interest. Then, verify that this response is significantly lower than the corresponding response of the structure, in which case it will have a negligible effect. However, the frequency response may not be measurable, but can still influence the test results.

There is not a best practical or appropriate method for supporting a structure for frequency response testing. Each situation has its own characteristics. From a practical standpoint, it would not be feasible to support a large factory machine weighing several tons in a free test state. On the other hand, there may be no convenient way to ground a very small, lightweight device for the constrained test state. A situation could occur, with a satellite for example, where the results of both tests are desired. The free test is required to analyze the satellite's operating environment in space. However, the constrained test is also needed to assess the launch environment attached to the boost vehicle. Another reason for choosing the appropriate boundary conditions is for finite element model correlation or substructure coupling analyses. At any rate, it is certainly important during this phase of the test to ascertain all the conditions in which the results may be used.

2.5.4 Location of excitation

For EMA testing it is important to excite the object at location(s) that will reveal most of its vibrational characteristics. For example, if an object is excited at a location where some vibration mode patterns always have minimum vibration amplitude: nodes of the structure, then these modes will not absorb enough energy to be excited, as represented in *Figure 2.13*:

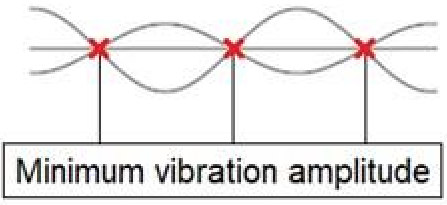

Figure 2.13 – Sketch of nodes position for a given mode

To identify proper excitation locations, pre-testing is often performed where different driving point locations are compared. If a Finite Element Model (FEM) is available this can also be used to determine good excitation locations.

2.5.5 Hardware and sensors to measure forces and responses

For EMA testing, input excitations are usually measured by force transducers or impedance heads at the driving points. An impedance head includes both a force sensor and an accelerometer and is often used to obtain driving point measurements. As an alternative to impedance heads, an accelerometer can be placed close to the force sensor at the excitation points. Response signals are very often measured with accelerometers, but other probes can also be used. Multiple accelerometers are often chosen to optimize data consistency and reduce measurement time, and for larger complex structures the number of accelerometers can easily get large. If the number of response sensors is limited, then "roving" measurement can be used. In this scenario a group of response sensors is moved around between test runs. These sub tests add up to a full measurement of all DOF locations. In the cases where different modes deflect in different orthogonal directions, triaxial accelerometers can be used, since they contain three sensors oriented in an X Y Z pattern. Sensors are available with different sensitivities and thus different frequency ranges. Select the sensors such that they support the frequency range and level range included in the modal test. The weight of the sensors is also important to consider since the object will vibrate differently when the Mass Loading from sensors is relatively high.

Another possibility to measure the deformation are non-contact methods. According to the literature, an example is the Laser Scanning Vibrometer LSV. It is recommended for light-damped and light-weight structures where the mass of cables and accelerometers strongly affect the results. In addition, non-contact methods are suitable nonplanar surfaces because they have a microscopic measuring point, while an accelerometer has a wide contact area. On the other side, one of the main disadvantages of LSV is the high cost of the measurement equipment which is composed by an emitter, a receiver, and a processor to compute the value.

In order to summarize:

Accelerometer		**Laser vibrometer**	
PROS	*CONS*	*PROS*	*CONS*
• High accuracy • Reliable • Easy to use • Price	• Added mass • Cable management • Attachment • Location offset	• Non-contact method • Suitable for curved surfaces • Remote measurement	• Requires reflective surfaces • Accessibility • Limited to small global displacements • Price

2.6 Material damping measurement methods and structures

In order to come out with an effective dynamic test rig for damping measurements, a detailed literature research has been performed in the early stages of the project. The crucial aspects are how to apply the excitation, how to measure the response of the specimen, boundary conditions and test bench set up.

The study conducted by Assarar, related to the "Evaluation of damping of hybrid carbon-flax reinforced composites" [25], derived the dynamic characteristics of the composite materials from the analysis of free flexural vibrations of the test specimens. The equipment is shown in *Figure 2.14*:

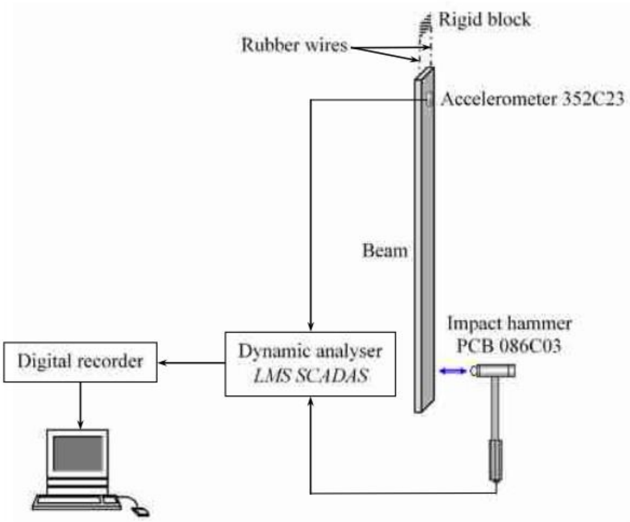

Figure 2.14 - Experimental equipment [29]

The test specimens were supported vertically by two fine rubber threads in such a way to have free-free boundary conditions of the part. An impulse hammer (PCB 086C03 model) was used to induce the excitation of the flexural vibrations of the composite beam. The specimen response was detected by an accelerometer (PCB 352C23 model) which measured the acceleration of the transverse vibrations. Next, the excitation and the response signals were digitalized by a dynamic analyzer that performs the acquisition of the signal, controls the acquisition conditions and the analysis of the acquired signal.

In a similar way, Prabhakaran performed the testing for "Sound and Vibration Damping Properties of Flax Fiber Reinforced Composites" [47]. The damping factor was determined by using the free vibration method as per the ASTM standard E756. The specimens coupon were placed in the form of a cantilever beam structure by using a fixture, then the excitation was applied by an impact hammer.

An accelerometer sensor was placed at the tip of the specimen at the free end, as represented in *Figure 2.15*:

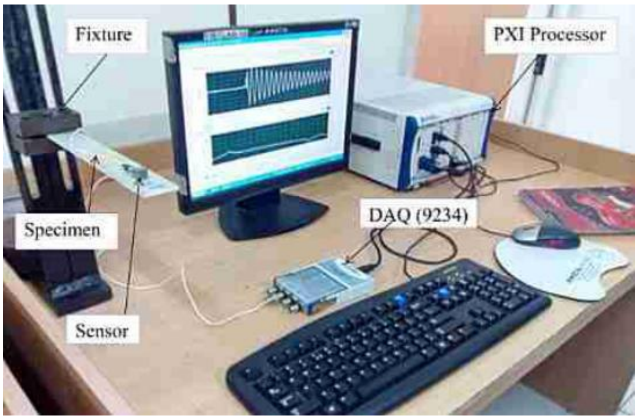

Figure 2.15 - Free vibration test set up [23]

The abovementioned studies aim at the determination of the damping properties at the material level rather than the component level also concerning the structural damping. For this reason, Assarar [25] tested the specimens in free vibration test with free-free boundary condition to avoid the effect of boundary conditions and characterize only the material.

Contrarily, Peumans [24] performed a realistic measurement on the tailplane of a glider to understand the advantages and disadvantages of its theoretical estimations. The system under test was the tailplane of a glider which was connected to a wall via its central mounting points. The tailplane was excited by two mini-shakers (B&K 4810) and the responses were measured at 5 different locations using impedance heads (B&K 8001). Both the generation (HPE 1445A) and recording (HPE 1430A) of the different signals were managed by the VXI measurement system which internally synchronizes these processes at the same sampling frequency. The experimental set up is represented in *Figure 2.16*:

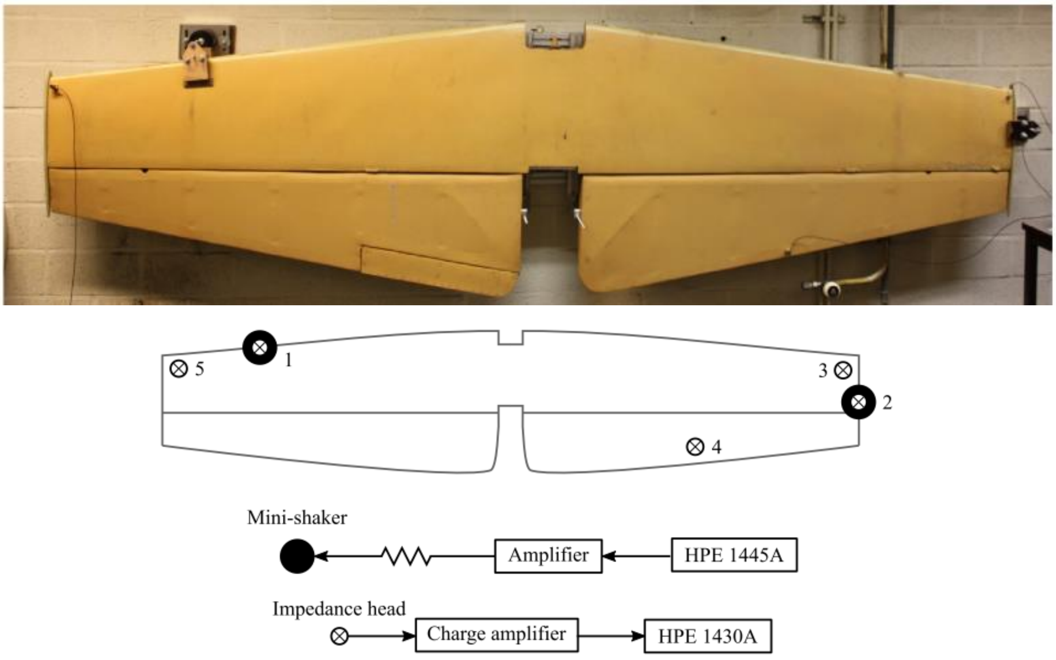

Figure 2.16 - Tailplane experimental set up [53]

In this configuration, opposite to [25], the effect of the central mounting as boundary conditions deeply influences the FRF and consecutively the damping of the component. But, in this case, the goal is not limited to the material point of view, but it is extended to the component level.

Regarding the measure of the response of the part as consequence of the excitation, according to the previous references, the measurements of the dynamic response of the specimens was executed by means of accelerometers. Contrarily, Schedlinski [83] investigated the effect of optical measurement techniques for experimental modal analysis of lightweight structures and its combination exciters, hammer, automatic hammer. At the end, the goal of the study was to compare all the different source of errors and uncertainties originated from each technique. Optical measurement techniques like laser scanning vibrometry (LSV) are most suited when lightweight structures have to be investigated especially if a high spatial measurement resolution of the test piece is demanded for. The lack of physical sensors with discrete mass fully removes the problem of mass-loading the structure during the test and therefore eliminates the risk of adverse varying frequency shifts which may occur when classical roving sensor measurement methods are employed. In the same way, in the “Vibration and damping analysis of a composite blade” [84], to reduce the influence of additional mass on the composite blade, a low mass accelerometer (0.5 g) was used for detecting the dynamic responses of the structure.

According to [83], due to the typically high spatial measurement resolution during LSV measurements manual excitation is prohibitive and thus the test must be automated. Here, shaker excitation is usually the method of choice. However, the required force measurement (sensor) and the coupling of the shaker to the structure (pushrod/stinger) can as well inflict significant perturbations on the system (additional mass of sensor, potential additional forces and moments due to stinger system, damping effects due to micro friction between structure and force sensor).

It was shown by [83], that one of the greatest advantages of LSV, namely the massless and practically interaction free automated response measurement with very high spatial resolution of lightweight structures can be compromised significantly if shaker excitation is employed. The effects observed in Schedlinski’s study included damping changes (presumably) due to micro friction between structure and impedance head, mass loading, and coupling of local stinger modes with global structural modes. The first two effects may have been minimized by selecting small and lightweight sensors; however, this was ultimately limited by physical boundaries. The latter effect may have been minimized by selecting dedicated stinger geometries, e.g. bending-stiff stingers with local, highly flexible coupling in bending direction to shaker and impedance head. Yet these stingers are not always at hand and a complete removal of the systematic errors may not be achieved anyway.

While the influence of the stinger assembly is obvious, the potential influence of a roving hammer, as used for the reference test, on the test results is less apparent: the location and angle of the roving hammer impact position cannot be determined and/or controlled for every measurement point and thus introduces uncertainties. Moreover, the amount of uncertainty may also be related to the actual geometry of the tested structure and to subjective criteria as skill and experience of the hammer operator.

The influences of these uncertainties now depend upon the mode shape of the structure to be investigated. For lower modes with moderate curvature eventual deviations from the ideal impact position will have negligible influence; for higher modes, however, curvatures are usually much more complex and deviations from the ideal impact position may introduce a significant error on amplitude and phase of the estimated mode shape component.

As an alternative to manual hammer excitation automated hammer measurements can be utilized. Next to the capability of fully automating the test sequence without the need for human interaction, automated hammers also bear the advantage of a very good reproducibility of the impact signal in direction, location, and force level. Since the force measurement is obtained at the hammer head itself, no force sensor needs to be attached to the structure to be measured. Thus, a practically interaction free automated measurement can also be achieved from the excitation side. Especially in combination with roving laser scanning measurements, which as well provide a very accurate control of the sensing location (the laser focus typically has a diameter of less than 100 µm), uncertainties as discussed above for the roving hammer test can be minimized which may be particularly beneficial for accurate measurements of higher order mode shapes.

All in one, promising results could be obtained applying the automated hammer technique in combination with LSV and highly reliable data were measured. For the shaker excitation, systematic errors could not be entirely avoided and also an implementation of the impedance head/stinger assembly to the finite element model could not fully account for these effects. Since an elimination of the effects was not possible, using the shaker data may especially jeopardize the successful outcome of subsequent model validation campaigns.

In addition, in case of lightly damped structures, as mentioned by Vantomme [85], the main problems in measuring modal damping ratios are encountered on the purely experimental level. The smallest modification of the structure (e.g. application of an accelerometer) introduces extraneous structural damping, which cannot be distinguished from the actual material damping. Experimentation with several types of excitation techniques and response measurement techniques has led to the conclusion that the only acceptable way of measuring material damping is by using exclusively non-contacting and measurement devices. The experimental set-up implemented by [85] was composed by a loudspeaker to induce the vibrations acoustically, while the response was measured by the Laser Doppler Vibrometer (LDV) in order to avoid any contact. Finally, the boundary conditions of the specimen were of major importance: the extraneous energy dissipated within a clamped boundary can be of the same order of magnitude as the energy dissipated due to material damping. To avoid this effect, completely free boundary conditions were used. Practically, they were realized by suspending the specimen by thin wires, attached at the nodal lines of the considered eigenmode. The suspension wires theoretically do not influence the free modal vibrations when they are fixed exactly on a nodal line. Moreover, according to Cesnik [86] who focused on the Ground Vibration Testing of an Airplane, the support system in free-free condition is typically designed such that its natural frequencies are much lower than the lowest frequency of the specimen to ensure dynamic decoupling from the structure being analyzed. This aspect is also confirmed by Siano [87], that for the “Testing of prototype foam for lightweight technological applications" constrained the specimens with free-free boundary conditions by mean of springs designed in a proper way that natural frequency is one order of magnitude less than first natural frequency of the specimens.

A similar experimental modal analysis of a tailplane was performed by Sadeghi [88]. Where, in order to investigate and verify the results of the numerical model by experimental tests, a cantilever beam was used which was inspired by the tailplane. In vibration analysis of the tails and wings of an aircraft, they could be taken as cantilever beams which are fixed at the base and does not experience any deflection in three directions of the coordinate system. To simulate the physical behavior of the tailplane with a beam, some prerequisites must be observed; therefore, according to Haddadpour and Moosavi [89, 90], the assumptions for modeling the tailplane with a beam are as follows:

1. The aspect ratio of the tailplane must be high enough to be able to express the deflection of the tailplane as one variable function
2. The elastic axis of the tailplane must be straight to avoid coupling between the bending and torsional modes
3. The ratio of thickness to chord in the cross-section of tailplane must be small to avoid bending in the direction of the chord.

The above-mentioned requirements have been investigated and ensured that there is the possibility to simplify the tailplane to a cantilever beam, therefore, in the study an aluminum beam with the rectangular cross-section was used to carry out the experimental tests, which was anchored at one end by rigid components. In the experiment performed by [88], in order to stimulate the beam in EMA test, a shaker was used to apply a random force with regard to the aforementioned requisites in material and methods section; the response of the beam was measured by three accelerometers which are installed to the beam. The setup is represented in *Figure 2.17*:

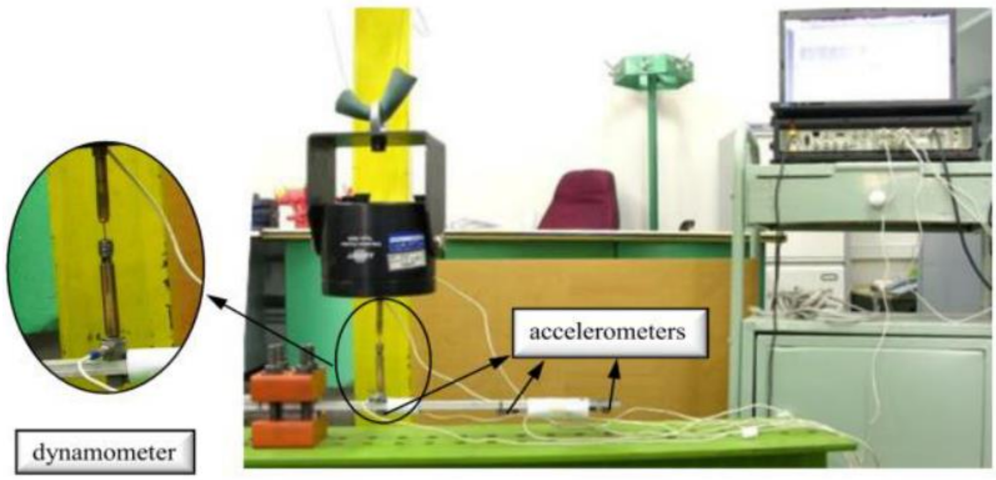

Figure 2.17 – Set up of the beam for modal test [59]

On the other side, in order to extract the modal parameters of the system by Operational Modal Analysis (OMA) method, one can use natural and environmental excitations, but to investigate the effects of noise in a controlled manner, and to be able to compare the results of EMA and

OMA in the same condition, the artificial excitation namely the shaker with the random force was used. The sampling frequency of the applied random force is 2000 Hz for extracting the modal parameters in the frequency range of 0-1000 Hz. The hardware equipment of tests setup consisted of B&K 48 N electromagnetic shaker model 4809, B&K piezo-electric accelerometer 100 mV/g sensitivity model 4508, B&K data acquisition model 3560C, B&K amplifier model 2706, anti-noise transfer cables.

Regarding accelerometers and cables to use in the experiments, Ruiz [91] tested honeycomb cells beam in cantilever boundary conditions. In the experiment, the beam response was detected near the free end of the beam using an ICP accelerometer (352C65 from PCB, weight 2 g). The connection cable (10 – 32 plug to BNC) was only 1.5 ft long and was taped on the clamping block to minimize the impact on damping. Another important aspect treated by [91] is related to fastened connections, where the screws must be tightened by a torque wrench to apply identical pressure on the clamping area and to insure measurement repeatability. Moreover, the clamping area of the specimen, should be properly prepared to ensure local stiffness and resistance to avoid localized effects.

According to Damping Technologies Inc. [92], the ASTM (American Society for Testing and Materials) E-756, Vibrating Beam Technique was utilized to characterize the dynamic mechanical properties of the viscoelastic materials. It consists of the evaluation of the resonance frequencies and modal loss factor of a cantilever beam consisting wholly of the test material, or of the test material combined with metal base beams (assuming that the test material cannot support its own weight). Using standard equations governing the particular test specimen configuration, this data is then combined with specimen geometry, specimen weight densities, and base beam modulus values to yield the dynamic mechanical properties of the test material itself. As presented by [92], the properties obtained are useful for material selection tasks based on modulus and material loss factor as a function of temperature and frequency.

Depending on the modulus of the viscoelastic material to be evaluated and the properties required, one of the four test specimens are constructed as shown in *Figure 2.18.* It represents the vibrating beam test article configurations by ASTM E-756:

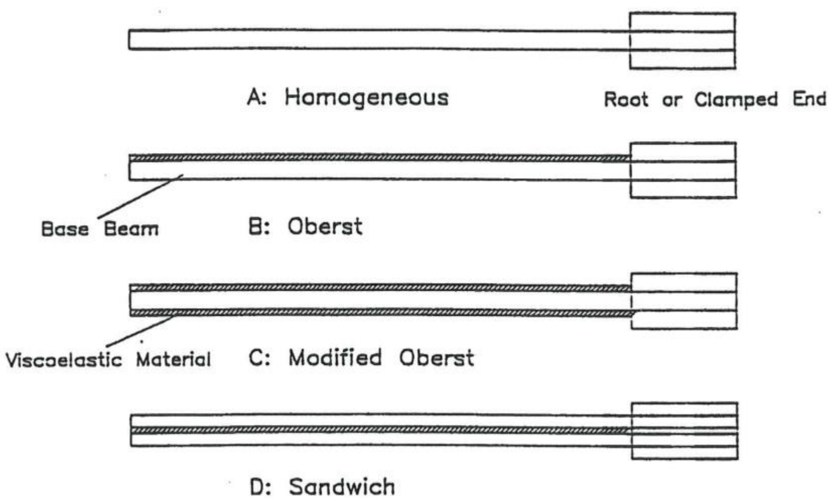

Figure 2.18 - ASTM E-756 Vibrating Beam Test Article Configurations

The experiment performed by Damping Technologies Inc. [92] according to ASTM E-756 considers a Modified Oberst beam. A piezoelectric crystal was bonded to the cantilever beam specimen near the clamped end using a very stiff structural adhesive that remain stiff for the entire range of interest. The piezoelectric crystal was utilized to measure the response of the cantilever beam during data acquisition. The cantilever beam sample was mounted in a test apparatus which provides a firm boundary condition at the clamped end. Excitation was provided at the free end of the beam using a non-contacting magnetic exciter. In conclusion, ASTM E-756 inputs the “composite property” data sets obtained via modified Oberst beam, the specimen geometry, the specimen densities, and the base beam modulus data into the characteristic standard equations which governs the particular test specimen configuration to yield the dynamic mechanical properties of the viscoelastic material itself, independent of the base beams or of geometry. This step yields discrete values of Young’s modulus and material loss factor for data acquisition test frequencies and temperatures.

Other important aspects regarding accelerometers positioning and exciters are provided by Zappino [93]. According to the dynamic testing of Dardo Aspect, a wet-laminate full-composite Very-Light Airplane (VLA) [93], accelerometers were located on the positions represented in *Figure 2.19*, with the aim of measuring all the important natural frequencies and mode shapes:

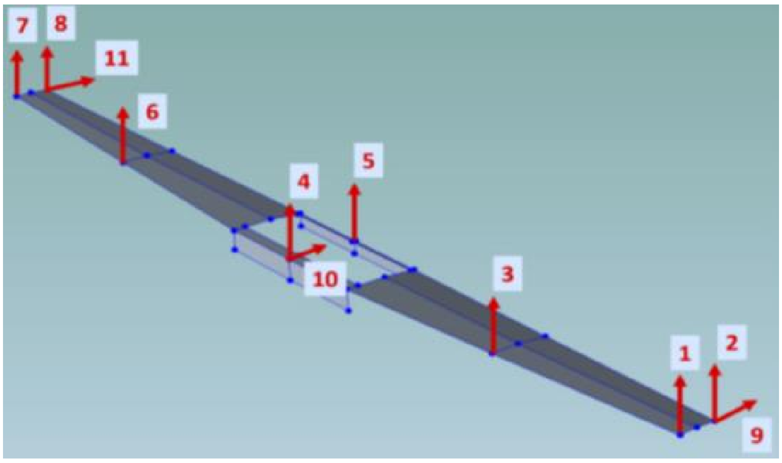

Figure 2.19 – Accelerometers in the in and out of plane directions

The figure represents the free-free boundary condition test of the wing of the Dardo Aspect VLA. Accelerometers were not positioned only in the longitudinal direction to measure deflection; they were arranged also in the transverse direction to detect the presence of possible torsional modes due to the excitation. The response of the structure due to the excitation was measured by 12 accelerometers from DeltaTron with a sensitivity of 10 mV/ms^2. The accelerometers are uniaxial.

Regarding the position of the accelerometers, a detailed consideration based on the experience and theoretical techniques was performed by Ciavarella [94] which carried out an extensive ground vibration test of the H145 Airbus® helicopter. The Ground Vibration Test (GVT) is one of the key milestones in the characterization of an aerospace structure, allowing to describe its structural dynamic behavior for validating and improving its structural dynamic model. Finding an optimal sensor placement is one of the main expectations behind the pre-test analysis. It is known that the choice of sensors locations has a strong influence on the quality and amount of modal test data, and therefore also in the correlation with FE Models. While in the past engineering experience was the main driver of the choice, nowadays several methods have been developed to support the test planning. The procedure followed by [94] started from a H145 FE model. The pre-test analysis began with the selection of target modes from the initial numerical modes set based on modal participation and energy considerations (e.g. modal effective mass or kinetic energy). A set of candidate sensor locations was then defined by the engineer, who had to consider with experienced eyes factors like accessibility, geometry, and costs. Fundamental was then the selection of the optimal locations and directions to position the acceleration sensors and to excite the structure. For this purpose, several methods were used: some metrics based their selection on the observability of target modes, using information about modal displacement or energy (normalized modal displacement, nodal kinetic energy); other methods proceeded to iteratively eliminate sensors from the set of candidates in a way to optimally maintain linear independence or orthogonality between mode shapes. This was the case of effective independence method, elimination by MAC or iterative Guyan reduction. After all these information were acquired and merged together yielding the final sensors setup, the FE model was truncated and converted to the test model using the retained sensor locations. Reduced mass and stiffness matrices were also calculated.

Regarding the exciter used to apply the excitation, important aspects to investigate are the type of shaker, the entity of the force and the connection to the test rig. The GVT performed by Peeters [95] on a large aircraft adopted six LDS permanent magnet shakers model V450 having a sine force peak of 311 N and a peak-to-peak stroke of 19 mm. Labworks Model PA-138 shaker amplifiers provided the power. The forces injected into the aircraft were measured by PCB 208C03 force cells and the aircraft vibration response was measured by PCB 333B32 and PCB 393B04 accelerometers.

Usually, most of the tests adopt a sine excitation, but there is no prescription about the amount of force to apply. According to Bono [96], which elaborated “Modal Testing Excitation Guidelines”, the excitation levels for modal testing are usually reasonably low. There is no need to provide large force levels for conducting a modal test especially if appropriate response transducers (accelerometers) are selected with good sensitivity and resolution, as well as high quality, high resolution (24-bit technology is standard in today’s commercial offerings) data acquisition systems. The level only needs to be sufficient to make good measurements. In fact, larger force levels tend to overdrive the structure, exciting nonlinear characteristics of the structure and providing poorer overall measurements than with lower-level force tests. For this reason, again, on larger structures, it is often desirable to use multiple shakers at lower force levels to distribute force than a single shaker operating at high level forces. In addition, the question on how many shakers are required by a certain modal test is often hard to answer. Often test systems are limited by the total number of output sources in the data acquisition system or shakers available in the test lab for modal testing. Usually, two to four shakers are sufficient for most tests, particularly when testing larger structures like automobiles or aircraft. Generally, tests with more than five shakers are rare. Ultimately, there need to be enough shakers acting as reference locations that are positioned so that the modes of interest of the structure are adequately excited and observed, and good frequency response measurements are obtained. This includes having multiple shaker/reference locations to resolve repeated roots and/or closely spaced modes.

Regarding the set-up of the force generator, according to [96], electrodynamic shakers or exciters are commonly used in experimental modal analysis. The practical aspects regarding the setup of the shakers, stingers and transducers are often the source of test difficulties and avoidable measurement errors. An important component to be added to the shaker is the stinger. According to [81], the stinger decouples the shaker system from the structure and applies force to the structure. The stinger is designed to be rigid in the axial direction and flexible in the lateral direction. Force transducers measure axial force but still transmit forces into the structure through the transducer's stiff casing. Therefore, any sideloads transmitted to the structure by the stinger through the force transducer are unmeasured and contribute noise on the measurement. A stinger that is properly designed, selected, and aligned will reduce or eliminate this potential problem.

2.7 PyFBS

According to Trainotti [97], pyFBS is a Python package for Frequency Based Sub-structuring, Transfer Path Analysis and, as a new addition, multi-reference modal identification. It enables the user to use state-of-the-art dynamic sub-structuring methodologies in an intuitive manner with a practical approach using data obtained from experiments, or theoretical by importing the FE model before performing the experiment. The features provided by pyFBS are:

- 3D display
- FRF synthetization
- Virtual Point Transformation
- System Equivalent Model Mixing
- Singular Vector Transformation
- Experimental Modal Analysis

The pyFBS was developed as a part of collaboration between the Laboratory for Dynamics of Machines and Structures (LADISK), University of Ljubljana, Faculty of Mechanical Engineering (UL FME) and the Chair of Applied Mechanics (AM), Technical University of Munich (TUM).

In detail, pyFBS will be used to perform dynamic sub-structuring of the assembly composed by the I-beam and the test rig by mean of the virtual point transformation.

2.7.1 Frequency Based Sub-structuring

The methodology to divide large and complex systems into several subsystems is a common practice in the field of structural dynamics. Structural dynamic analyses can be carried out more efficiently if complex systems are divided into smaller subsystems, analyzed separately, and later coupled using dynamic sub-structuring (DS) methods. In terms of the modeling domain, a frequency-based sub-structuring (FBS) is often preferred by experimentalists due to its ease of use and implementation with directly measured Frequency Response Functions (FRFs). In this context, datasets of measured transfer functions constitute the dynamic models of the substructures involved in the assembly/disassembly process. One can distinguish between coupling and decoupling of dynamic systems as follows:

- Coupling is the process of assembly sub-systems by imposing physical boundary conditions to the common interface
- Decoupling aims at identifying a standalone sub-system from the assembly by removing the influence of the other subsystem exerted through the interface connection.

In any case, the dynamic interaction between sub-systems (or substructures) is confined to a set of interface DOFs. Let's consider the linearized equations of motion (*Equation 2.9*) of a system composed by n - substructures in the frequency domain:

$$Z(\omega)u(\omega) = f(\omega) + g(\omega) \tag{2.9}$$

In *Equation 2.9,* $Z(\omega)$ represents the block-diagonal frequency-dependent dynamic stiffness matrix of individual subsystems impedances, the vector $u(\omega)$ represents the displacements to the external force vector $f(\omega)$, applied to the assembly, and $g(\omega)$ is the vector of reaction forces between the substructures. Each term is detailed in *2.10*:

$$Z(\omega) = \begin{bmatrix} Z^1(\omega) & \cdots & 0 \\ \vdots & \ddots & \vdots \\ 0 & \cdots & Z^n(\omega) \end{bmatrix},\ u(\omega) = \begin{bmatrix} u^1(\omega) \\ \vdots \\ u^n(\omega) \end{bmatrix},\ f(\omega) = \begin{bmatrix} f^1(\omega) \\ \vdots \\ f^n(\omega) \end{bmatrix},\ g(\omega) = \begin{bmatrix} g^1(\omega) \\ \vdots \\ g^n(\omega) \end{bmatrix} \quad \textbf{(2.10)}$$

Let's now assume two interacting sub-systems to be assembled, represented in *Figure 2.20*:

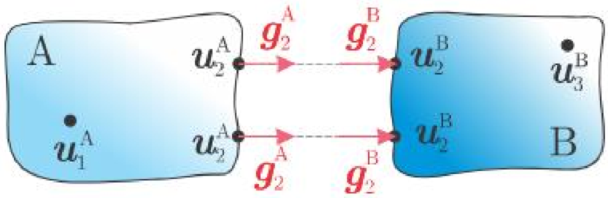

Figure 2.20 - Two sub-systems to be dynamically assembled (pyFBS)

Considering a partition between internal $(\star)1$, $(\star)3$ and interface $(\star)2$ DOFs, the vector of displacements, forces and reaction forces can be written as represented in *2.11*:

$$u = \begin{bmatrix} u_1^A \\ u_2^A \\ u_2^B \\ u_3^B \end{bmatrix}, \qquad f = \begin{bmatrix} f_1^A \\ f_2^A \\ f_2^B \\ f_3^B \end{bmatrix}, \qquad g = \begin{bmatrix} 0 \\ g_2^A \\ g_2^B \\ 0 \end{bmatrix} \quad \textbf{(2.11)}$$

In order to assembly/disassembly the sub-systems' dynamics, two physical conditions must be enforced:

- Compatibility of displacements, the first interface condition, represented in *Equation 2.12*, to be fulfilled is the compatibility of displacements at the matching interface DOFs of the two subsystems:

  $$u_2^A = u_2^B \quad \textbf{(2.12)}$$

  This can be re-formulated by operating on the full set of physical DOFs u as represented in *Equation 2.13*:

  $$B = 0; \qquad B = [0 \quad -I \quad I \quad 0] \quad \textbf{(2.13)}$$

  The signed Boolean matrix B maps the corresponding matching interface DOFs. Each row of the matrix identifies a single pair of interface DOFs to be connected.

Alternatively, as represented in *Equation 2.14*, by substituting the physical coordinates u with a set of unique generalized coordinates q:

$$u = Lq \longrightarrow \begin{cases} u_1^A = q_1 \\ u_2^A = q_2 \\ u_2^B = q_2 \\ u_3^B = q_3 \end{cases}; \qquad L = \begin{bmatrix} I & 0 & 0 \\ 0 & I & 0 \\ 0 & I & 0 \\ 0 & 0 & I \end{bmatrix} \tag{2.14}$$

The localization Boolean matrix L maps the physical DOFs of all sub-systems to the generalized global set q. By using a unique set of coordinates q, according to *Equation 2.15*, it is made implicit that the compatibility of displacements for u is automatically satisfied:

$$Bu = BLq = 0 \qquad \forall q \tag{2.15}$$

This means that, according to *2.16*, B and L are each other's null-spaces:

$$\begin{aligned} L &= null(B), \\ B^T &= null(L^T) \end{aligned} \tag{2.16}$$

- Equilibrium of forces, the second condition requires the force equilibrium at matching interface DOFs to be satisfied according to the "actio et reactio" principle, *Equation 2.17*:

$$g_2^A = -g_2^B \tag{2.17}$$

By back projecting the vector of reaction forces g to the Boolean localization space L, as represented in *Equation 2.18*, the interface forces are directly paired:

$$L^T g = 0 \longrightarrow \begin{cases} g_1^A = 0 \\ g_2^A + g_2^B = 0 \\ g_3^B = 0 \end{cases} \tag{2.18}$$

Alternatively, by using the signed Boolean matrix B the reaction forces g, are replaced by a set of Lagrange multipliers λ, as represented in *Equation 2.19*, which represent the intensity of the interface forces:

$$g = -B^T\lambda \longrightarrow \begin{cases} g_1^A = 0 \\ g_2^A = \lambda \\ g_2^B = -\lambda \\ g_3^B = 0 \end{cases} \tag{2.19}$$

Using the definition of Lagrange multipliers for the interface forces automatically satisfies the equilibrium condition.

This can be verified by exploiting the mathematical relationship between L and B, represented in *Equation 2.20*:

$$L^T g = -L^T B^T \lambda = 0 \qquad \forall g \tag{2.20}$$

Combining the equation of motion with the introduced interface conditions, the frequency-based formulation of the sub-structuring problem becomes (*Equation 2.21*):

$$\begin{cases} Z(\omega)u(\omega) = f(\omega) + g(\omega) \\ Bu(\omega) = 0 \\ L^T g(\omega) = 0 \end{cases} \tag{2.21}$$

From here on the frequency-dependence will be omitted for simplicity. Solving the above equations of motion could be expensive due to the interface unknown to be resolved, i.e. u and g. Hence, the primal and dual formulations:

- Primal: satisfying a priori compatibility and solving for a unique set of interface displacements
- Dual: satisfying a priori the equilibrium condition and solving for a new set of interface forces.

The dual decoupling problem consists of finding the interface forces that suppress the influence of A on AB, thus isolating the uncoupled response of subsystem B. Starting from the general formulation of the sub-structuring problem, the dual approach chooses Lagrange multipliers λ as set of coupling forces according to the relation $g = -B^T\lambda$. The equilibrium is thus satisfied a priori. The equations of motion of the sub-structuring problem become *Equation 2.22*:

$$\begin{cases} Z^{A|B}u = f - B^T\lambda \\ Bu = 0 \end{cases} \tag{2.22}$$

This is often written in a symmetrical form as *Equation 2.23*:

$$\begin{bmatrix} Z^{A|B} & B^T \\ B & 0 \end{bmatrix} \begin{bmatrix} u \\ \lambda \end{bmatrix} = \begin{bmatrix} f \\ 0 \end{bmatrix} \tag{2.23}$$

Following the definition of decoupling, the equilibrium condition states that the interface forces that ensure the compatibility act in opposite direction on the assembled system AB. To solve the system equations, let's first write them in the admittance notation as represented in *Equation 2.24*:

$$\begin{cases} u = Y^{AB|A}(f - B^T\lambda) \\ Bu = 0 \end{cases}, \qquad Y^{AB|A} = \begin{bmatrix} Y^{AB} & 0 \\ 0 & -Y^A \end{bmatrix} \tag{2.24}$$

The decoupling can be formulated as a standard coupling procedure with a negative admittance for the system to be disassembled.

By substituting the first line in the second line (compatibility constraint) and solving for λ, as represented in *Equation 2.25*:

$$\lambda = (BY^{AB|A}B^T)^{-1}BY^{AB|A}f \tag{2.25}$$

As represented in *Equation 2.26*, by substituting back the λ in the first line of the governing equation of motion:

$$u = Y^{AB|A}(f - B^T\lambda) \longrightarrow u = Y^{AB|A}f - Y^{AB|A}B^T(BY^{AB|A}B^T)^{-1}BY^{AB|A}f \tag{2.26}$$

Due to its derivation, this formulation is referred to as Lagrange multipliers - frequency based sub-structuring (LM-FBS). The dually assembled admittance is written as *Equation 2.27*:

$$\hat{Y}^B = \left[I - Y^{AB|A}B^T(BY^{AB|A}B^T)^{-1}B\right]Y^{AB|A} \tag{2.27}$$

2.7.2 Virtual Point Transformation - VPT

The main challenges when decoupling two sub-structures are given by the interface of the two or more parts, as represented in *Figure 2.21*:

- Non-collocated degrees of freedom on neighboring substructures
- Lack of rotational degrees of freedom due to limitations in measurement equipment and excitation capabilities
- Random and systematic measurement errors.

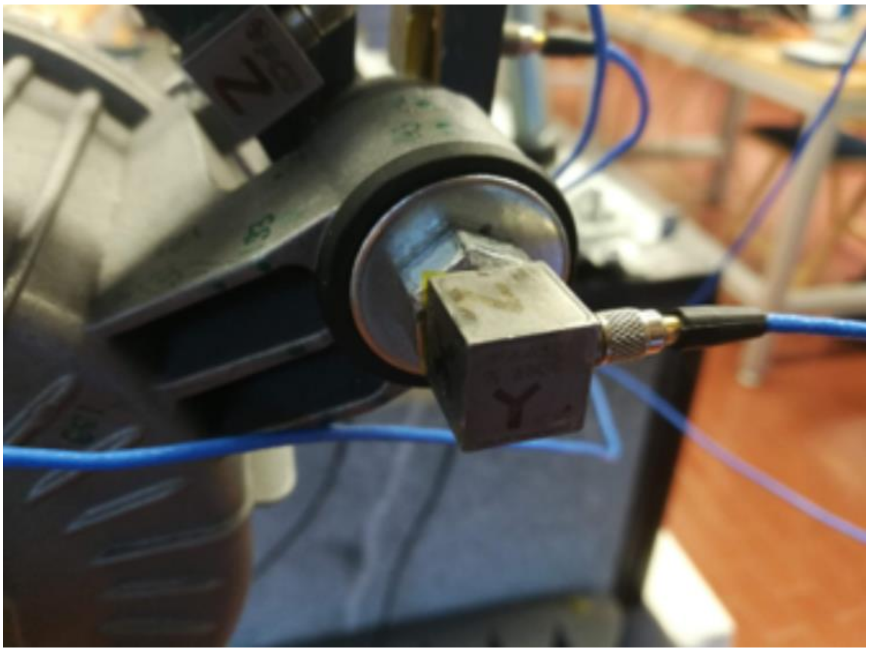

Figure 2.21 – Interface of two sub-structures (pyFBS)

The VPT offers a solution for each of the abovementioned problems as follows:

- Admittance matrix can be reconstructed at any point at the interface
- Rotational degrees of freedom can be reconstructed from ordinary translational measurement campaigns
- Due to the reduction of measured responses and forces measurement errors are filtered out.

In order to explain the Virtual Point Transformation, let us consider a simple interface of two parts where the response is captured using tri-axial accelerometers and excited with unidirectional forces around the interface and the as depicted below. The virtual point is placed in the middle of the hole, *Figure 2.22*:

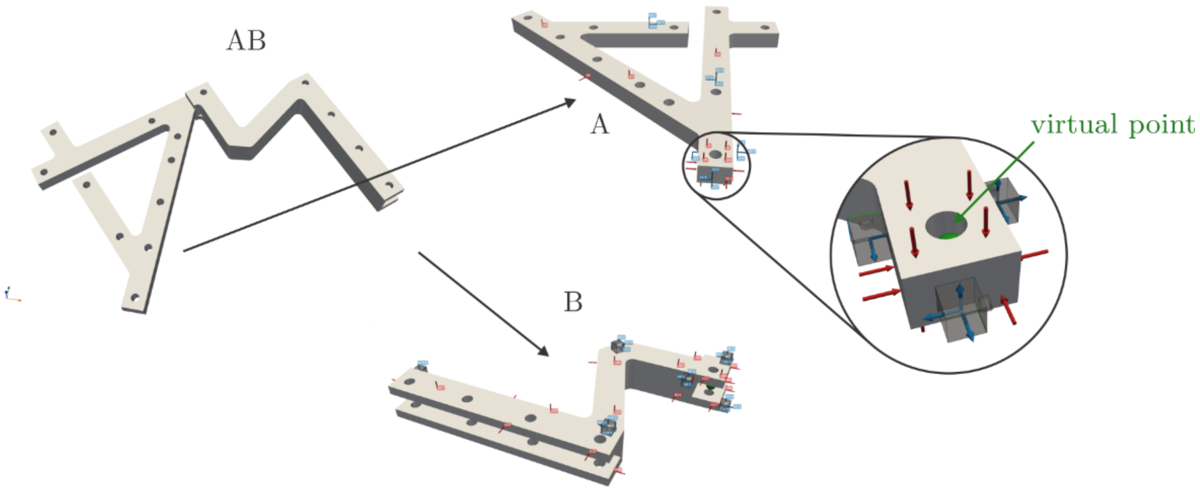

Figure 2.22 – Virtual Point position of two decoupled sub-systems (pyFBS)

By observing the interface in the magnified view, the modes that dominantly represent the response at the translational motions in x, y and z axis, as well as rotations about x, y and z. Rather that considering it as a solid interface between two bodies, a more intuitive way to represent rigid connection is to use spider elements (RBE2 or RBE3), connecting the virtual point to the center of mass of the accelerometers. Therefore, the first assumption to apply to VPT is to reduce the area of interest to the interface which can be considered rigid. Then, tri-axial accelerometer is used to measure the response in the proximity of the interface, *Figure 2.23*:

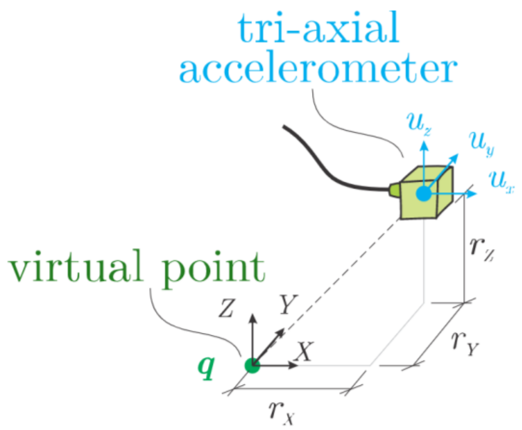

Figure 2.23 – Position of the tri-axial accelerometer with respect to the VP (pyFBS)

By assuming the interface as perfectly rigid, according to *Equation 2.28*, the VP has only six rigid displacements:

$$q = \left[q_X,\ q_Y,\ q_Z,\ q_{\theta_X},\ q_{\theta_Y},\ q_{\theta_Z}\right]^T \tag{2.28}$$

While displacement u_X (and in the other directions as well) can be expressed from q (displacements of the Virtual Point), the movements of the VP contributing to the u_X response (in the VP coordinate system XYZ) can be indicated as (*Figure 2.24*):

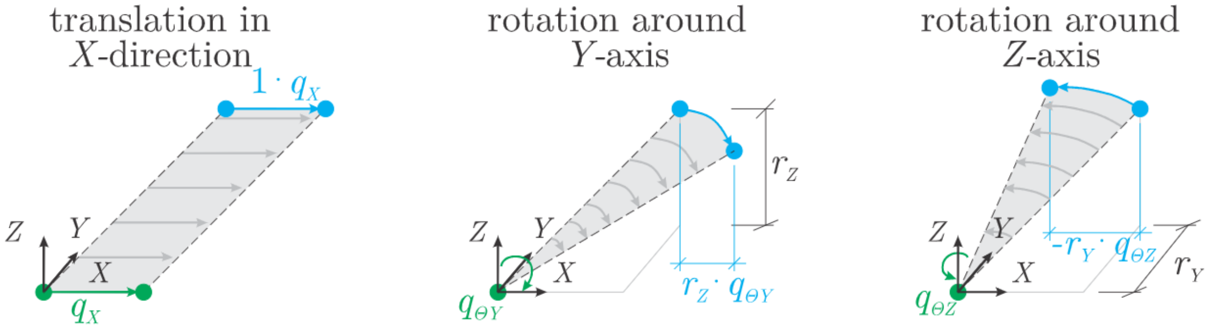

Figure 2.24 – Displacements u_X, u_Y, u_Z expressed with respect the VP (pyFBS)

By repeating also for Y and Z coordinates, the responses are represented in *Equations 2.29*, *2.30* and *2.31*:

$$u_X^i = \underbrace{1 \cdot q_X}_{\text{contribution from X translation}} + 0 \cdot q_Y + 0 \cdot q_Z + 0 \cdot q_{\theta_X} + \underbrace{r_Z \cdot q_{\theta_Y}}_{\text{contribution from Y rotation}} + \underbrace{-r_Y \cdot q_{\theta_Z}}_{\text{contribution from Z rotation}} \tag{2.29}$$

$$u_Y^i = 0 \cdot q_X + \underbrace{1 \cdot q_Y}_{\text{contribution from Y translation}} + 0 \cdot q_Z + \underbrace{-\, r_Z \cdot q_{\theta_X}}_{\text{contribution from X rotation}} + 0 \cdot q_{\theta_Y} + \underbrace{r_X \cdot q_{\theta_Z}}_{\text{contribution from Z rotation}} \tag{2.30}$$

$$u_Z^i = 0 \cdot q_X + 0 \cdot q_Y + \underbrace{1 \cdot q_Z}_{\text{contribution from Z translation}} + \underbrace{r_Y \cdot q_{\theta_X}}_{\text{contribution from X rotation}} - \underbrace{r_X \cdot q_{\theta_Y}}_{\text{contribution from Y rotation}} + 0 \cdot q_{\theta_Z} \tag{2.31}$$

By casting the three equations in matrix form, the relation between one tri-axial sensor and a virtual point can be written as follows in *Equation 2.32*:

$$\begin{bmatrix} u_X^i \\ u_Y^i \\ u_Z^i \end{bmatrix} = \begin{bmatrix} 1 & 0 & 0 & 0 & r_Z & -r_Y \\ 0 & 1 & 0 & -r_Z & 0 & r_X \\ 0 & 0 & 1 & r_Y & -r_X & 0 \end{bmatrix} \begin{bmatrix} q_X \\ q_Y \\ q_Z \\ q_{\theta_X} \\ q_{\theta_Y} \\ q_{\theta_Z} \end{bmatrix} \tag{2.32}$$

The columns of the matrix are rigid body motions, which are assembled from relative sensor position with regard to the VP. For cases where the orientation of sensor channels and VP mismatch, the rigid body motions are transformed in the direction of the sensor channels, *Figure 2.25*:

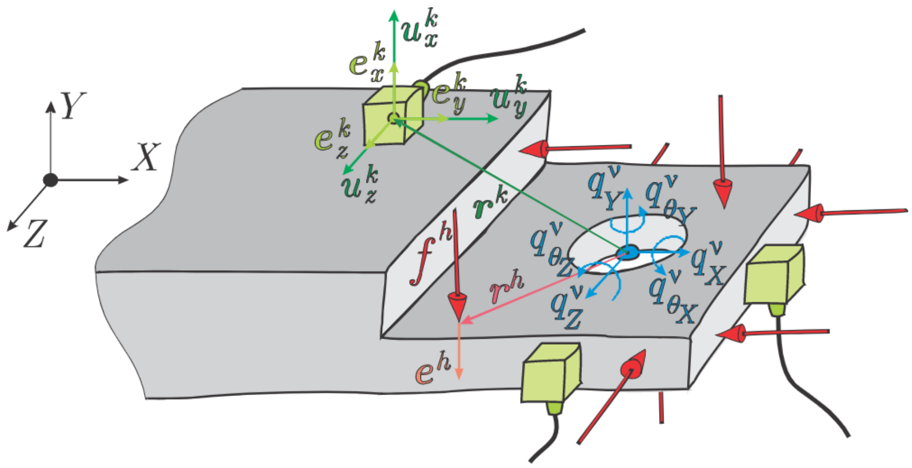

Figure 2.25 – Orientation of sensor channels and VP mismatch (pyFBS)

Where $[e_{x,X}, e_{x,Y}, e_{x,Z}]^T$ is the orientation of x sensor channel, $[e_{y,X}, e_{y,Y}, e_{y,Z}]^T$ is the orientation of y sensor channel and $[e_{z,X}, e_{z,Y}, e_{z,Z}]^T$ is the orientation of z sensor channel, all in XYZ coordinates system. The three equations are represented in matrix form in *Equation 2.33*:

$$\begin{bmatrix} u_X^i \\ u_Y^i \\ u_Z^i \end{bmatrix} = \begin{bmatrix} e_{x,X} & e_{x,Y} & e_{x,Z} \\ e_{y,X} & e_{y,Y} & e_{y,Z} \\ e_{z,X} & e_{z,Y} & e_{z,Z} \end{bmatrix} \begin{bmatrix} 1 & 0 & 0 & 0 & r_Z & -r_Y \\ 0 & 1 & 0 & -r_Z & 0 & r_X \\ 0 & 0 & 1 & r_Y & -r_X & 0 \end{bmatrix} q \longrightarrow u^i = R_i q \tag{2.33}$$

In order to describe q, two tri-axial accelerometers (or 6 channels) are not sufficient as it is not possible to describe all three rotations of the VP. Therefore, as according to *Figure 2.26*, it is suggested to use three or more tri-axial accelerometers:

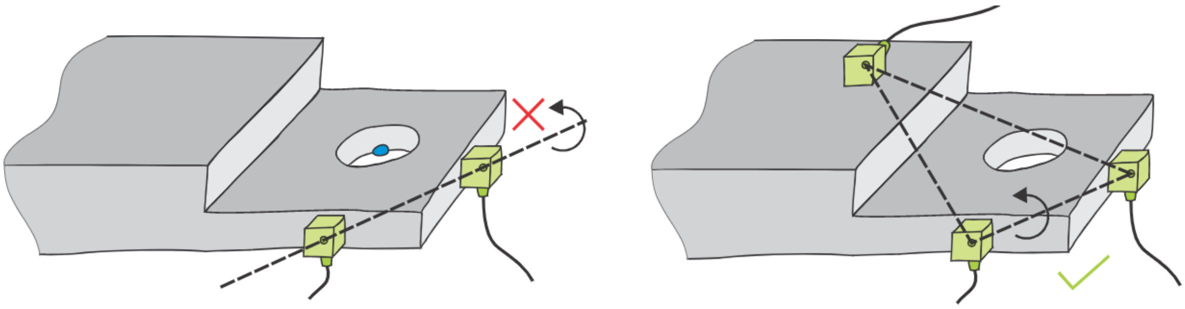

Figure 2.26 – Position of the accelerometers (pyFBS)

In addition, as represented in *Figure 2.26*, the accelerometers cannot be placed along the same line otherwise it will not be possible to uniquely characterize the VP. So, let us assemble all relations between measured sensors displacements u and q in *Equation 2.34*:

$$\begin{bmatrix} u^1 \\ u^2 \\ u^3 \\ \vdots \end{bmatrix} = \begin{bmatrix} R_1 & & & \\ & R_2 & & \\ & & R_3 & \\ & & & \ddots \end{bmatrix} q \longrightarrow u = Rq \tag{2.34}$$

According to the above-mentioned procedure, the principal assumption of the method is the rigidity of the interface, but is the interface really rigid? Unfortunately, rigidity assumption is not always valid. Therefore, it is not possible to exactly determine the vector u from q. This is illustrated in *Equation 2.35* by introducing a residual μ:

$$u = Rq + \mu \tag{2.35}$$

To gain more flexibility over the transformation, symmetric weighting matrix $W$is introduced. If necessary, it could be possible to add more weight or even exclude specific displacements from the VPT. The W can also be defined per frequency line, so various displacements can be managed across the entire frequency range. In most of the cases, W is simply selected to be an identity matrix, which means that the experimental results are reliable, and all displacements from u are treated equally (*Equation 2.36*):

$$Wu = WRq + W\mu \tag{2.36}$$

Now, let us pre-multiply the *Equation 2.36* by R^T, obtaining *Equation 2.37*:

$$R^TWu = R^TWRq + R^TW\mu \tag{2.37}$$

Assuming that the interface is rigid, $R^TW\mu$ can be neglected. *Equation 2.37* is solved for q, obtaining *Equation 2.38*:

$$q = (R^TWR)^{-1}R^TWu = T_u u \longrightarrow T_u = (R^TWR)^{-1}R^TW \tag{2.38}$$

The matrix T_u is a displacement transformation matrix that projects displacements captured by the tri-axial accelerometers into the virtual point. q is found in a least-square sense. Since only rigid body motions are assumed, flexible interface motion is also filtered out from q. That means that the interface problem is weakened. For cases where the interface exhibits non-neglectable flexible behavior, additional DOFs can be added to the VP to describe this flexible motion. Simplistic extension that also incorporates interface extension, torsion, skewing, and bending was already proposed. If one would include these DOFs to the VP, care should be taken that the collocated VPs all have identical DOFs or else they are not compatible (due to this use of singular vectors in R is discouraged). Inclusion of flexible motions reflects in modified R_u matrix, where additional motions are added to the columns. Also, additional measurements of u are required to preserve a full-rank matrix. Hence it is advised only dominant motions are picked.

Similar procedure (standard optimization is used instead of least-squares solution) is applied to transform interface loads onto the VP. If rigid interface is again the case, as represented in *Equation 2.39*, three translational forces and three moments in the VP $\left(m = [m_X, m_Y, m_Z, m_{\theta_X}, m_{\theta_Y}, m_{\theta_Z}]^T\right)$ are reconstructed by projecting measured excitations around VP onto the displacement of the accelerometers:

$$f = WR(R^TWR)^{-1} \qquad m = T_f^T m \longrightarrow T_f^T = WR(R^TWR)^{-1} \tag{2.39}$$

With both transformation matrices, virtual point FRFs can be computed according to *Equation 2.40* (it's the admittance at the virtual point, it is based on the measured responses and excitations around the interface Y_{uf}):

$$Y_{qm} = T_u Y_{uf} T_f^T \tag{2.40}$$

where Y_{uf} is the measured FRF matrix and Y_{qm} is the full-DOF VP FRF matrix with perfectly collocated motions and loads. That means that the VP FRF matrix should be reciprocal. Therefore, reciprocity criteria can be used to evaluate transformation quality, as represented in *Figure 2.27*:

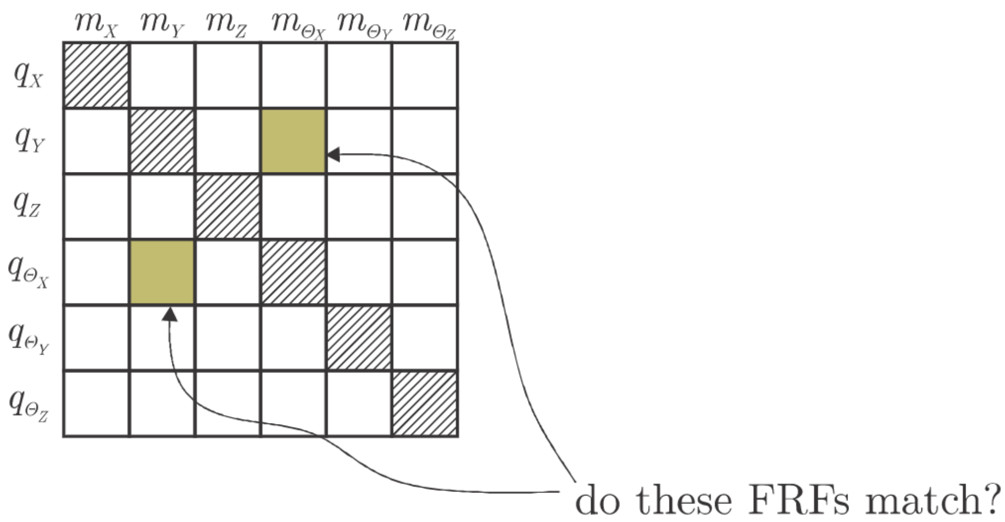

Figure 2.27 – Reciprocity criteria (pyFBS)

3 Chapter 3: Methods

The Methods section presents the activities performed in the thesis to reach the final goal of producing a dynamic test rig for damping characterization of tailplane component in carbon-flax hybrid design. Starting from the input data and requirements provided by the project partner, and based on the abovementioned theoretical knowledges, the system has been designed producing a 3D assembly.

The first version has been modeled and simulated by mean of Finite Elements, then, in order to optimize the functioning of the test bench, an iterative procedure between design and simulation allowed to head to the final optimized version of the test rig. Before production, the functionality of the test rig has been verified by the FE simulations executed on the system applying the real excitations and boundary conditions.

In conclusion, the Experimental Modal Analysis has been applied to the test rig to experimentally verify its functionality. Initially, each sub-group of the assembly has been independently tested to evidence eventual irregularities between simulation and experiment, then the entire system has been proved. After the verification of the functionality, regarding the comparison of the experimental results with the theoretical results of the simulation, the test bench has been used to test TT2 (full carbon) and TT7 (almost full flax) I-beams. The purpose was to evidence the major differences between the materials and prove the effective functionality of the system. In future, the test rig will be used to test all the produced I-beams and the hybridized tailplanes.

3.1 Input data and requirements

The hybridization with flax fiber aims at increasing the damping of the tailplane to minimize the risk in the design. *Figures 3.1* represents the symmetric mode shape and *Figure 3.2* the asymmetric mode shape of the horizontal tailplane with the relative excitations (the helicopter represented in the picture has only the graphical purpose of the representation). In particular, the increase of damping reduces the deformation related to the mode shapes. The focus is on the symmetric and asymmetric mode shapes represented in *Figures 3.1* and *3.2*. The correspondent mode shapes are represented by the dashed line, and they are induced by the excitations represented by the red arrows. These are two low frequency modes. The first one is induced by a dynamic vertical force generated by the air flow moved by the main rotor and the corresponding shape is symmetric and, if the stiffness along the part is constant, it represents a semi-circle. While the second, is induced by a dynamic moment generated by the coupling of the moving parts and it is transmitted by the helicopter chassis to the tailplane. The corresponding mode shape is asymmetric.

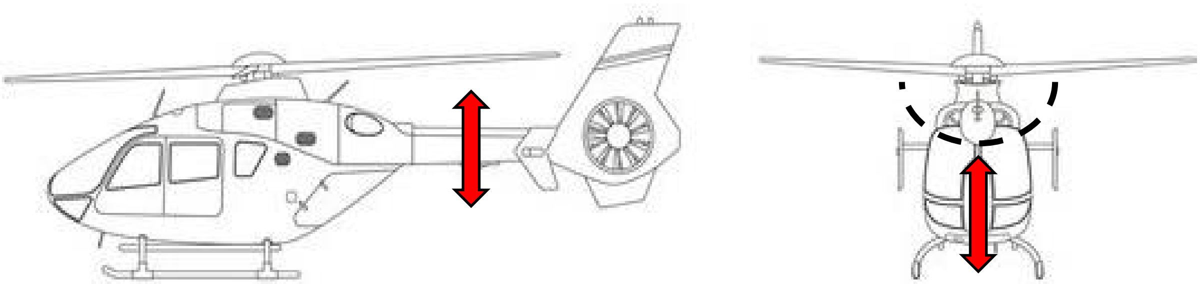

Figure 3.1 – Symmetric mode shape and excitation

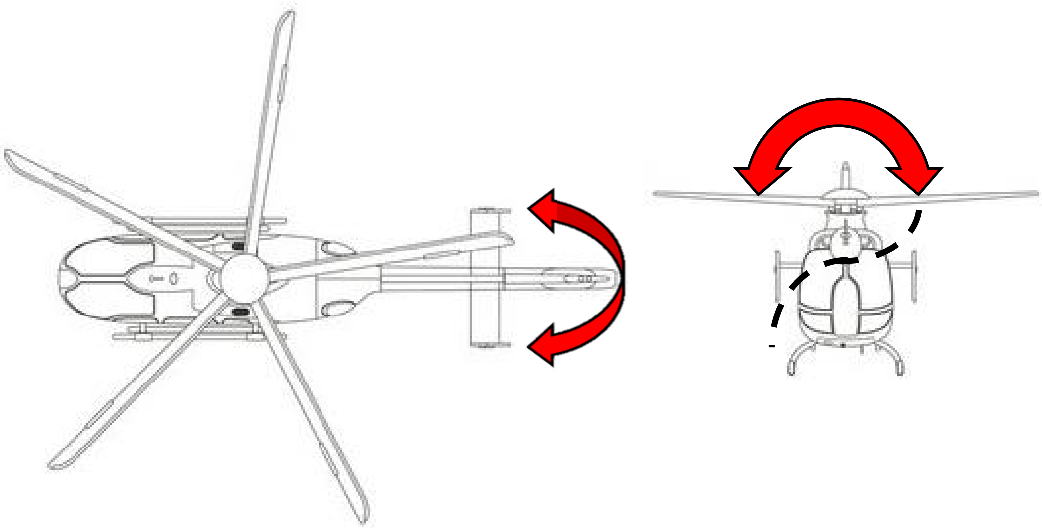

Figure 3.2 – Asymmetric mode shape and excitation

Other requirements of the test bench are the simplicity in the design to keep it cost effective and, furthermore, to simplify the dynamic testing of the test rig itself and of the test rig with the I-beam and the tailplane.

3.2 Design

The current paragraph presents the final design of the test rig with the description of its functionality and the motivation of the choices that have been made according to the literature and to what is available in the laboratory. Moreover, a comparison with the previous design version has been presented. The 2D drawings of the parts are attached to the thesis.

3.2.1 Functionality of the test rig

According to the requirements of the project, the horizontal tailplane must be hybridized to increase the overall damping. As consequence, this limits the deformation of the part itself, because some energy is subtracted from the deformation, and it is absorbed by the material. For this reason, the test rig should be designed with proper mounting set-up and to provide adequate excitations to properly evidence the two eigenmodes of interest.

According to the provided mode shapes, *Figure 3.3*, it is possible to notice that the highest amount of deformation caused by the dynamic load is present in the central part, where the horizontal tailplane is connected to the vertical tailplane. Contrarily, in the external parts where there is the highest displacement, it is originated by rigid body motion as consequence of the strain of the central part:

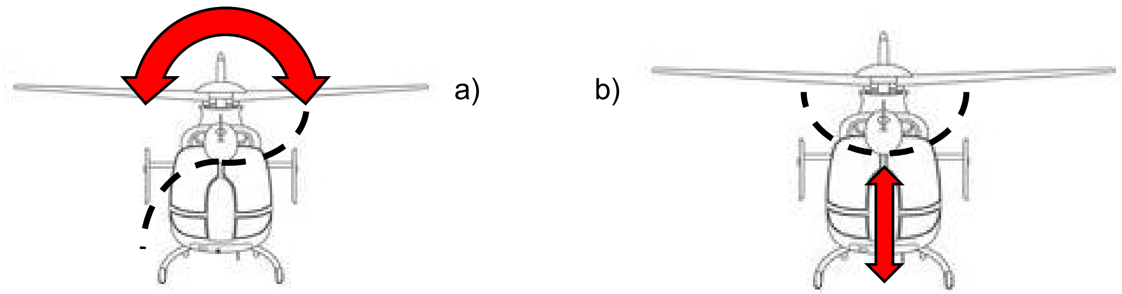

Figure 3.3 – Modal shapes of the horizontal tailplane

According to the purpose of the project, in order to increase the damping, the hybridization has to be located in the areas of the horizontal tailplane characterized by the highest deformation. Therefore, it will be applied mainly to the central part of the component allowing to dissipate some energy that is currently responsible of the deformation. For this reason, it is necessary to include in the experiment also the interface between the horizontal and vertical tailplane, which is exactly in the middle of the part, and replicate the same with the I-beam because it will be influent for the damping of the component. Thus, it has been decided to test the specimen according to how it is really mounted in the helicopter and not in free-free conditions.

The real mounting is composed by a vertical tailplane which constrains the horizontal tailplane to the helicopter as represented in *Figure 3.4* (it refers to a general tailplane):

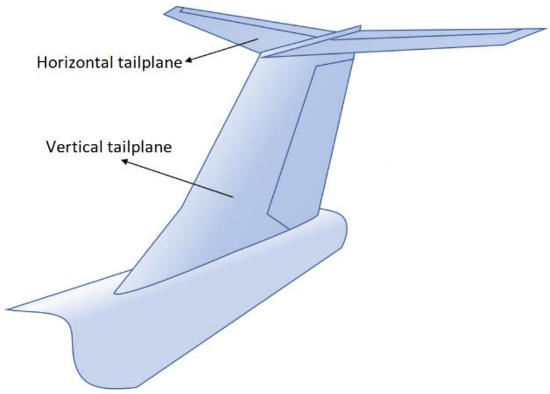

Figure 3.4 – Tailplane mounting

According to the real mounting, the horizontal tailplane is constrained to the vertical beam to represent the vertical and horizontal tailplane connection. This is the first motivation, from a functional aspect, of using the vertical beam. The second reason, from a practical aspect, is that by applying a force excitation to the vertical beam perpendicularly to its neutral axis it will correspond to a moment excitation to the I-beam. This makes it possible to apply a moment excitation as highlighted in *Figure 3.3 a)* because most of the exciters in commerce apply only a force excitation and not a moment. The other reasons will be investigated in the next paragraphs.

According to the excitations represented in *Figure 3.3*, a FE model of the simplified test rig has been tested with a frequency direct simulation that allows to impose a dynamic load on the parts. The simplified model is composed by a vertical beam with a square cross section with the I-beam fixed on the top using an RBE2 connection. While the vertical beam is fixed as a cantilever beam representing the connection of the vertical tailplane to the helicopter. Then, to obtain the symmetric and the asymmetric mode shapes it has been realized that is necessary to apply two different types of loads, as represented in *Figures 3.5* and *Figure 3.6*:

Moment excitation

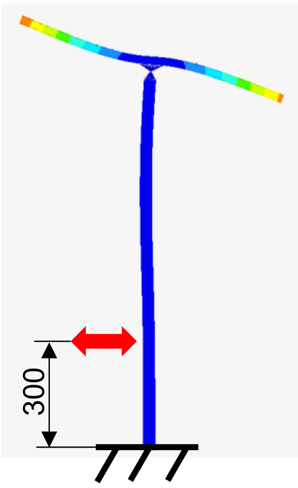

Figure 3.5 – Moment excitation

Where:

- The load is applied perpendicularly to the neutral axis of the vertical beam at 300 mm of distance
- The free length of the vertical beam is 1000 mm

Force excitation

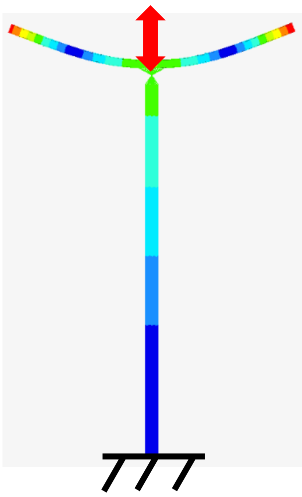

Figure 3.6 – Axial excitation

Where:

- The load is applied in the top, exactly in the middle of the I beam
- The free length of the vertical beam is 1000 mm

From the simulation, it comes out that the test rig must be able to apply two types of different excitations with the same boundary conditions. This would increase cost, complexity, and set-up time to a major level, for this reason, it has been decided to uncouple the two tests but trying to use as much as possible the same test rig with the minimum amount of changes from one experiment to the other. Therefore, the design of the test rig, and, from a wider point of view of the experiments itself, will be carried out separately for each case considering the flexibility of the test bench. The detailed description of the two experiments will be carried out in the next paragraphs.

Another practical advantage of using the vertical beam is related to the possibility of executing larger number of experimental measurements on the same specimen with different layout of the test rig. By shifting the position of the vertical beam and repeating the experiment for each configuration it will be possible to measure different FRFs, each one with different eigenfrequencies. Thus, the number of modal damping factors that can be measured increases. As consequence, by increasing the number of experimental measurements it will be possible to reduce the influence of the measurement errors from the measurement campaign as well as gain more information about the different varying damping over the frequencies. In addition, in case the natural frequencies of the desired mode shapes of the tailplane are known from flight test, by shifting the length it will be possible to tune the eigenfrequency of the entire system exactly to the reference value.

The influence of changing the length of the vertical beam has been firstly investigated on the first basic FE model represented in *Figures 3.5* and *3.6*. In order to make a comparison with the simulation carried out with 1000 mm free length, all the other parameters have been kept constants and only the free length has been reduced to 700 mm. The comparison of the two models is represented in *Figures 3.7* and 3*.8*:

Moment excitation

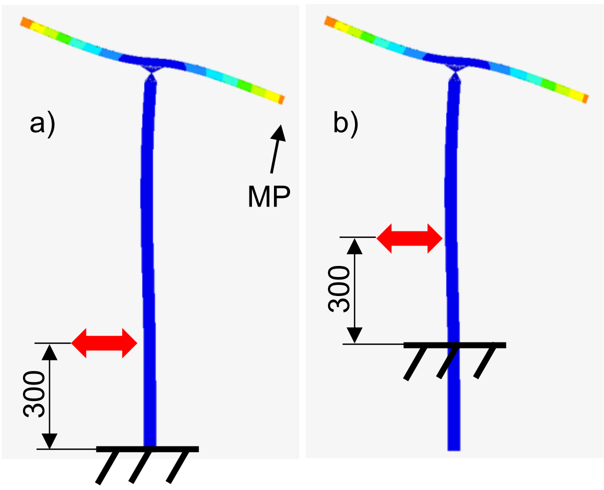

Figure 3.7 – Moment excitation simulation comparison

Where:

- The load is always applied perpendicularly to the neutral axis of the vertical beam at 300 mm of distance from the constrain
- The free length of the vertical beam in a) is 1000 mm, while in b) is 700 mm
- MP = measuring point where the displacement is measured

Force excitation

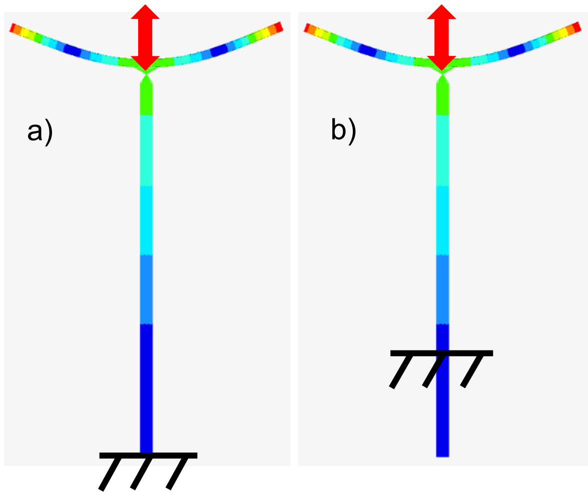

Figure 3.8 – Force excitation simulation comparison

Where:

- The load is always applied on the top, exactly in the middle of the I beam
- The free length of the vertical beam in a) is 1000 mm, while in b) is 700 mm
- MP = measuring point where the displacement is measured for the computation of the FRF

The output of the simulation is the FRF diagram obtained for a) and b) for both the excitations obtained for the force applied as shown in *Figures 3.9* and *3.10*, and the displacement is measured at the extreme point of the I-beam. The purpose of this simulation is to determine the effect of the change in length of the vertical beam, the FRFs of the moment excitation and force excitation are displayed in *Figures 3.9* and *3.10*:

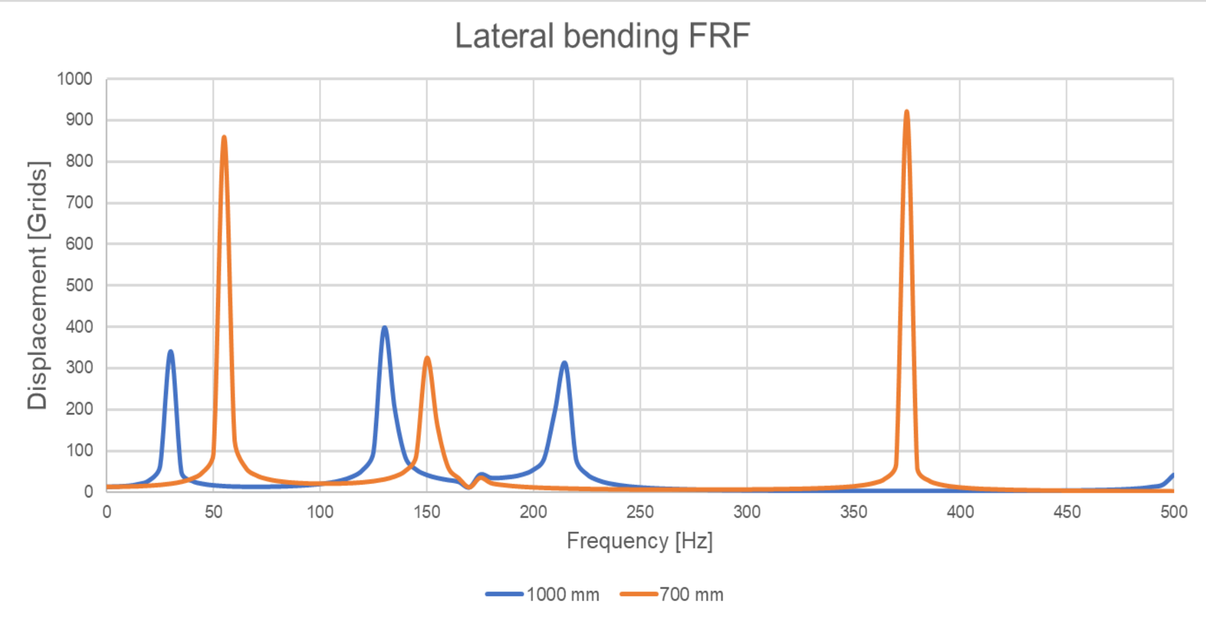

Figure 3.9 - Lateral bending FRF

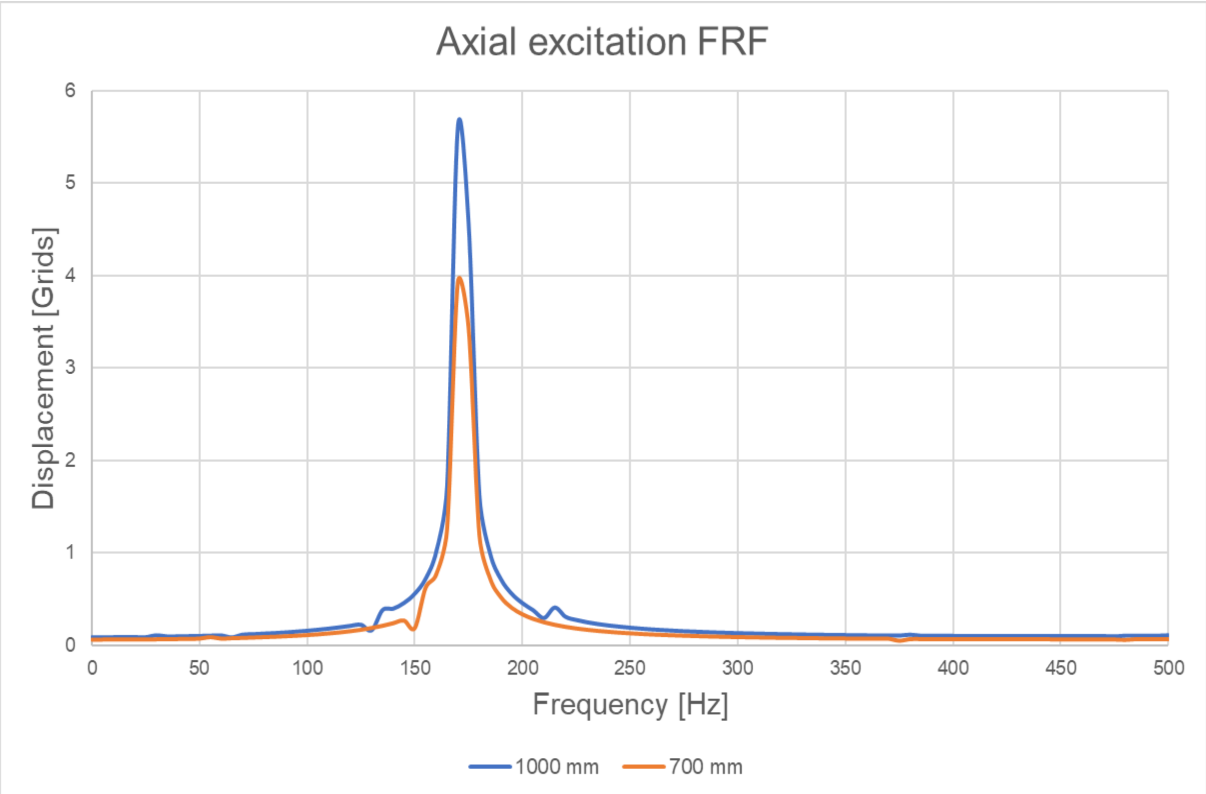

Figure 3.10 - Axial excitation FRF

The simulation is performed from 0 Hz to 500 Hz, which is the range of interest of the tests. From the interpretation of the results of the simulation comes out that for the vertical excitation, according to *Figure 3.10*, the eigenfrequency is not influenced by the change of free length of the vertical beam. Only the amplitude of the FRF is affected, it means that by applying the same force, the entity of the displacement will be different. Contrarily, according to *Figure 3.9*, both the eigenfrequencies and the module of the FRF are influenced by the change of free length of the vertical beam.

From what has already been anticipated about the possibility to shift the frequency range, the interest is not on the change of amplitude of the frequency response function, but on the possibility of shifting the eigenfrequencies. For this reason, the conclusion is that it is meaningless to perform the vertical force experiment on the complete test rig because it does not add any value to the experiment. On the contrary, it brings a benefit to perform the moment excitation test on the full test rig because it allows to compute several damping coefficients from the FRF obtained from different lengths. As consequence, it has been decided to perform the vertical force test using only the I-beam connected to the interface which simulates its real connection to the vertical tailplane. Therefore, the sub-assembly mounted on the top of the vertical beam is detached from the test rig to perform the test separately. Despite of there is the need of subdividing the experiments, the I-beam constraint sub-group used in the axial force experiment is the same of the one used in the bending experiment. In conclusion, in order to be efficient from the economical and timing points of view, the axial test rig will be a reduced version of the bending test rig.

In the next paragraphs, the complete test rig adopted for the lateral bending will be explained in detail in each part. In addition, the reduced test rig used for the vertical force excitation experiment will be also presented.

3.2.2 Final design of the bending test rig: description and analysis

The final design of the bending test rig with the I-beam is represented in *Figure 3.11,* and parts are listed in *Table 3.1*, and it will be detailed in each part in the next paragraphs:

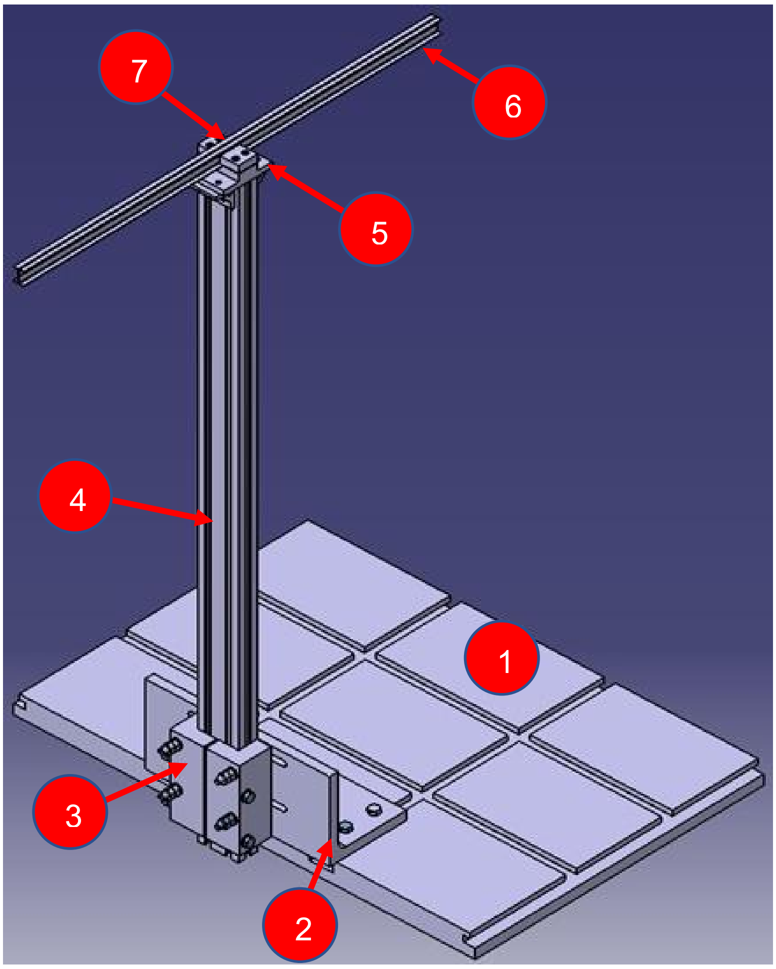

Figure 3.11 – Bending test rig

Part	N°
Table	1
L Base	2
Vertical constraint (right and left)	3
Vertical beam	4
Interface	5
I-beam	6
Clamp (right and left)	7

Table 3.1 - Legend of the parts

The Table (1) represents only a portion of the pneumatic insulated table from external environment, this allows to reduce vibrations induced from the external environment. The L Base (2) connects the test rig to the table thanks to a fastened connection on the bottom surface, while the frontal surface is used to constrain the vertical beam (4) which is the key component of the test rig. The vertical beam is constrained to the L Base thanks to the right and left vertical constraints (3), and by untightening the screws, (4) can vertically slide to reduce its length. On the top of the vertical beam, there is the Interface (5) which connects the I-beam (6) to the test rig. The I-beam that has to be tested is locked by the right and left clamps (7).

3.2.2.1 Sub-groups of the complete test rig

Lower constraint

The purpose of the lower constraint sub-assembly is to provide an ideal fixed constraint of the vertical beam, as schematized in *Figure 3.12*:

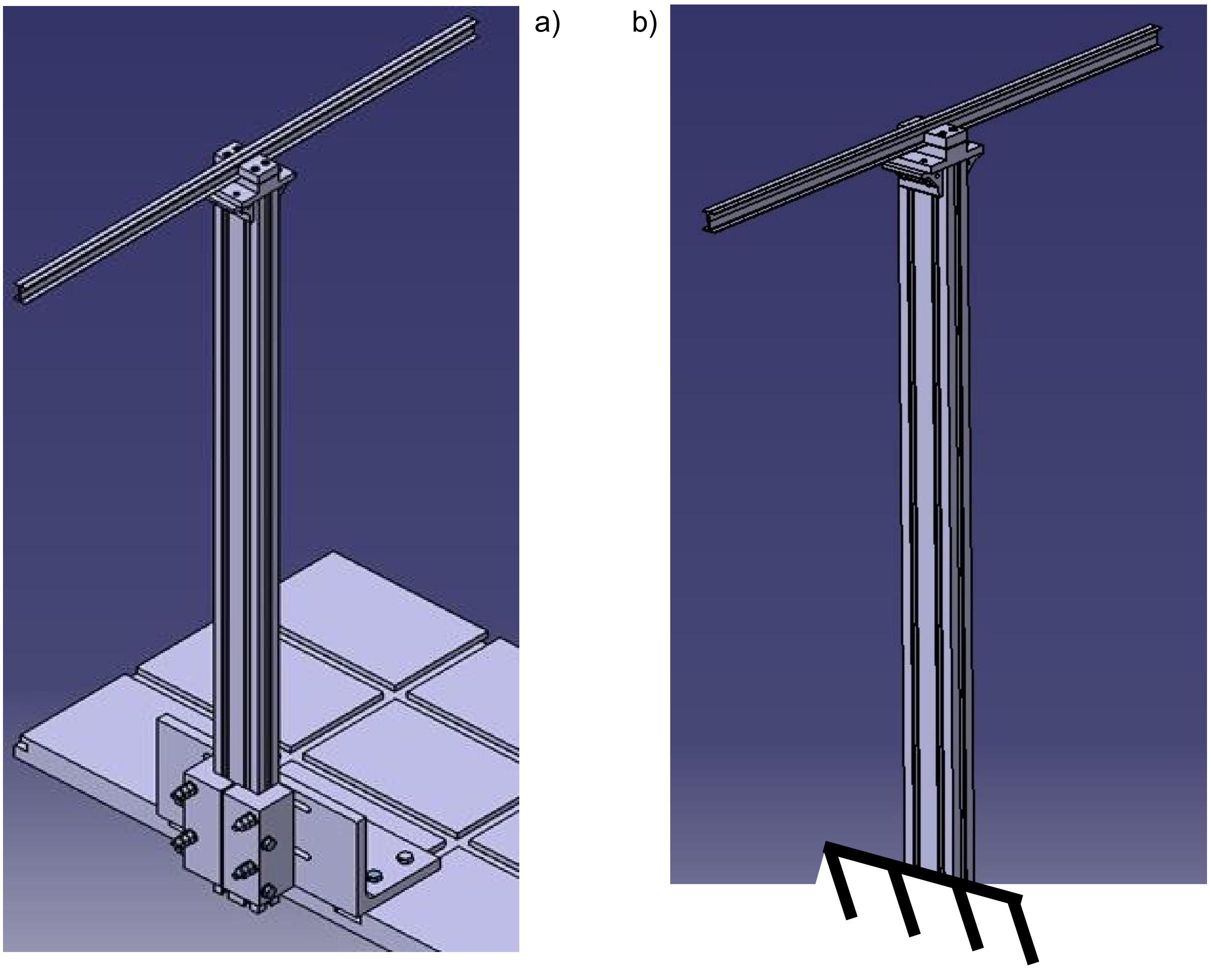

Figure 3.12 – Comparison between the real (a) and the ideal (b) lower constraint

The ideal constraint is realized by the sub-assembly represented in *Figure 3.13*:

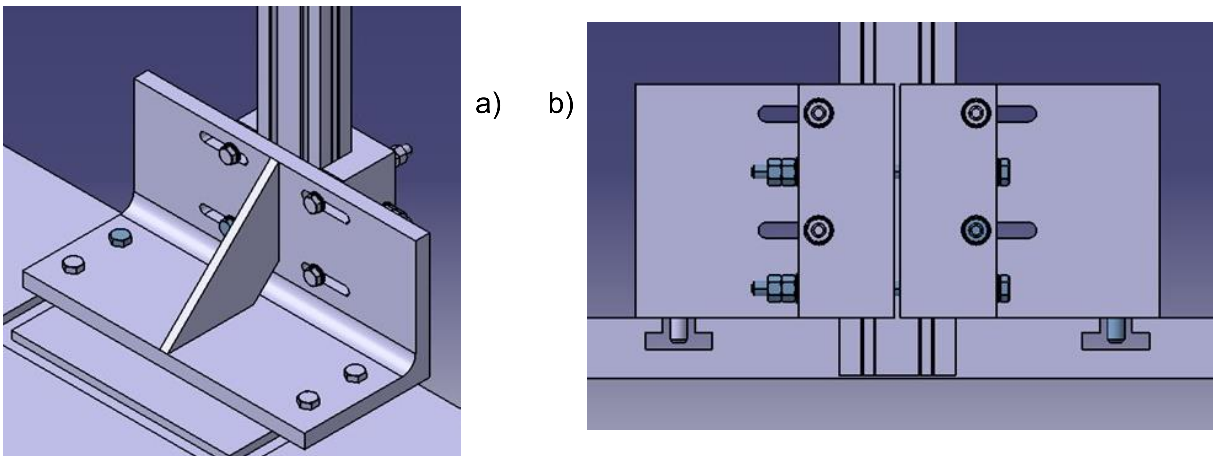

Figure 3.13 – Isometric (a) and frontal (b) views of the lower constraint

The constraint is composed by the L Base which is connected to the insulated table by mean of four M10 screws connected to threaded pads (not represented in the 3D model) sliding inside the T-slots. The L Base is obtained from a standard L cross section beam which is stiffened by welding an intermediate rib in the middle. In the frontal surface there are four elongated holes for the screwed connection between the vertical clamps and the L base with the vertical beam in the middle: they provide the ideal fixed boundary condition to the beam. The elongated holes add complexity to the machining process, but they have been designed with a preventive perception in case in the future application of the test bench will be decided to adopt a vertical beam with a different cross section.

In order to get as close as possible to the ideal situation, the L base and the right and left vertical constraints are obtained from steel which provides, on one side, higher stiffness compared to aluminum, but on the other side the mass is roughly three times higher. The vertical beam constraint sub-group has been designed to be massive by purpose to decrease its dynamic influence on the I-beam. The mass of the parts is listed in *Table 3.2*:

Part	**Mass [kg]**	
L Base	15.9	
Vertical constraint (right plus left)	7.0	
	22.9	*Total*
Vertical beam	3.4	
I beam + Clamps + Interface	0.6	

Table 3.2 - Mass of the parts

In total, the mass of the lower constraint sub-group is around 23 kg including the screws, nuts, and washers. In addition, also the table is massive. From the point of view of the mass, since it is more than five times than the mass of the vertical beam plus the other components, the lower constraint sub-group is assumed to be an ideal boundary condition. From the point of view of the stiffness, the use of steel and the rib improves the stiffness of the boundary condition, but, in practice, it will not behave as fully ideal constraint with infinite stiffness. It could be modeled as a completely rigid constraint with a spring with the stiffness of the connection, but the theoretical determination of its stiffness is difficult, therefore it will be then determined during the test campaign. Finally, the FE model will be compared to the measurement in the laboratory and the model will be refined by adjusting the stiffness to get close to the reality.

The boundary condition sub-group is designed considering functional and practical aspects. According to an ideal tridimensional clamp, the beam has to be compressed in all direction (in all the faces). Furthermore, taking in consideration also the fact that the cross section of the vertical beam could be changed for future tests, the L Base, the right and left constraints must be flexible to changes. For this reason, by changing the length of the screws and modifying the distance between the clamps it is possible to adopt a larger cross section ensuring that at least a portion of each surface will be compressed by the vertical constrains against the L Base.

Moreover, as represented in *Figure 3.14*, in order to guarantee that the compressive load is borne by the vertical beam rather than the vertical constrains, a gap of 2 mm has been kept between the L Base and the constrains on the sides, and the constrains in the front:

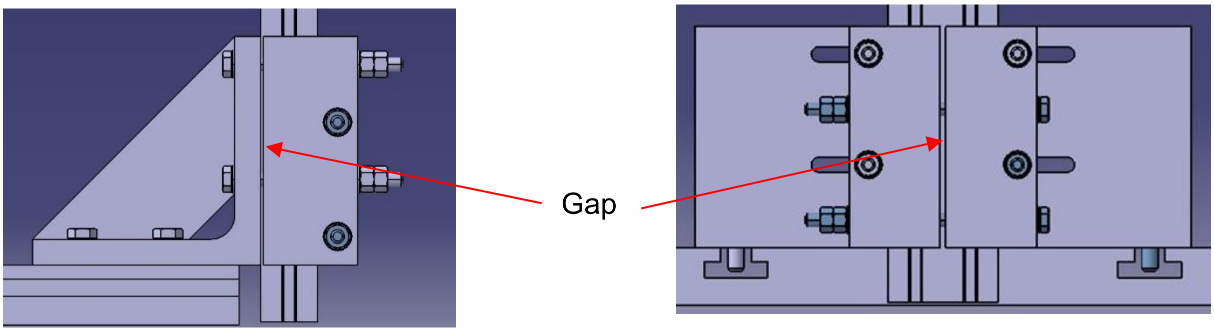

Figure 3.14 – Gap between the L base and the constraints

Vertical beam

The vertical beam is the characteristic component of the test rig. Its constructive and functional main advantages have been presented in the previous paragraphs; while the purpose of the current section is to investigate the cross section, the material, and the length of the adopted beam.

Regarding the type of beam, it has been decided to use an aluminum profile from the catalogue "Mk Technology Group – Profile Technology" with a standard rectangular cross section 40 x 80 mm and length = 1200 mm, represented in *Figure 3.15*:

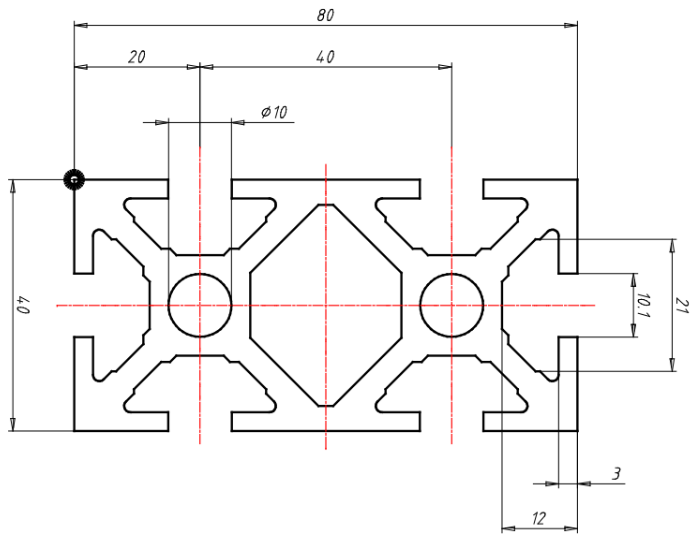

Figure 3.15 – Vertical beam cross section 40 x 80

The reason of using a standard cross section is a constructive aspect. Thanks to the T-slots realized on the external surfaces and the standard components present in the catalogue as sliding nuts and 90° supports is easier to constrain the I-beam and the tailplane upper sub-assembly to the vertical beam. In addition, it is possible to add concentrated masses in the vertical beam to change the eigenfrequencies of the entire system.

There are different cross sections available on the market, for example 25 x 50 mm or 60 x 120 mm, but the decision of the 40 x 80 mm has been made according to the result of the simulation carried out on the FE model of the beam. The simulation consists of its modal analysis constrained as a cantilever beam at different positions, according to how it will actually work on the test rig, represented in *Figure 3.16*.

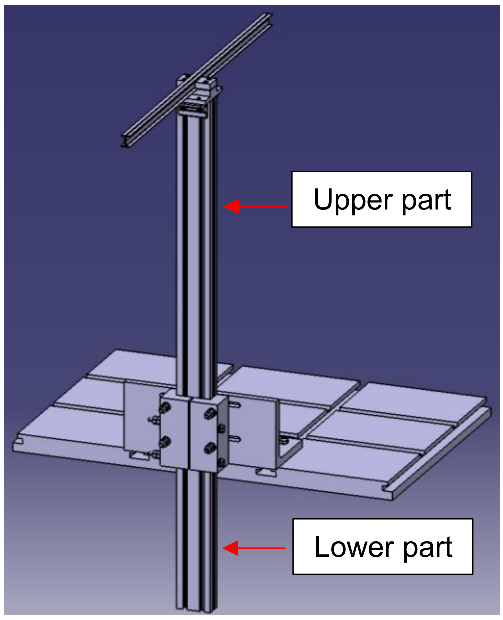

Figure 3.16 – 700 mm free length test rig

The first consideration about the cross-section determination has been the comparison between the square and the rectangular cross sections. Since the square cross section is symmetric along two axes (x and y), the first and second eigenfrequencies of the beam are equal, the only difference between them is the mode shape because the excited profile deforms along two different directions. On the contrary, the rectangular cross section is symmetric along only one axis, therefore, the first and second eigenfrequencies are different. Since one of the requests of the test rig is the flexibility, because it must have the possibility to shift the eigenfrequencies, it has been decided to use the rectangular cross sections because it has the first two eigenfrequencies different while the third one is far away from the frequency range of interest. For this reason, by having two different natural frequencies in the range of interest, it will be possible to tune them according to the requirements. While, with two equal frequencies it will be possible to tune only one value; for this reason, the rectangular section provides more freedom for the tuning. After the decision of the rectangular cross-section, is necessary to define the dimensions.

I-beam constraint

The I-beam sub-group is adopted as a precursor of the investigation of the tailplane. Meanwhile, in the final assembly, the I-beam is used as reinforcement of the tailplane; therefore, its constraint is analyzed in the current paragraph.

Although the vertical tailplane is missing in CoAX2D (*Fig. 3.17 and 3.18*), which is the helicopter where the horizontal tailplane comes from. It has been decided to include the vertical tailplane in the test rig since it is used in most of the commercial applications.

Figure 3.17 – Rear representation of CoAX 2D

Figure 3.18 - Lateral representation of CoAX 2D

Similarly, as represented in *Fig. 3.17* and *3.18*, the tailplane is connected to an interface to the helicopter's chassis. In this case there is not an extended vertical tailplane as in *Figure 3.5* and most of the helicopters in commerce. In addition, in the CoAX 2D, the horizontal tailplane is mounted from the bottom, contrarily to the other where it is mounted from the top. But, since the purpose of this investigation is not related to aerodynamic tests, the reversed orientation does not make any difference.

A simplified drafting of the tailplane is provided in *Figure 3.19* to provide the main dimensions and the shape of the interface with the vertical tailplane:

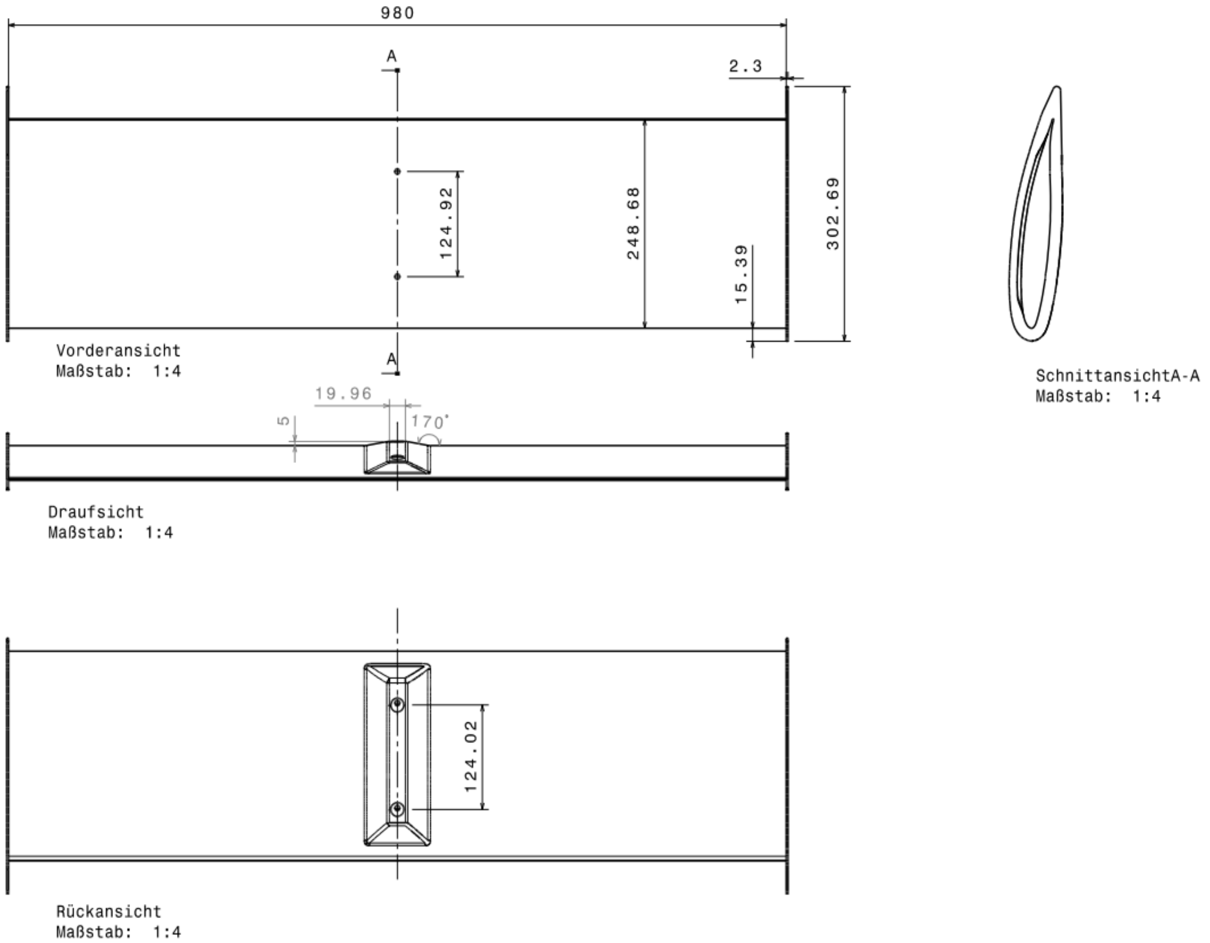

Figure 3.19 - Drafting of the intermediate tailplane

As already mentioned, the I-beam is placed inside the cross section of the tailplane as reinforcement to increase the stiffness of the airfoil, as it is schematized in *Figure 3.20*. In addition, it outstands that the horizontal tailplane it is in contact with the vertical by the lower surface. The green dashed lines represent the two screws that fit the holes present in *Figure 3.20*:

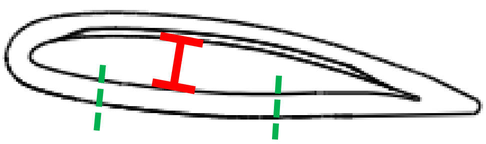

Figure 3.20 – Schematized I-beam reinforcement

The connection of the tailplane to the test rig has to be done according to its real mounting represented in *Figures 3.19* and *3.20* to replicate the real conditions. For the same reason, the I-beam has to be constrained only from the lower surface in order to replicate the constraint of the tailplane, which means only from one flange. This is assumed to be valid also for the connection of the I-beam reinforcement inside the horizontal tailplane, where the flanges of the I-beam are glued to the inner surface of the tailplane.

Other constraints regarding the design of the interface sub-assembly are related to the simplicity of the design. It has to be as simple as possible to reduce costs and, moreover, to simplify the measurement during the execution of the dynamic experiment.

By combining all the above-mentioned characteristics of the interface between test bench and I-beam, the sub-assembly represented in *Figure 3.21* has been designed:

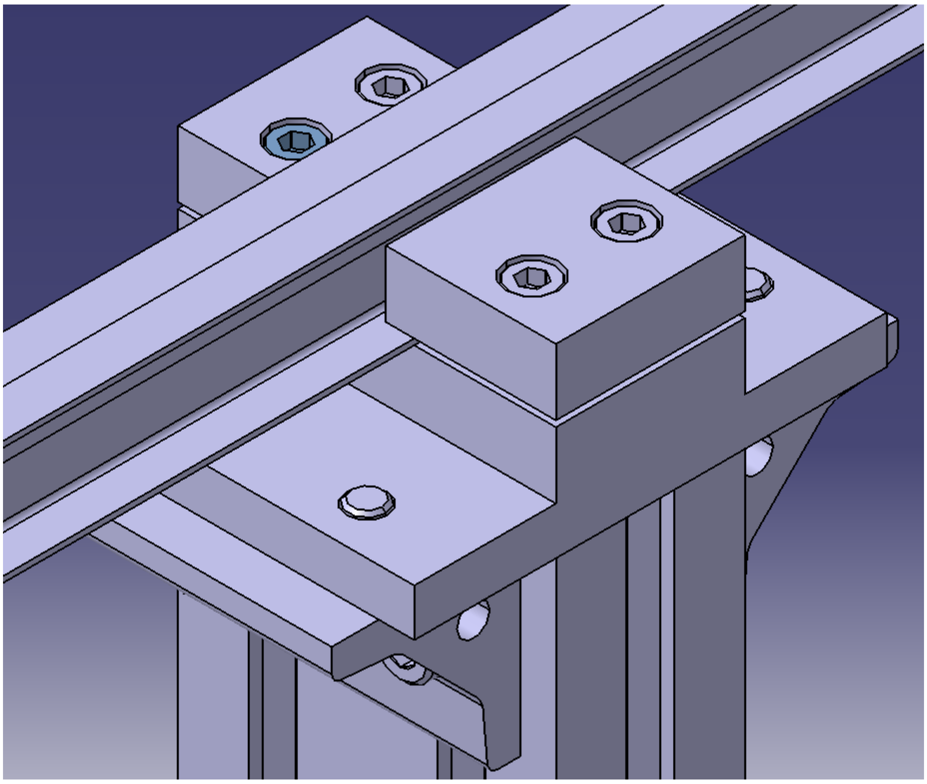

Figure 3.21 – I-beam interface

In addition, as represented in *Figure 3.21*, the I-beam is placed on a surface located at a major height to avoid the interference of the composite beam during the deformation with the clamping system. The amount of height of the location has been defined according to the deformation of the I-beam under the loading condition measured in the FE model.

3.2.3 Final design axial test rig

According to the purpose of the thesis, it has been necessary to develop two different test rigs: lateral bending moment excitation (bending) and vertical force excitation (axial). In order to be cost effective and limit the production of extra parts, the axial test rig derives by the upper part of the bending test bench. The axial test rig is represented in *Figure 3.22.* Since the variation of length of the vertical beam does not affect the vertical force test, the axial version is composed only by the I-beam constraint sub-group of the bending test rig.

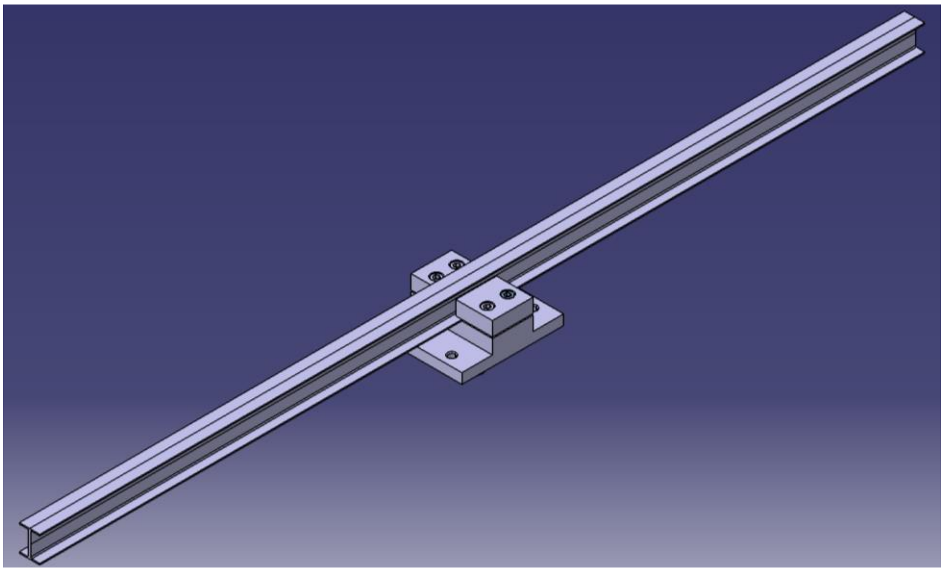

Figure 3.22 - Axial test rig

The additional parts composing the axial test rig which were not included in the bending test rig are the interfaces between the I-beam constraint sub-group, the impedance head, and the shaker. The mounting solution is not visible in *Figure 3.22*; therefore, it is represented in *Fig. 3.23 and 3.24*. *Figure 3.24* shows the exploded view of the mounting solution to connect the parts. Starting from the top, the constraint sub-group is connected to the 5860B Impedance Head by mean of a M6 to 10-32 UNF-2B adapter. Then, there is another threaded interface between the impedance head and the M6 to M4 female-female adaptor which is the only new machined part. Below, through the M4 grub screw, the test rig is connected to the shaker:

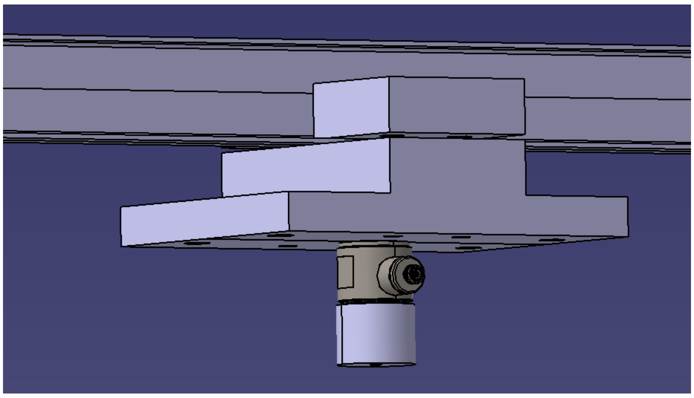

Figure 3.23 - Detail of the axial test rig

Figure 3.24 – Exploded view of the axial test rig

3.2.4 Evolution of the design

As principal requisite, the possibility of shifting the eigenfrequencies of the test rig has always been considered. For this reason, according to the theory, the natural frequency is computed as the ratio between stiffness and mass. Therefore, in order to vary the natural frequency, is necessary to act on the stiffness or on the mass.

The above-mentioned test rig is based on the variation of mass of the test rig by modifying the length of the vertical beam. This solution has been adopted due to several reasons:

- Simplicity of the design and construction
- Possibility of replicating the same experiment with the same conditions: limited set up operations, it is only necessary to position the vertical beam at the same height
- Simplicity of the simulation, the vertical beam and the total test rig can be simulated by a linear static or dynamic simulation according to the purpose with Hypermesh® or Ansys®. Therefore, also the results from the simulation will be more reliable.

On the contrary, the first version of the design was based on the opposite concept: tuning the stiffness of the test rig. This was realized by using cables where, by acting on the pre-tension of the cable it is possible to control its stiffness, and, as consequence, the stiffness of the structure. This is represented in *Figure 3.25*:

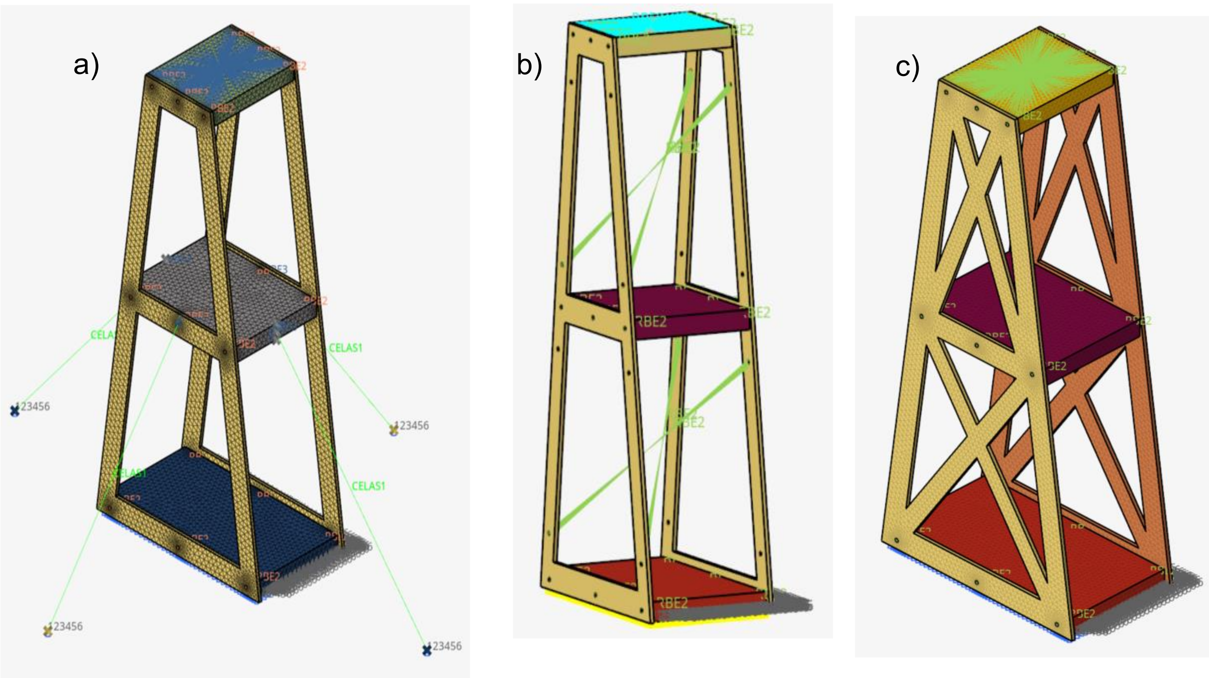

Figure 3.25 – Stiffness tuning test rig

The test rig is represented with three different solutions to adopt to vary the stiffness. In *Figure 3.25 a)* the structure is connected to four cables where, by acting on the tension of the cables, is possible to regulate the stiffness of the system. In *Figure 3.25 b)* the structure has cross–reinforcement elements used to increase its torsional stiffness, while in *Figure 3.25 c)* the structure has lateral-reinforcement elements used to increase its bending stiffness.

This solution has been discarded due to:

- Due to the usage of cables, it is complex to replicate the experiment with the same conditions. It would be necessary to control the position of the cable and its pre-tension
- The cable has to be simulated as a non-linear element since it behaves differently in tension and compression. This further complicates the simulation and the design of the test rig. Moreover, the results from the simulation will be less reliable.

3.3 Finite Element Simulation of the test rig

The Finite Element Simulation has been carried out in parallel with the design activity to obtain, iteration after iteration, the optimal test rig according to the requirements of the project. The software adopted for the FE modelling, simulation and post-processing is Hypermesh® 2021.2. Initially, as illustrated in Chapter 2, a T structure similar to the vertical and horizontal tailplane mounting, composed by two square cross-section beams has been simulated. The purpose was to understand which layout, excitations, and constraints apply to the test rig to get the required mode shapes of the specimen (Simulation 1: T structure). Next, the vertical beam has been simulated to determine the optimal dimensions of its cross-section allowing to have the eigenfrequencies as close as possible to the range of interest. For this purpose, a “Normal Mode” simulation has been conducted considering the boundary conditions and the frequency range of interest (Simulation 2: Vertical beam). It is a linear dynamic analysis considering the applied boundary conditions which solves the eigenvalue problem with the mass and stiffness matrixes obtained from the adopted mesh.

Apart from this case, according to their functionalities, the other components have not been simulated independently because it was assumed that was not necessary. In detail, the parts involved in the lower vertical beam constraint sub-group are designed to be as stiff and mass effective as possible to represent a rigid and ideal constraint. Therefore, there are no problems related to stress and deformation of the components. In addition, the upper part of the test rig representing the interface of the I-beam and tailplane is designed to provide the proper constrain of the specimen according to how it is really mounted in the helicopter. From the static loading point of view, these parts have to solely withstand the stress originated by the bolted connections. And dynamically, compared to the vertical beam and the specimens, it is assumed that they can be considered as rigid concentrated masses. Therefore, there are no problems related to stress and deformation of the components; and their dynamic behavior does not influence the I-beam under test.

After the completion of the design, the complete bending test rig has been simulated to determine its behavior during functioning with real boundary conditions and load. For this purpose, it was necessary to execute a dynamic simulation that allows to apply the load according to how the test rig will be excited and not solving only the eigenvalue problem; therefore, the “Normal Mode” simulation has not been used. The “Frequency Response (direct)” suits the requirements because it is a dynamic simulation, it requires the application of dynamic load and frequency range, and it is linear as the surface contacts imposed in the model to characterize the interfaces (Simulation 3: Bending test rig dynamic simulation). With respect to the “Normal mode”, it has been necessary to apply this type of simulation because the goal is to extract only the bending eigenmodes of the test rig, neglecting the torsional contributions. The “Normal mode” simulation corresponds to solving the eigenvalue problem with mass and stiffness matrixes set according to the defined mesh. Therefore, it does not allow to consider only bending deformed configurations. On the contrary, in the “Frequency Response (direct)”, by imposing a dynamic load (with module variable over the frequency range, direction, orientation, position and frequency range of action), it is possible to position it such as to obtain the desired deformed configurations. In addition to this model, the natural frequencies of the complete bending test rig are computed by mean of a “Normal Mode” simulation by solving the eigenvalue problem (Simulation 4: Bending test rig natural frequencies determination).

Finally, before the experimental testing, the I-beam Full Carbon Fiber model performed by Scheffler [23] was added to the model of the bending test rig and a “Frequency Response (direct)” has been executed. For this global simulation, the point of interest was not the displacement of the test rig but became the displacement of the double T beam (Simulation 5: Bending test rig + I-beam dynamic simulation). In conclusion, the double T beam model has been included in the axial test rig model which has been tested with a “Frequency Response (direct)” simulation with the purpose of determining the eigenfrequencies and the corresponding eigenmodes in the frequency range of interest (Simulation 6: Axial test rig + I-beam dynamic simulation). The abovementioned models are detailed in the next paragraphs.

3.3.1 Simulation 1: T structure

Simulation 1 is executed with the purpose of defining the layout of the test rig, the excitation to apply to obtain the symmetric and the asymmetric eigenmodes of the I-beam, and to verify the influence of the length of the vertical beam representing the vertical tailplane over the FRFs of the two modes. The model is composed by:

- Vertical beam, length 1000 mm and square cross-section 40x40 mm made by aluminum alloy
- Horizontal beam, length 870 mm and double T cross-section according to the manufactured specimens made by aluminum alloy

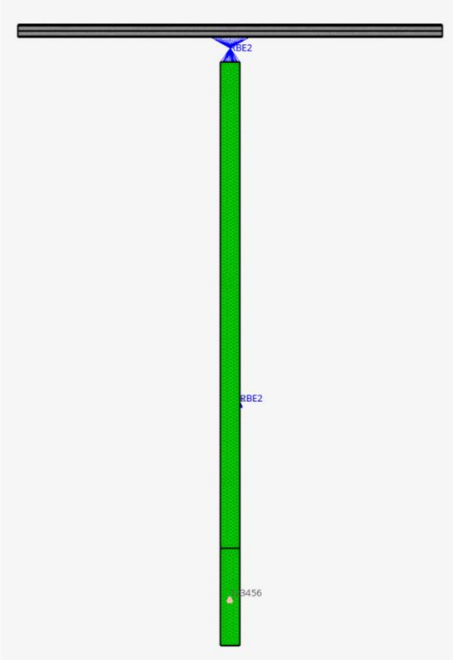

Figure 3.26 – T structure

The shape of the structure, represented in *Figure 3.26*, originates from the simplification of the mounting of the horizontal tailplane on the vertical tailplane, which is similar to a T shape. The two beams are connected by a RBE2 connection which is a multi-point constraint (single node connected to many nodes) which distributes the force and the moment equally among the all the connected nodes irrespective of position of force or moment application.

The RBE2 is also used to connect the node where the excitation is applied to the surrounding nodes to distribute it and avoid localized effects of load concentration. The structure is constrained according to its real mounting at the bottom of the vertical beam as a cantilever beam.

The model is used to run the same simulation with different free lengths of the vertical beam since there is the interest of verifying the influence of the length over the response of the system. The load and the boundary conditions of the two simulations are schematized in *Figure 3.27*.

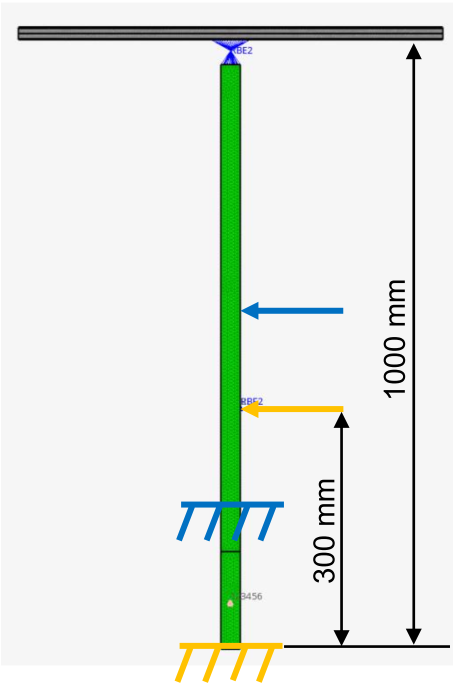

Figure 3.27 – T structure load and BC

Legend:

- 1000 mm free length, 700 mm from the load
- 700 mm free length, 400 mm from the load

The load is applied at 300 mm above the constraint. The model is meshed with a 3D Tetra Mesh (CTETRA4) with the recommended characteristic size to ensure the fulfillment of the quality criteria of the elements. According to the purpose of this simulation, it is not necessary to apply a refined mesh. The goal is to verify whether the T structure is effective for the extraction of the two modes of interest and the influence of the length of the vertical beam on the FRF of the modes.

The material data are collected in *Table 3.3*:

Aluminum	
$E\ [MPa]$	70000
$G\ [MPa]$	26515
ν	0.32
$\rho\ [kg/m^3]$	2700

Table 3.3 – Aluminum data

According to the purpose of the simulation, the typology of simulation is the “Frequency response (direct)” which is a linear dynamic simulation. The structure and the material are both set linear. In addition, the RBE2, which is the additional component involved in the simulation, behaves linearly and all the non-linearities and friction are assumed negligible to simplify the model. This type of simulation allows to apply a variable load over the frequency range, where both the load and the frequency range can be manually imposed. As it was already mentioned in Chapter 4, the result from the simulation is the displacement FRF obtained at the end node of the horizontal beam highlighted in *Figure 3.28*:

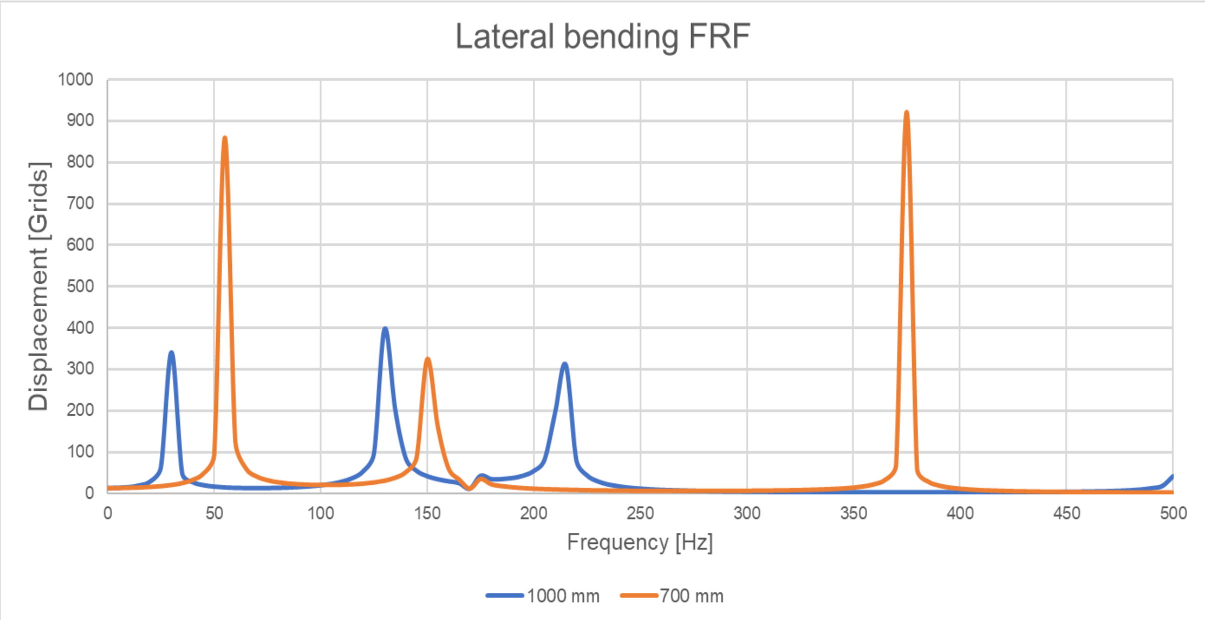

Figure 3.28 - Lateral bending FRF

From a qualitative analysis of the FRF diagram comes out that the variation of free length of the vertical beam influences the displacement of the horizontal beam. While, from the deformed shape comes out that the layout of the test rig is possible to extract the asymmetric mode shape at different lengths of the vertical beam, as highlighted in *Figure 3.29*:

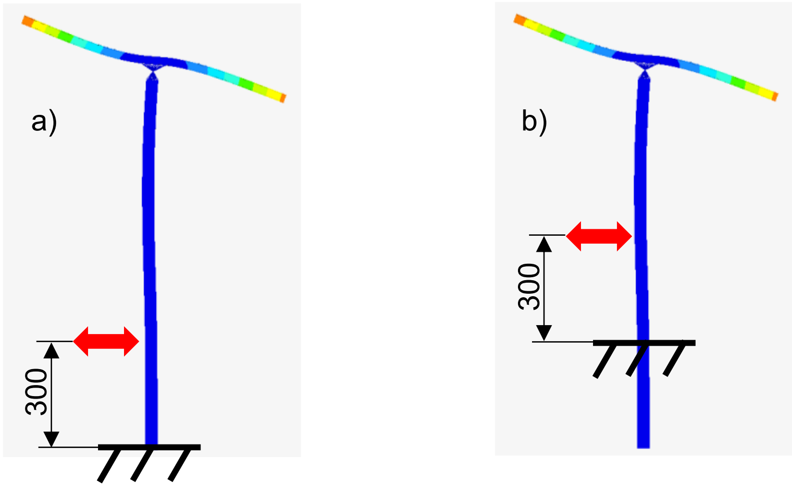

Figure 3.29 – Lateral bending deformed configuration a) 1000 mm b) 700 mm

From this configuration it is not possible to extract the symmetric mode. In order to extract the mode, it is necessary to modify the position of the load and move it to the center of the horizontal beam, as represented in *Figure 3.30*:

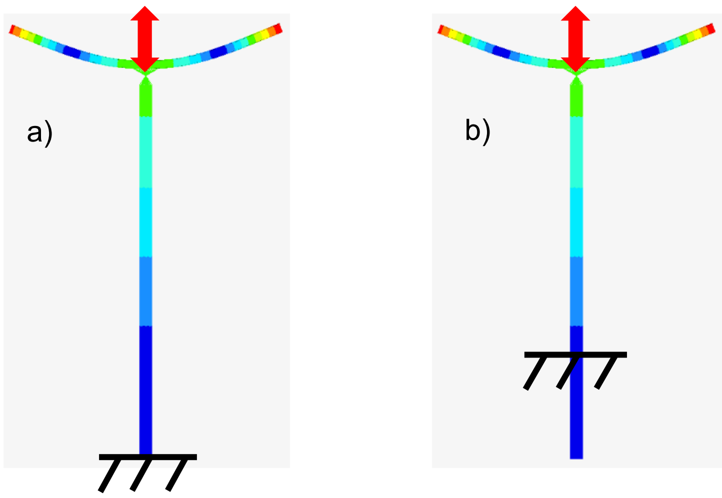

Figure 3.30 – Axial force excitation set-up and deformed configuration a) 1000 mm b) 700 mm

In conclusion, from a qualitative analysis of the displacement FRF represented in *Figure 3.31*, it comes out that the variation of free length of the vertical beam does not have any influence on the displacement of the horizontal beam:

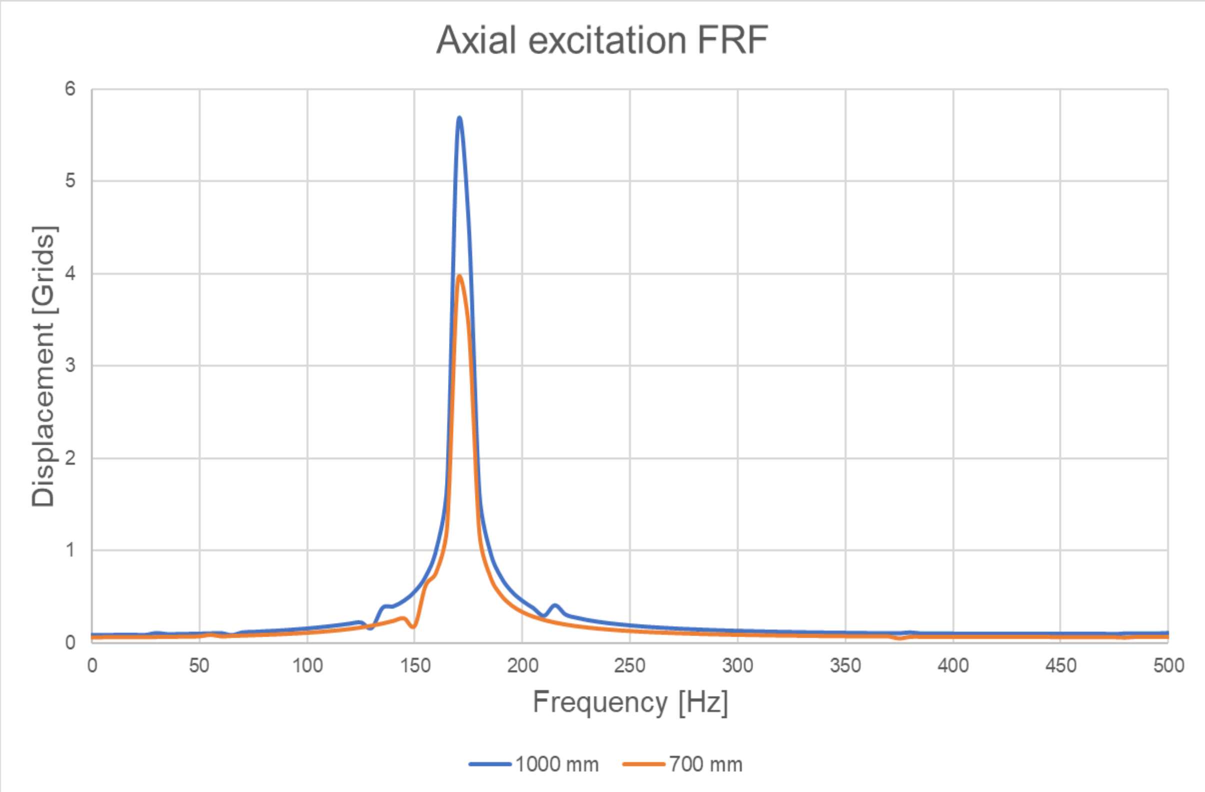

Figure 3.31 – Axial excitation FRF

The conclusions obtained from the Simulation 1 confirm the T structure as the suitable layout of the test rig to extract the two modes of interest. In addition, it is obtained that the variation of free length influences only the asymmetric mode, while the symmetric mode is not influenced.

3.3.2 Simulation 2: Vertical beam

Simulation 2 is executed with the purpose of defining the dimensions of the cross-section of the vertical beam of the test rig with the constraint of having its eigenfrequencies in the range of interest. For this reason, the results to extract from the current simulation are the eigenfrequencies of the beam. The simulation is repeated for different cross-section beams, but for brevity the model is described only for the ITEM profile with a rectangular cross-section 40x80 mm, represented in *Figure 3.32*, which is the one finally employed in the test rig.

Figure 3.32 – Vertical beam model

According to the catalogue, the material assigned to the component is aluminum alloy. The assigned properties of the material are represented in *Table 3.4*.

In order to avoid the generation of one model for each length, all the tests are incorporated on the same model creating different load steps with different boundary conditions. This is the reason why the outer surface of the beam represented in *Figure 3.32* is partitioned in different zones. As it is indicated by the colored triangles representing the constraints, there are six different constrained lengths from 1000 mm to 500 mm with 100 mm of pitch. This strategy allows to run only one simulation and output the natural frequencies for each length.

In addition, at this stage of the project, the amount of mass of the components added to the top of the beam was not known yet. Despite of this, a localized mass of 1 kg has been added by the CONM2 to the central node of the upper cross section of the vertical beam, then as it is represented in *Figure 3.33*, it is connected by a RBE2 to the other nodes of the cross section to transmit the force:

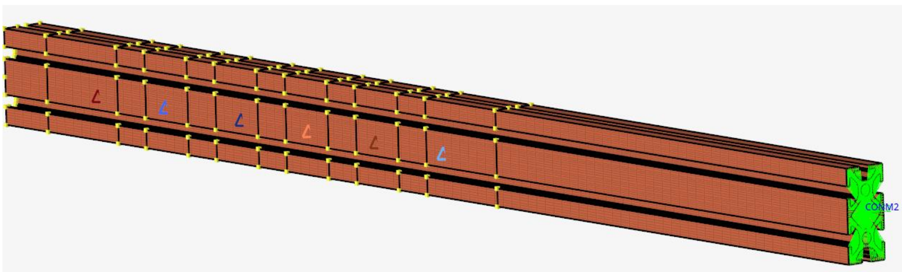

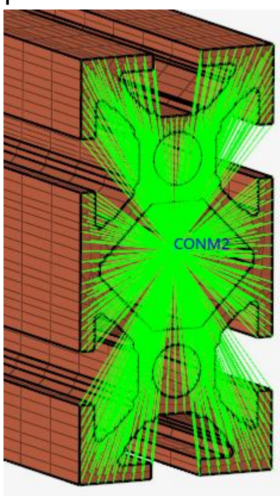

Figure 3.33 – Localized mass representation

The function of the localized mass is to simplify the components added to the top of the beam that will have a certain volume and mass. To be conservative, the mass has been set to 1 kg, but, for sure, the overall mass of the components supported by the vertical beam, including the I-beam, will be lower than 1 kg. Therefore, the natural frequencies of the real system will be included between the eigenfrequencies of the model with no mass added and the model with 1 kg concentrated mass added.

According to the type of component, a 2D mesh, represented in *Figure 3.34*, has been manually generated on the cross section of the beam to fulfill the quality criteria and then extruded along the z direction with a pitch of 6 mm, obtaining 63402 elements:

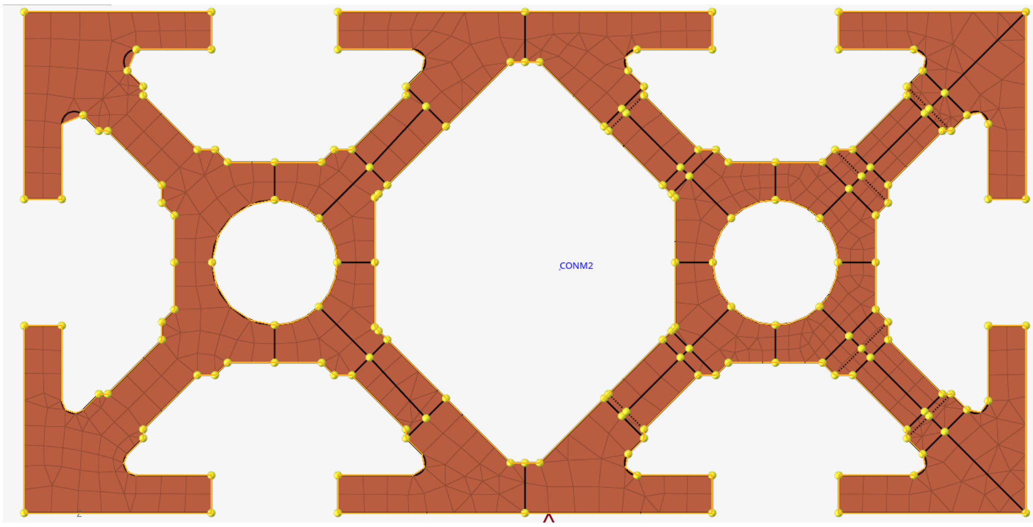

Figure 3.34 - 2D mesh of the vertical beam

According to the purpose of the simulation, the typology of simulation is the "Normal mode" which is a linear dynamic simulation. The component and the material, considering the elastic region, are both linear. This type of simulation allows to apply the constraint and indicate the number of modes to extract, while it is not required to apply the load because the "Normal mode" solves the eigenvalue problem with the mass, stiffness, and damping matrixes.

Different ITEM beams have been simulated to define the most suitable for the application. The resulting mode shapes are the same for all the beams. *Figure 3.35* represents the mode shapes of the rectangular cross-section 40x80 mm with a length of 1000 mm:

- *Mode 1 – 33.7 Hz*

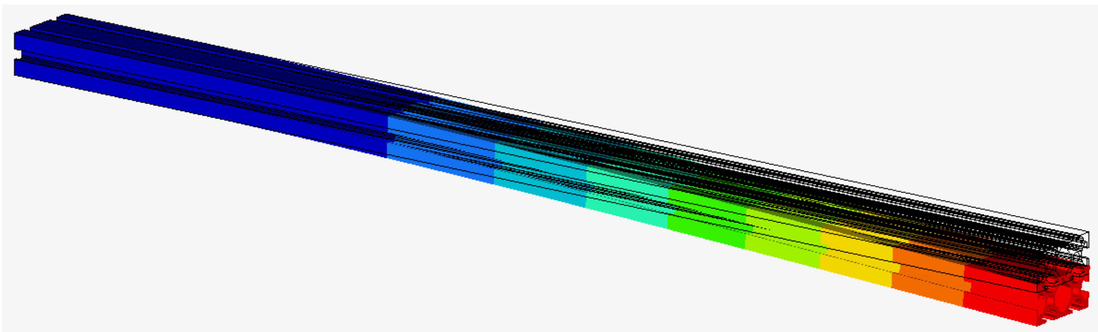

- *Mode 2 – 64.1 Hz*

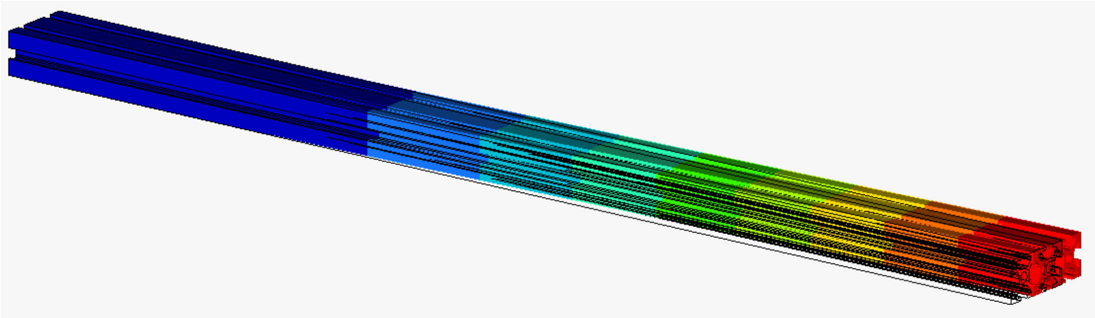

- *Mode 3 – 207.8 Hz*

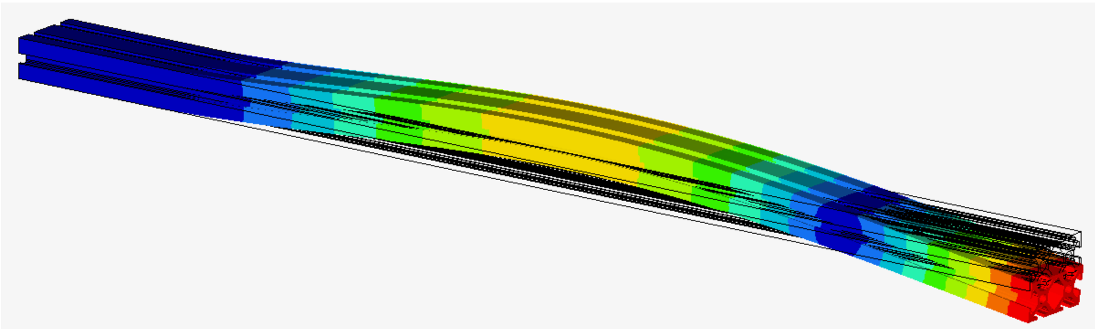

Figure 3.35 – 40x80 mm mode shapes

The eigenfrequencies of each cross section both for the no mass and 1 kg point mass added are collected in *Table 3.4*. After the decision of the rectangular cross-section for the vertical beam, is necessary to define the dimensions. The analysis is carried out on the columns "1 kg" because there will be the I-beam and tailplane sub-group with a mass lower than 1 kg added on the top of the vertical beam. It has been decided to use the 40 x 80 mm because the eigenfrequencies of the first mode for each length are spread in the frequency interval of interest from 20 Hz to 100 Hz. Oppositely, the first eigenfrequency of the 60 x 120 mm is 44.5 Hz, which is at the length of 1000 mm, is already above the minimum level of interest, because this beam is too stiff. On the other side, the 25 x 50 mm beam is not stiff enough since the maximum eigenfrequency, which is at the length of 500 mm is only 35.5 Hz, and this is not high enough for the frequency range of interest.

	Rectangular 25 x 50						Rectangular 40 x 80					
	No added mass [Hz]			1 kg [Hz]			No added mass [Hz]			1 kg [Hz]		
Length [mm]	1°	2°	3°	1°	2°	3°	1°	2°	3°	1°	2°	3°
1000	23.2	44.4	144.6	11.6	22.2	108.4	37.0	70.3	227.8	25.5	48.5	183.7
900	28.4	54.3	176.7	13.7	26.1	131.9	45.3	85.8	277.6	30.3	57.6	222.1
800	42.9	81.7	265.6	19.0	36.3	196.5	56.7	107.0	345.3	36.7	69.7	274.1
700	47.5	90.2	293.3	20.6	39.3	216.6	75.4	141.8	437.6	46.9	88.6	358.1
600	63.8	120.9	392.3	26.0	49.6	288.2	101.2	189.0	509.9	60.0	112.9	469.6
500	94.6	178.3	576.9	35.5	67.4	421.8	142.7	264.1	610.9	79.9	149.4	607.9

	Square 40 x 40						Rectangular 60 x 120					
	No added mass [Hz]			1 kg [Hz]			No added mass [Hz]			1 kg [Hz]		
Length [mm]	1°	2°	3°	1°	2°	3°	1°	2°	3°	1°	2°	3°
1000	36.1	36.1	194.5	20.8	20.8	171.1	55.8	106.7	284.2	44.5	85.6	285.7
900	44.6	44.6	216.9	24.8	24.8	208.8	70.4	133.6	320.8	54.9	105.0	321.7
800	56.3	56.3	245.1	30.0	30.0	245.2	88.5	166.4	361.4	67.5	128.1	362.9
700	73.4	73.4	281.8	37.3	37.3	281.9	114.4	212.5	413.9	84.9	159.6	416.3
600	99.5	99.5	331.4	47.7	47.7	333.2	153.6	280.2	483.8	110.1	204.2	488.3
500	142.6	142.6	402.2	63.7	63.7	402.6	216.7	385.0	581.5	148.9	270.6	590.7

Table 3.4 – Vertical beams eigenfrequencies

3.3.3 Simulation 3: Bending test rig dynamic simulation

Simulation 3 is executed after the completion of the design with the purpose of verifying the dynamic behavior of the test rig according to the applied excitation and boundary conditions. Then, the simulation will be repeated also including the I-beam to determine its dynamic behavior. The model is represented in *Figure 3.36*.

According to the design, the materials assigned to the part are steel and aluminum alloy. Data of the material are collected in *Table 3.5*:

	Aluminum	Steel
$E\ [MPa]$	70000	210000
$G\ [MPa]$	26515	80769
ν	0.32	0.30
$\rho\ [kg/m^3]$	2700	7850

Table 3.5 – Test rig materials' data

Steel is assigned to the Vertical Right Constraint, Vertical Left Constraint and the L base. While, according to the design, aluminum is assigned to all the other parts.

Initially, the geometry of the test rig has been imported from Catia®. Then, the layout has been reduced to generate the geometry of the model. It includes all the parts of the test rig except for screws, washers and nuts which have been removed to simplify the test rig. The purpose of the simplification is to model the real test rig according to the reality by reducing its complexity according to what is assumed to be negligible such as friction and non-linearities, by admitting a certain amount of error.

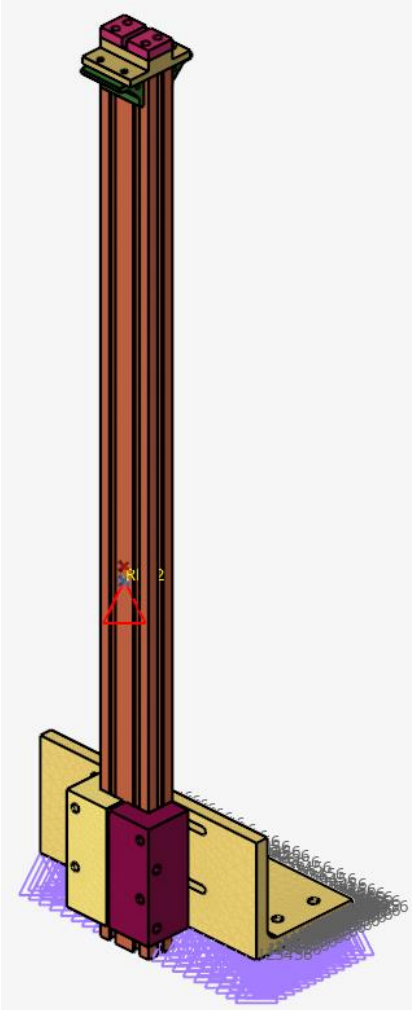

Figure 3.36 – Test rig model

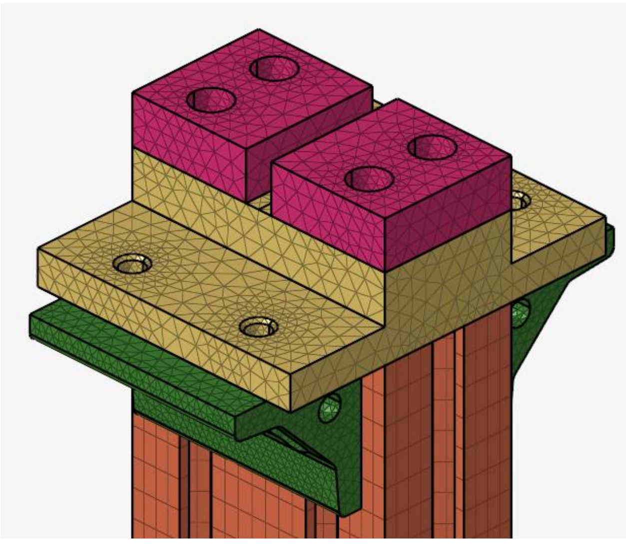

Figure 3.37 – I-beam constrain sub-group

In addition, another modification has been performed in the I-beam clamping sub-group. Where, as represented in *Figure 3.37*, due to the absence of the I beam, the two clamps were shifted downward to reach the contact with the interface. Otherwise, having these two parts suspended and simply connected by a connector representing the bolted connection could have generated some irregularities in the results since a suspended part vibrates easily. The free length of the vertical beam above the constraint is 1000 mm.

After the model simplification, all the parts were meshed. The vertical beam has been meshed in the same way of Simulation 2, starting from a 2D mesh of the cross-section which was then extruded toward the vertical direction. All the other components, according to their shape, have been mesh with a Tetra 3D mesh with an element size fulfilling the quality criteria. Finally, according to *Figure 3.37*, the quality of the mesh has been refined in the critical areas of the I-beam constraint sub-group. Where, due to the small size of the parts compared to the rest, as emerges from the parts of *Figure 3.38*, it is beneficial to reduce the mesh size for a proper contact definition between the components.

The final step of the model preparation is the contact definition. In order to replace all the bolted connections, it has been decided to simplify the model by applying surface contact between the parts in contact. This has to be done after the mesh because the surface contact is defined between the two meshed areas of the parts. The contacts of the I-beam constraint sub-group are represented in *Figure 3.38*:

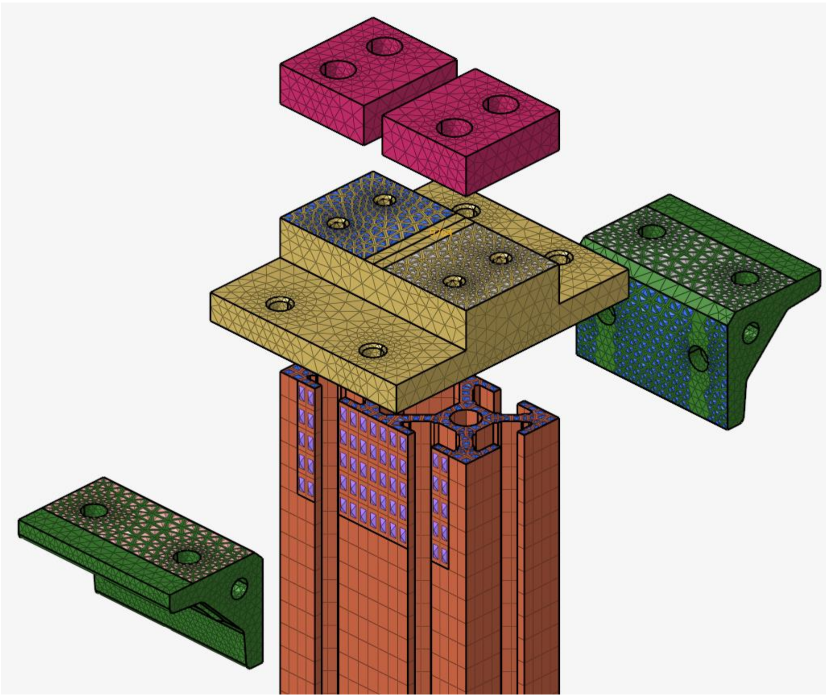

Figure 3.38 – Contacts in the I-beam constraint sub-group

On the other side, *Figure 3.39* represents the contacts in the lower constraint sub-group. Since the dimensions of these contact areas are wider compared to the I-beam constraint sub-group, and the contact is distributed on a large surface, it is possible to generate a coarser mesh:

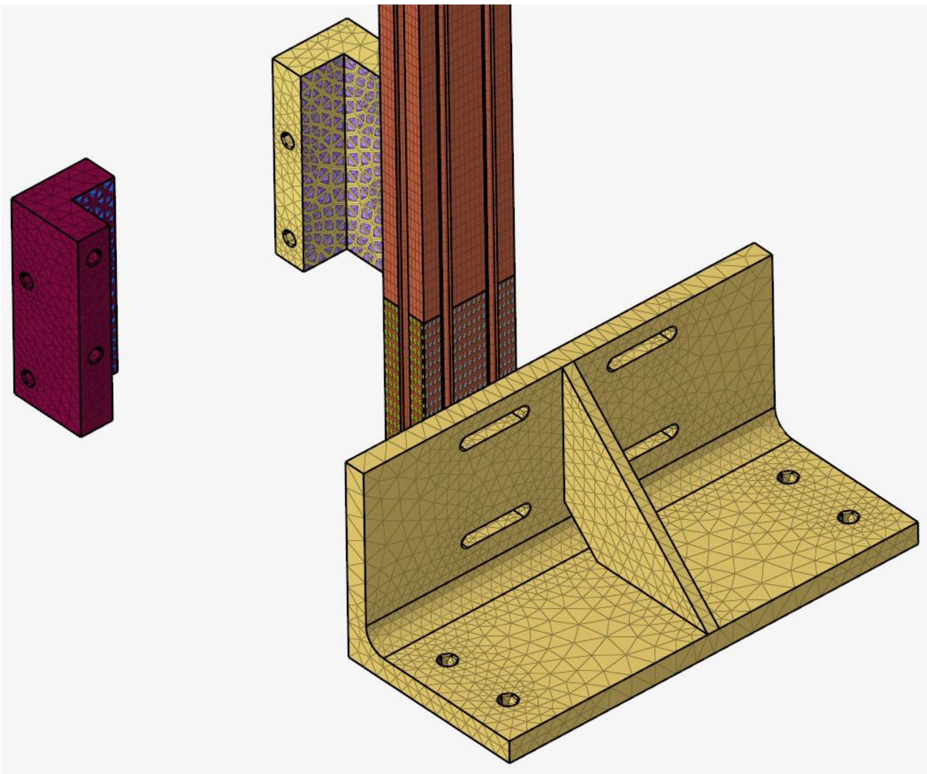

Figure 3.39 – Lower constraint sub-group

After the model preparation, load and boundary conditions are assigned to the model. Regarding the boundary condition, according to the real mounting of the L base on the suspended table by four bolted connections; as represented in *Figure 3.40*, the lower surface of the L base has been fixed by a SPC (Single Point Constrain) for each point of the mesh preventing the displacement of the six degrees of freedom.

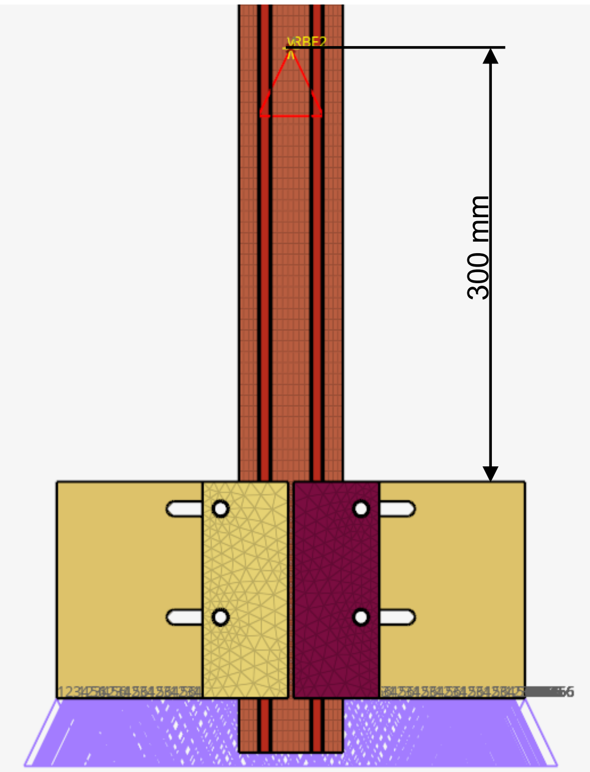

Figure 3.40 – Load and BC of the test rig

Regarding the load, as it was done in Simulation 1, it is applied at a distance of 300 mm from the upper limit of the constraint and in the middle of the surface to avoid the generation of torsional effects on the vertical beam along the z axis, which are not included among the excitations. As it is represented in *Figure 3.41*, which is a detailed view of *Figure 3.40*, the application point of the DAREA load is connected to the nearby nodes by a RBE2 element to avoid localized effects due to the application of the load on a single node. The entity of the load is 100 N.

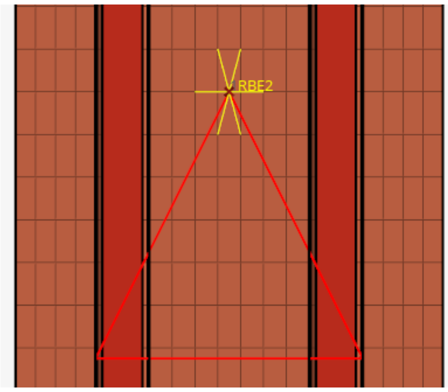

Figure 3.41 – DAREA load

According to the purpose of the simulation, the typology of simulation is the "Frequency response (direct)" which is a linear dynamic simulation. The structure and the material, considering the elastic region, are both linear. In addition, the RBE2, which is the additional component involved in the simulation behaves linearly and all the non-linearities and friction are assumed negligible to simplify the model. The frequency range of the simulation is from 0 to 1000 Hz with an increment of 5 Hz for each computation.

The result extracted from the simulation is the displacement of the structure. Consisting of the displacement measured on the top of the test rig: Node 9476 represented in *Figure 3.42*, and the deformed configurations for each peak of the graph.

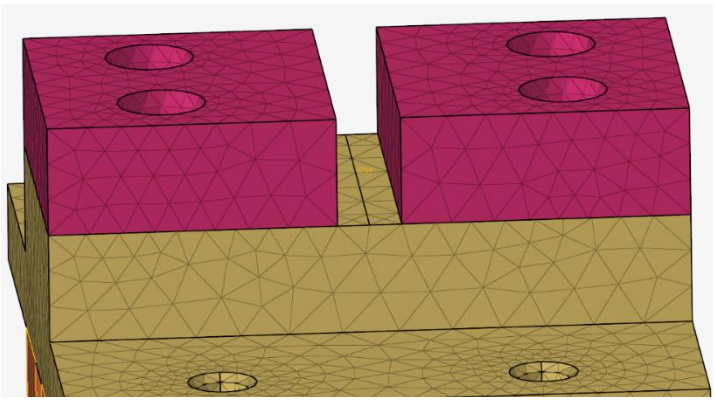

Figure 3.42 – Node 9476 location

The displacement FRF measured at Node 9476 in Z direction (vertical direction) is represented in *Figure 3.43*:

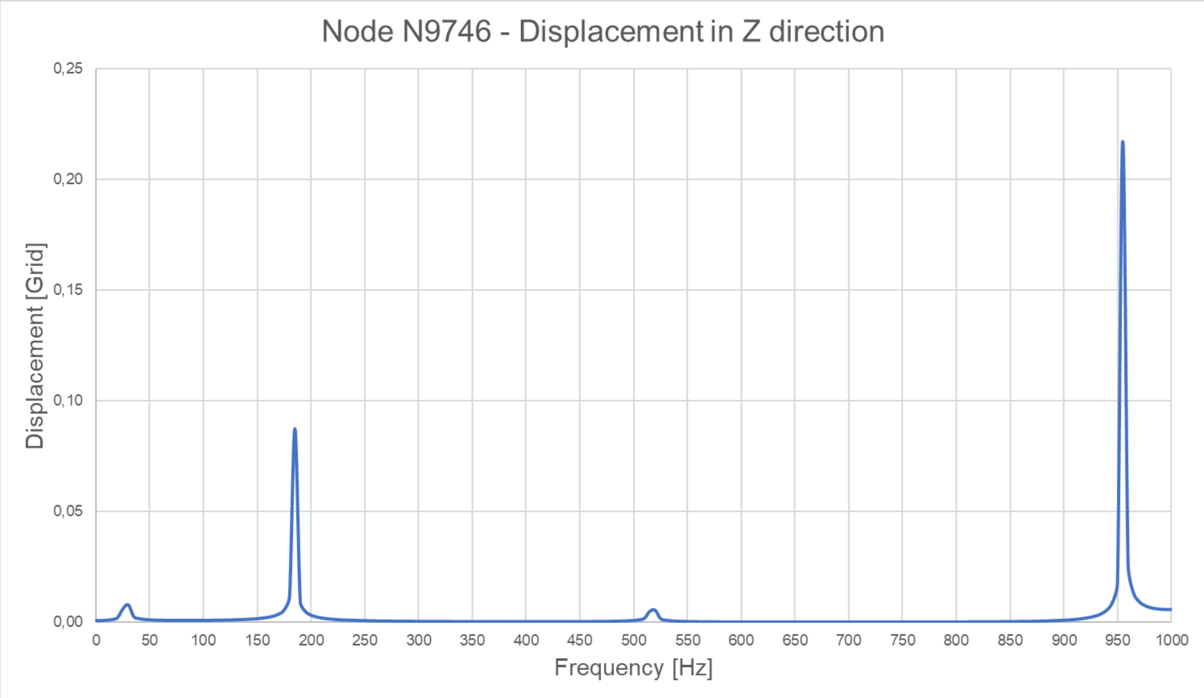

Figure 3.43 – Node 9476 – Displacement in Z direction

The frequencies of the characteristic peaks are collected in *Table 3.6*:

Peak	Frequency [Hz]
1	30
2	185
3	520
4	955

Table 3.6 – Peaks of the Node 9476 – Displacement in Z direction

From the analysis of the graph, it shows that the response of the 1st and 3rd peaks have a lower entity compared to the 2nd and 4th peaks. This can be also noticed from the legend of *Fig. 3.44* and *3.45* which represent the deformed configurations of the four peaks of the test rig in the frequency range 0 – 1000 Hz. Although the color legend is the same for each deformed configuration, the threshold of each level is different.

Figure 3.44 represents the deformed configurations for the 1st (a) and 2nd (b) peaks of the FRF diagram:

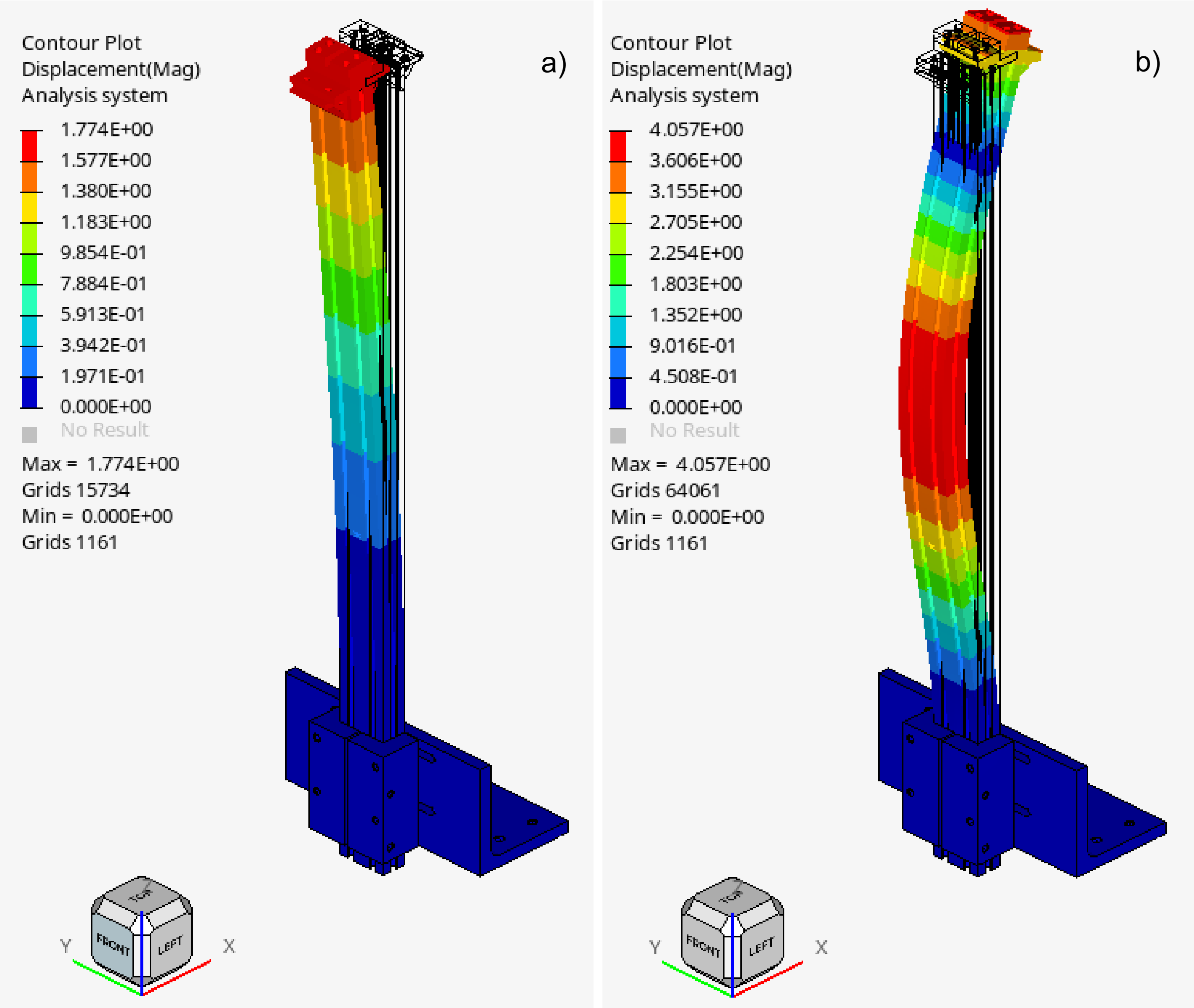

Figure 3.44 – a) 1st peak and b) 2nd peak deformed configurations

The deformed configurations represented in *Figure 3.44* are two flexural modes, similar to the first two modes characteristic of the cantilever beam. The similarity with the cantilever beam was already expected. For this reason, Simulation 2 was executed as the simulation of the vertical beam constrained as a cantilever beam with the addition of 1 kg concentrated mass on the top. By highlighting the differences, the vertical beam is constrained as a cantilever beam (this is the purpose of the lower constraint sub-group) while the mass on the top of the beam is almost half of 1 kg and is a distributed mass.

Figure 3.45 represents the deformed configurations for the 3rd (c) and 4th (d) peaks of the FRF diagram:

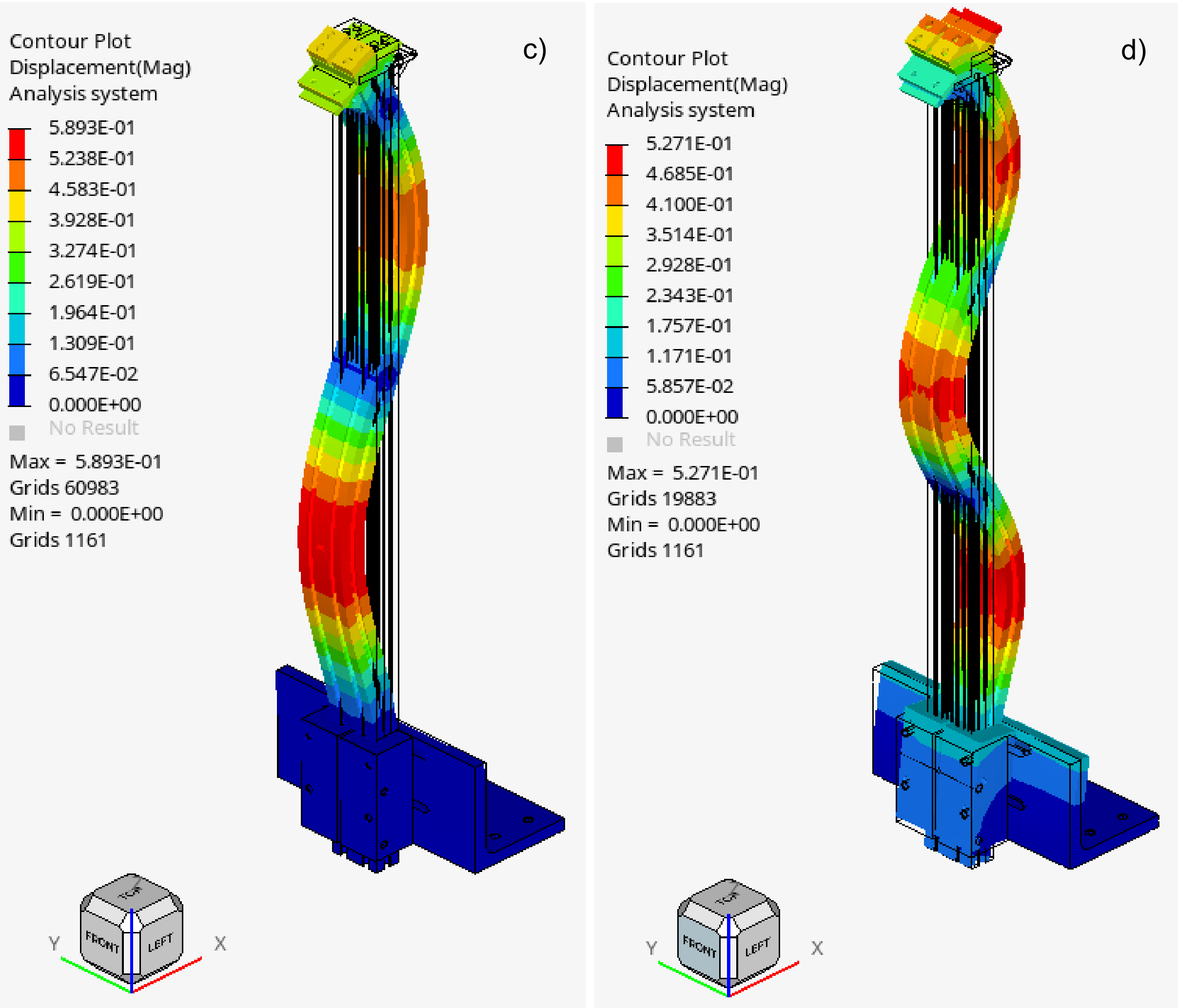

Figure 3.45 – c) 3rd peaks and d) 4th peak deformed configurations

The deformed configurations represented in *Figure 3.45* are two flexural modes, similar to the third and fourth mode shapes of the cantilever beam. *Figure 3.45 d)* represents the 4th eigenmode at 955 Hz. It is possible to consider that, although the L base was designed including cross-reinforcements with the purpose of being stiff, at high frequency values its deformation has the same order of magnitude of the deformation of the vertical beam.

In order to obtain the symmetric mode shape of interest of the I-beam, the load is applied in the middle of the 80 mm edge of the vertical beam to avoid the induction of torsional excitations. This is the reason why the deformed shapes obtained from the simulation are only flexural configurations.

After the detailed analysis of the dynamic behavior of the test rig, the I-beam will be included in the model shifting the focus from the test rig to the dynamic behavior of the beam.

3.3.4 Simulation 4: Bending test rig natural frequencies determination

Simulation 4 is executed after the completion of the design with the purpose of determining the eigenfrequencies and eigenmodes of the test rig according to the applied boundary conditions. The model used for the simulation is the same of Simulation 3, therefore it will not be presented anymore. The only difference is the adopted load step, which is the “Normal modes” analysis in this case. Therefore, it is not necessary to apply a load because the solution is computed by solving the eigenvalue problem. The imposed frequency range is the same of Simulation 3: 0 – 1000 Hz. The free length of the vertical beam is 1000 mm. The results are the nine eigenfrequencies in the given frequency range collected in *Table 3.7*, and the correspondent eigenmodes, represented in *Figure 3.46*:

Peak	Frequency [Hz]	Type of mode
1	27.8	Flexural (x)
2	52.8	Flexural (y)
3	184.4	Flexural (x)
4	244.8	Torsional (z)
5	340.2	Flexural (y)
6	517.5	Flexural (x)
7	782.3	Torsional (z)
8	915.1	Flexural (y)
9	955.5	Flexural (x)

Table 3.7 – Eigenfrequencies of the test rig

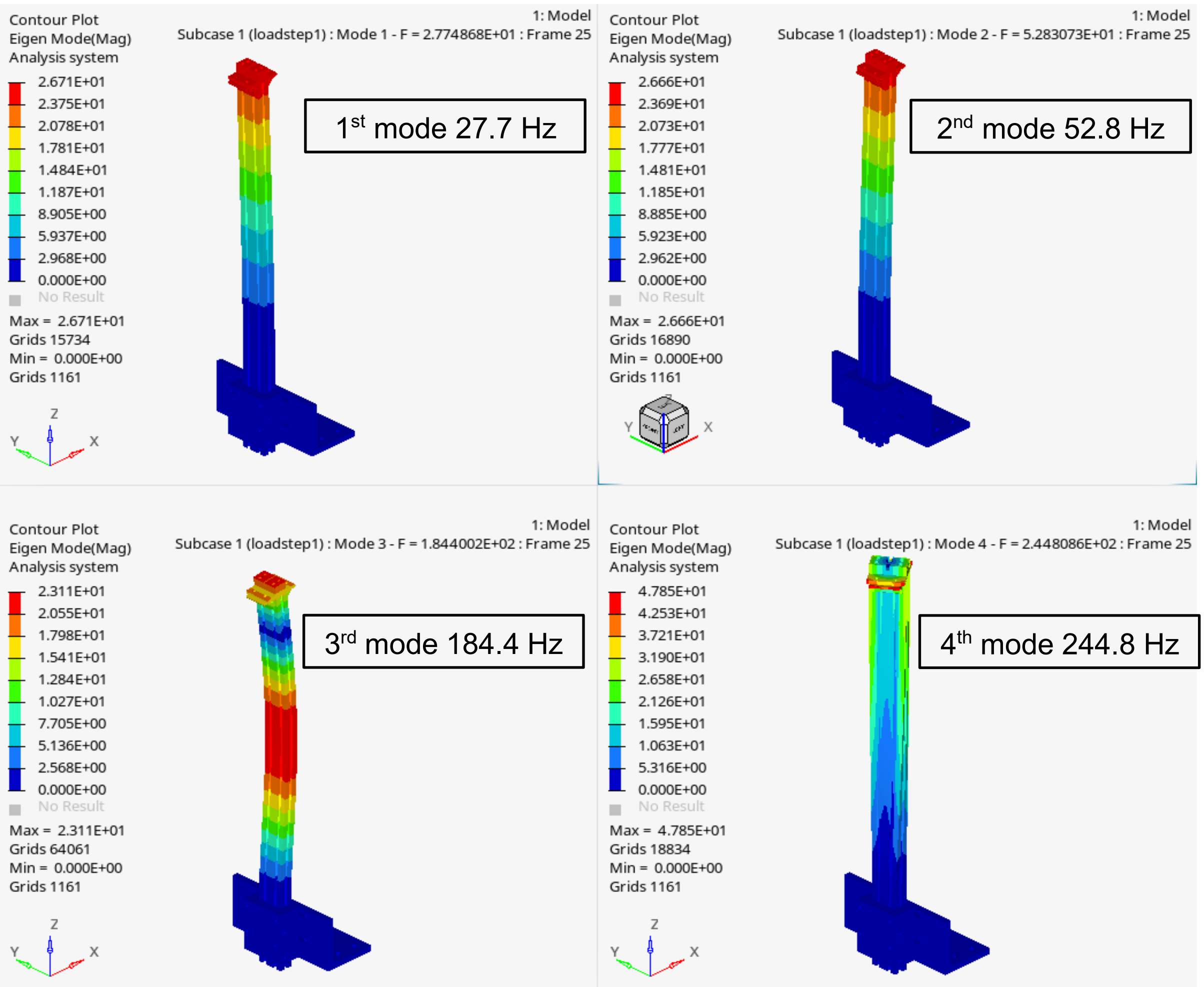

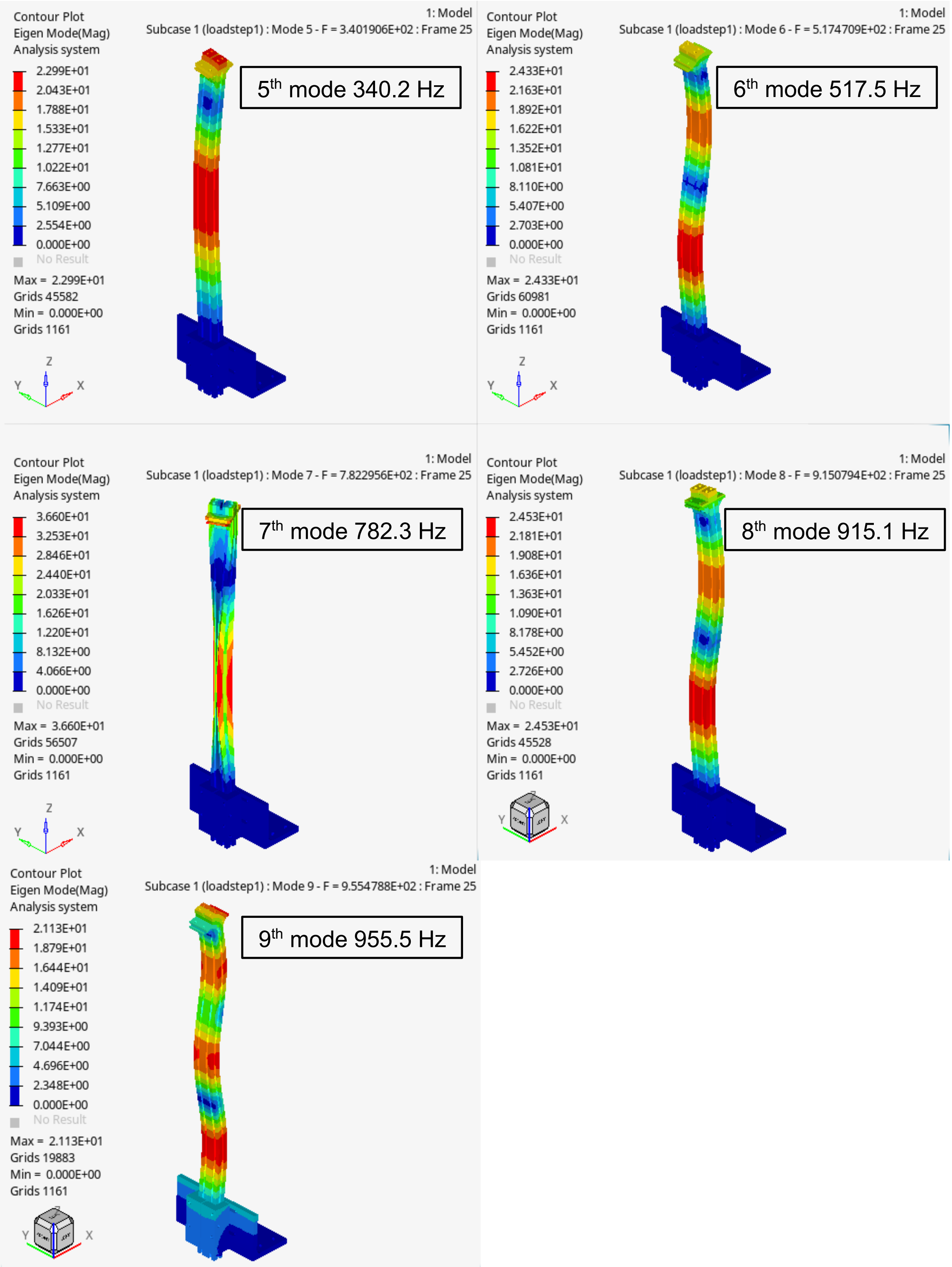

Figure 3.46 – Eigenmodes of the test rig

From the analysis of the mode shapes and the correspondent eigenfrequencies it is possible to compare Simulation 3 to Simulation 4. According to the excitation applied in Simulation 3, is not possible to obtain torsional modes and flexural modes in Y direction (according to the coordinate system of *Figure 3.46*). On the contrary, since Simulation 4 is the solution of the eigenvalue problem, all the possible modes can be computed, regardless the excitation. According to *Table 3.7*, the flexural deformed shapes in the X direction (according to the reference system of *Figure 3.46*) obtained from Simulation 3, are close to the mode shapes of Simulation 4 and the eigenfrequencies correspond as well. The natural frequency comparison is reported in *Table 3.8:*

Peak	Freq. Simulation 3 [Hz]	Freq. Simulation 4 [Hz]	Type of mode
1	30	27.8	Flexural (x)
2	-	52.8	Flexural (y)
3	185	184.4	Flexural (x)
4	-	244.8	Torsional (z)
5	-	340.2	Flexural (y)
6	520	517.5	Flexural (x)
7	-	782.3	Torsional (z)
8	-	915.1	Flexural (y)
9	955	955.5	Flexural (x)

Table 3.8 – Results comparison Simulations 3 and 4

The eigenfrequencies obtained from the “Normal mode” simulation have a different resolution respect to what was imposed in Simulation 3 since these are mathematically computed from the solution of the eigenvalues problem.

3.3.4.1 Bending test rig model simplification and comparison of the results with Simulation 4

In addition to the Simulation 4 executed on Hypermesh Optistruct®, the same simulation was run on Ansys Mechanical® with a simplified model to obtain the mass and stiffness matrixes to import in pyFBS for dynamic sub-structuring, because pyFBS is only compatible to this platform.

11It has been decided to reduce the model to simplify the sub-structuring. Therefore, according to the purpose, the lower part of the model is mass and stiffness effective to be considered as ideal as possible and has limited interest for the dynamic simulation. It has been decided to simplify this sub-group rather than the I-beam constraint which plays a characteristic role.

In order to simplify the model to import in pyFBS, the contacts of the lower constraint sub-group have been reduced, as detailed in *Figure 3.48*. The vertical right and left constraints have been removed and only the contact of the vertical surface of the L base with the vertical beam has been imposed; while the I-beam constraint sub-group is the same of Simulation 4, as represented in *Figure 3.47*:

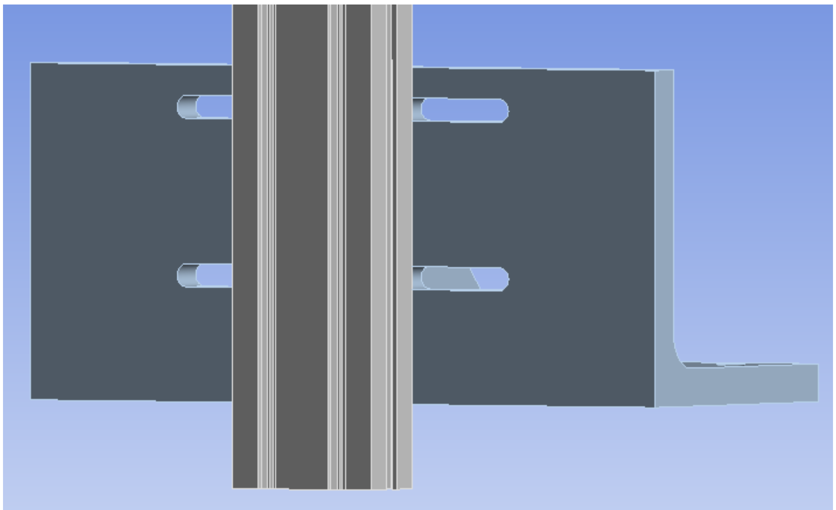

Figure 3.47 – Lower constraint sub-group simplification of Ansys model

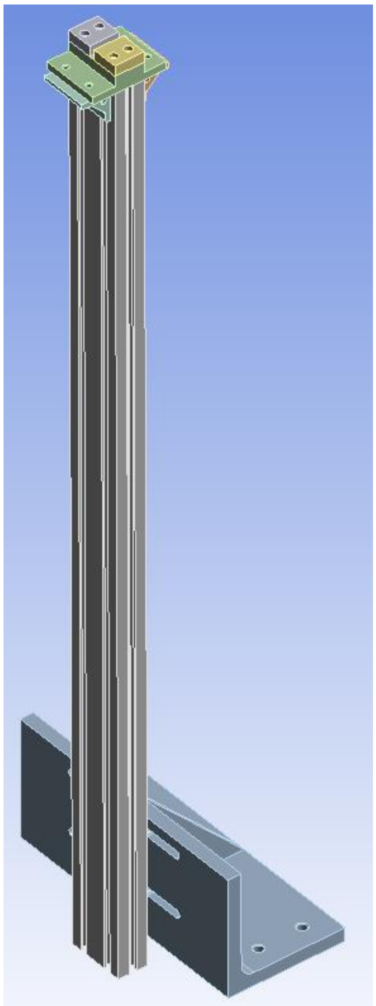

Figure 3.48 – Ansys model

Another element causing a difference between the two results is provided by the mesh, because the meshed in the two models are not equal. From the comparison of the results of the same analysis performed on similar models with different platforms, it is possible to evidence that the eigenmodes are equal while the natural frequencies, collected in *Table 3.9*, are similar.

The difference increases as the frequency increases, this could be due to the raise of influence of non-linearities at higher frequencies:

Peak	Freq. Ansys® Simulation [Hz]	Freq. Hypermesh® Simulation [Hz]	Type of mode
1	26.7	27.8	Flexural (x)
2	50.2	52.8	Flexural (y)
3	177.2	184.4	Flexural (x)
4	243.9	244.8	Torsional (z)
5	324.9	340.2	Flexural (y)
6	498.3	517.5	Flexural (x)
7	779.2	782.3	Torsional (z)
8	878.1	915.1	Flexural (y)
9	922.6	955.5	Flexural (x)

Table 3.9 – Ansys® and Hypermesh® eigenfrequencies comparison

3.3.5 Simulation 5: Bending test rig + I-beam dynamic simulation

Simulation 5 consists of the dynamic simulation of the model used for Simulation 4 adding also the full carbon (TT2) I-beam. The model of the implemented horizontal beam is not part of this thesis, it has been provided by Scheffler [23] who analyzed the hybridization of the I-beams. Contrarily to Simulation 4, the purpose of this simulation is to determine the dynamic behavior of the I-beam mounted on the test bench. And to verify that the deformed configuration is the same of the desired asymmetric mode shape, which has been obtained in Simulation 1 with a T layout simplified test rig. The free length of the vertical beam is 1000 mm.

The entire model is represented in *Figure 3.50*. The carbon beam has been located symmetrical to the test bench and the right and left clamps are not in physical contact with the interface anymore since they are shifted upwards by the same amount of the thickness of the lower flange of the I-beam. But the surface contact constraints of the two clamps and the interface are still maintained. As it was already done in Simulation 3, the connections are modeled by mean of surface contacts. In detail, as it emerges from the exploded view of *Figure 3.50*, the added contacts are:

- I-beam lower flange – Right clamp
- I-beam lower flange – Left clamp
- I-beam lower flange – Interface upper surface

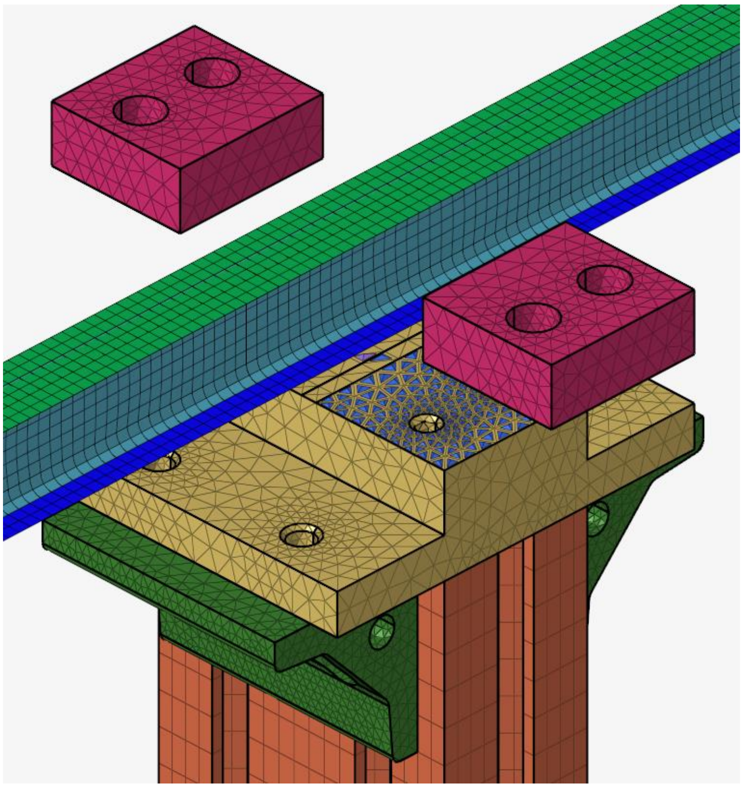

Figure 3.49 – Detailed view of the I-beam constraint

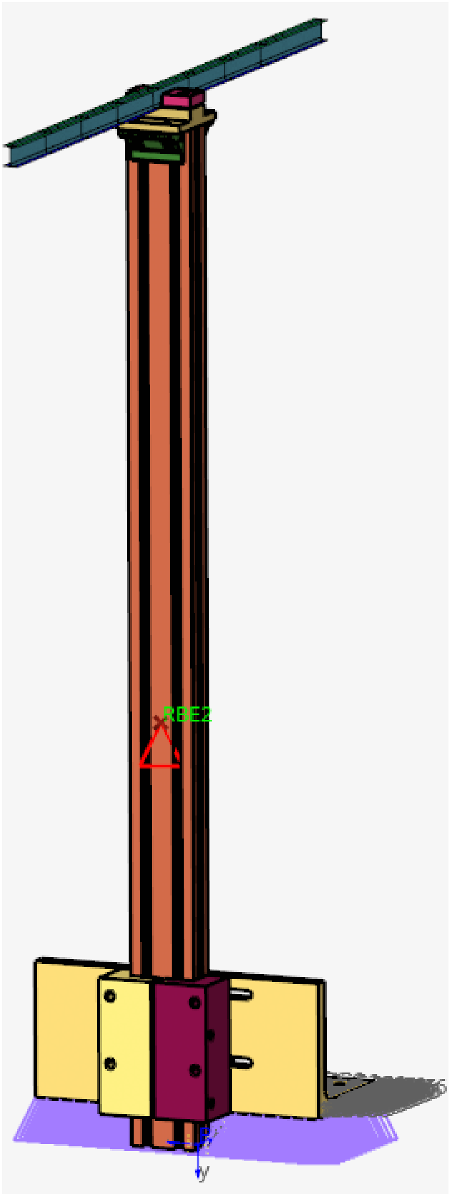

Figure 3.50 – Simulation 5 model

According to Simulation 3, the frequency range of the simulation is 0 – 1000 Hz and the boundary condition is applied to the lower surface of the L base to simulate its connection to the suspended table. The applied load is the DAREA load in X direction with absolute value of 100 N. The entity of the load is assigned based on the experience coming from other dynamic experiments. The exact entity will be determined during the experiment by adopting the lowest load which provides a result measurable by the accelerometers according to their resolution.

The displacement is measured in Z direction (vertical direction) at Node 74335, which is represented in *Figure 3.51*:

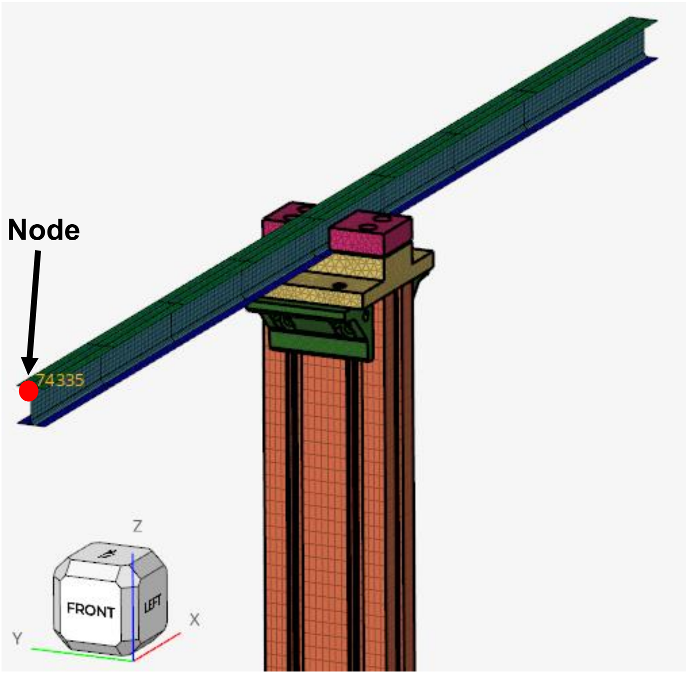

Figure 3.51 – Node 74335 location

The displacement FRF measured at Node 74335 in Z direction (vertical direction) is represented in *Figure 3.52*:

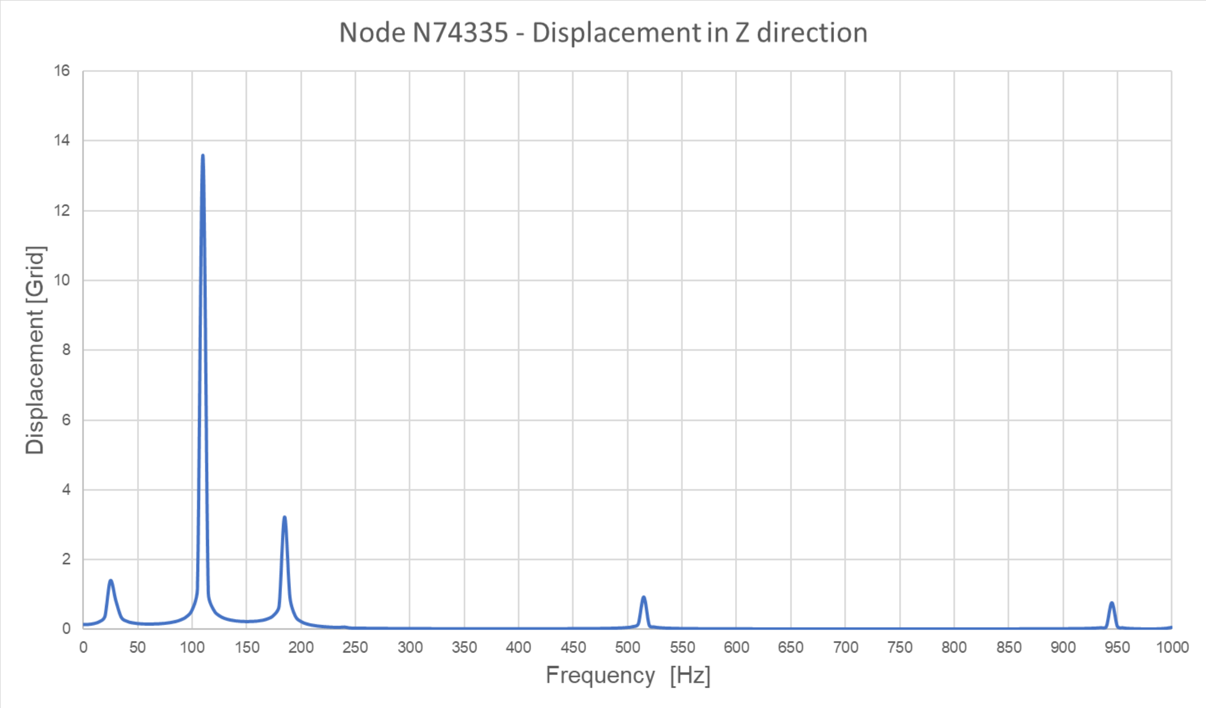

Figure 3.52 - Node 74335 – Displacement in Z direction

The frequencies of the characteristic peaks are collected in *Table 3.10*:

Peak	Frequency [Hz]
1	25
2	110
3	185
4	515
5	945

Table 3.10 – Peaks of the Node 74335 – Displacement in Z direction

The deformed configurations of the test rig including the full carbon I-beam are reported in *Figure 3.53*. From the analysis of the deformed shapes is possible to conclude that the 1st, 2nd and 3rd coincide to the desired asymmetric mode shape. Therefore, the test rig used for the lateral bending excitation behaves according to how it was conceived:

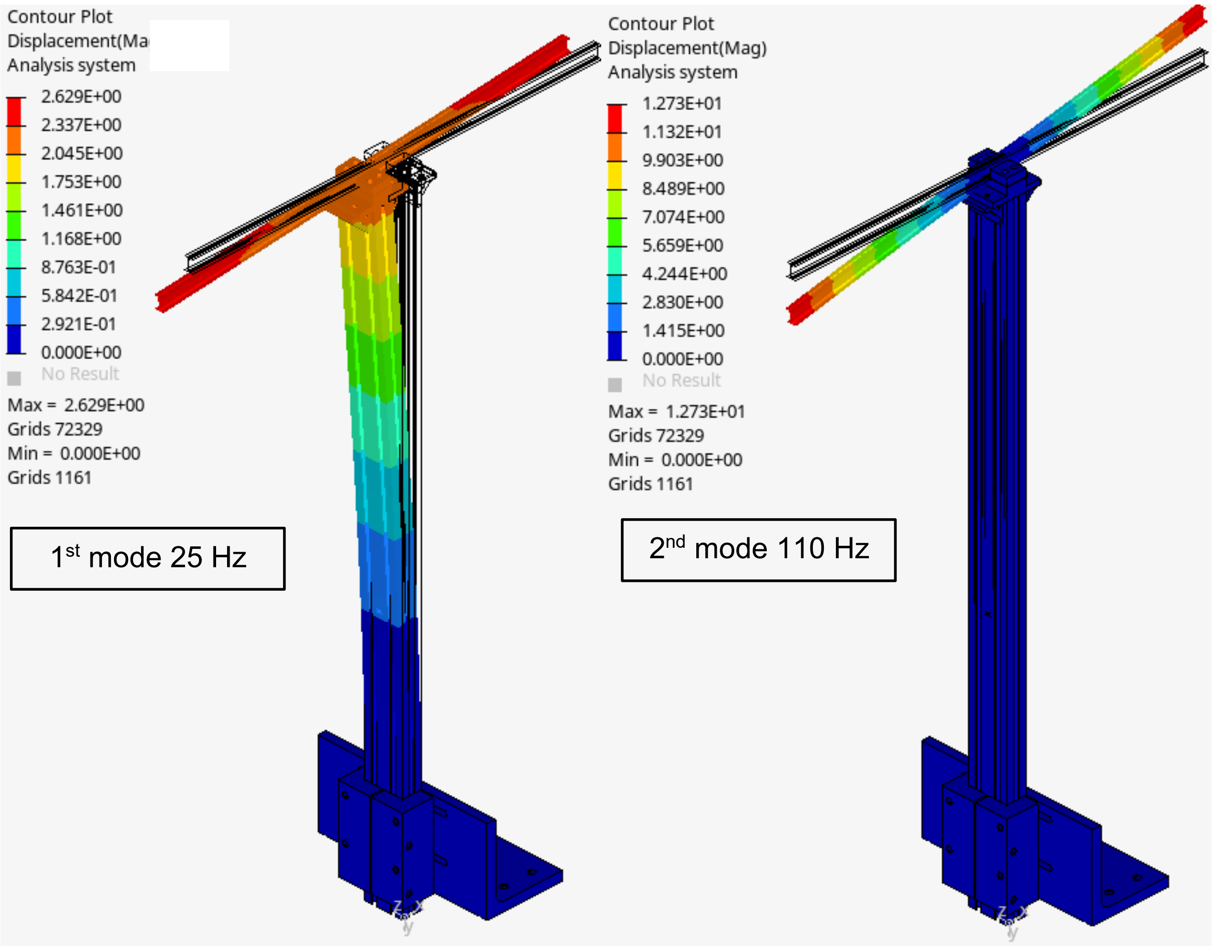

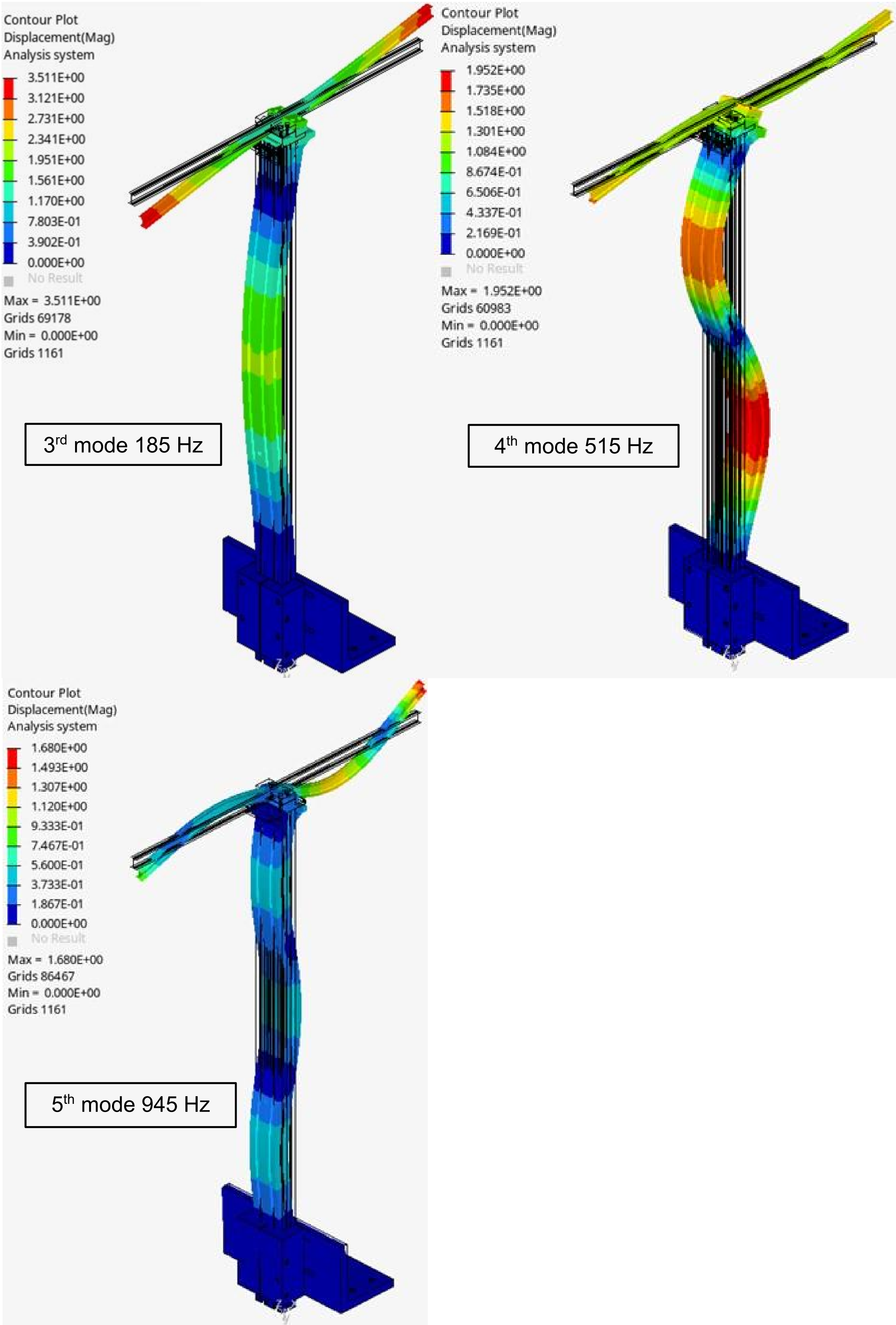

Figure 3.53 - Test rig + TT2 mode shapes

3.3.6 Simulation 6: Axial test rig + I-beam dynamic simulation

Thanks to the previous simulations, the dynamic behavior of the I-beam mounted on the test rig has been obtained highlighting the asymmetric mode shape. Simulation 6 consists of the dynamic simulation of the test rig including the I-beam used for the axial excitation to highlight the symmetric mode shape. The purpose of this simulation is to determine the dynamic behavior of the I-beam and to verify that the deformed configuration is the same of the desired symmetric mode shape, which has been obtained in Simulation 1 with a T layout simplified test rig. Since the simulation of the complete test rig provided positive results regarding the mode shape, it is expected to obtain the desired deformed configuration also with the reduced test bench. Therefore, the main goal is to determine the frequency response diagram measured at the end of the horizontal beam.

According to the purpose of the simulation, the typology of simulation is the "Frequency response (direct)" which is a linear dynamic simulation. The structure and the material are both linear; and all the non-linearities and friction are assumed negligible to simplify the model. The frequency range of the simulation is from 0 to 1000 Hz with an increment of 5 Hz for each computation, equivalently to the previous simulations. The model adopted for the simulation, represented in *Figure 3.54*, consists of the upper part of the model used for Simulation 5:

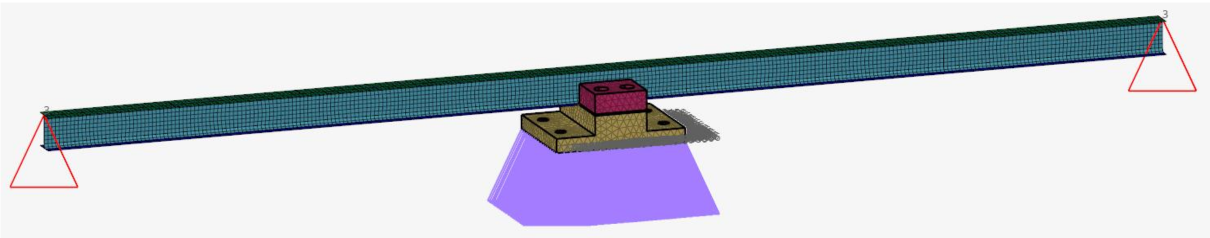

Figure 3.54 – Simulation 6 model

The model is composed by the I-beam which is constrained to the interface by the right and left clamps. The lower surface of the interface, which is connected to the top of the vertical beam in the full test rig, is fixed to the ground.

It is important to evidence that the symmetric mode shape of Simulation 1 is obtained by applying the load in the node located in the middle of the I-beam, which, according to the configuration of the mode shape, is a node of the beam. Therefore, according to the theory, by applying the load in a node there should not be any displacement in the system. However, it is evident that, even though the load is applied in a node, the horizontal beam deforms. From a detailed analysis, it is possible to conclude that there is displacement because the interface is connected to the vertical beam which is not rigid. Thus, by applying the dynamic load, the vertical beam compresses and extends with the same frequency of the excitation and a phase delay. Consequently, since the horizontal beam is characterized by a proper mass, with the acceleration induced by the dynamic excitation, it undergoes to a dynamic force which causes its deformation.

It has been decided to execute the experiment without the vertical beam since it does not influence the test and it is not useful for this application.

The boundary condition consists of a SPC (Single Point Constraint) applied to each node of the lower surface of the interface. Regarding the load, the dynamic load induced by the acceleration in Simulation 1 acts equivalently both on the right and left sides of the I-beam, since these are characterized by the same mass and length. For this reason, in order to replicate the same effect, the dynamic load DAREA required by the “Frequency response (direct)” simulation is applied both on the right and left end nodes of the horizontal beam.

The results of the simulation are the deformed configurations and the FRF diagram built according to the displacement measured at Node 74355 (the same of Simulation 5) with the load applied at both extremities of the horizontal beam. The displacement FRF measured at Node 74335 in Z direction (vertical direction) is represented in *Figure 3.55*:

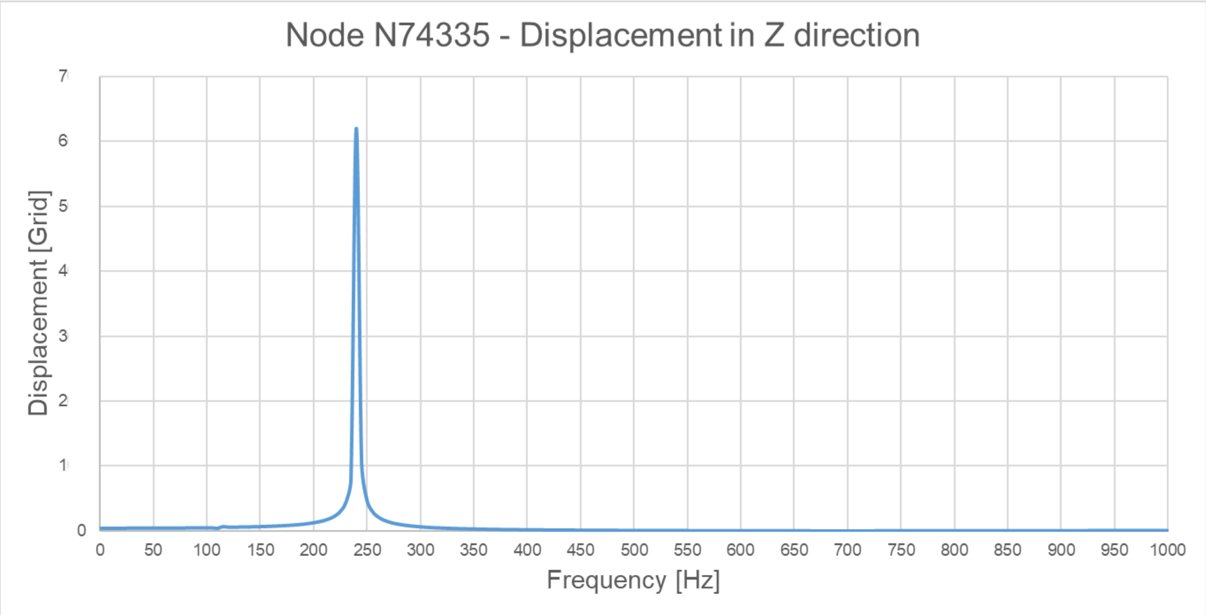

Figure 3.55 – Node 74335 – Displacement in Z direction axial test rig

According to *Table 3.11*, the peak is located at:

Peak	Frequency [Hz]
1	245

Table 3.11 – Peak of the Node 74335 – Displacement in Z direction

The deformed configuration correspondent to the peak is represented in *Figure 3.56*:

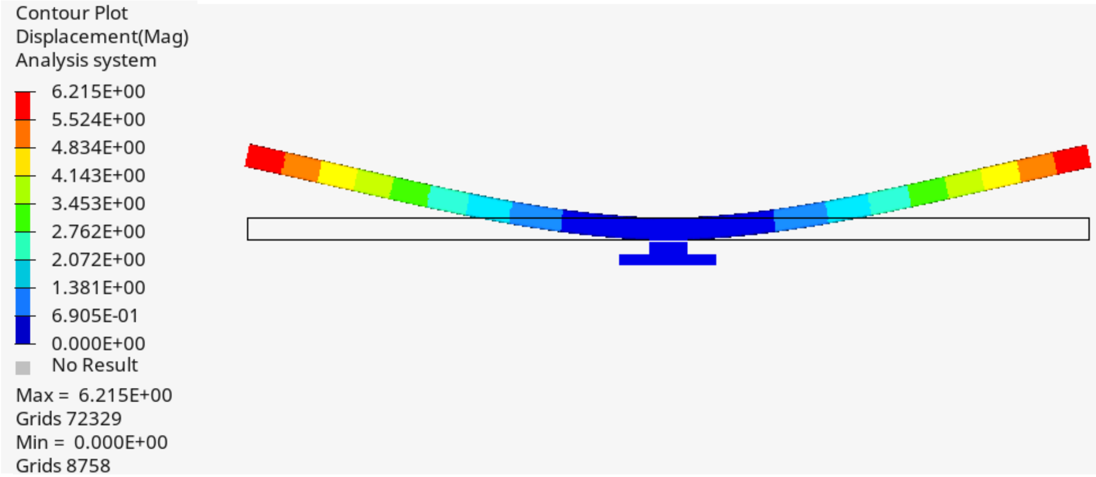

Figure 3.56 – Simulation 6 deformed shape correspondent to the peak

From the graph represented in *Figure 3.55* emerges that there is only one peak with the relative eigenmode represented in *Figure 3.56*. Nevertheless, by amplifying the lower part of the vertical axis of the plot, it is possible to determine the presence of other peaks with a smaller entity of the displacement with respect to the other. These peaks, with the corresponding eigenmodes, are represented in the next figures. It comes out that there is another symmetric configuration approximately at 400 Hz. As represented in *Figure 3.57*, this symmetric deformed configuration is characterized by a different shape with respect to the previous:

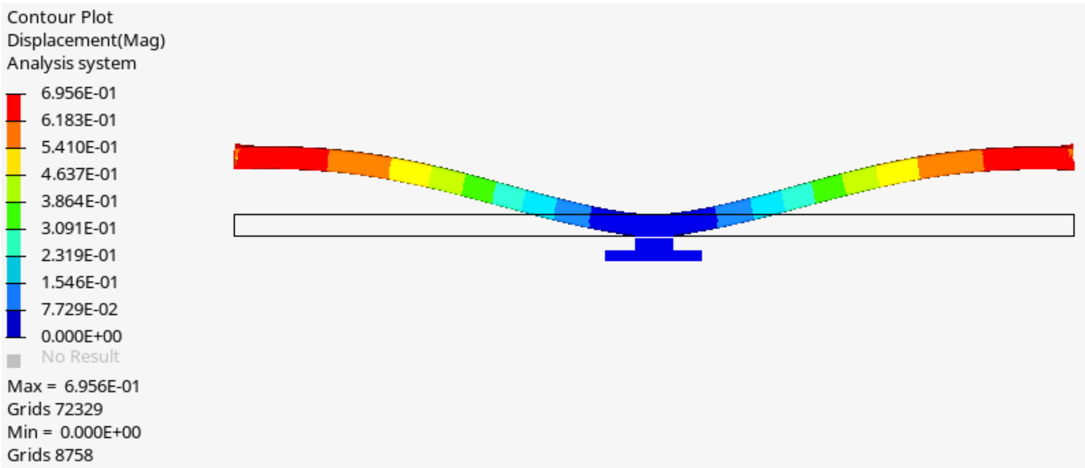

Figure 3.57 – Simulation 6 deformed shape at 550 Hz

In *Figure 3.57* it is possible to evidence the presence of a peak in each branch of the I-beam. The peak introduced in each branch becomes more evident as the frequency increases. *Figure 3.58* represents the deformed configuration at 650 Hz:

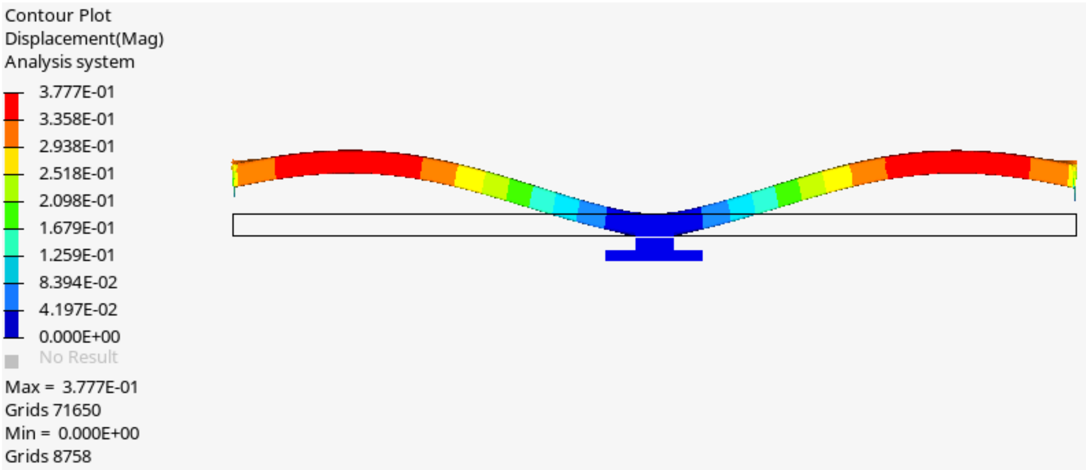

Figure 3.58 – Simulation 6 deformed shape at 650 Hz

According to *Figure 3.59*, which represents the deformed configuration at 950 Hz, by increasing the frequency value, the peak moves to the center of the branch:

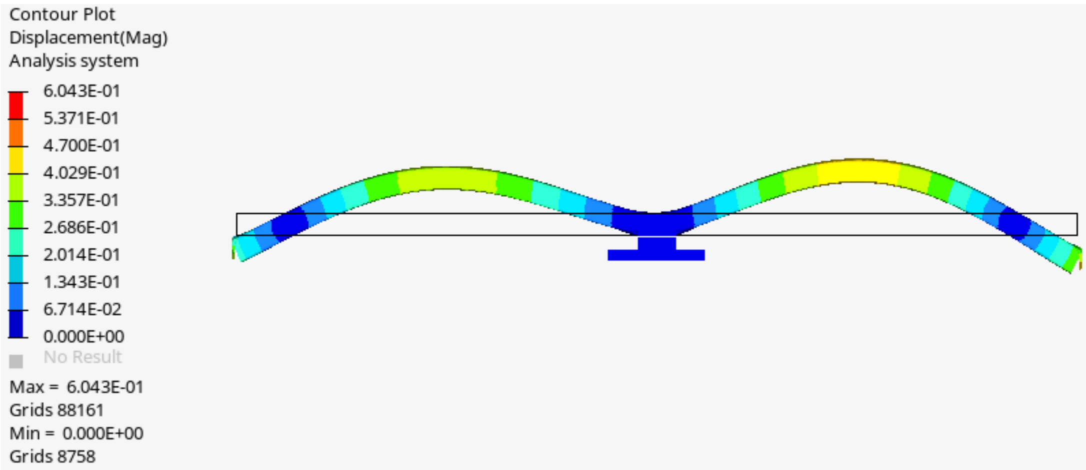

Figure 3.59 – Simulation 6 deformed shape at 950 Hz

3.4 Experimental modal analysis vs simulation comparison

After the theoretical validation of the bending and axial test rigs obtained by virtual simulation, the parts have been produced and assembled.

Different experiments have been executed to compare the real functioning to the simulation. The validation of the test rig has been performed by a “Bottom to Top” approach. It consists of breaking the entire assembly in sub-groups and adding a single group to the experiment and comparison at each time, only after having validated the previous test. Despite of it increases the number of experiments, this approach makes it easier to understand the single parts. On the contrary, by directly analyzing the complete test rig plus the specimen, it would be complicate to identify the causes of eventual discrepancies due to the wide number of phenomena in consideration.

The axial test rig is composed by the upper sub-group of the bending test rig. Therefore, the bending test rig has been verified first. And, after its validation, it is expected also the validation of the axial test rig. Initially the vertical beam with the lower constraint sub-group have been tested and compared to the simulation. After the comparison and the tuning of the model, the I-beam constraint sub-group has been added to the experiment. In conclusion, the axial test rig has been analyzed and validated.

Finally, after the validation of the test rigs, also the I-beam has been added to the experiments. In order to make a comparison, the two extreme conditions are considered: TT2 - full carbon beam and TT7 - almost full flax beam. Then, the test rigs will be used in the next steps of the eVolve project to test the behavior of the I-beams and the tailplanes.

3.4.1 Bending test rig

According to what has been anticipated, with the “Bottom to Top” approach the entire bending test rig has been tested starting from each sub-group independently before considering it completely. The purpose is to simplify the understanding of each part.

3.4.1.1 Experiment 1: Vertical beam – 1100 mm

The set-up is composed by the vertical beam constrained to the table by mean of the lower constraint sub-group and the L base. With respect to the designed components, the L base is different because it has been decided to use a standard L support already present in the laboratory. Its main dimensions are 140 x 100 mm, and it is made up of cast iron. As consequence, the dimensions of the lower constraint sub-group have been adapted to the adopted support to ensure the clamping of the vertical beam. The assembly is represented in *Figure 3.61*, and the lower constraint sub-group is detailed in *Figures 3.60* and *3.62*:

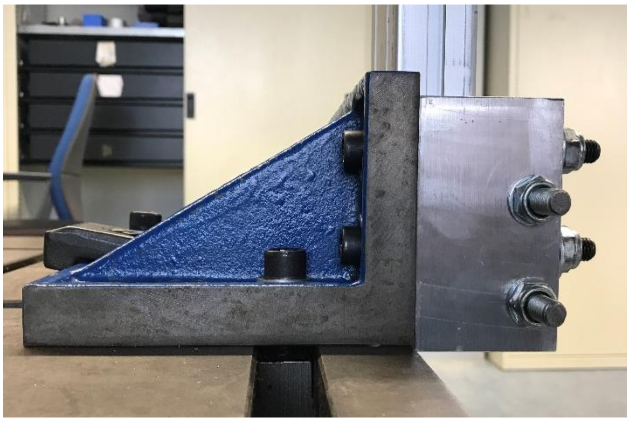

Figure 3.60 - Experiment 1: lower constraint sub-group

Figure 3.61 – Experiment 1: set-up

The L base is fixed to the suspended table by five M10 threaded connections; therefore, analogously to the simulations, it is assumed to be completely fixed. According to the design, as it emerges from *Figure 3.62,* a 2 mm gap has been kept between the constraints and the L base to guarantee the clamping of the vertical beam:

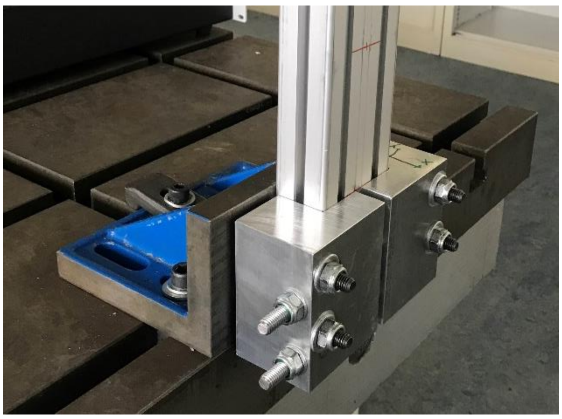

Figure 3.62 - Experiment 1: Vertical beam clamping

It is important to mention that the height of the L base is 100 mm, and the vertical beam is 1200 mm long. In Experiment 1, the vertical beam is mounted with a length of 1100 mm above the upper limit of the constraint; therefore, there is no free length below the constraint. Moreover, in order to ensure the repeatability of the experiment, all the screws have been tightened by mean of a torque wrench.

After assembling the Device Under Testing (DUT), the excitation and the measuring system have been set. According to the literature research, as it is represented in *Figure 3.63*, it was decided to apply a sine sweep excitation from 0 Hz to 1000 Hz using a shaker. However, after the first execution of the experiment, it was repeated with the impact hammer excitation, and it came out that the FRF is cleaner by using an impact excitation, always at 300 mm from the upper limit of the constraint, as represented in *Figure 3.64.* The shaker used in Experiment 1 is a Vibration Test System manufactured by TIRA model TV 50018, while the Impulse Force Hammer is manufactured by PCB and is equipped with a plastic tip (Sensitivity = 10.27 mV/N):

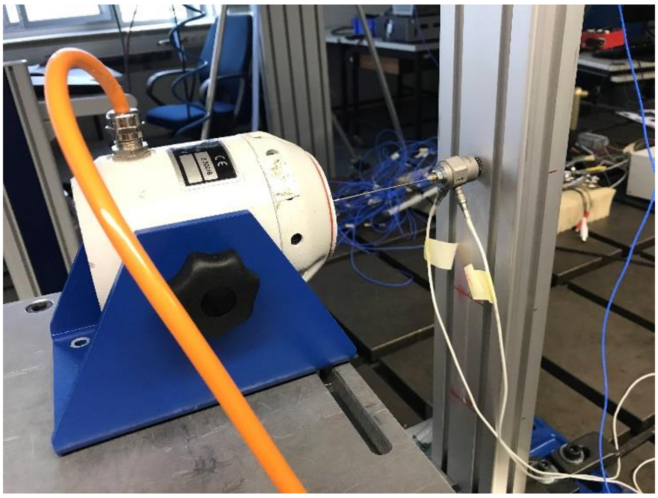

Figure 3.63 – Experiment 1: Shaker excitation

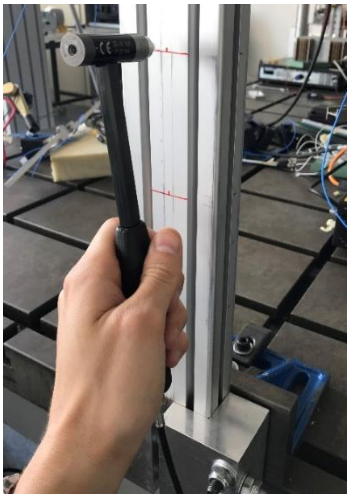

Figure 3.64 – Experiment 1: Impact excitation

The impact excitation will be adopted for all the experiments related to the bending test rig. It is easier and quicker to repeat the experiments compared to the shaker; on the contrary, it is less repetitive because it is difficult to hit the vertical beam always in the same position.

The output is measured with the tri-axial accelerometer PCB Piezotronics model 356A03 positioned on the top of the vertical beam. The calibration data of the transducer are collected in *Table 3.12*:

	Sensitivity [mV/g]	Output bias [VDC]
X axis	11.21	12.2
Y axis	11.89	11.8
Z axis	10.95	12.2

Table 3.12 - Experiment 1: Calibration data of the accelerometer

Figure 3.65 - Experiment 1: accelerometer mounting

The weight of the accelerometer is 0.04 oz (1.14 g) and it is assumed that it does not affect the results since it is glued on a metallic structure, as represented in *Figure 3.65*, with a relevant weight compared to the transducer itself. For this reason, the effect of the cable connecting the transducer to the acquisition system is considered negligible.

Although the accelerometer measures the acceleration, the acquisition system "Simcenter Testlab Impact Testing" directly provides the FRF computed as the ratio of displacement divided by the applied force. The experiment is repeated three times and the resulting FRF is the average of each repetition. This is valid for all the next measurements. Analogue to the simulation, the FRF is obtained only for the Z coordinate. The FRF is plotted with the same graph obtained from the simulation in *Figure 3.66*:

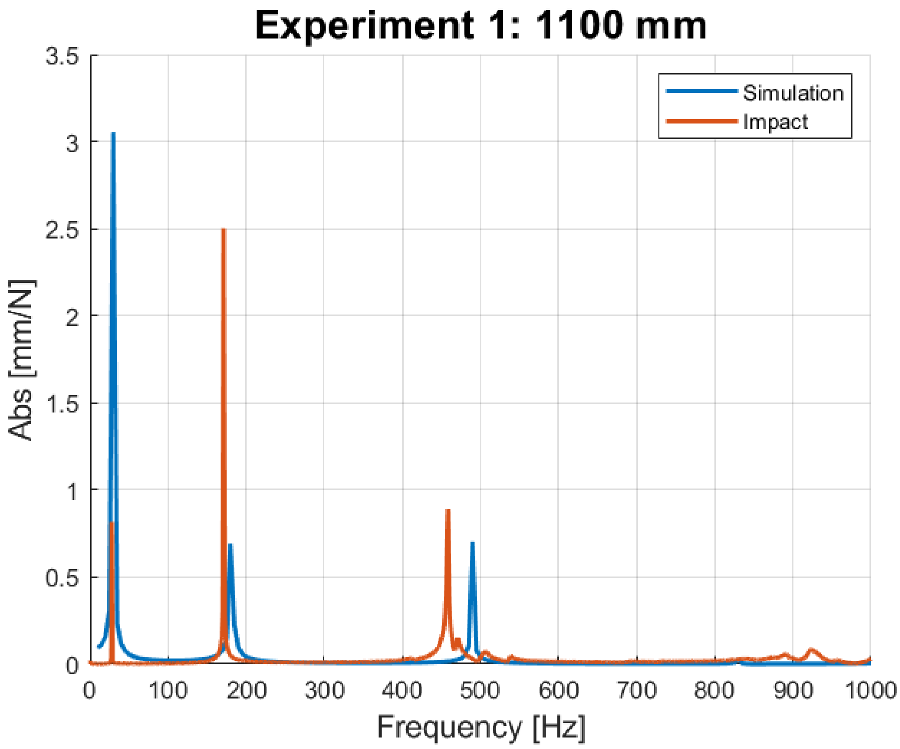

Figure 3.66 - Experiment 1: 1100 mm FRFs comparison

From the analysis of the graph, it is possible to conclude that the experimental measured signal is quite clean even though there are some disturbs, especially in the high frequency field above 700 Hz. This is according to the initial expectations where at higher frequencies, due to non-linearities, the measured signal is more divergent with respect to lower frequencies.

By considering the eigenfrequencies, there are three peaks below 600 Hz. The first two peaks are equivalent for both curves, while the third peak of the impact curve is more irregular compared to the simulation and there are three smaller peaks which are not considered. These could be induced by torsional effects due to an impact applied not exactly in the middle of the vertical beam, in addition there could be disturbs and non-linearities present in the lower constraint sub-group which does not behave ideally like in the simulation. Furthermore, it is possible to notice that the peaks of the simulation curve always precede the peaks of the impact curve; this means that the model is stiffer than the real test rig.

Table 3.13 collects the frequency of the peaks and the relative error among the curves:

	Impact curve [Hz]	Simulation curve [Hz]	Error [%]
Peak 1	27.9	30	**7.5**
Peak 2	171.2	180	**5.1**
Peak 3	458.4	490	**6.9**

Table 3.13 - Experiment 1: Impact vs Experiment relative error

In case of different specification, the resolution of the experiments is set to 0.1 Hz. The relative errors between the peaks are acceptable. In addition, the frequency increment of each computational step adopted in the simulation affects the error. In this case 5 Hz has been set to have a trade-off between computational cost and quality of the FRF curve. Anyway, by reducing the increment it would be possible to refine the peaks and reduce the error. Another source of error is the simplification of the model with respect to the reality. The main differences are:

- Materials' data are obtained from the catalogue and are not directly measured
- In order to simplify the model, all the fastened connections present in the assembly are replaced by fix linear surface contact connections between the parts. Therefore, the mass of the screws is missing
- The bottom surface of the L base is set fixed in the model, while in reality there are five bolted connections to the table which allow to hold the fixed assumption
- The mesh of the vertical beam. Initially the 2D cross-section is manually meshed, then it is extended by solid map linear drag along the Z coordinate. The resulting 3D mesh is composed by CHEXA8 and CPENTA elements. According to the theory, CPENTA and CTETRA elements, increase the stiffness of the model (from the curves comparison emerges that the model is stiffer). For this reason, it would be better to shift all the elements to CHEXA8, or better, to CHEXA20 which is the corresponding second order to the CHEXA8. Unfortunately, due to the complex cross-section of the beam, it is not possible to modify the type of elements, because it is not possible to fill this tri-dimensional geometry with hexagonal elements (independently from the order). The focus is only on the vertical beam because is the component with a higher deflection compared to the other parts of the lower constraint sub-group, which are designed to be considered "rigid" with respect to the ITEM beam.

Other causes of the discrepancies could be related to the assembly. More in detail:

- The bolted connection of the L base to the table and the connection of the right and left constraints to the L base are not rigid and ideal and there are dissipating phenomena in the contact of the bodies
- The impact is applied by hand and is not possible to guarantee the repeatability of the application at the same height and in the middle of the beam to avoid torsional effects

In conclusion, after the analysis of all the discrepancies, since the errors are below the limit of 10% it is possible to validate the behavior of the vertical beam constrained to the table by mean of the lower constraint sub-group. Next experiment will add the I-beam constraint sub-group to the assembly to validate the complete bending test rig.

Model vs Reality remarks – 800 mm experiment

An important remark that emerged from the comparison of the model and the reality is related to the shifting of the vertical beam. During the design of the test rig, one of the most important aspects was the possibility to shift the eigenfrequencies of the system by mean of shifting the position of the vertical beam. For this reason, it has been conducted an experiment with 800 mm length above the constraint.

The model and the assembly set-up are equal to Experiment 1: 1100 mm; therefore, *Figure 3.67* represents the comparison graph between the simulation and experimental FRFs:

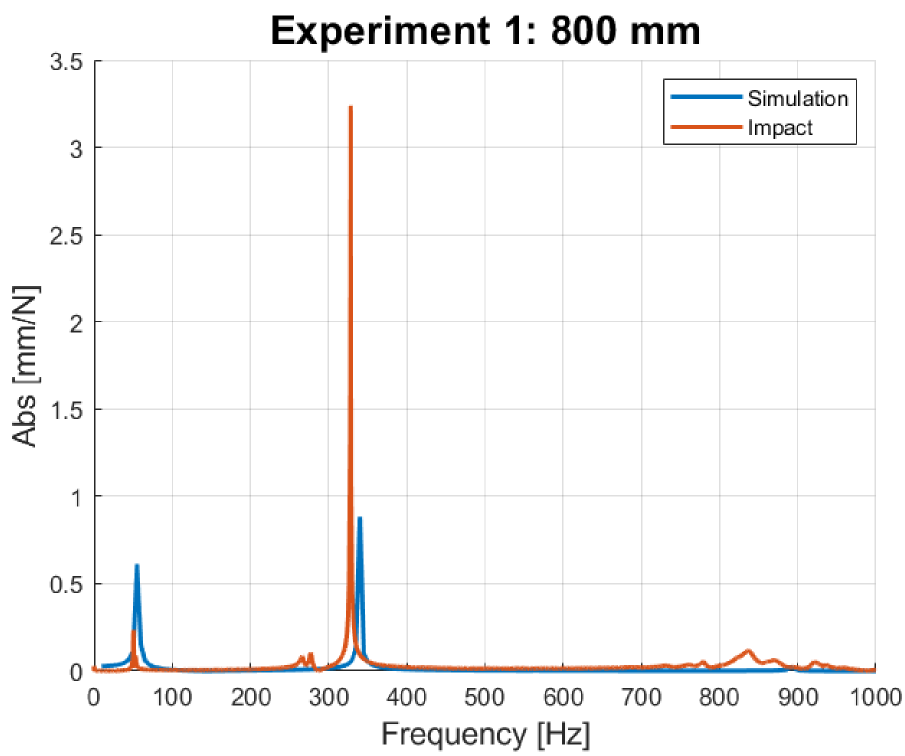

Figure 3.67 - Experiment 1: 800 mm FRFs comparison

By analyzing the graph, it is possible to determine consistent discrepancies between the experimental and the simulated results. Contrarily to the result obtained in Experiment 1: 1100 mm, the difference does not consist only of the shifting of the two curves, which could be caused by a difference of stiffness or mass; but in the impact curve there is also a double peak at 250 Hz. In addition, the relative error between the two curves in proximity of the peaks is always above 10%, therefore the comparison between real and experimental is not validated.

This result is critical, because the comparison executed in Experiment 1: 1100 mm withstands the expected quality criteria, and it is in concordance with the initial expectations. As first attempt to try to reduce the discrepancy, it has been tried to arrange the model by adding the mass of the screws as concentrated mass, by refining the mesh, and by modifying the materials' data. Despite of the arrangements, the outcome was not changing consistently for the approval of the comparison, because the overall reduction of the discrepancy was limited.

For this reason, it has been realized that the main cause is the effect of the lower part of the vertical beam below the bottom edge of the constraint. Initially, during the design, it was considered that, thanks to the stiff and massive (with respect to the rest) lower constraint sub-group, the constraint would act as an ideal cantilever beam, without any effect of the lower part of the beam.

In reality, after the execution of the experiments, it comes out that, in presence of a lower portion of the beam below the constraint, the configuration of the system changes from a cantilever beam to a hinged configuration, therefore, as represented in *Figure 3.68,* is meaningless to compare the model to the real system:

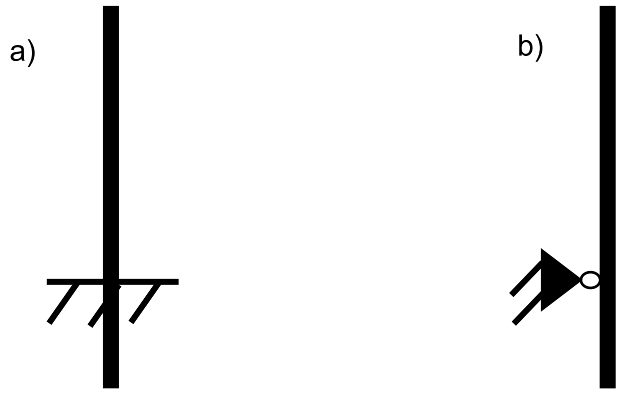

Figure 3.68 – Experiment 1: 800 mm BC comparison a) ideal b) real

After this conclusion, other experiments of the vertical beam have been carried out at different length: 900 mm and 1000 mm to verify the influence of the lower part of the beam. The experimental FRF is compared to the simulated FRF for both lengths, *Fig. 3.69* and 3.*70*:

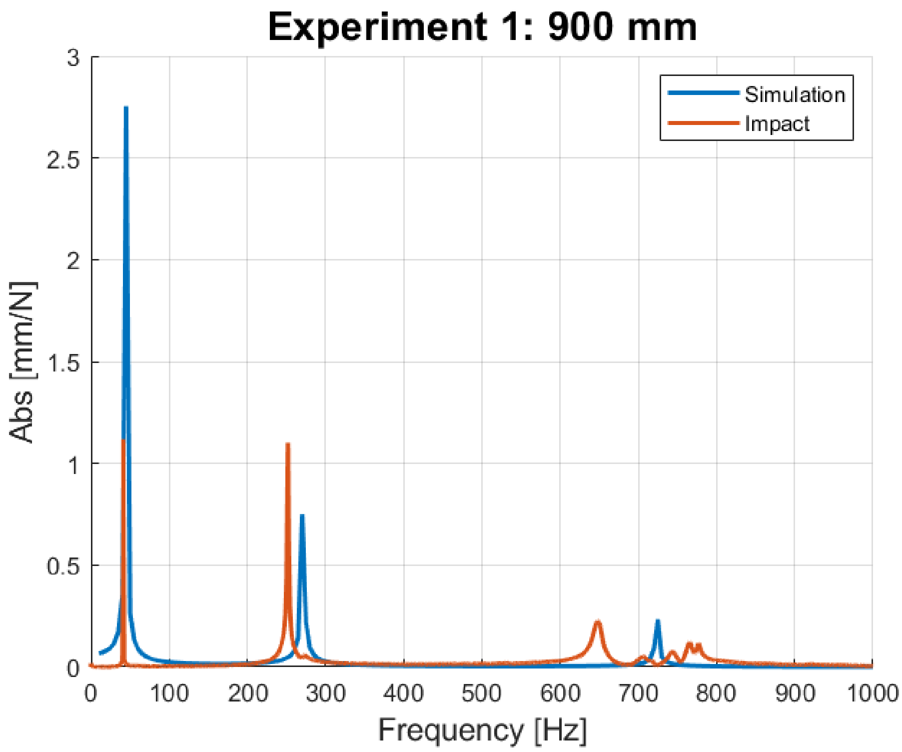

Figure 3.69 - Experiment 1: 900 mm FRFs comparison

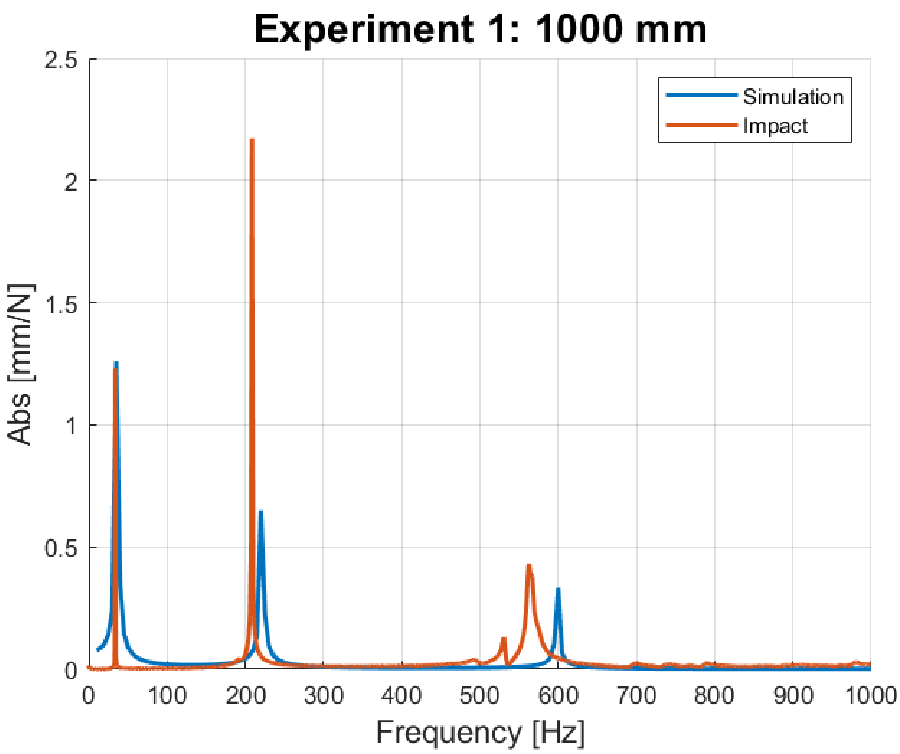

Figure 3.70 - Experiment 1: 1000 mm FRFs comparison

By analyzing each graph, it is possible to compare the experimental and the simulated curves. It comes out that by reducing the length above the constraint, which consists of increasing the free length below the constraint, the similarity between the curves is reduced due to the presence of double and triple peaks. In addition to a qualitative comparison, also the relative errors for each length are computed and collected in *Table 3.14*. According to the expectation, the relative errors increase with the reduction of the length:

	Error [%]			
	1100 mm	**1000 mm**	**900 mm**	**800 mm**
Peak 1	7.5	3.3	8.9	9.1
Peak 2	5.1	5.5	7.2	3.5
Peak 3	6.9	6.7	11.9	-

Table 3.14 - Experiment 1: Relative error for different lengths

In conclusion, contrarily to what was initially expected, it is not possible to use a single vertical beam to cover all the lengths because below a certain threshold the comparison does not stand anymore. Therefore, it has been decided to use the above-mentioned vertical beam with a free length starting from 1100 mm up to 900 mm. Then, in order to have a consistent number of experimental data, a second beam with the same cross-section and a free length starting from 600 mm to 400 mm has been used. In addition, a third beam with a length from 900 to 700 has been bought but due to time constraint it will not be tested in this thesis.

Tuning of the model – 1100 mm

According to the results of Experiment 1: 1100 mm presented in Paragraph 3.4.1.1, despite of the validation of the DUT, there is a certain error between the experimental and the simulated results, which is below the acceptance threshold set to 10%.

Considering the final goal of the bending test rig, the focus will be shifted to the specimen to test rather than on the test bench itself. For this reason, after the validation of the complete bending test rig (Paragraph 3.4.1.2), the I-beam will be measured and compared to the simulation. Thus, in order to evidence only the behavior of the I-beam and next of the tailplane, it has been decided to artificially tune the model of the test rig up to reach the complete match of the experimental and simulated curves. Therefore, by excluding the effect of errors of the test rig, eventual differences between the curves will be caused only by the specimen. The purpose is to highlight the specimen and analyze only its behavior.

From the analysis of the plots, it is always evident that the model is stiffer compared to the real test rig. For this reason, in order to tune the model, it is necessary to reduce the stiffness or increase the mass. By dividing the complete test rig in three parts: lower constraint sub-group, I-beam constraint sub-group and vertical beam, it has been decided to act on the vertical beam since it is the component which deflects more under the effect of the excitation. On the contrary, the other two sub-groups are orders of magnitude stiffer and, for most of the considered frequency range, coherently to the purpose of their design, they move by rigid body motion. For simplicity, it has been decided to reduce the E modulus of the Aluminum of the vertical beam which was set to E = 70000 MPa up to reach an acceptable match of the curves. By using an iterative process, the resulting data of the material are collected in *Table 3.15*:

Aluminum	
$\boldsymbol{E}$ $[\boldsymbol{MPa}]$	**59000**
G $[MPa]$	22348
ν	0.32
ρ $[kg/m^3]$	2700

Table 3.15 - Experiment 1: new Aluminum's data

The resulting FRFs comparison is represented in *Figure 3.71*:

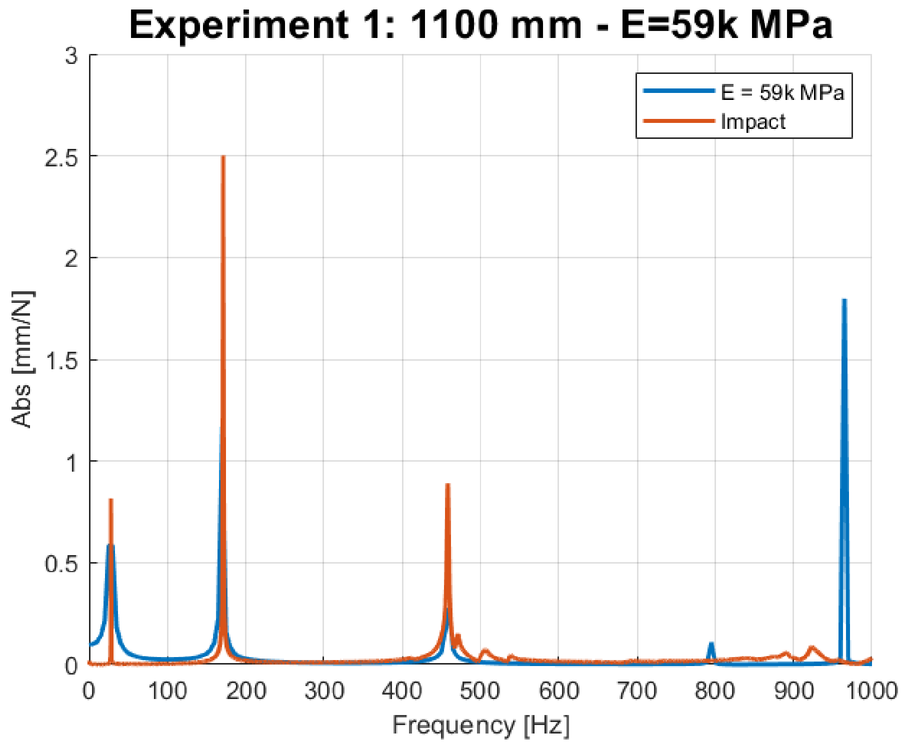

Figure 3.71 - Experiment 1: 1100 mm - E=59k MPa

In order to refine the results, the simulation has been refined in correspondence of the peaks at 50 Hz, 180 Hz and 450 Hz. The resulting curves are represented in *Fig. 6.72, 6.73 and 6.74*:

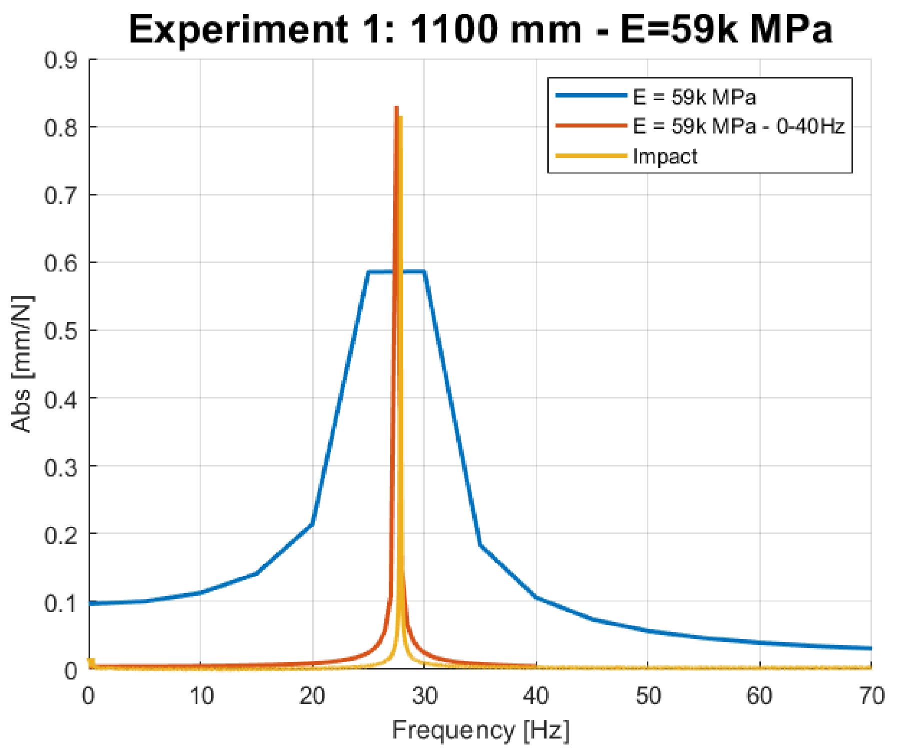

Figure 3.72 - Experiment 1: 1100 mm E=59k MPa 0-70 Hz

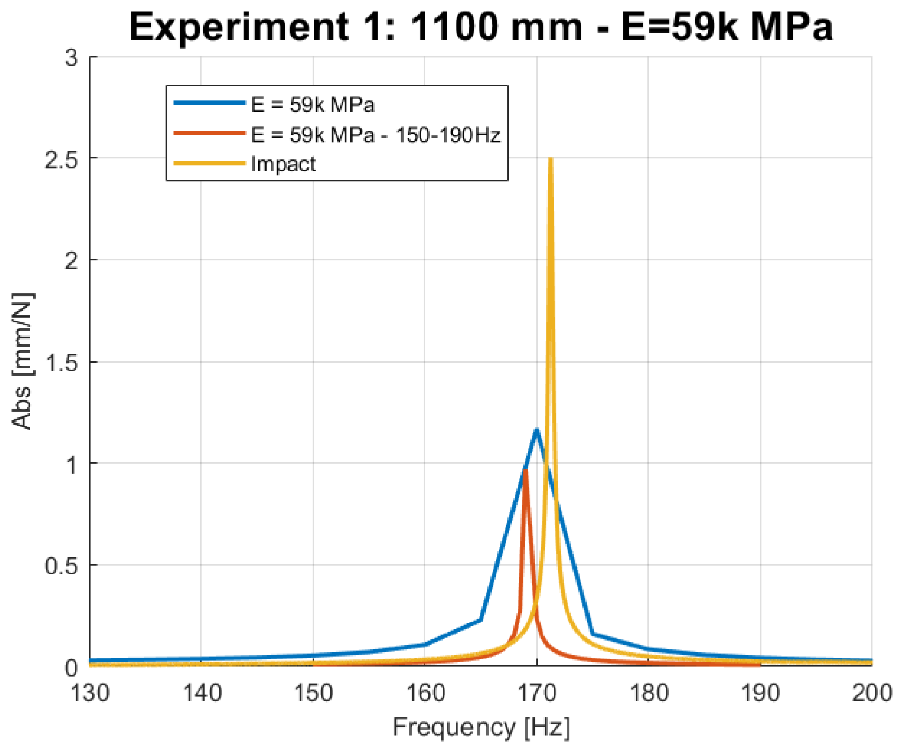

Figure 3.73 - Experiment 1: 1100 mm E=59k MPa 130-200 Hz

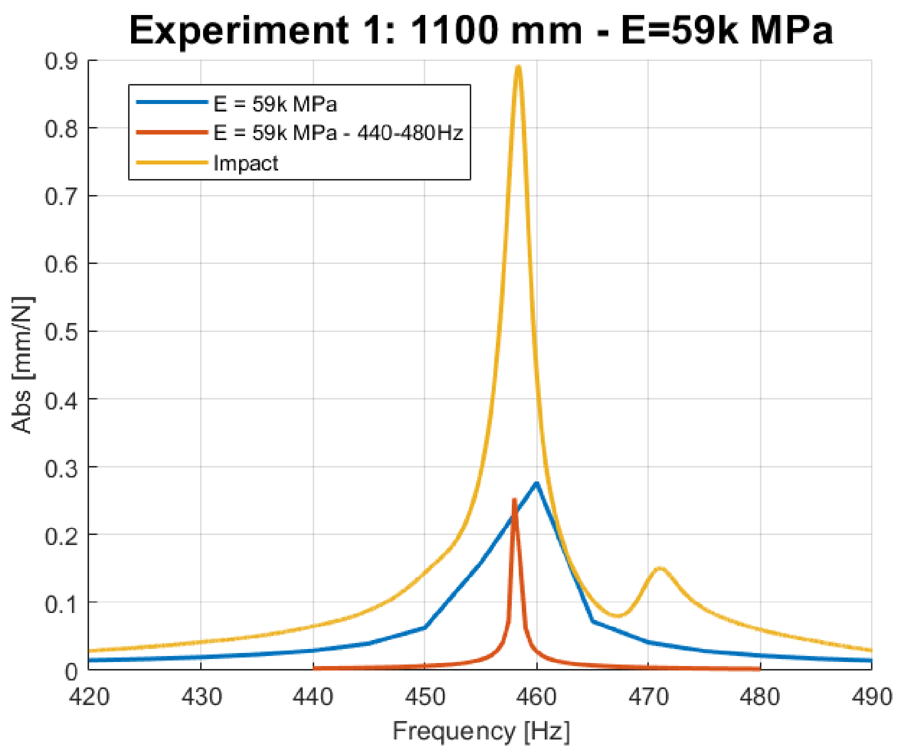

Figure 3.74 - Experiment 1: 1100 mm E=59k MPa 420-490 Hz

From the analysis of the plots, it is evident that with E = 59000 MPa the model is slightly less stiff compared to the real assembly.

The relative errors are collected in *Table 3.16*:

	Impact curve [Hz]	**Simulation curve [Hz]**	**Error [%]**
Peak 1	27.9	27.5	**1.4**
Peak 2	171.2	169.0	**1.3**
Peak 3	458.4	458.0	**0.08**

Table 3.16 - Experiment 1: 1100 mm E=59k MPa relative error comparison

3.4.1.2 Experiment 2: Complete bending test rig – 1100 mm

After the Experiment 1, the vertical beam constrained by the lower constraint sub-group to the table has been validated. Consequently, the next step consists of the addition of the I-beam constraint sub-group to the assembly to test the complete bending test rig. The I-beam constraint has been designed to be orders of magnitude stiffer compared to the ITEM beam. Because its function is to lock the specimen during the test preventing any relative motion; thus, the addition of this sub-assembly is similar to adding a concentrated mass on the top of the beam. For this reason, since there are not many phenomena taking place, the initial expectation is that the discrepancy between the experimental and simulated curves will be limited.

The set-up is equal to Experiment 1 plus the I-beam constraint sub-group mounted on the top of the vertical beam by four 90° brackets. The assembly is represented in *Figure 3.76*, and the I-beam constraint sub-group is detailed in *Figures 3.75*:

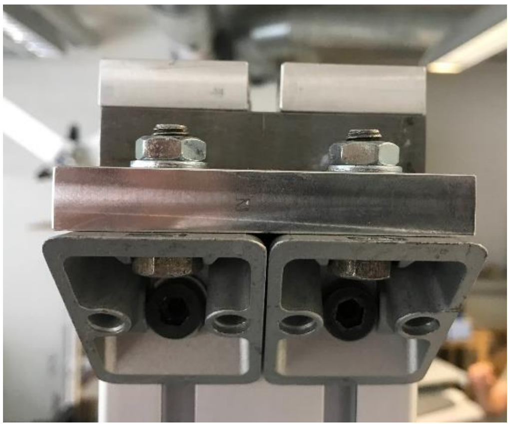

Figure 3.75 - Experiment 2: I beam constraint sub-group

Figure 3.76 - Experiment 2: set-up

The impact excitation is always applied 300 mm above the upper edge of the constraint by the Impulse Force Hammer is manufactured by PCB and is equipped with a plastic tip (Sensitivity = 10.27 mV/N) and the output is measured by a tri-axial accelerometer PCB Piezotronics model 356A03 (calibration data *Table 6.1*) positioned on the top of the interface plate, according to the measuring point in the simulation, as represented in *Figure 3.77*:

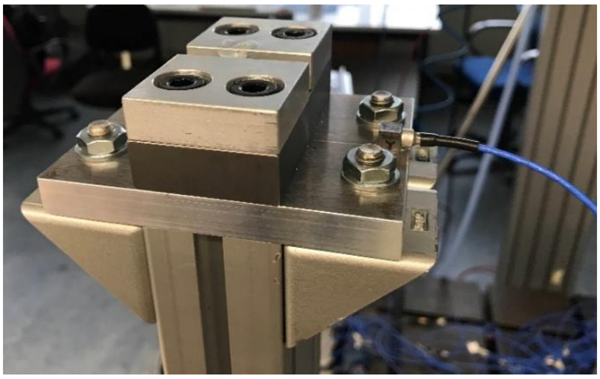

Figure 3.77 - Experiment 2: accelerometer position

Although the accelerometer measures the acceleration, the LMS acquisition system directly provides the FRF computed as the ratio of displacement divided by the applied force. Analogue to the simulation, the FRF is obtained only for the Z coordinate. The FRF is plotted with the same graph obtained from the simulation in *Figure 3.78*:

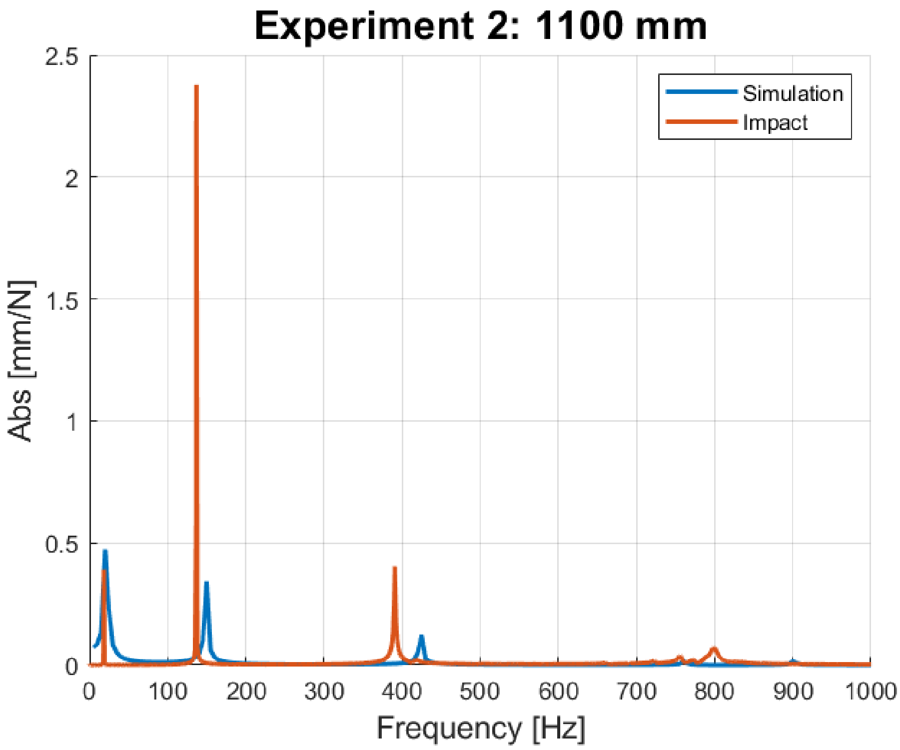

Figure 3.78 - Experiment 2: 1100 mm FRFs comparison

Table 3.17 collects the frequency of the peaks and the relative error among the curves:

	Impact curve [Hz]	Simulation curve [Hz]	Error [%]
Peak 1	18.4	20	**8.7**
Peak 2	136.9	150	**9.6**
Peak 3	390.7	425	**8.8**

Table 3.17 - Experiment 2: Impact vs Experiment relative error

The relative errors between the peaks are below the threshold of 10%, therefore the bending test rig is validated.

In the same way of Experiment 1, the E modulus of the vertical beam has been tuned to E = 59000 MPa to evaluate only the effect of the addition of the I-beam sub-group. The FRFs comparison is represented in *Figure 3.79*:

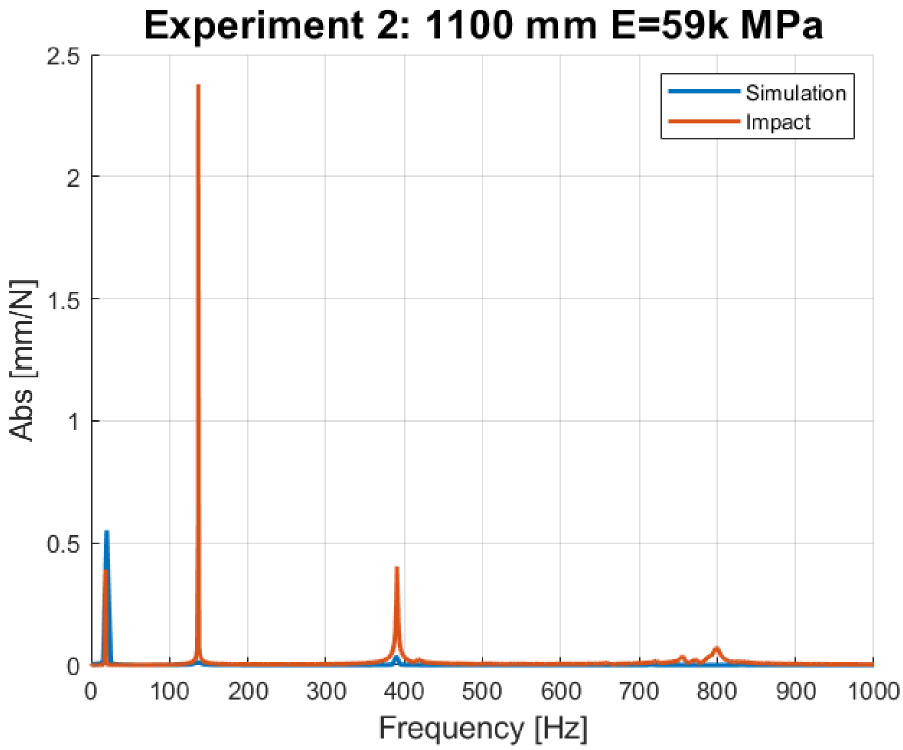

Figure 3.79 - Experiment 2: 1100 mm E=59K MPa FRFs comparison

From the analysis of the graph, according to the expectations, it is possible to conclude that the refinement of the E modulus of Aluminum reduces the shifting of the experimental and theoretical curves without affecting the high frequency zone above 700 Hz. From the analysis of the plots, it is evident that with E = 59000 MPa the model is slightly less stiff compared to the real assembly. The relative errors are collected in *Table 3.18*:

	Impact curve [Hz]	**Simulation curve [Hz]**	**Error [%]**
Peak 1	18.5	20.0	**8.1**
Peak 2	136.9	137.0	**0.07**
Peak 3	390.7	390.5	**0.05**

Table 3.18 - Experiment 2: 1100 mm E=59k MPa relative error comparison

The errors of the three peaks are all below the limit of 10%. The first peak that has a higher relative error, while the other errors are negligible. The complete bending test rig model with the refined E modulus will be used to compare the experimental measurements of the I-beam with the theoretical data from the simulation avoiding any influence of the discrepancy between the model and the real assembly.

The verification of the model has been executed solely for the length of 1100 mm, assuming that it will be respected also for the other lengths because, a part for the length of the vertical beam, there are no changes.

3.4.1.3 Experiment 3: Bending test rig + I-Beams

After the validation, the bending test rig is applied to the I-beams (2 D). Therefore, with respect to Experiments 1 and 2, in addition to evaluate the shifting of the experimental and theoretical FRFs is also necessary to compute the damping factor of the peaks. For the computation of the damping factor, it has been decided to adopt the Half Power Method (3 dB method). In conclusion, it will be possible to compare the results of each beam. In this thesis it will be tested only two I-beams to prove the functionality of the test rig. Then, in the next steps, the test rig will be used to test all the produced I-beams being part of the iterative procedure characterized by evaluating new composites materials, simulation, production of the specimen, test and comparison up to define the best I-beam to apply as reinforcement in the tailplane. Then, it will be used with the same approach to test the horizontal tailplane.

Although the goal of Experiment 3 is the evaluation of the I-beams, finalized to prove the effective functionality of the test rig, the accelerometer is still applied to the same position of Experiment 2 to evaluate the effect of the addition of the specimen of the FRF of the test rig. *Figure 3.80* represents the schematization of set-up of the experiment:

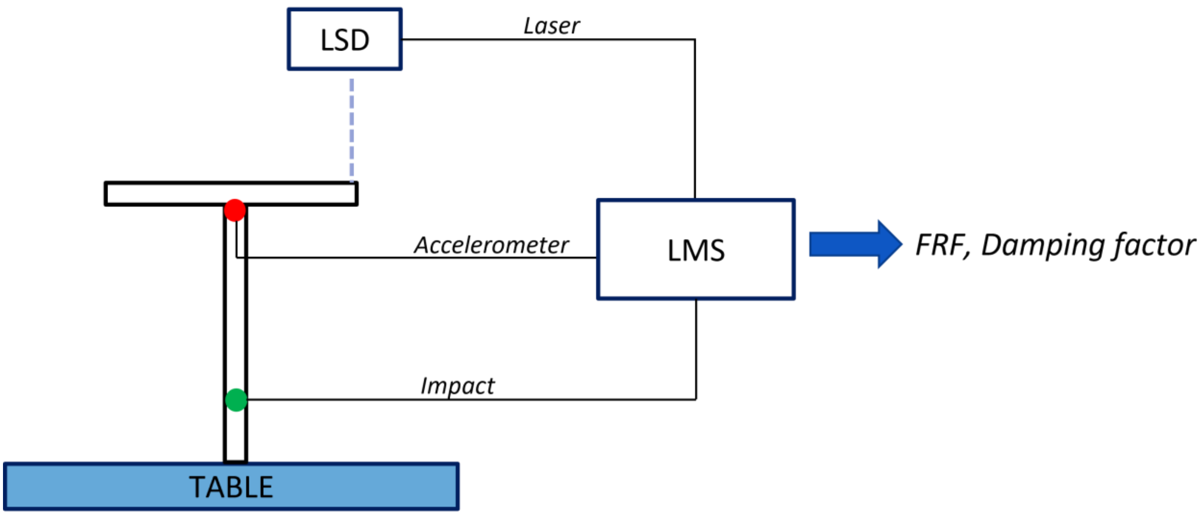

Figure 3.80 - Experiment 3: I-beams set-up

The excitation is the same of the previous experiments. The output is measured in two different positions:

- Interface plate (*Figure 3.77*), the output is measured by a tri-axial accelerometer PCB Piezotronics model 356A03 (calibration data *Table 3.13*) positioned on the top of the interface plate, according to the measuring point of the simulation and Experiment 2. As previously mentioned, the addition of weight and the cables exert a negligible effect on the entire bending test rig. The purpose of this measurement is to evaluate the effect of the addition of the specimen on the FRF of the test rig. It is expected that, due to the addition of mass on the top, the eigenfrequencies will be shifted downward by a limited amount since the mass of the I-beams is limited in comparison to the test rig (80 – 150 g)

- Extreme point of the I-beam (*Fig. 3.81* and 3*.82*), the output is measured by the 1D - LSD equipment. The pro of the laser is that the output of the I-beam is not affected by the mass of the accelerometer and of the cable which, according to Scheffler [23], would be consistent given the limited mass and stiffness of the composite beam. Moreover, the extension of the measured point is comparable to a point, so it can be used for localized measurements, which is not possible to execute with an accelerometer since it is characterized by an extended area. On the other side, the drawback is that the laser measures only a single point for each time and, to shift from one point to the other is necessary to manually move it repeating the focusing procedure and applying the reflective tape on the measuring point. *Figure 3.81* represents a measuring point where the laser hits the reflective tape, and the signal is received by the receiver. *Figure 3.82* represents the location of the measured points of the I-beam for each length increment of the vertical beam. The configuration of the beam is symmetric, therefore the result for the two mirrored couple of points is expected to be the same, while the central node of the I-beam should provide a measurement similar to the accelerometer placed on the interface plate of the rig since the specimen moves rigidly to the test bench in that position:

Figure 3.81 - LSD measurement

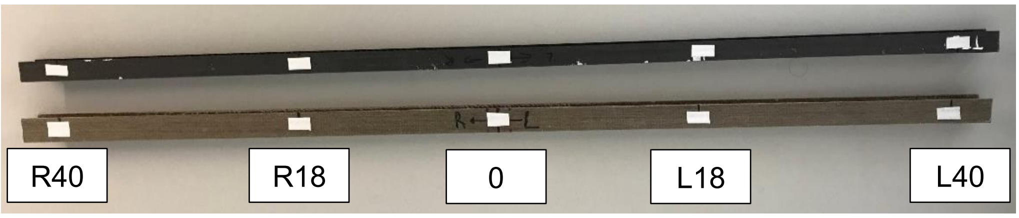

Figure 3.82 - I-beam measurement locations

It is important to evidence that the FRF obtained from the measurement of the LSD is computed as velocity/force because the system measures the velocity of the reflected laser beam and the LMS acquisition system does not transform it. On the contrary, the FRF obtained from the measurement of the accelerometer is computed as displacement/force because the LMS automatically integrates the measured acceleration two times up to obtain the displacement. Therefore, it is not possible to compare the FRFs obtained from the LSD and accelerometer because they are expressed with two different units of measurement. This is not a problem for the experiment because:

- The x coordinate of the peaks is not affected by the integration; therefore, the shifting of the curves can be evaluated by overlapping the two curves even though they have different units
- The damping factor computed by the Half Power Method obtained by the mobility and receptance curves is similar. This has been verified comparing the curve obtained from

the LSD measurement to the same curve divided by $i\omega$ to move from velocity to displacement in frequency domain.

After the description of each element of the system, the complete set-up of the test rig including the I-beam is represented in *Fig. 3.83* and 3.*84* and is equivalent for each beam tested:

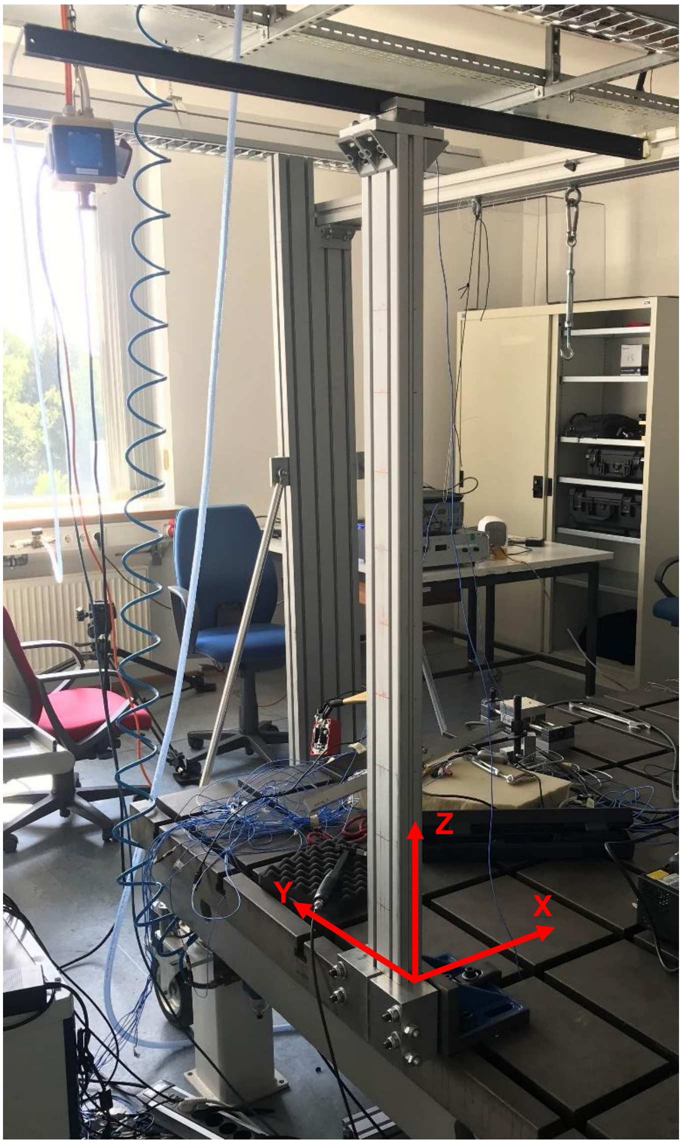

Figure 3.83 – Experiment 3: set-up lateral view

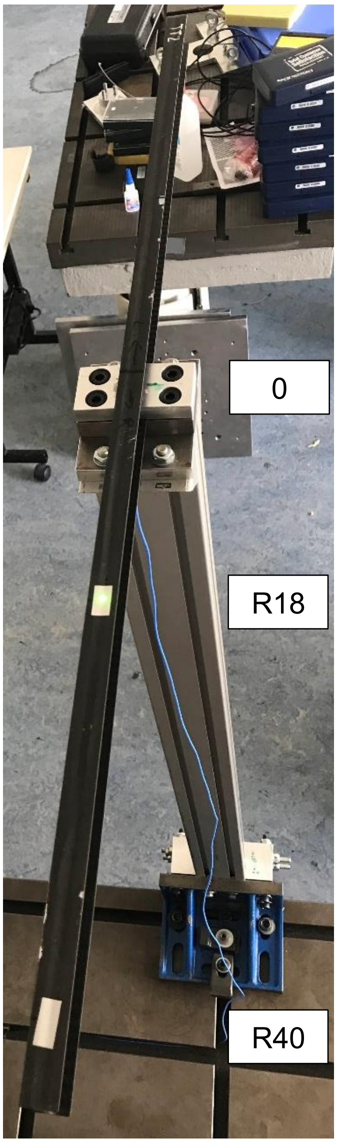

***Figure 3.84* – Experiment 3: set-up lateral view**

An important aspect of the set-up is the repeatability of the experiment with different I-beams considering the symmetric configuration in X and Y directions (*Figure 3.83*). The beam has to be centered exactly in the middle of its length over the interface plate (X direction), and, at the same time, the center of the double T cross-section has to be positioned in the middle of the interface plate (Y direction).

In order to ensure the symmetricity of the mounting, during the manufacturing process of the interface plate, it has been marked in the middle both in X and Y directions. Then, regarding the beam, before the test, the length of each beam is measured, and it is marked in the middle. Therefore, the symmetricity in the X coordinate consists of matching the two marks and it is verified by eyes. Then, considering the Y direction, the point of interface of the web and the flange of the beam is curved due to the lack of material; therefore, the symmetricity in the Y coordinate consists of matching the two marks and it is verified by eyes. *Figure 3.84* represents also the points of measurement of the laser, called R40 (right at 40 cm, which is the end of the beam), R18, 0, then the symmetric L18 and L40.

In addition, the beam must be straight along the X direction. For this reason, before tightening the screws, its position is verified and adjusted by a 90° bracket. Finally, the screws of the clamps are tightened by a torque wrench to guarantee the repeatability of the experiment.

The detail of the I-beam constraint sub-group is highlighted in *Fig. 3.85* and *3.86. Figure 3.85* contains also the accelerometer placed on the interface plate for the comparison of the test rig with Experiment 2:

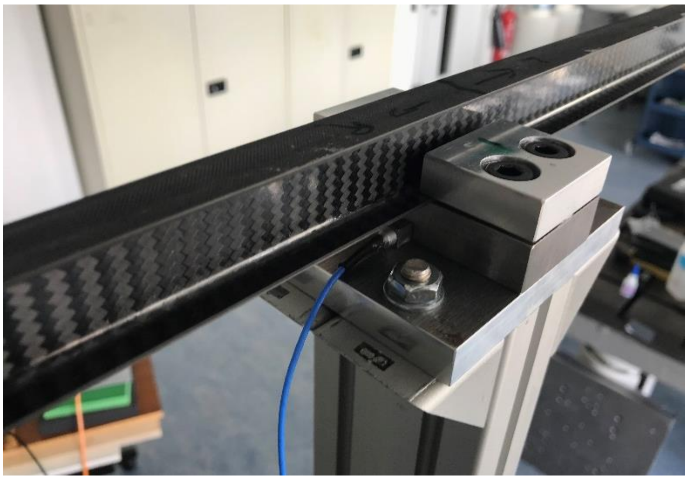

Figure 3.85 – Experiment 3: I-beam constraint sub-group lateral view

Figure 3.86 - Experiment 3: I-beam constraint sub-group top view

The I-beams tested in Experiment 3 are called TT2 and TT7, represented in *Fig. 3.87* and *3.88*. TT2 is composed by carbon UD with 0° and 90° according to the scheme. The web is made up of 8 alternated plies with 0° and 90° orientations, while the flanges are composed by 4 alternated plies and 4 0° plies with the function of connecting the two C. The web of TT7 is composed by 8 alternated plies of Flax UD +45° and Flax UD -45°, while the flanges are made up of Flax UD 0°, Carbon UD 0°, Flax UD +45° and -45°:

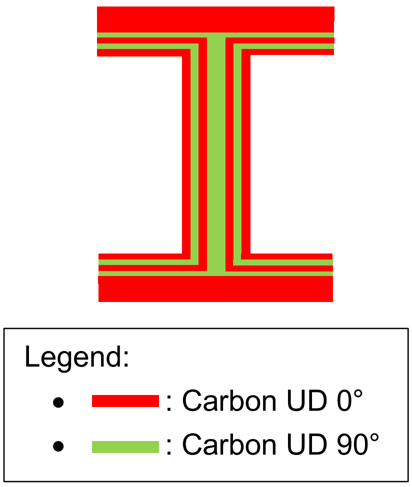

Figure 3.87 - TT2 beam plies layout

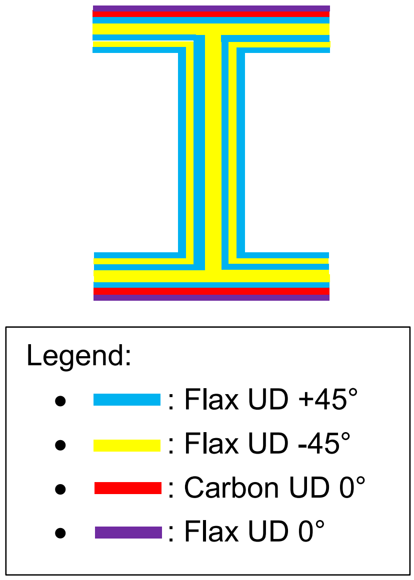

Figure 3.88 - TT7 beam plies layout

The TT2 beam used in the experiments was not composed by carbon UD 90° but it was made up of carbon twill. It is less stiff that the unidirectional fiber but concerning damping it is assumed that the difference is not relevant. This is another reason why the model is stiffer than the real system.

The flow-chart adopted to present the results of Experiment 3, represented in *Figure 3.89*, consists of:

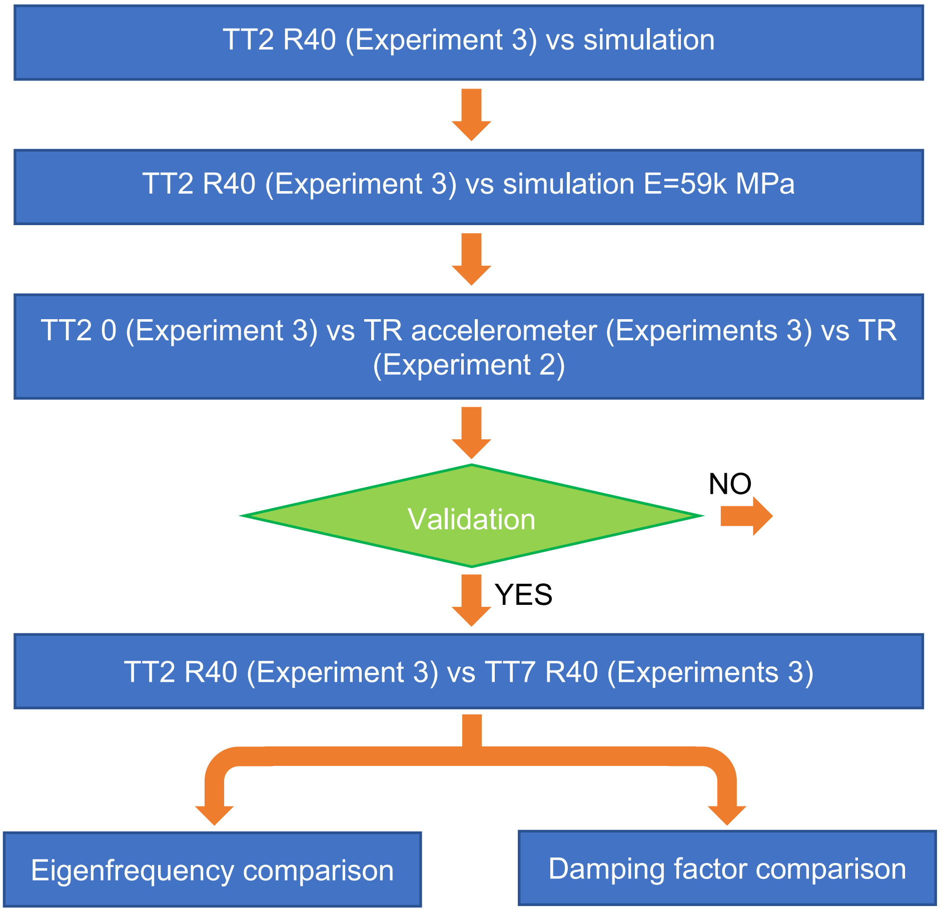

Figure 3.89 - Experiment 3: data comparison flow-chart

The comparison between simulation and experiment is carried out only for the TT2. In addition, in order to evaluate the influence of the addition of the I-beam on the test rig, the test rig measured in Experiment 2 is compared to TT2 0 and the test bench measured in Experiment 3. Since the mass of the beam is an order of magnitude inferior respect to the rest, it is expected to have a limited influence.

After the comparison between simulation and experiments, which allows to validate the test rig plus the specimen, there is the comparison of the I-beams' FRFs for each length of the vertical beam. It is oriented in two directions: eigenfrequency comparison, which is influenced by the mass and the stiffness of the beam; and damping factor comparison, which depends on the material's properties. Finally, the experiment can be repeated for different lengths to increase the amount of available data to determine conclusions about the effectiveness of the designed I-beams. This thesis contains the experiments repeated for 1100 mm and 600 mm free length. In the next steps of the project, after the approval of the test rig, the experiments will be executed for all the other lengths.

1100 mm free length

TT2 R40 (Experiment 3) vs simulation

The FRFs comparison between TT2 R40 (Experiment 3) and the simulation is represented in *Figure 3.90*:

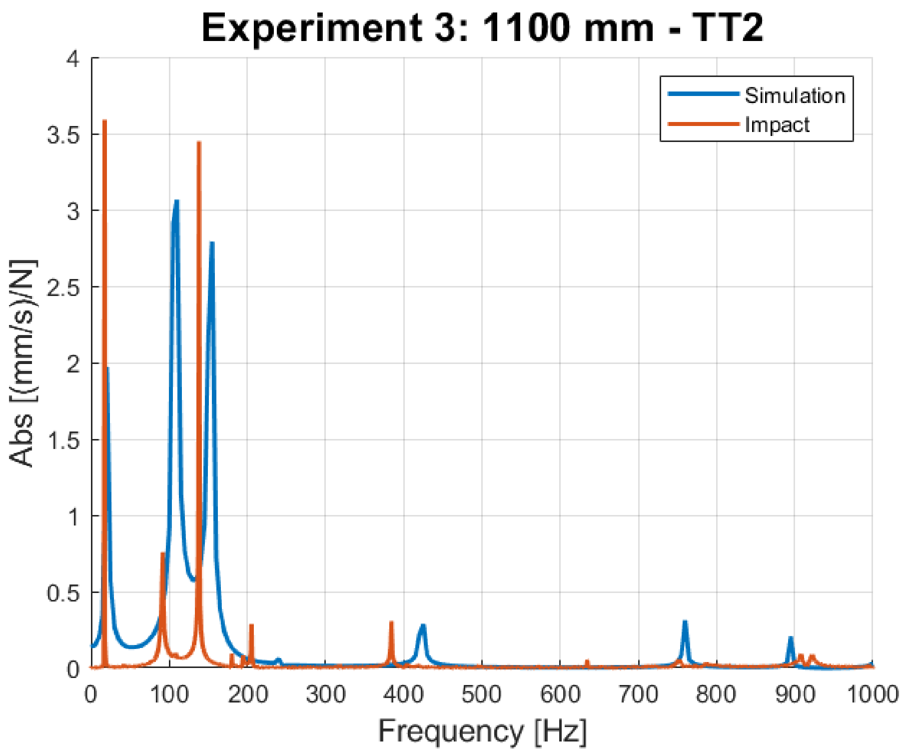

Figure 3.90 - Experiment 3: TT2 R40 FRFs comparison

It is possible to conclude that, in the low frequency area below 700 Hz, there is a direct correspondence of the theoretical and experimental curves. There is a first peak around 30 Hz which is evident in both curves, then, there are two peaks close to each other at 100 Hz and 130 Hz. Usually, according to previous data analysis, the presence of the double peak is not caused by the I-beam. Therefore, it could be caused by the coupling of the test rig and the beam, which means that one eigenfrequency is characteristic of the beam while the other is proper of the test rig, therefore it measures the rigid body motion and deformation of the specimen amplified by the natural frequency of the test rig. This can be determined by plotting the test rig combined to TT2 R40 in the same graph. Then, around 130 Hz there is another peak which is present in both curves, contrarily to the previous, the experimental curve is characterized by waves in proximity of this peak. However, it is still clear and evident; therefore, it can be compared to the simulation.

The model results stiffer with respect to the simulation, but it is not due to the test rig only. As it was evidenced by Scheffler [23], who made the TT2 I-beam model, the material data assigned in the simulation which are extracted from the datasheet were not coherent with the real behavior of the material. Especially for carbon, in reality, it was exhibiting higher stiffness with respect to what was indicated in the datasheet.

Figure 3.91 represents the graph containing the experimental curve of the TT2 I-beam measured at R40 coordinate and the curve of the test rig itself to investigate the presence of the double peak:

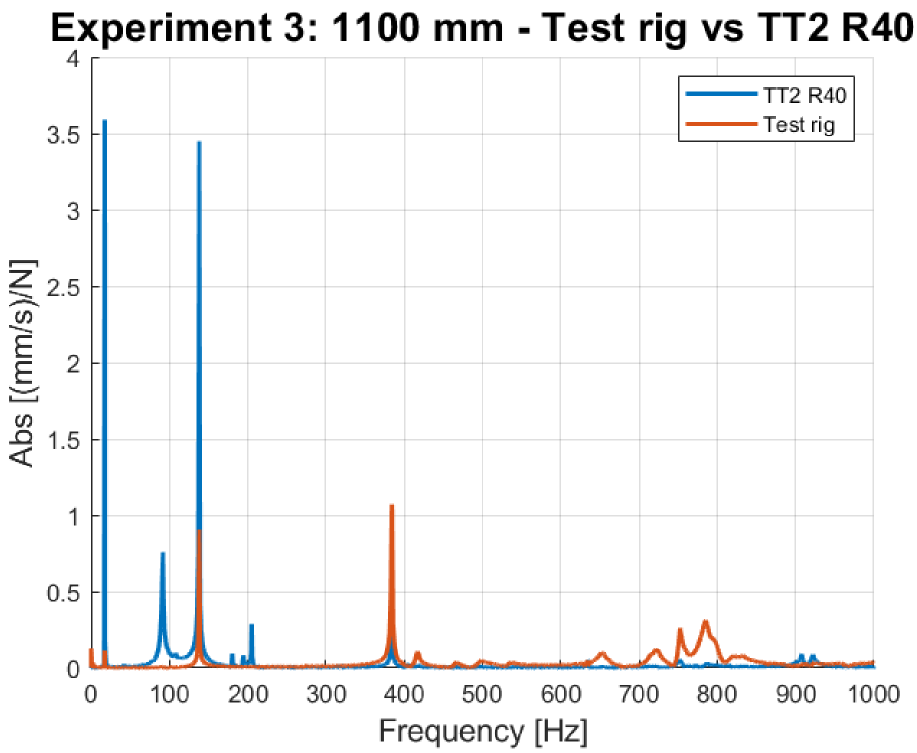

Figure 3.91 – Test rig (Experiment 2) vs TT2 R40 (Experiment 3)

The graph of *Figure 3.91* confirms what was initially assumed about the presence of a double peak. The peak at 100 Hz is characteristic of TT2 I-beam, while the peak at 130 Hz is proper of the test rig; therefore, it is present in both curves. On the contrary, the other peaks at 30 Hz, 130 Hz and 400 Hz (this will not be considered) correspond for both curves, therefore these are characteristics of the test rig. In addition, it is possible to anticipate that, for the characterization of the I-beam only, it will be necessary to evaluate the peak at 100 Hz because it is not influenced by the rest of the system.

TT2 R40 (Experiment 3) vs simulation E = 59k MPa

The FRFs comparison between TT2 R40 (Experiment 3) and the simulation with E = 59k MPa of the vertical beam is represented in *Figure 3.92*:

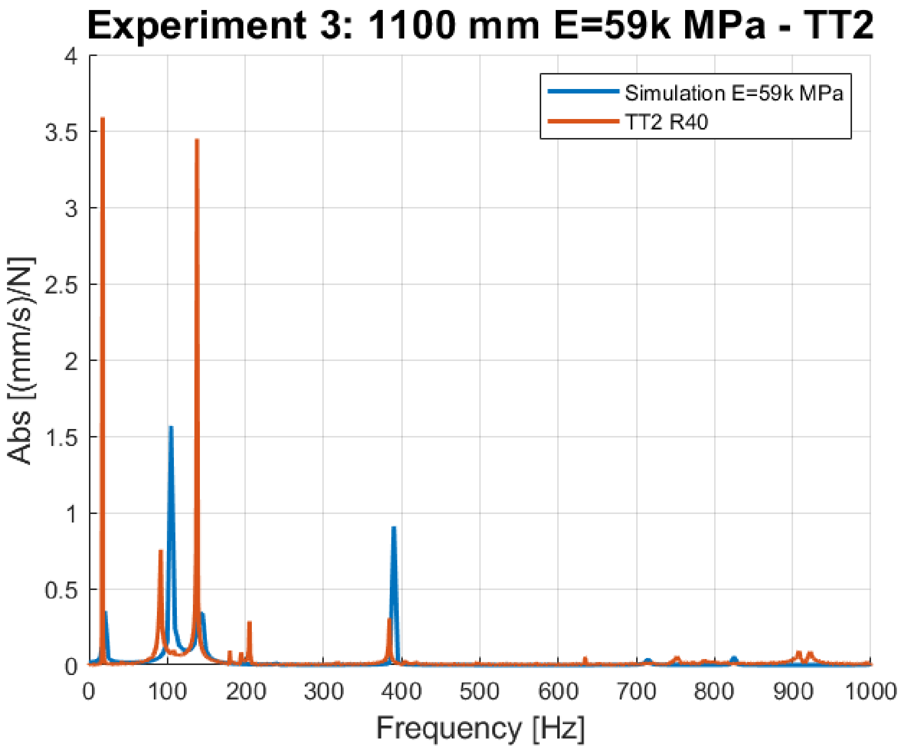

Figure 3.92 - Experiment 3: TT2 R40 FRFs E=59k MPa comparison

According to the model tuning of Experiments 1 and 2, it is evident that also for Experiment 3 there is a match between the experimental and the refined simulation curves.

Therefore, it is possible to conclude that the TT2 I-beam model is coherent to the real behavior of the part. The relative errors of *Figures 3.91 and 3.92* are collected in *Tables 3.19* and *3.20*:

Figure 3.91	**Impact curve [Hz]**	**Simulation curve [Hz]**	**Error [%]**
Peak 1	17.6	20	**13.6**
Peak 2	103.6	110	**6.2**
Peak 3	143.2	155	**8.2**

Table 3.19 - Experiment 3: *Figure 6.34* relative errors

The entity of the relative errors between the experiment and the simulation, collected in *Table 3.19*, is above 10% only for the first peak. With respect to Experiments 1 and 2, it was expected an increase of the entity of the error because there is a new component added to the model which includes several contacts between itself and the I-beam constraint sub-group and it is made up of composites; therefore, its modelling is more critical respect to isotropic materials. For this reason, although one relative error overcomes the threshold, the comparison is validated. *Table 3.20* collects the error between the experiment and the simulation with E = 59k MPa, refining the frequency increment to 0.5 Hz in correspondence of the peaks. With the refined model, all the relative errors are below the threshold. Therefore, the comparison is validated.

According to the expectation, the errors are reduced with respect to *Table 3.20*:

Figure 3.92	Impact curve [Hz]	Simulation curve [Hz]	Error [%]
Peak 1	17.6	19.5	**10.8**
Peak 2	103.6	105.5	**1.8**
Peak 3	143.2	142.5	**0.5**

Table 3.20 - Experiment 3: *Figure 6.36* relative errors

TT2 0 (Experiment 3) vs TR accelerometer (Experiments 3) vs TR (Experiment 2)

The FRFs comparison related to the influence of the addition of TT2 I-beam on the test rig is represented in *Figure 3.93*:

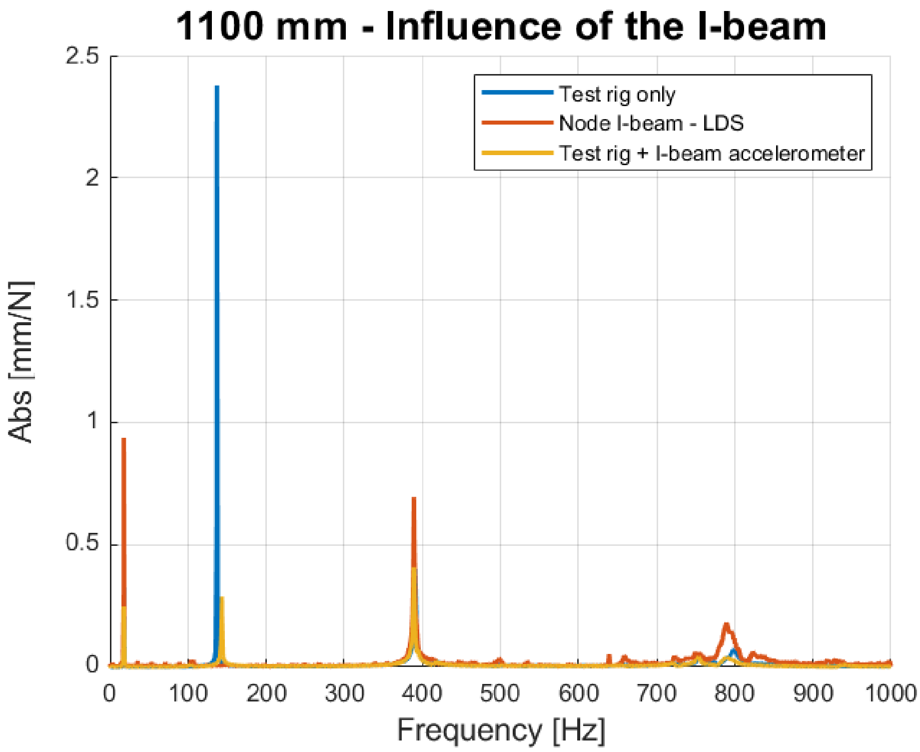

Figure 3.93 - Experiment 3: influence of TT2 I-beam on the test rig

Figure 3.93 combines the curves obtained from: FRF of the bending test rig measured in Experiment 2, FRF of TT2 0 (center of the beam) measured by the laser in Experiment 3 and FRF of the bending test rig measured by the accelerometer in Experiment 3. The plot has a double purpose: evaluate the effect of the addition of TT2 (and more in general of an I-beam since all the weights are similar) on the test rig and verify the similarity of the behavior of the node of the I-beam with the interface of the test rig.

Regarding the effect of the I-beam on the test rig, it is expected that, due to the addition of mass, the experimental curve "Test rig + I-beam accelerometer" precedes the curve "Test rig only". The expectation is confirmed by the graph represented in *Figure 3.93*, provided that, since the increase of mass in only 117.070 g, the shifting of the two curves is limited to less than 1 Hz. The only point where the order of the curves is not respected is the second peak.

Regarding the node of the I-beam, it is possible to conclude that the yellow and orange curves quasi-overlap except for the peak located at 130 Hz, where the node of the I-beam's curve does not have a peak. This is due to the deformation of the eigenmode, represented in *Figure 3.94*:

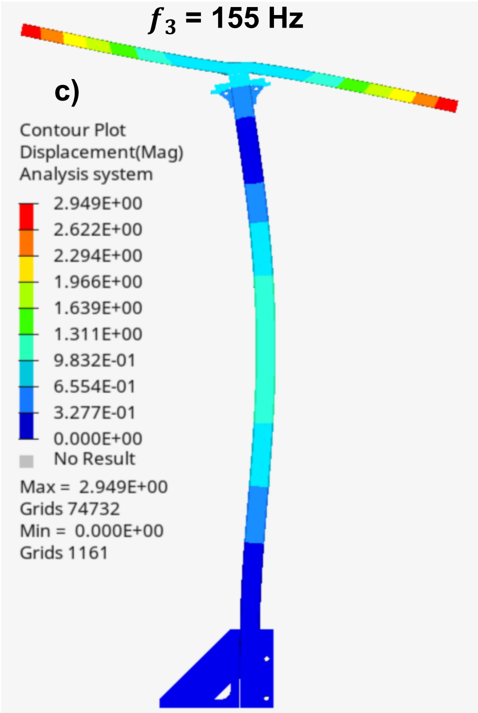

Figure 3.94 – Experiment 3: TT2 eigenmode of the 3rd peak

The deformation represented in *Figure 3.94* highlights that, due to the current eigenmode, the TT2 0 measurement point is almost in its resting position because the interface plate is affected by rotation rather than displacement. On the contrary, due to the rotation, the point where the accelerometer is placed is displaced respect to its normal position; and this is the reason why there is a peak.

TT2 R40 (Experiment 3) vs TT7 R40 (Experiment 3)

After the validation of the test rig plus the I-beam, it is possible to start the comparison of the I-beams. TT2 and TT7 beams will be compared to highlight the difference between the two extreme cases: full carbon and almost full flax beam. The FRFs are compared at the measurement point R40, but according to the eigenmodes, it would be possible to compare also R18 because the deformation is located at the center of the beam, while the two branches move by rigid body motion. This will be proved in the next paragraphs. The FRFs are represented in *Figure 3.95*:

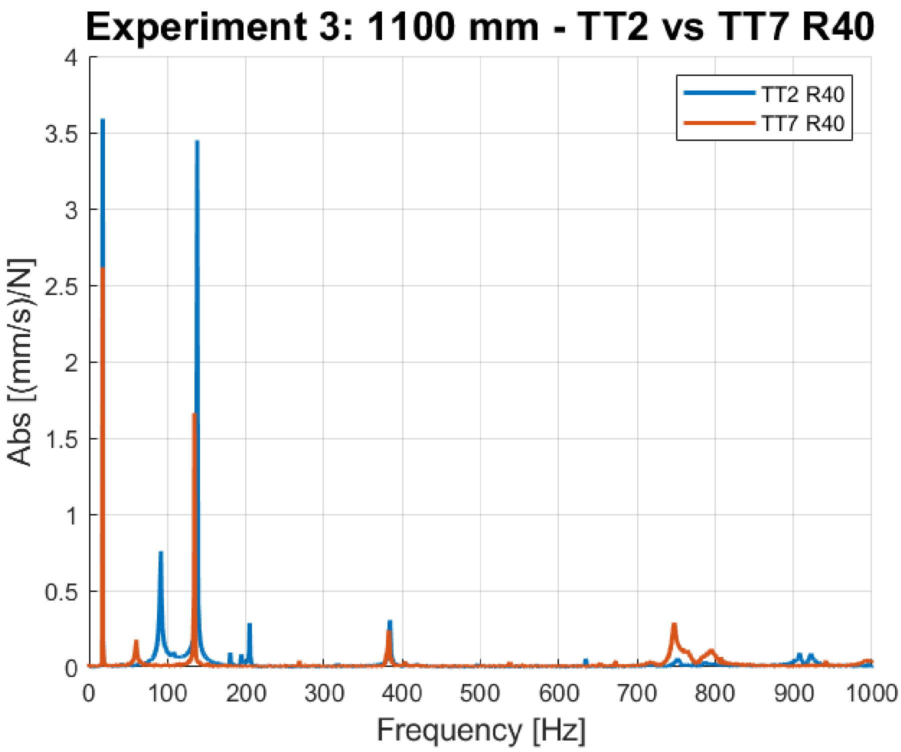

Figure 3.95 - Experiment 3: TT2 R40 vs TT7 R40

Regarding the eigenfrequencies comparison, it is expected that TT7 curve precedes TT2 curve because the flax beam is heavier compared to the carbon beam. In addition, flax is less stiff compared to carbon. The masses of the I-beams are grouped in *Table 3.21*:

	TT2	TT7
Mass [g]	117.070	126.990

Table 3.21 - Mass of TT2 and TT7

By the analysis of *Figure 3.95*, it is possible to confirm the expectation since the TT7 curve always precedes the TT2 curve. The shifting is not that relevant as it would be by testing only the I-beam in free-free conditions or clamped as a cantilever beam, because, in this case, the overall FRF and consequently the damping factor, are affected by the behavior of the beam plus the test rig.

For this motivation, the stiffness of the test rig is relevant with respect to the I-beam itself; therefore, the increment of stiffness of the TT2 with respect to the TT7 does not provide a disruptive change to the eigenfrequencies. The same is valid for the increment of mass of TT7 with respect to TT2, where its contribution, weighted by the mass of the complete test rig is almost negligible. Anyway, despite of the limited effect weighted by the entire test bench, TT2 tends to be stiffer and lighter compared to TT7; for this reason, the natural frequencies are higher.

On the contrary, by focusing on the second eigenfrequencies located at around 100 Hz, which is a peak characteristic only of the I-beam, it is possible to evidence a wider displacement between the two curves. This is according to the expectations because, in this case, the increment of mass and the reduction of stiffness are not added to a consistent quantity, but they are directly compared.

Despite of the influence of the test rig in terms of damping and eigenfrequency, it is important to test the I-beams and the final tailplane on the test rig because it is structured in the same way according to how the parts will be mounted on the helicopter. Where, in addition to the material damping of the component, the structural damping of the entire assembly will play a consistent role.

After having analyzed the FRFs of TT2 and TT7 represented in *Figure 3.95*, a Python® code has been developed to compute the damping factors corresponding to each peak of the curves. According to what has already been mentioned, there are some peaks characteristics of the test rig and another characteristic of the I-beam. The approach adopted for damping comparison, represented in *Figure 3.96*, consists of:

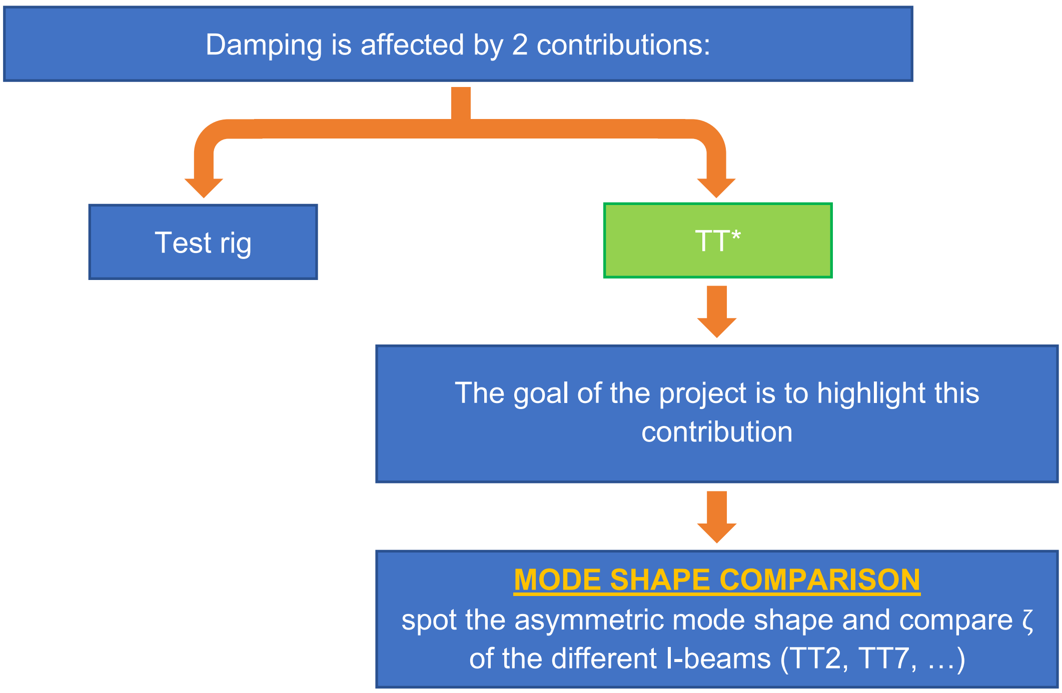

Figure 3.96 - Experiment 3: damping comparison approach

The damping factors obtained for TT2 and TT7 for the 1st, 2nd, and 3rd peaks (*referring to Figure 3.95*) are grouped in *Table 3.22*:

	Peak 1		**Peak 2**		**Peak 3**	
	f_1 $[Hz]$	ζ_1 [%]	f_2 $[Hz]$	ζ_2 [%]	f_3 $[Hz]$	ζ_3 [%]
TT2	17.7	0.219	**103.6**	**0.777**	143.2	0.296
TT7	17.7	0.388	**88.1**	**1.085**	139.2	0.299

Table 3.22 - Experiment 3: TT2 - TT7 damping comparison 1100 mm

Comparing the damping factor of TT2 and TT7 of Peak 2, according to the expectations, flax I-beam is characterized by higher damping compared to the carbon beam. In detail, ζ_{TT7} is 40% higher compared to ζ_{TT2}; this is the reason of the hybridization of the tailplane with flax fiber. In order to analyze the variation of damping factor of TT2 in the frequency range of interest, is necessary to represent the eigenmodes of TT2 corresponding to the three peaks, *Figure 3.97*:

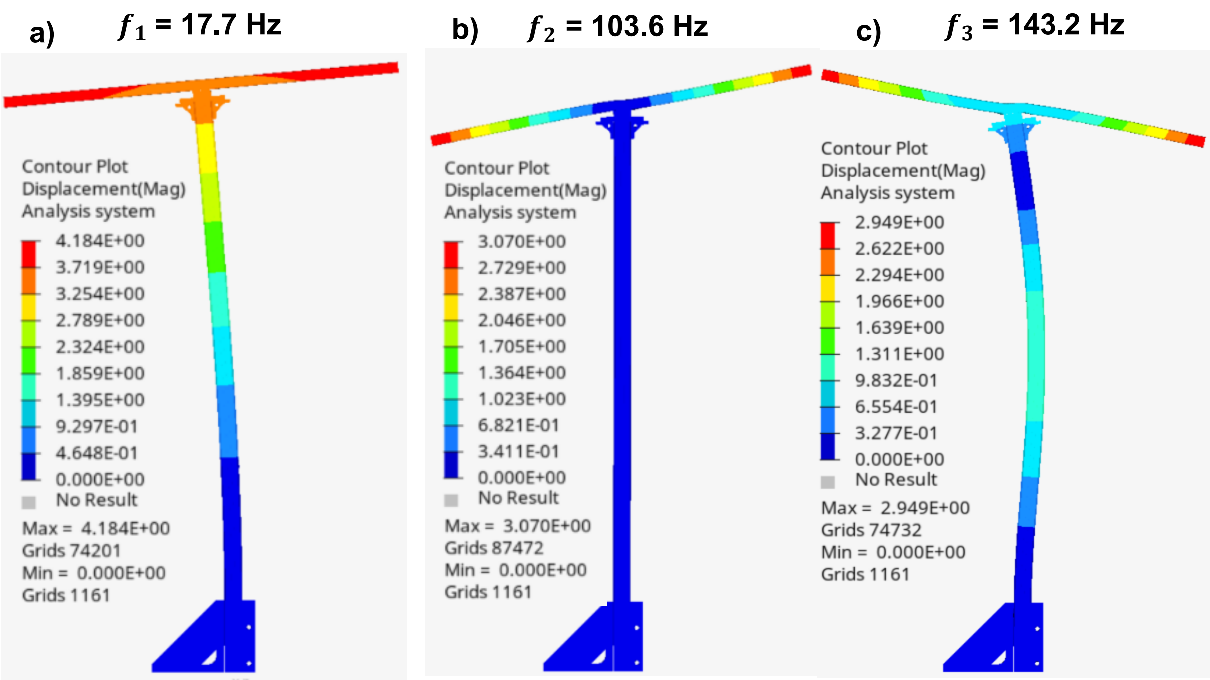

Figure 3.97 – Experiment 3: TT2 eigenmodes of the 1st a), 2nd b), and 3rd c) peaks

It is known from theory that damping consists of the conversion of mechanical energy of the structure into deformation; therefore, damping is not present in case of rigid body motion of the system. This is reason why ζ_1 is the lowest among the three peaks, where, according to *Figure 3.97 a)*, TT2 moves rigidly, and the calculated damping factor is given only by the deformation of the vertical beam. On the contrary, ζ_2 is the highest because, according to *Figure 3.97 b)*, the test rig is almost undeformed and the interface plate is straight, therefore the asymmetric configuration of the beam is provided only by its deformation. The third eigenmode, illustrated in *Figure 3.97 c)*, shows that the displacement of the beam is partially induced by its deformation but also given by the deformation of the test rig that induces rigid body motion to the beam. In order to further investigate the damping factors, *Figure 3.98* represents the Von Mises maximum stress of the entire system (test rig + TT2) for each peak:

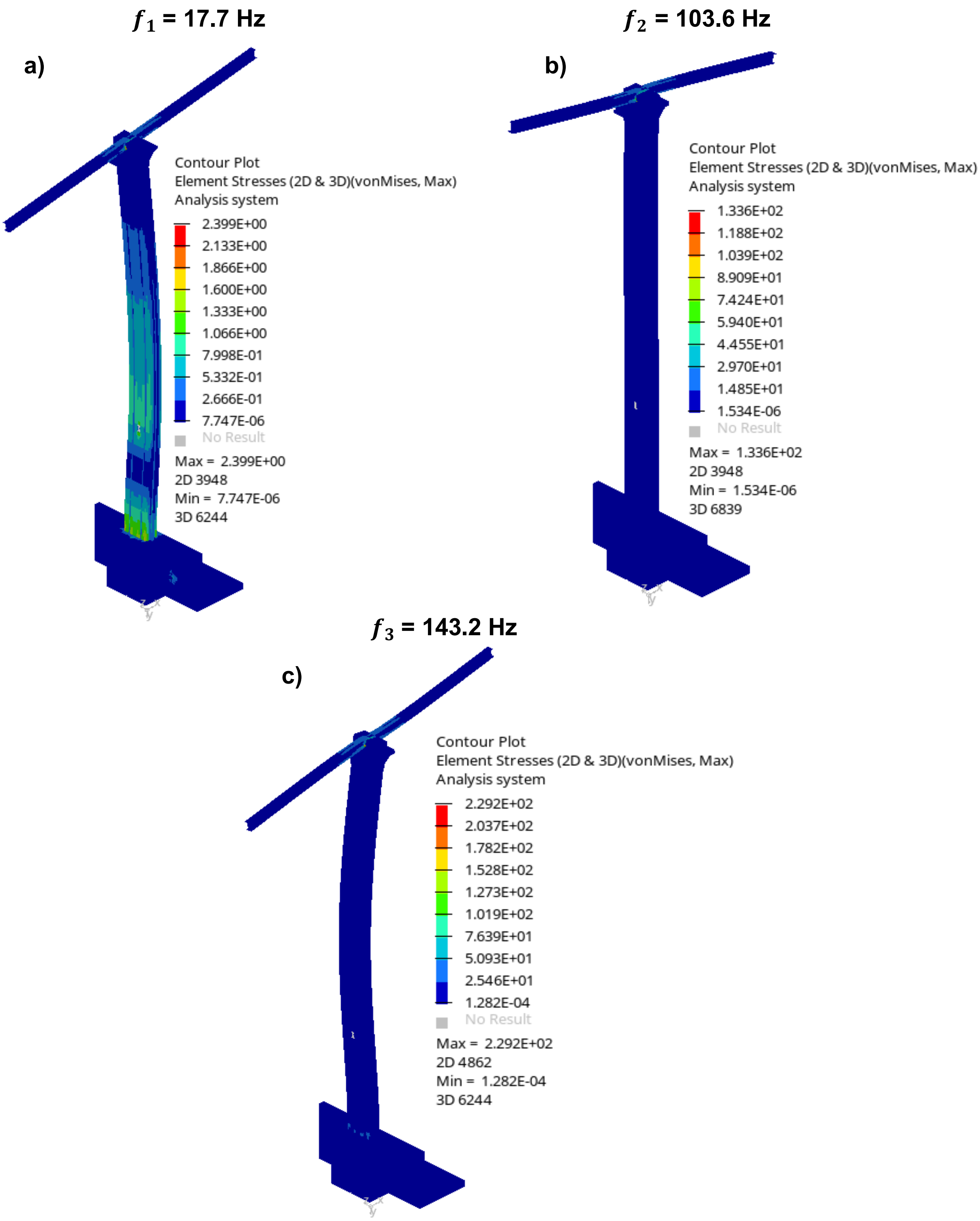

Figure 3.98 – Experiment 3: TT2 Von Mises max stress: a) 1st, b) 2nd and c) 3rd peaks

It has been decided to also include the stress plots because, in a linear simulation, it is proportional to the strain which is responsible for damping. According to the expectations, for all the peaks the deformation of the composite beam is restricted to the central area. Therefore, the hybridization of the tailplane should be applied in the middle. In addition, *Table 3.23* collects the damping factors of the test rig regarding its characteristic peaks:

Length [mm]	1st peak [%]	3rd peak [%]
1100	0.181	0.160

Table 3.23 – Damping factors of the test rig 1100 mm

From *Figure 3.98 a)* emerges that the stress of TT2 in the 1st peak is limited with respect to the 2nd peak, *Figure 3.98 b).* In addition, according to *Table 3.23,* in order to reach ξ_1=0.219%, the damping factor of the test rig of the 1st peak is slightly increased by the effect of the deformation of TT2. Contrarily, in the 2nd peak the effect of the test bench is negligible. Therefore, the increase of stress of TT2 with respect to the 1st peak justifies the increase of the correspondent global damping factor. Comparing the 1st and the 3rd peak, however the test rig is characterized by a higher damping factor for the 1st peak, considering the overall damping factor the situation is the opposite. But, according to *Figure 3.98 c)*, the 3rd peak of TT2 is characterized by higher stress (also strain $\sigma = E\varepsilon$) compared to the 1st peak. This effect causes that ζ_3 is higher than ζ_1.

Regarding the comparison of the peaks of the two beams, the 2nd peak is characterized by the largest difference between TT2 and TT7. Therefore, since the effect of the test rig is negligible, it is confirmed that this is induced by the behavior of flax fiber respect to the carbon fiber. On the contrary, since the effect of the I-beam is less evident, the 1st peak is characterized by a limited difference of damping factor than the 2nd peak. The 3rd peak has a relevant deformation of the vertical beam of the test rig. And it undergoes to high stresses in the lower part where it is constrained (green area at around 120 MPa). Therefore, this peak is less interesting for the damping analysis of the I-beam with real boundary conditions and excitation. Anyway, the relative difference between the two beams is limited respect to the other peaks. Although the FE model of TT7 is not present, it is assumed that its stress and deformation are responsible for this limited variation. This should be verified by simulating also the TT7.

The comparison between TT2 and TT7 has been executed at 1100 mm and in the next paragraph at 600 mm length of the vertical beam above the upper edge of the constraint. In the next stages of eVolve project it will be extended to all the other lengths of the vertical beam and with the simulations of all the beams to get more data to draw conclusions.

TT7 R40 (Experiment 3) vs TT7 L40 (Experiment 3)

In order to verify the symmetricity of the composite beam, the graph of *Figure 3.99* represents the FRF measured at the locations R40 and L40 of the TT7 horizontal beam:

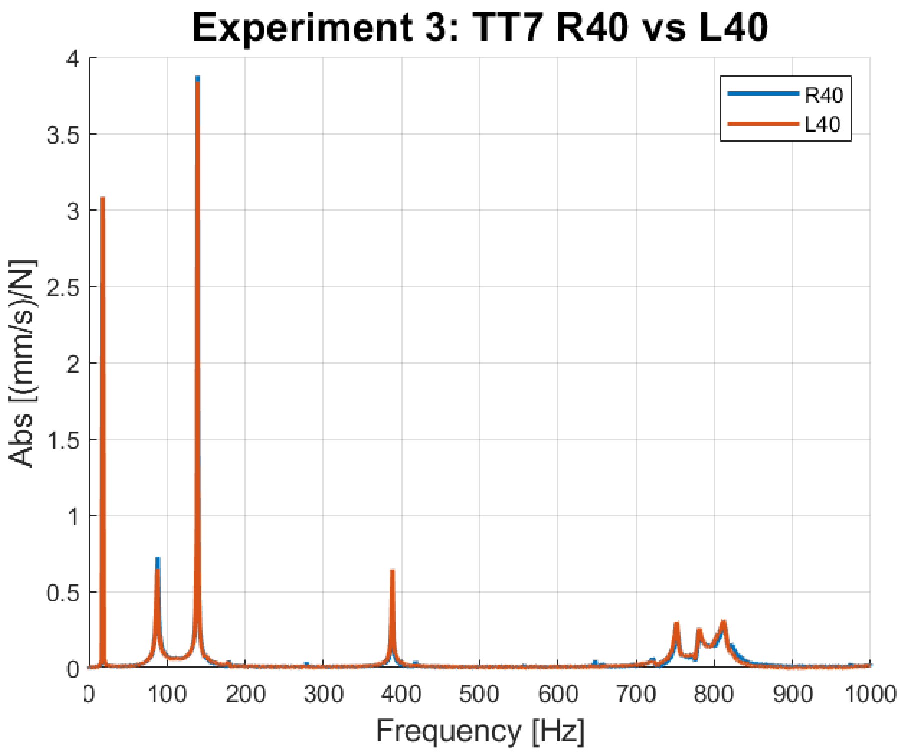

Figure 3.99 – Experiment 3: TT7 R40 vs TT7 L40

From a qualitative analysis of the graph is possible to confirm that there is a correspondence between the two curves. *Table 3.24* collects the damping factors calculated from the first three peaks of both curves R40 and L40:

	1st peak [%]	**2nd peak [%]**	**3rd peak [%]**
TT7 R40	0.388	1.085	0.299
TT7 L40	0.392	1.071	0.305

Table 3.24 - TT7 R40 vs TT7 L40 damping factors

It emerges that there is a limited discrepancy between the damping factors calculated for both sides of the composite beam. There is not a characteristic trend between the right and left part of the beam, they are randomly distributed. Therefore, the assumption of symmetricity of the composite beam is verified. Thus, it will be enough to measure only one half of the I-beam. This can be extended also to the other I-beams, provided that they are characterized by a symmetric distribution of the material.

TT7 R40 (Experiment 3) vs TT7 R18 (Experiment 3)

The deformation of the I-beam is located mainly in the central part close to the constraint. Therefore, up to now, it was assumed that the damping factor calculated at R18 would have been close to the one calculated at R40. This is the reason why all the curves have always referred to R40 measuring point. In order to verify this assumption, *Figure 3.100* represents the graph with the R40 and R18 curves:

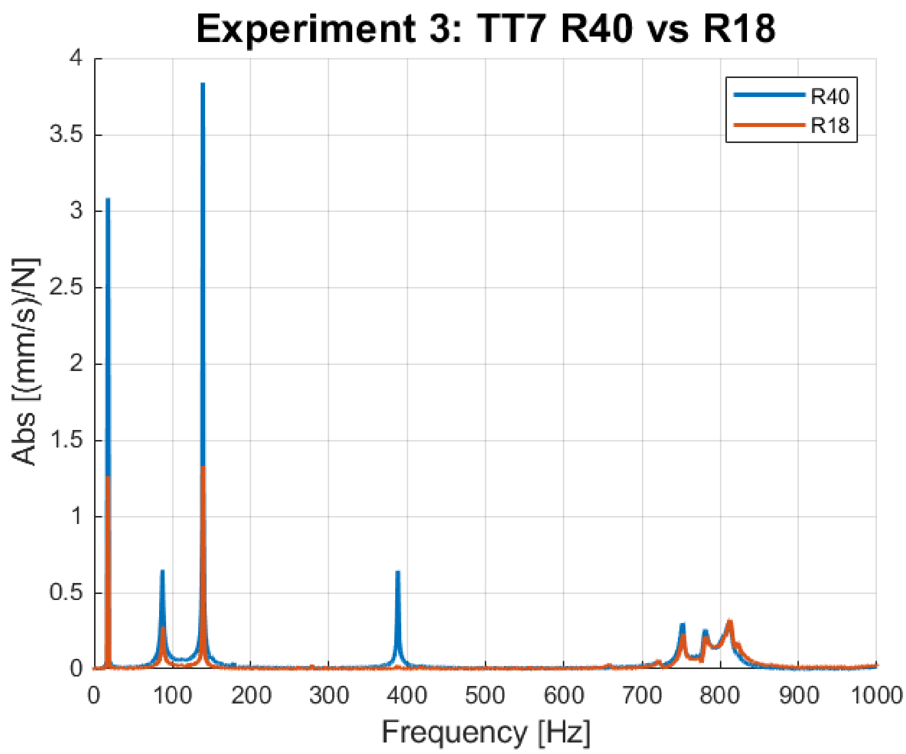

Figure 3.100 - Experiment 3: TT7 R40 vs TT7 R18

From a qualitative analysis of the graph is possible to confirm that there is a correspondence between the two curves. According to the expectations, the entity of the FRF curve of R40 is higher than the R18. This is because, due to the rigid body motion, the farthest coordinate has a higher displacement. *Table 3.25* collects the damping factors calculated from the first three peaks of both curves:

	1st peak [%]	**2nd peak [%]**	**3rd peak [%]**
TT7 R40	0.388	1.085	0.299
TT7 R18	0.384	1.091	0.304

Table 3.25 – TT7 R40 vs TT7 R18

The damping factors have been calculated for the first three peaks of the R40 and R18 and the results are similar. Therefore, the assumption of symmetricity of the composite beam is verified. Thus, it will be enough to measure only the last point of the beam. This can be extended also to the other I-beams.

600 mm free length

Test rig 1100 mm vs Test rig 600 mm

The FRFs comparison between the test rig 1100 mm and the test rig 600 mm is represented in *Figure 3.101*:

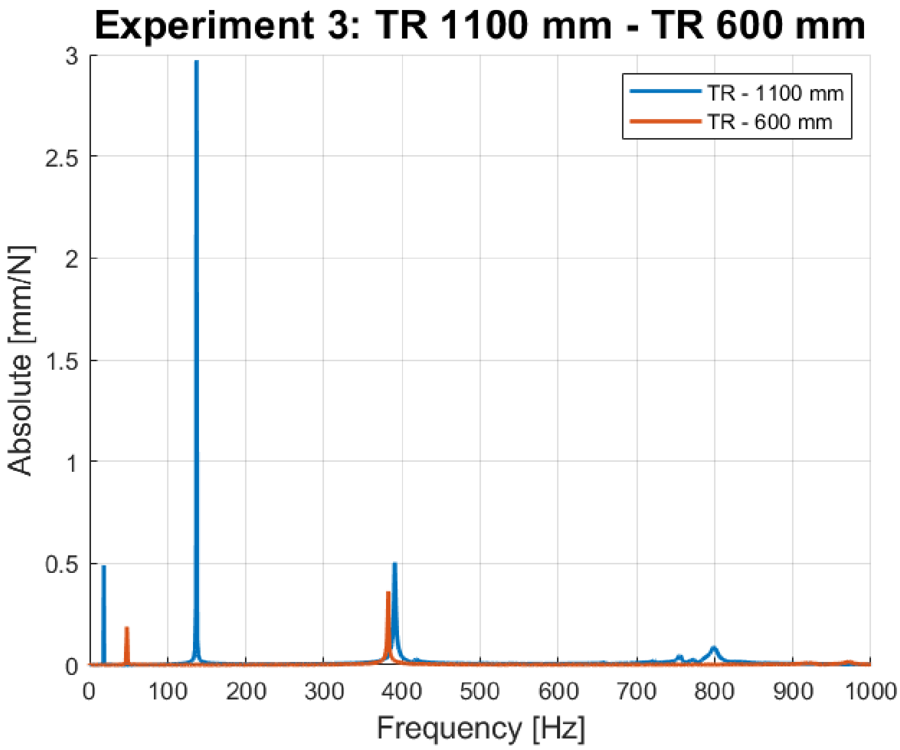

Figure 3.101 – Experiment 3: Test rig 1100 mm – Test rig 600 mm comparison

It is expected that by reducing the length of the vertical beam the stiffness of the test rig increases and, at the same time, the mass decreases. Therefore, according to the expectations, the eigenfrequency of the 600 mm free length should be higher compared to the 1100 mm free length. This is confirmed by *Figure 3.101* where the orange curve of 600 mm always follows the blue 1100 mm curve. The first three peaks are collected in *Table 3.26*:

	$f_1\ [Hz]$	$f_2\ [Hz]$	$f_3\ [Hz]$
TR – 1100 mm	17.8	143.4	389.5
TR – 600 mm	45.5	382.3	965.5

Table 3.26 – Experiment 3: TR 1100 mm – TR 600 mm eigenfrequencies comparison

TT2 R40 (Experiment 3) vs simulation

The FRFs comparison between TT2 R40 (Experiment 3) and the simulation with E = 59k MPa is represented in *Figure 3.102*:

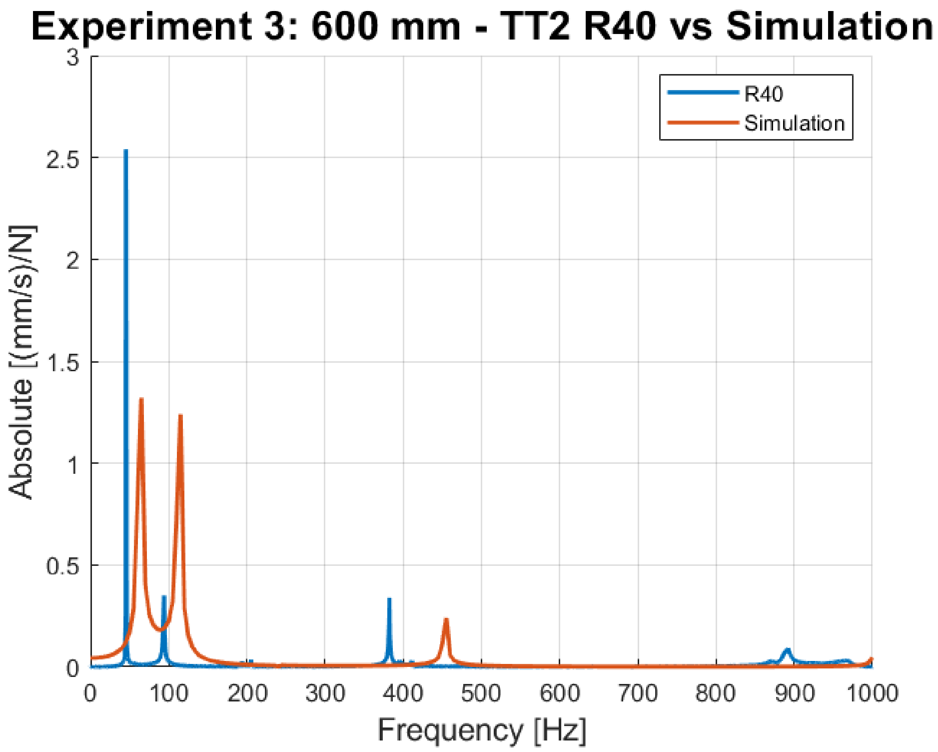

Figure 3.102 - Experiment 3: TT2 R40 FRFs comparison

It is possible to conclude that, in the low frequency area below 700 Hz, there is a direct correspondence of the theoretical and experimental curves. There are two peaks close to each other at 80 Hz and 100 Hz and there is another peak at 400 Hz which are evident in both curves. Usually, according to previous data analysis, the presence of the double peak is not caused by the I-beam. Therefore, it could be caused by the coupling of the test rig and the beam, which means that one eigenfrequency is characteristic of the beam while the other is proper of the test rig, therefore it measures the rigid body motion and the deformation of the specimen amplified by the natural frequency of the test rig. This can be determined by plotting the test rig combined to TT2 R40 in the same graph. The graph of *Figure 3.102* confirms what was initially assumed about the presence of a double peak. The peak at 100 Hz is characteristic of TT2 I-beam, while the peak at 80 Hz is proper of the test rig; therefore, it is present in both curves. In addition, it is possible to anticipate that, for the characterization of the I-beam only, it will be necessary to evaluate the peak at 100 Hz because it is not influenced by the rest of the system. Finally, the last peak which can be clearly compared is at around 400 Hz and is present in both curves.

According to 1100 mm free length experiment, it is again possible to confirm that the model is stiffer with respect to the experiment. It is due to the same reasons specified in the previous case.

Figure 3.103 represents the graph containing the experimental curve of the TT2 I-beam measured at R40 coordinate and the curve of the test rig itself to investigate the presence of the double peak:

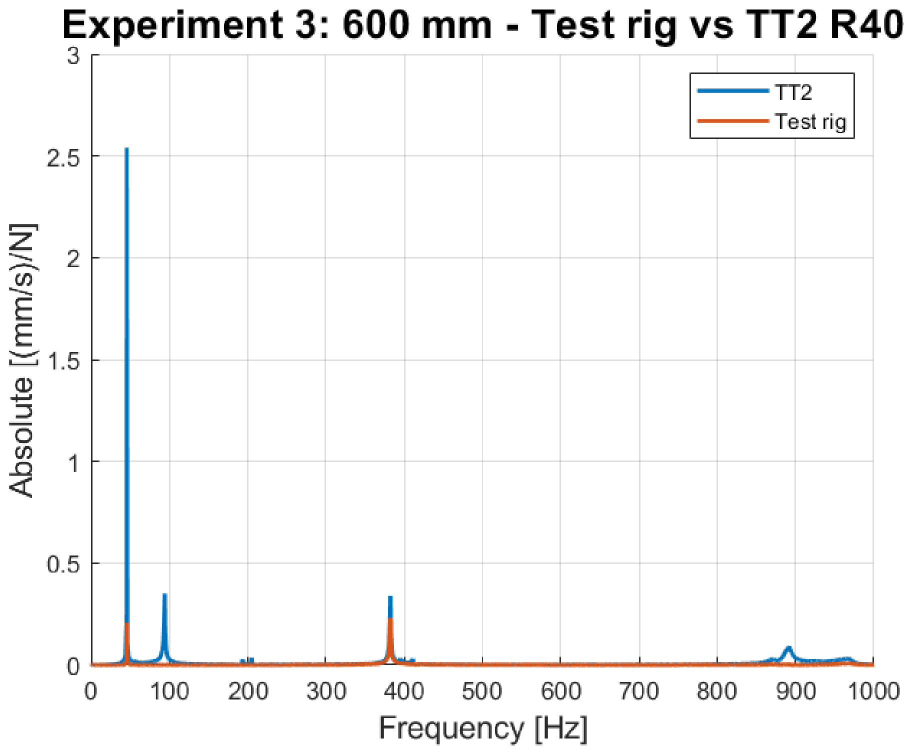

Figure 3.103 – Test rig (Experiment 2) vs TT2 R40 (Experiment 3)

According to *Figure 3.103* it is evident that the peak located at approximately 100 Hz is induced solely by the I-beam.

TT2 R40 (Experiment 3) vs TT7 R40 (Experiment 3)

After the validation of the test rig plus the I-beam completed in the previous paragraphs, it is possible to start the comparison of the I-beams. The FRFs are compared at the measurement point R40. The FRFs are represented in *Figure 3.104*:

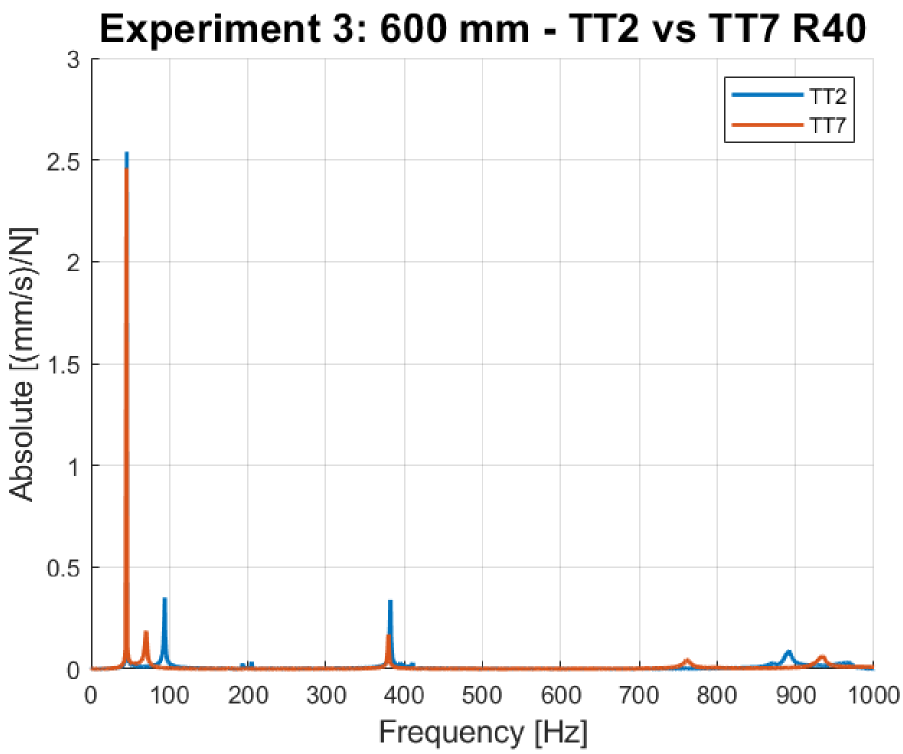

Figure 3.104 - Experiment 3: TT2 R40 vs TT7 R40

Regarding the eigenfrequencies comparison, it is expected that TT7 curve precedes TT2 curve because, flax beam is heavier compared to carbon beam. In addition, flax is less stiff compared to carbon.

By the analysis of *Figure 3.104*, it is possible to confirm the expectation since the TT7 curve always precedes the TT2 curve. As in the 1100 mm free length, the shifting is not that relevant as it would be by testing only the I-beam in free-free conditions or clamped as a cantilever beam, because, in this case, the overall FRF and consequently the damping factor, are affected by the behavior of the beam plus the test rig. For this motivation, the stiffness of the test rig is relevant with respect to the I-beam itself; therefore, the increment of stiffness of the TT2 with respect to the TT7 does not provide a disruptive change to the eigenfrequencies. The same is valid for the increment of mass of TT7 with respect to TT2, where its contribution, weighted by the mass of the complete test rig is almost negligible. Anyway, despite of the limited effect weighted by the entire test bench, TT2 is stiffer and lighter compared to TT7; for this reason, the natural frequencies are higher.

On the contrary, by focusing on the second eigenfrequencies located at around 100 Hz, which is a peak characteristic only of the I-beam, it is possible to evidence a wider displacement between the two curves. This is according to the expectations because, in this case, the increment of mass and the reduction of stiffness are not added to a consistent quantity, but they are directly compared.

After having analyzed the FRFs of TT2 and TT7 represented in *Figure 3.104*, a Python® code has been developed to compute the damping factors corresponding to each peak of the curves. According to what has already been mentioned, there are some peaks characteristics of the test rig and another characteristic of the I-beam. The approach adopted for damping comparison in the same of 1100 mm free length and it is represented in *Figure 3.96.*

The damping factors obtained for TT2 and TT7 for the 1st, 2nd, and 3rd peaks (*referring to Figure 3.101*) are grouped in *Table 3.27*:

	Peak 1		**Peak 2**		**Peak 3**	
	f_1 $[Hz]$	ζ_1 [%]	f_2 $[Hz]$	ζ_2 [%]	f_3 $[Hz]$	ζ_3 [%]
TT2	45.7	0.319	**94.1**	**1.942**	382.4	0.391
TT7	45.1	0.454	**70.1**	**4.862**	380.0	0.406

Table 3.27 - Experiment 3: TT2 - TT7 damping comparison 600 mm

Comparing the damping factor of TT2 and TT7 of Peak 2, according to the expectations, flax I-beam is characterized by higher damping compared to the carbon beam. In detail, ζ_{TT7} is 150% higher compared to ζ_{TT2}.

In order to analyze the variation of damping factor of TT2 in the frequency range of interest, is necessary to represent the eigenmodes of TT2 corresponding to the three peaks, *Figure 3.105*:

a) f_1 **= 45.7 Hz**

b) f_2 **= 94.1 Hz**

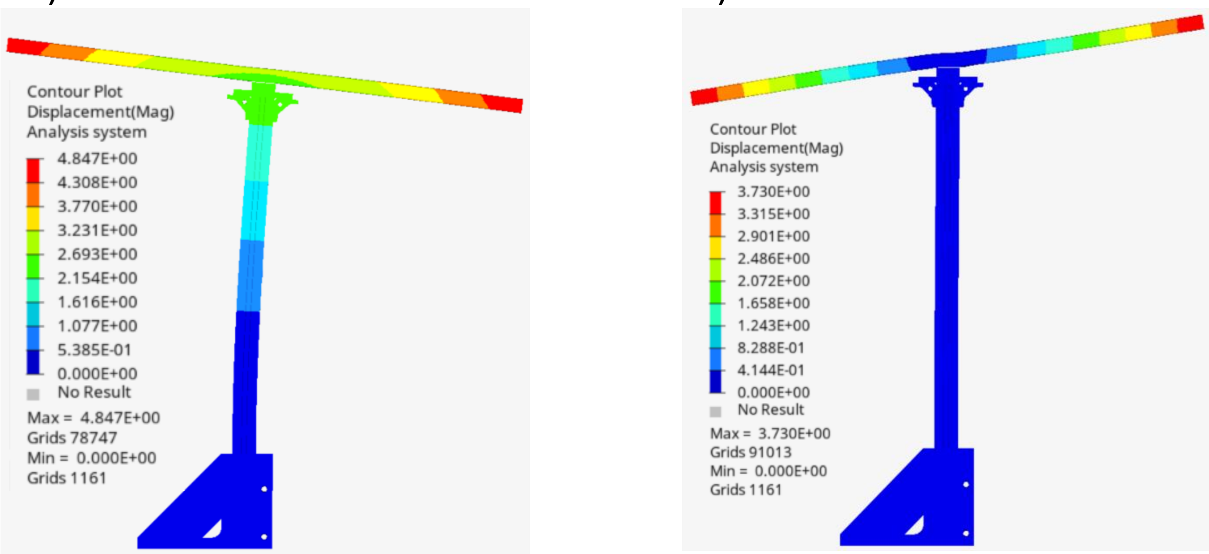

c) f_3 = 382.4 Hz

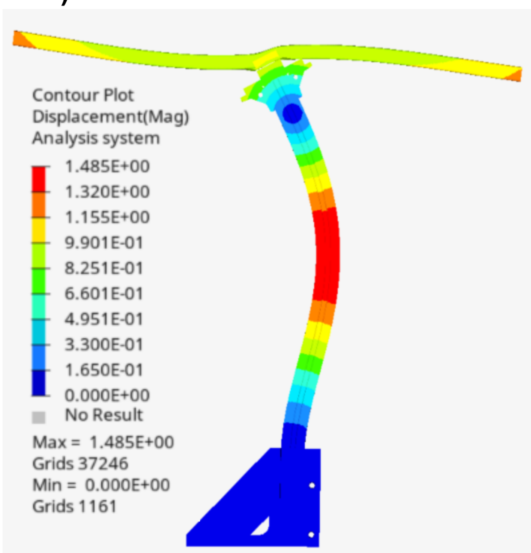

Figure 3.105 – Experiment 3: TT2 eigenmodes of the 1st a), 2nd b), and 3rd c) peaks

According to *Figure 3.105 a)*, TT2 moves rigidly, therefore ζ_1 is given only by the deformation of the vertical beam. On the contrary, ζ_2 is the highest and, according to *Figure 3.105 b)*, the test rig has a limited deformation, and the interface plate is almost straight; therefore, the asymmetric configuration of the beam is provided only by its deformation. The third eigenmode, illustrated in *Figure 3.105 c)*, shows that the displacement of the beam is partially induced by its deformation but also given by the deformation of the test rig that induces rigid body motion to the beam. *Table 3.28* collects the damping factors of the test rig regarding its peaks:

Length [mm]	1st peak [%]	3rd peak [%]
600	0.208	0.214

Table 3.28 – Damping factors of the test rig 600 mm

In addition, *Figure 3.106* includes the stress plots:

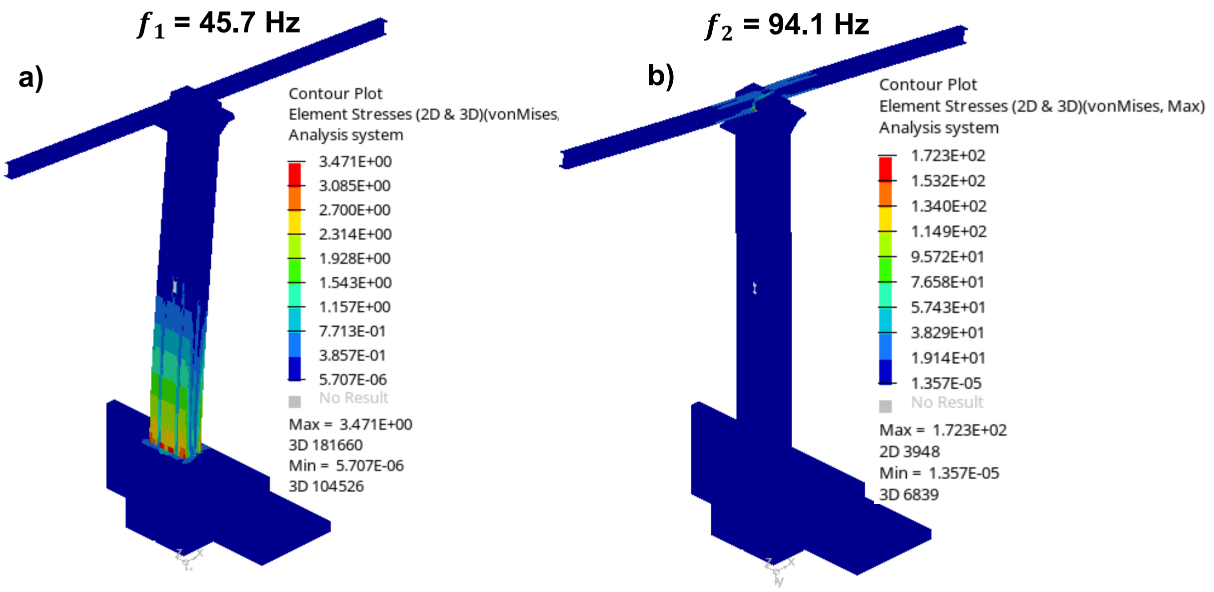

f_3 = 382.4 Hz

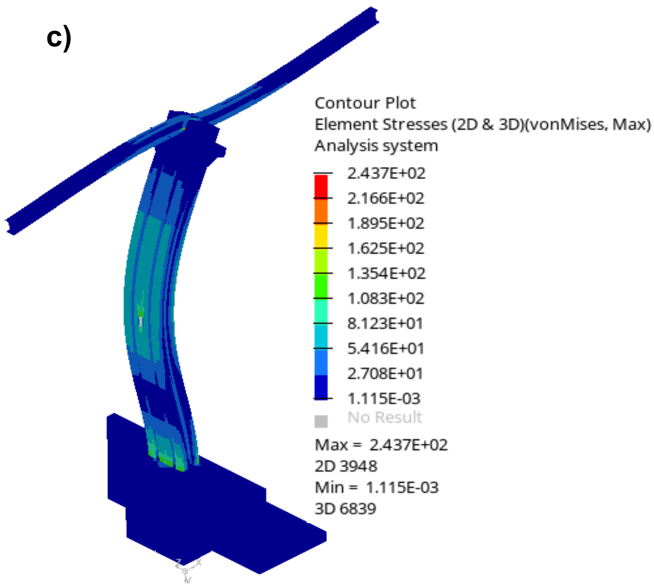

Figure 3.106 - Experiment 3: Von Mises maximum stress a) 1st, b) 2nd and c) 3rd peaks

The comparison between the 1st and 2nd peak is similar to the 1100 mm length. From *Figure 3.106 a)* emerges that in TT2 the stress of the 1st peak is limited with respect to the 2nd peak, *Figure 3.106 b).* According to *Table 3.28*, in order to reach ξ_1=0.319%, the damping factor of the 1st peak of the test rig is slightly increased by the effect of the deformation of TT2. Contrarily, in the 2nd peak the effect of the test bench is negligible. Therefore, the increase of stress of TT2 with respect to the 1st peak justifies the increase of the correspondent damping factor. Regarding the comparison between the 1st and the 3rd peak, however the test rig is characterized by a slightly higher damping factor for the 3rd peak, it does not justify the increase of damping between the two peaks of TT2. Therefore, according to *Figure 3.106 c)*, the higher stress of the composite beam is responsible for the increase of damping. The 3rd peak is characterized by a relevant deformation of the test rig and, in addition, TT2 has an asymmetric eigenmode but different from the configuration of interest (that one of the 2nd peak). Therefore, this peak is not considered in the damping investigation. Anyway, regarding TT7, contrarily to the other cases, it emerges that the damping factor of the 3rd peak is lower than the 1st peak, even though the damping of the test rig is opposite. It is assumed that it is caused by the composite beam.

In the same way of Experiment 3: 1100 mm, regarding the comparison of the peaks of the two beams, the 2nd peak is characterized by the largest difference between TT2 and TT7. Therefore, since the effect of the test rig is negligible, it is confirmed that this is induced by the behavior of flax fiber respect to the carbon fiber. On the contrary, since the effect of the I-beam is less evident, the 1st peak is characterized by a limited difference of damping factor than the 2nd peak.

Comparison between TT2 and TT7 at 1100 mm and 600 mm

After the execution of the experiments at the two lengths it has been decided to compare the FRFs of the two I-beams obtained at both lengths and the damping factors over the frequency range. *Figure 3.107* represents the FRFs of TT2 obtained at both lengths, while *Figure 3.108* represents the FRFs of TT7:

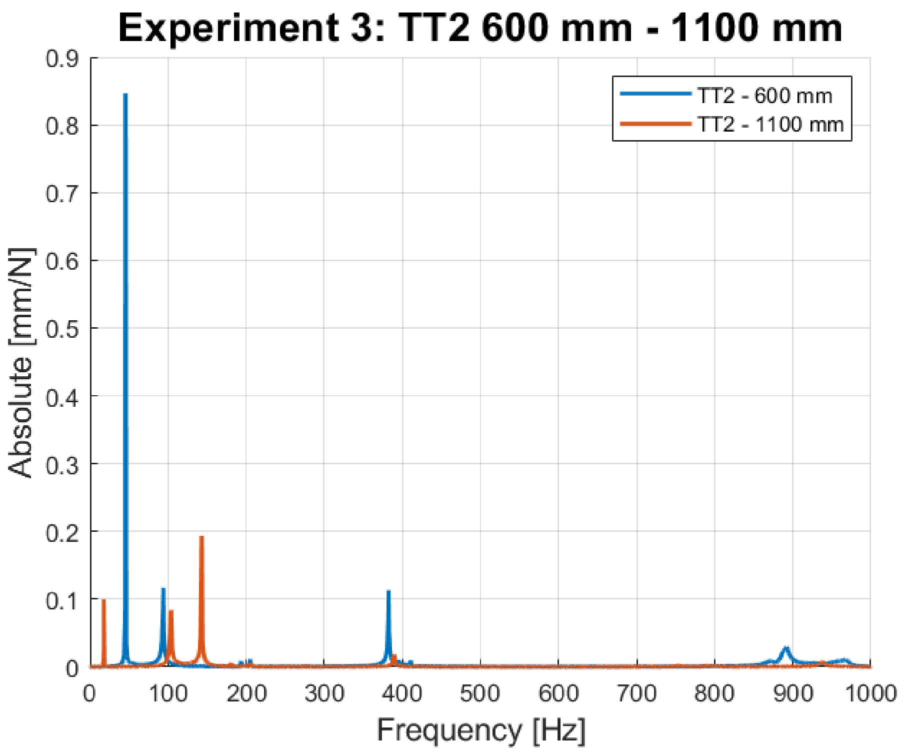

Figure 3.107 - Experiment 3: TT2 600 mm vs 1100 mm

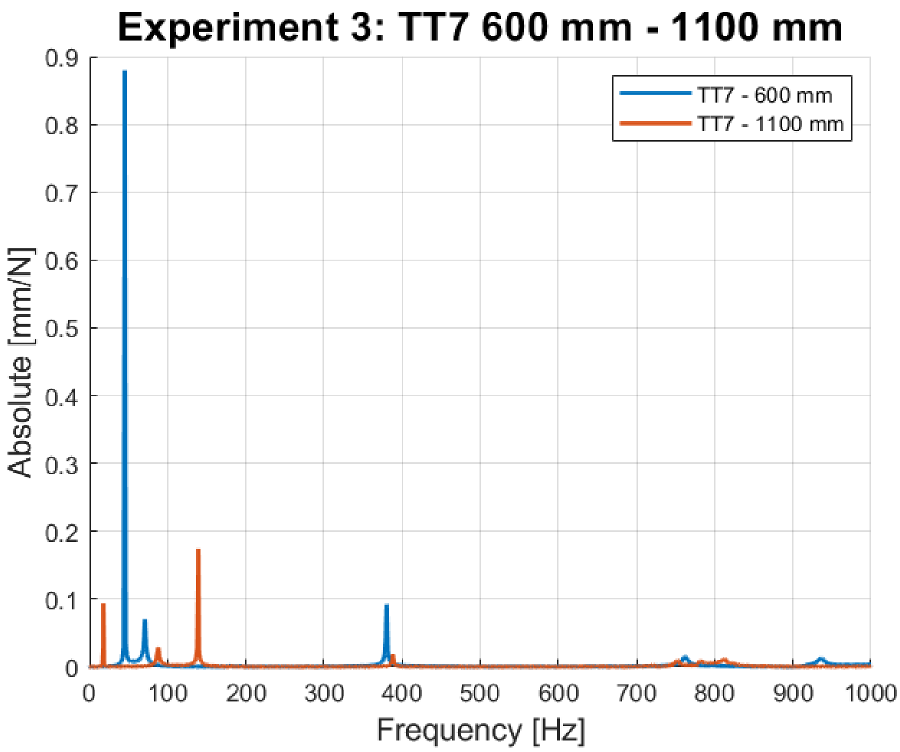

Figure 3.108 - Experiment 3: TT7 600 mm vs 1100 mm

From the analysis of the graphs, it is possible to evidence that in the low frequency range below 200 Hz the 1100 mm has an additional peak. While there is correspondence for the peak located approximately at 400 Hz. It is evident that, for all the peaks, TT7 peaks always precede the TT2 peaks due to the fact that TT7 is less stiff and heavier compared to TT2.

The damping ratios related to the low frequency range below 400 Hz where there is a direct correspondence between the curves are collected in *Table 3.29.* The units are omitted for graphical reasons, the frequency is expressed In Hz and the damping factor in %:

	Peak 1				**Peak 2**				**Peak 3**			
	1100 mm		**600 mm**		**1100 mm**		**600 mm**		**1100 mm**		**600 mm**	
	f_1	ζ_1	f_1	ζ_1	f_2	ζ_2	f_2	ζ_2	f_3	ζ_3	f_3	ζ_3
TT2	17.7	0.219	45.7	0.319	**103.6**	**0.777**	**94.1**	**1.942**	143.2	0.296	382.4	0.391
TT7	17.7	0.388	45.1	0.454	**88.1**	**1.085**	**70.1**	**4.862**	139.2	0.299	380.0	0.406

Table 3.29 - Damping ratios TT2 vs TT7

Considering the frequencies of the peaks, it comes out that in peaks 1 and 3 the eigenfrequencies of 600 mm free length are higher than the eigenfrequencies of 1100 mm free length. On the contrary, in peak 2 it is the opposite. It is concluded that for the peaks depending on the test rig: peaks 1 and 3, the eigenfrequency of 600 mm must be higher than the 1100 mm because the test rig is stiffer and lighter. Whereas, for the 2nd peak that depends only on the I-beam, it is not compulsory that the 600 mm eigenfrequencies follows the 1100 mm because, since the peak does not depend on the test bench, the increase of stiffness of the test rig does not affect as in the others two peaks. Regarding the 2nd peak, it makes sense to limit the comparison of the frequencies to each free length, highlighting the fact that, according to the expectations, TT2 always follows TT7. The damping factors of 600 mm are higher compared to 1100 mm free length for all the peaks. In addition, according to the initial expectations, the damping factors of TT7 are higher compared to the damping factors of TT2.

Table 3.30 collects the damping factors of the bending test rig calculated for both 1100 mm and 600 mm lengths for the first and third peaks, which are characteristic of the test rig.

Length [mm]	**1st peak [%]**	**3rd peak [%]**
1100	0.181	0.160
600	0.208	0.214

Table 3.30 – Damping factors of the bending test rig

From the analysis of the damping factors of the bending test rig (*Table 3.30*) emerges that the 600 mm test rig damps more than the 1100 mm test rig. This is also what emerges from the overall damping factor including composite beam and test rig (*Table 3.29*). Therefore, it is possible to conclude that the increase of damping factor of the test rig contributes to the increase of damping factor of the global system. By considering the increment of damping between the 600 mm and the 1100 mm of the 1st peak, it is caused both by the effect of the test rig and by the increase of stress of the composite beams (*Fig. 3.98* and *3.106*). On the contrary, in the 2nd peak there is a relevant increase of damping, and it is induced by the composite beam. In order to investigate, *Figure 3.109* represents the stress comparison of the 2nd peak for both lengths:

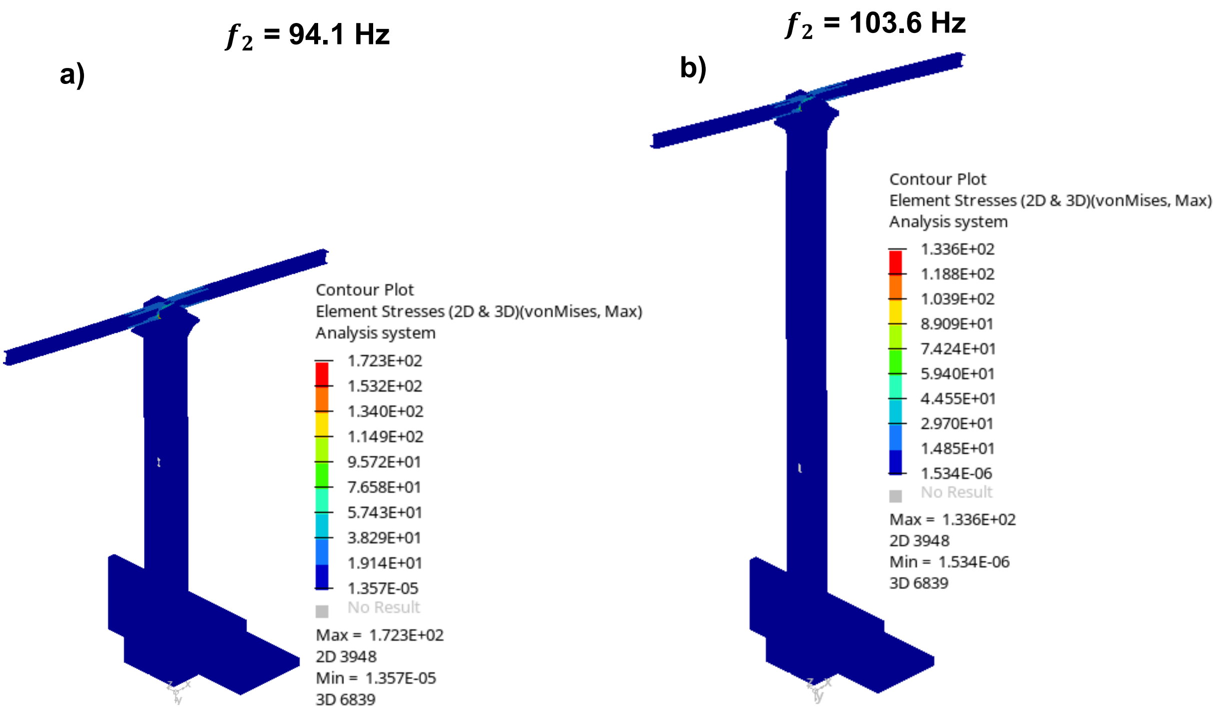

Figure 3.109 – 2nd Peak stress comparison a) 600 mm b) 1100 mm

Considering this peak, the stresses of the TT2 600 mm are substantially higher than the 1100 mm. In the other peaks the difference of stress in the two lengths is more limited. This justifies the relevant increase of damping of the 2nd peak with respect to the others. In addition, according to the color legend, the test rig is colored in blue for both lengths, but the 600 mm is characterized by a slightly higher threshold for this color. But this does not justify the relevant increase of damping since the test rig does not play a major role in the 2nd peak. This is both valid for TT2 and TT7. The TT7 is characterized by higher values of damping factor. This is caused by the effect of flax with respect to carbon fiber. In the 600 mm, by applying the same excitation, the TT2 deforms more than in the 1100 mm always obtaining the asymmetric mode shape of interest.

The 3rd peak has a limited interest for the investigation because it is consistently affected by the deformation of the vertical beam of the test rig. In addition, in the 600 mm it is not characterized by the mode shape of interest.

3.4.1.4 py-FBS: Frequency Based Sub-structuring to isolate the I-beam

Depending on what has been anticipated about the contribution of the test rig to the damping extracted by FRF obtained by the LSD measurement, it has been tried to apply Frequency Based Sub-structuring (FBS) to isolate the FRF of the I-beam and compare it to the experimental measurement of the beam in free-free condition where damping is provided only by the I-beam.

In order to decouple the I-beam (B) from the entire system (AB), it has been decided to write a code on Python® based on py-FBS® library and 3D-tool. The code receives in input the theoretical data obtained from the simplification of Simulation 4 performed on Ansys®: mass and stiffness matrix, mesh, eigenfrequencies and eigenmodes. The model of the test rig is represented in *Figure 3.110*, there are three accelerometers and nine impacts in correspondence of the interface to obtain the Virtual Point transformation. In addition, there are other transducers and impacts along the test rig to obtain the FRF in the point of interest. The vertical beam of the test rig is not the ITEM beam because its discretization requires a high number of nodes, which would not be possible to deal with on Python®. *Figure 3.111* represents a detail of the interface. The yellow arrows in proximity of the red ones represent the adjustment of the position of impacts and accelerometers in correspondence of nodes of the mesh:

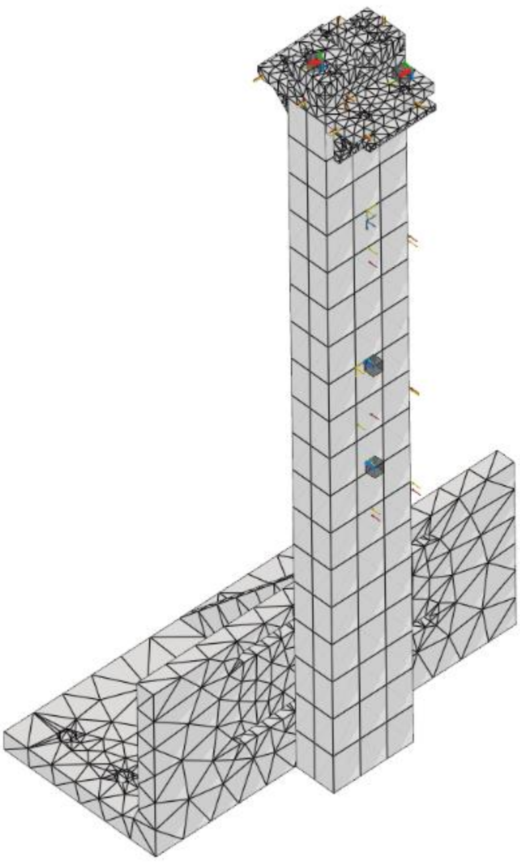

Figure 3.110 - Test rig (A) FBS set-up

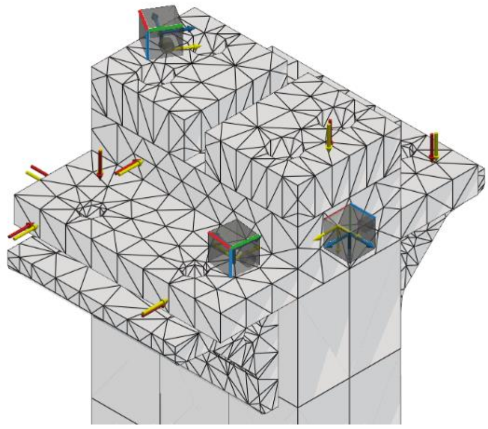

Figure 3.111 – Detail of the interface of the test rig (A) FBS

Py-FBS® tool has a 3D interface which allows to position impacts and accelerometers on the structure in the locations of interest for the calculation of the FRF according to the mass and stiffness matrixes provided in input.

The same is repeated for the entire model, composed by test rig and I-beam, addressed as AB where impacts and accelerometers are added to the beam in the points of interest and the test rig has the same configuration. AB model is represented in *Figure 3.112*:

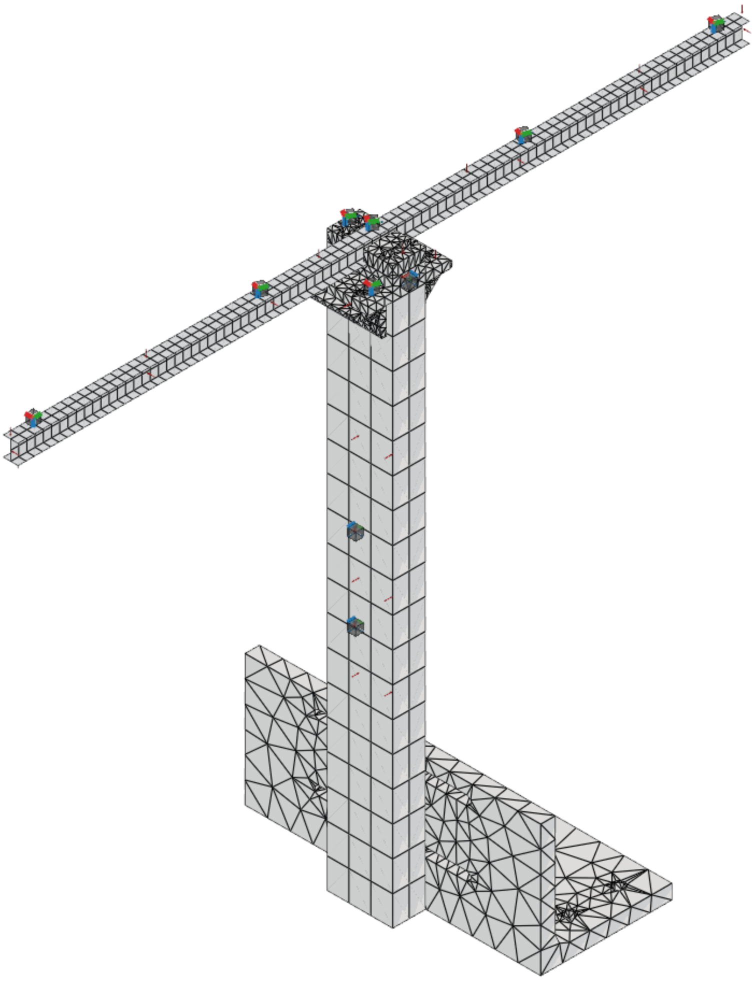

Figure 3.112 - Test rig + I-beam (AB) FBS set-up

The code decouples the I-beam (B) from the entire assembly (AB) obtaining as result the FRF of the I-beam in free-free conditions excited at one end, as schematized in *Figure 3.113*:

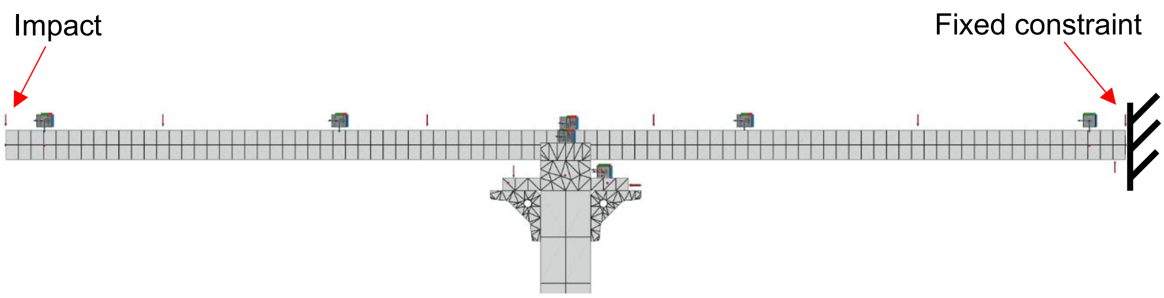

Figure 3.113 - I-beam (B) set-up FBS

The procedure consists of, first, assembling the admittance matrix for the coupled system containing the sub-structure admittances:

$$Y^{AB|A} = \begin{bmatrix} Y^{AB} & 0 \\ 0 & -Y^{A} \end{bmatrix} \tag{3.1}$$

Next, the compatibility and the equilibrium conditions have to be defined through the signed Boolean matrixes $\mathrm{B_u}$ and $\mathrm{B_f}$, which are equals according to the definition of impacts and accelerometers, represented in *Figure 3.114*:

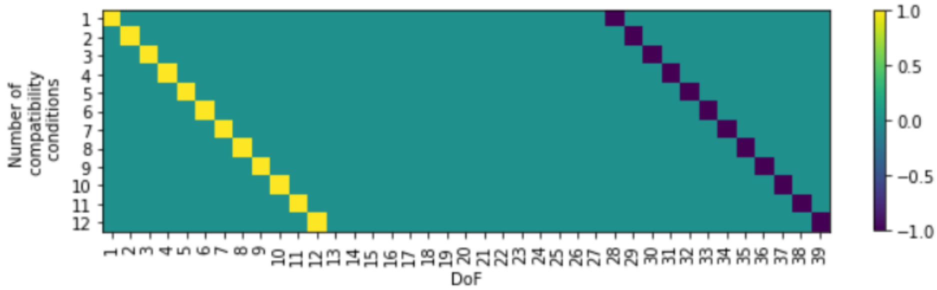

Figure 3.114 - Compatibility and Equilibrium conditions FBS

In conclusion, according to the Lagrange's Method – Frequency Based Sub-structuring, with the defined positions of accelerometers and impacts, $\mathrm{Y^B}$ is computed as:

$$Y^{B} = Y^{AB|A} - Y^{AB|A}B^{T}(BY^{AB|A}B^{T})^{-1}BY^{AB|A} \tag{3.2}$$

The graph column of interest of the admittance matrix, composed by the locations indicated in *Figure 3.111*, is represented in *Figure 3.115*:

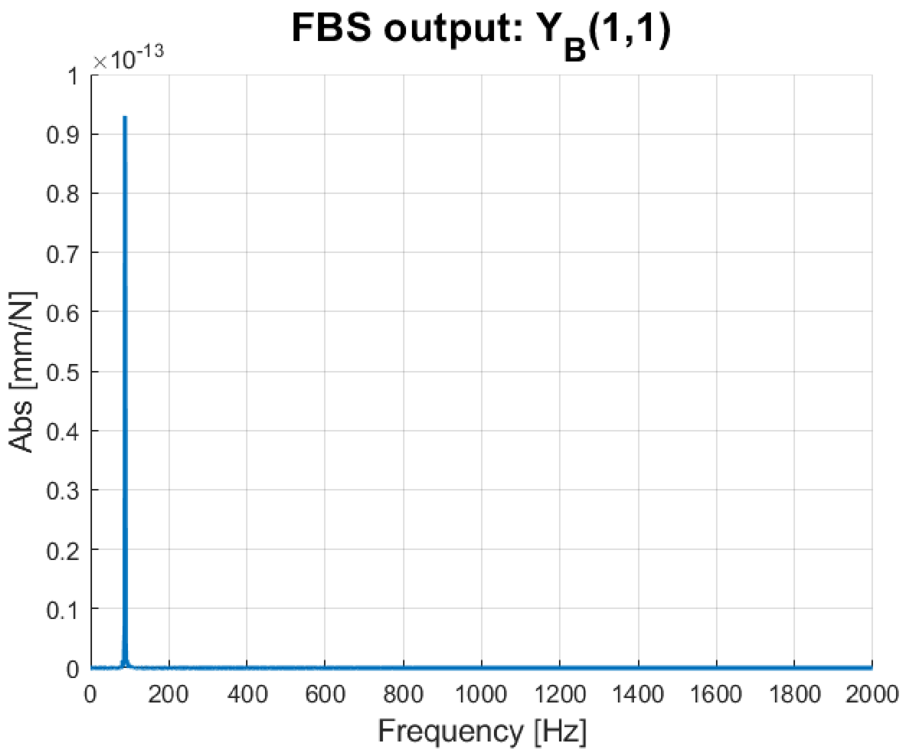

Figure 3.115 - $Y^{B}{}_{(1,1)}$ FRF plot

The decoupled FRF is compared to the experimental FRF directly measured on the I-beam tested in clamped-free condition with the impact applied to the free end, executed by my Scheffler [23]. The curve is represented in *Figure 3.116*:

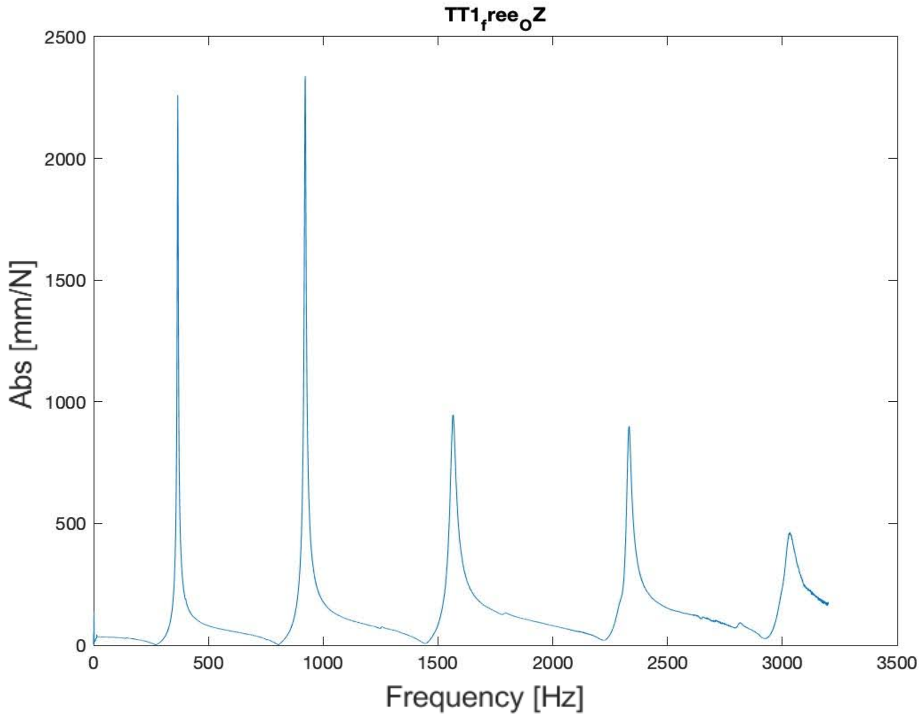

Figure 3.116 - TT2 clamped-free with impact experimental FRF

From the comparison of the curves, it is evident that there is a complete mismatch between the two graphs. It is thought that the motivation of the discrepancy is given by the fact that the input data obtained from Ansys® are related to the "Normal mode" analysis, which consists on the determination of the eigenvalues and the eigenmodes. This is consistent for the test rig (A) which is entirely composed by metal materials, with comparable stiffnesses. On the contrary, the entire assembly (AB) composed by test rig and I-beam is made up of metal materials and composite, which are characterized by different stiffnesses. Therefore, the eigenmodes obtained from the solution of the eigenproblem mainly consists of the deformation of the composite I-beam, while the test bench remains almost undeformed. Accordingly, during the subtraction the admittance of AB does not include the deformation of the test rig, while the admittance of A includes the deformation. In addition, they also include the torsional modes that are not excited in the experiment. For this reason, it would be more coherent to input the data obtained from "Frequency direct" analysis, but this is not included in py-FBS®.

A possible solution to this inconvenience would be to perform the experimental sub-structuring, where Y^{AB} and Y^{A} are experimentally derived from Experiments 2 and 3 and then inputted to the code. Then, the accelerometers and impacts' positions are manually assigned according to the experiment. By this way, since also in AB both the test rig and the I-beam are coherently deformed, it is expected to obtain a FRF consistent to the experimental curve of *Figure 3.116*. This has not been performed in this thesis due to time constraint and because it is not the topic of the project.

3.4.2 Axial test rig

In order to evaluate the symmetric deformed configuration, according to Simulation 1, it is necessary to test the I-beam with the axial test rig, which is derived from the bending test rig. For this experiment, the layout is completely different because it is not required to shift the frequency range, thus, the vertical beam is not used. The axial test bench, without the specimen, is represented in *Figure 3.117*:

Figure 3.117 – Experiment 4: axial test rig set-up lateral view

The test rig is composed by the shaker Vibration Test System TV 50018 produced by TIRA GmbH that is rigidly constrained to the isolated table by means of two threaded connections. The shaker is rotated by 90° with respect to its standard position; then, the impedance head which measures the force and the acceleration is mounted on the top. Finally, it is connected to the upper part of the interface of the complete bending test rig with the right and left clamps for constraining the I-beam. The top view of the axial test rig is represented in *Figure 3.118*:

With respect to the corresponding Simulation 6, the experiment is carried out by reversing the position of the boundary conditions and the excitation. In the simulation, the interface is fixed to the table, while the dynamic load is induced to both the extremities of the horizontal beam. While in the experiment the interface plate is fixed to the shaker which applies a vertical excitation. This is done with the purpose of simplifying the simulation but at the same time inducing the same excitation to the system.

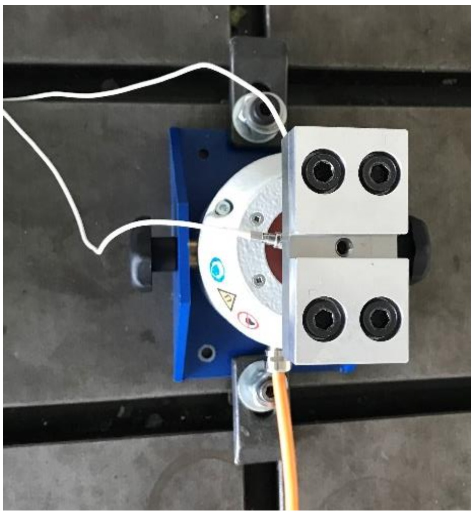

Figure 3.118 – Experiment 4: axial test rig set-up top view

In order to measure the entity of the excitation applied by the shaker, it is necessary to adopt an impedance head. For the experiment the model 5860B Impedance Head produced by Dytran Instruments with a sensitivity of 22 mV/N was used.

In detail, the components are mounted to the shaker using a threads adapter due to the presence of threads with different dimensions, according to the exploded view represented in *Figure 3.119:*

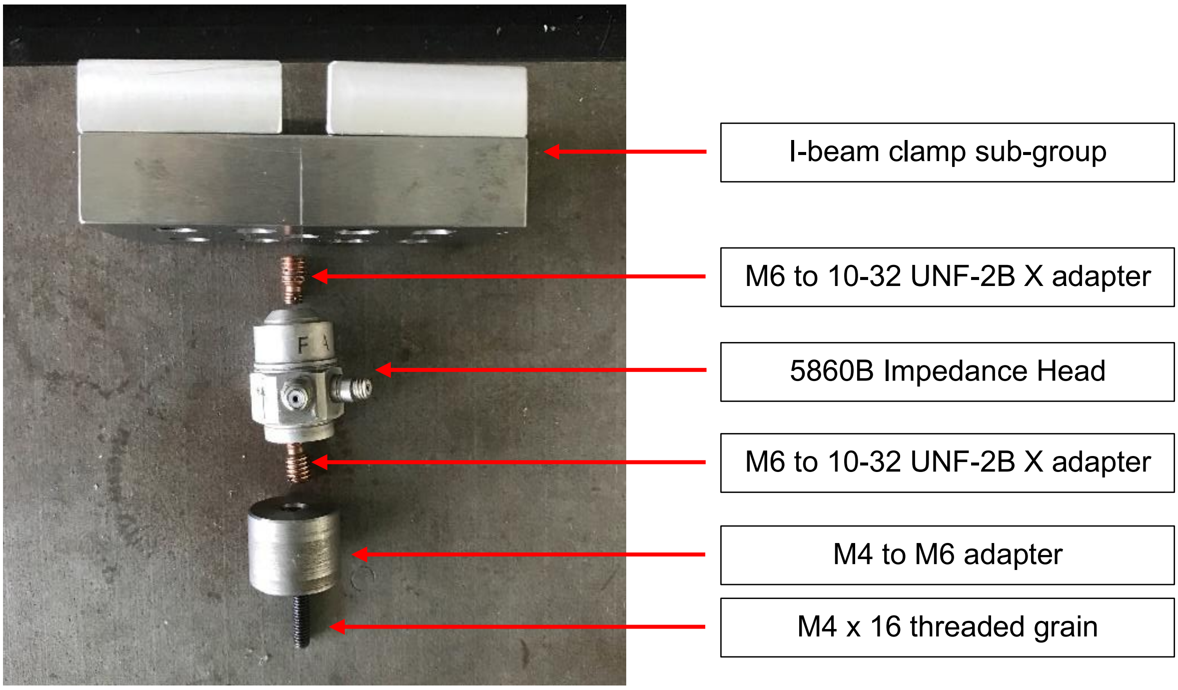

Figure 3.119 – Experiment 4: axial test rig exploded view

The set-up including TT2 I-beam is represented in *Figure 3.120*:

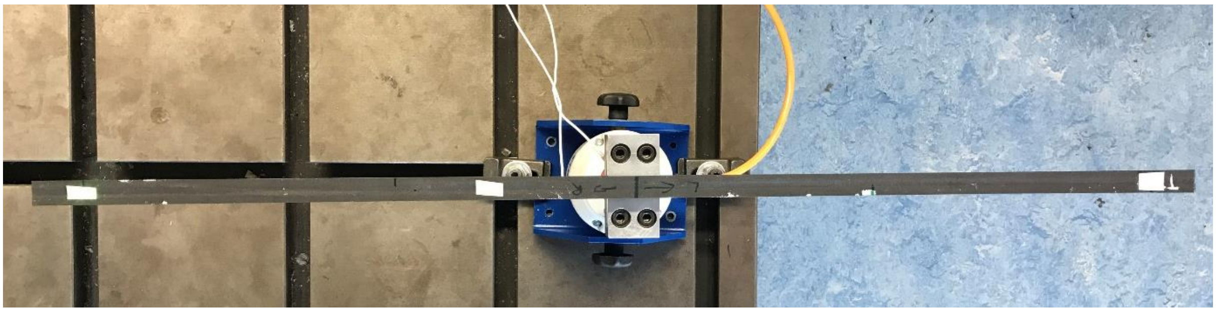

Figure 3.120 – Experiment 4: axial test rig + TT2 set-up

The I-beam is mounted on the axial test rig in the same way of the bending test rig, respecting the same alignments and perpendicularities with respect to the I-beam constraint sub-group. The output is measured with the LSD laser system which is hanged to the ceiling of the room. The laser beam hits the I-beam in correspondence of the reflective tape and the signal is captured by the receiver. With respect to the bending test rig, it is thought that is not necessary a “Bottom to Top” approach because the test rig is composed only by the I-beam sub-group which simply behaves as a concentrated mass on the top of the shaker. Therefore, Experiment 4 directly considers the I-beam mounted on the axial test rig.

During the execution of the experiment, it has been evidenced that the moving part of the shaker is not constrained to move in a guide; therefore, limited transversal movements are allowed. Due to the configuration of the assembly, the length of TT2 results predominant with respect to the dimensions of the other components. For this reason, due to this length and due to the fact that during the shaking the center of mass of the constraint sub-group misaligns with respect to the axis of the shaker, there are some transversal movements. Due to the structure of the I-beam, where, although the addition of a carbon wire it has lack of material in the junction of the two C molds, the laser is affected by the change of altitude induced by the transversal oscillations. In order to reduce the influence of this phenomena, it has been decided to apply some filling material (wax) to level the gap and obtain the same planarity in the flanges.

The result of the experiment is the FRF measured at R40 is represented in *Figure 3.121*:

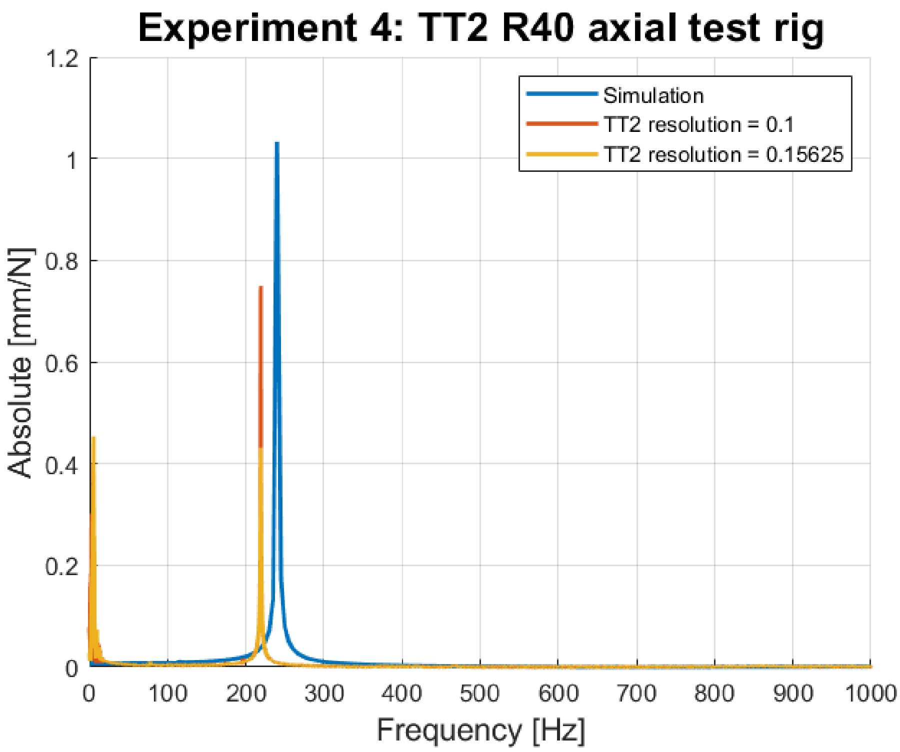

Figure 3.121 - Experiment 4: TT2 - simulation FRF comparison

From the analysis of the graph, it is possible to realize that, with respect to the bending test rig, there is an initial part up to 20 Hz which can be neglected since it can be referred to rigid body motion. In addition, it has been realized that the experimental curves are affected by noise and disturbs in a higher amount with respect to the bending test rig output. For this reason, the experiment has been repeated several times arranging the experimental parameters such as the resolution.

This is the reason why *Figure 3.121* contains two experimental curves, the orange with 0.1 Hz resolution and the yellow with 0.15625 Hz resolution. Among the executed experiments, these are the cleanest and most refined curves.

Despite of the experimental tuning, the FRF it is not as smooth as the bending test rig. The two curves are highlighted in proximity of the peak in *Figure 3.122*:

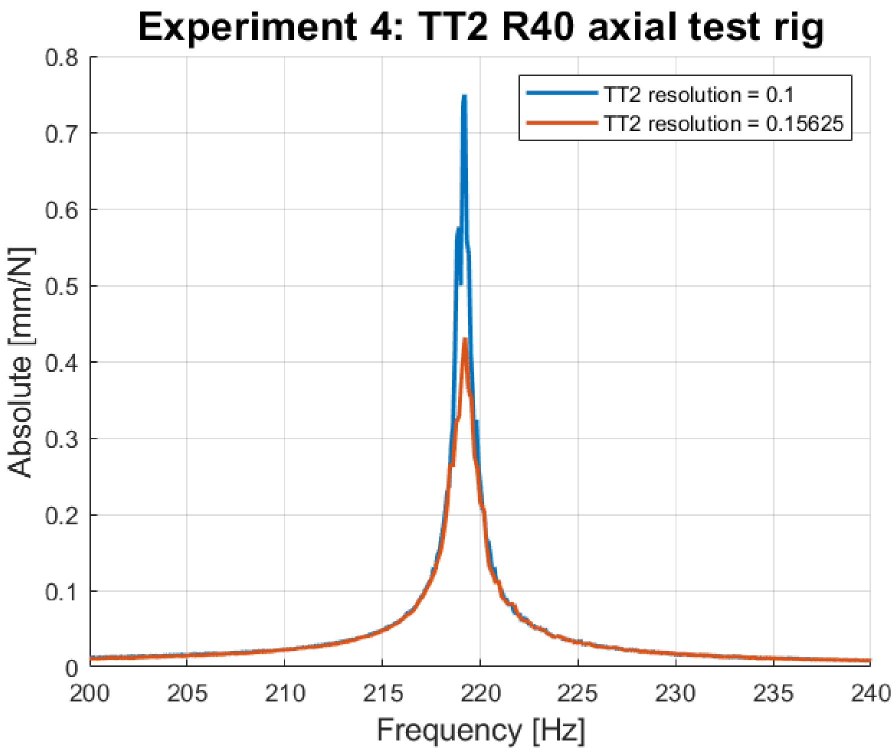

Figure 3.122 - Experiment 4: experimental FRF 1st peak highlight

By comparing the eigenfrequency of the experimental and simulated curves in the frequency range of interest it is evident that the model is stiffer with respect the reality. In this case, contrarily to the bending test rig, since there are no other parts, the only cause of the stiffness is given by the carbon data. The eigenfrequencies are collected in *Table 3.31*:

Curve	1st Peak [Hz]	Relative error [%]
Simulation	240.7	-
TT2 0.1	219.2	9.8
TT2 0.15625	219.21875	9.8

Table 3.31 - Experiment 4: 1st peak relative errors

The relative errors are below the threshold of 10%. In relation to the above-mentioned undesired phenomena characteristic of the experiment such as the transversal vibration, the obtained relative errors are acceptable.

The same experiment has been repeated for TT7 and the FRF is represented in *Figure 3.123*:

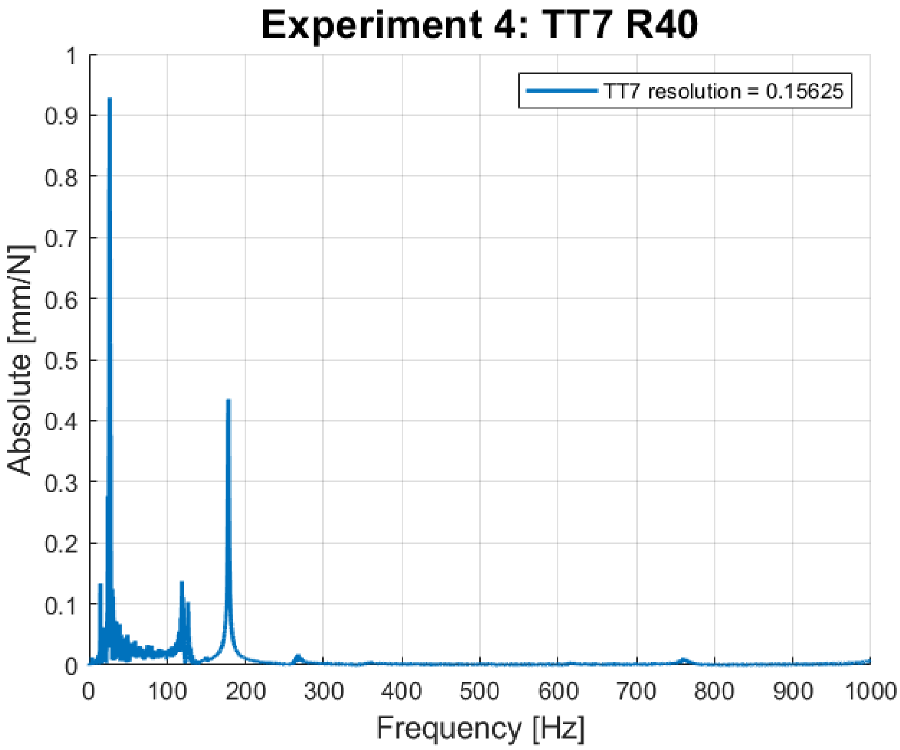

Figure 3.123 - Experiment 4: TT7 FRF

According to the bending test rig, since the TT7 model has not been realized yet, it is not possible to hold an experimental-theoretical comparison. From the experimental curve is possible to define three major peaks. The first two peaks are neglected due to their irregularities: the first one is expected to be the rigid body motion of the system, and due to its limited absolute value, the second peak is neglected. Therefore, the reference peak is the third one, located at 178.4375 Hz.

In order to compare the damping factors, TT2 and TT7 FRFs are plotted in *Figure 3.124*:

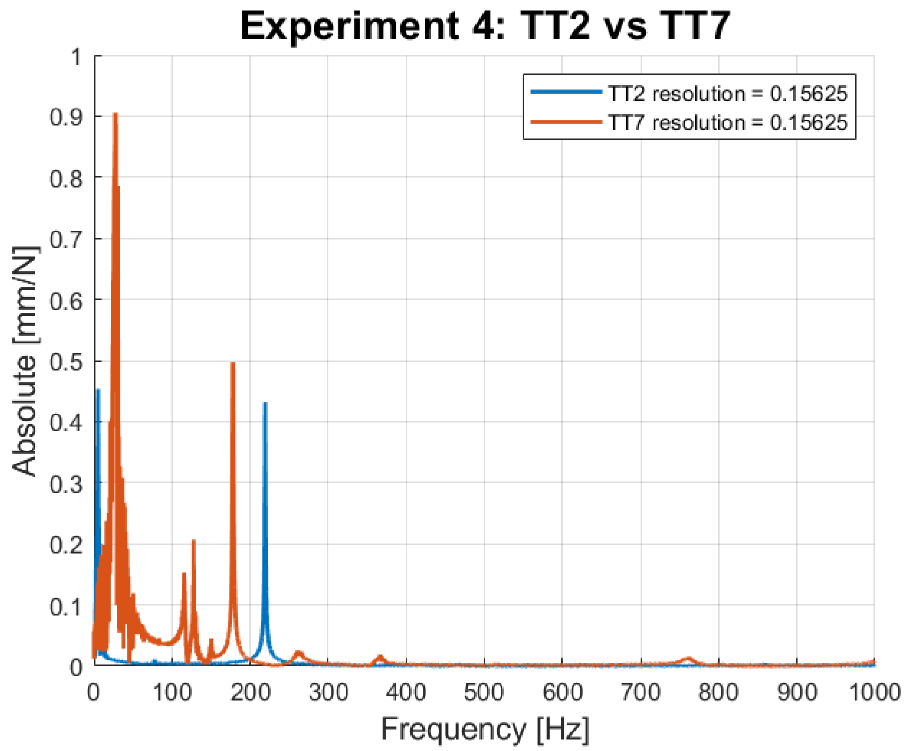

Figure 3.124 - Experiment 4: TT2 vs TT7 R40

The damping factors have been computed with the Half Power Method. According to the two graphs, the only clear peak for which is possible to make a direct comparison is located at approximately 200 Hz. The graph is detailed between 160 Hz and 250 Hz in *Figure 3.125*:

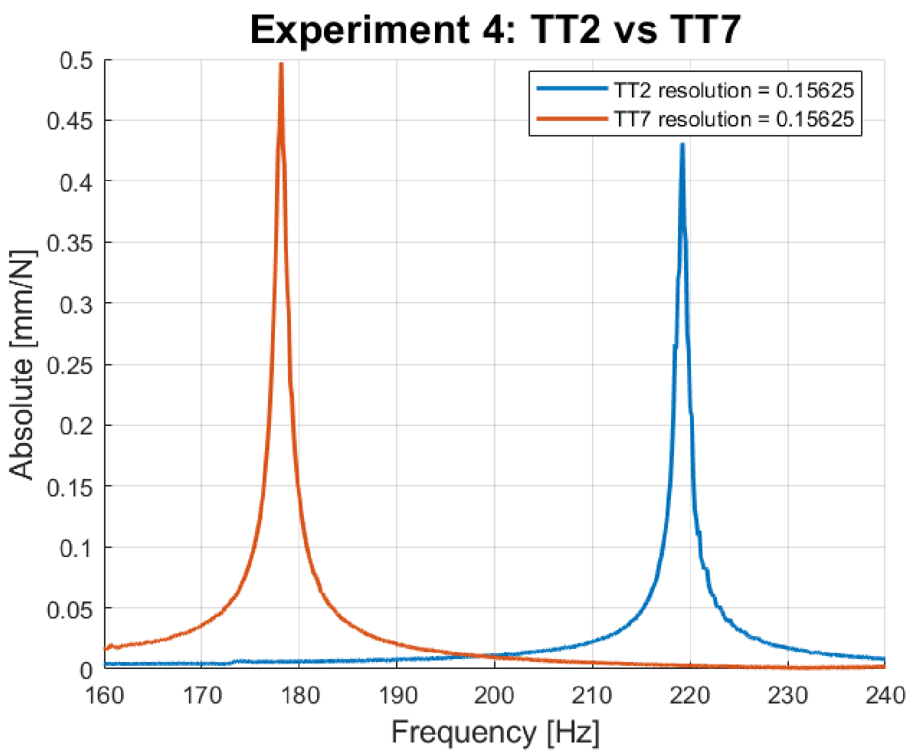

Figure 3.125 - Experiment 4: TT2 vs TT7 R40 comparison peak

From the analysis of the graph is possible to conclude that, despite of the resolution of the two experiments was the same, the TT7 curve is characterized by a lower amount of disturbs and irregularities with respect to TT2. *Table 3.32* collects the damping factors and the characteristic eigenfrequency:

Curve	**1st Peak [Hz]**	**ζ [%]**
TT2	219.21875	0.785
TT7	178.4375	1.105

Table 3.32 – Experiment 4: TT2 – TT7 damping factor comparison

It is evident that, according to the expectations, the eigenfrequency of TT7 is lower respect to TT2, because TT7 is less stiff and lighter compared to TT2. From a qualitative analysis, it is possible to see that base of the peak of the orange curve is wider than the base of the blue curve, which means that the flax I-beam damps more than the carbon I-beam. This is also confirmed by the damping factors collected in *Table 3.32*.

3.4.3 TT2 – TT7 damping factors comparison

Table 3.33 collects the damping factors and the corresponding frequencies of the peaks regarding the bending 1100 mm (2nd peak), the axial test rig, and the I-beams tested by Scheffler [23]:

Beam	Bending test rig *(1100 mm)*		Axial test rig		*Cantilever beam* [23]			
	$f\ [Hz]$	ζ [%]	$f\ [Hz]$	ζ [%]	$f\ [Hz]$	ζ [%]	$f\ [Hz]$	ζ [%]
TT2	103.6	0.777	219.21875	0.785	100	0.35	200	0.38
TT7	88.1	1.085	178.4375	1.105	90	0.54	180	0.57

Table 3.33 – TT2-TT7 axial and bending test rig damping factor comparison

The purpose of the test rigs is to investigate the damping provided by the I-beam and the constraint, without including the influence of the other parts of the test rig such as the vertical beam. For this reason, even though the effect of the test rig is limited for the 2nd peak of the bending test, from the comparison of the 600 mm and axial tests emerges that it is not possible to hold an absolute comparison between the two different experiments. Because, although the I-beam constraint sub-group is the same, the test rigs, the deformation, and stress distribution of the composite beam are different. However, it is meaningfull to hold a relative comparison between them. It confirms that in both cases TT2 beam is stiffer than TT7 but, on the other side, TT7 is more damped than TT2.

By analyzing the values of the damping factors, it comes out that the axial test rig is close to the bending test rig with a length of 1100 mm. While it is different respect to the 600 mm length. From the analysis of *Figure 3.126* it comes out that, although the effect of the vertical beam is almost negligible for the 2nd peak, the stress distribution and the entity are different for the two configurations. Thus, it is not expected that the different lengths are similar to the axial test rig. Therefore, it is a coincidence that the 1100 mm bending test is almost equal to the axial test.

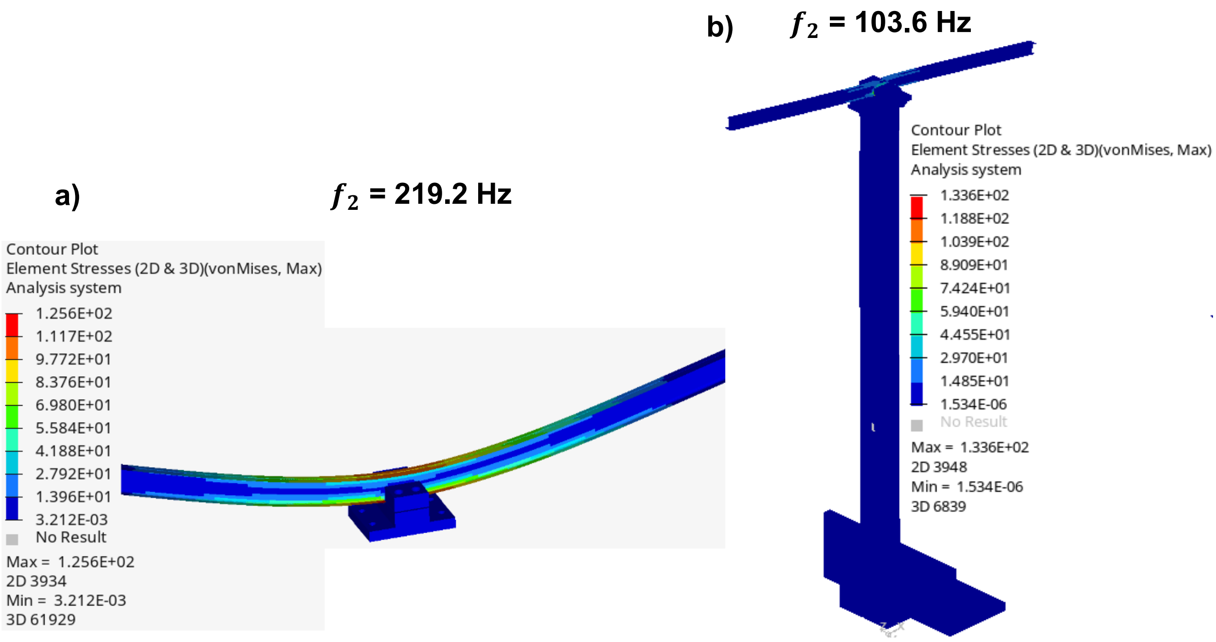

Figure 3.126 – a) Axial vs b) Bending 1100 mm stress comparison

The damping factors of the axial and bending test rig with a length of 1100 mm are close but the eigenfrequencies are different. In addition, it is possible to compare the damping factors obtained from the test rigs with the one calculated by Scheffler [23] testing the I-beams constrained as cantilever beams. According to the expectations, it emerges that the damping factors of the cantilever beams at the same frequencies of the axial and bending 1100 mm are lower both for TT2 and TT7 since the contribution of the constraint is missing. Apart from this aspect, considering the variation over the frequency, according to Scheffler [23] it comes out that by increasing the frequency the damping factor increases as well. This emerges also from the bending and axial test rigs, where the peaks characterized by the I-beams are located at different frequencies.

By considering the 2nd peak of 1100 mm and the axial test, it comes out that there is almost a factor of 2 between the cantilever beam damping factors and the axial and bending 1100 mm tests. It looks like, since the actual constraint subdivides the I-beam in two parts, the cantilever beam is only one branch of the composite beam. While, by analyzing the 600 mm this does not stand anymore due to the increased strain of the composite beam.

4 Conclusions

In this thesis, the dynamic test rig for damping investigations of tailplane components in carbon-flax hybrid design has been conceived, designed, produced, and successfully tested. For this purpose, in order to accomplish the initial requirements, two test benches, where the axial is partially included into the bending test rig to save resources, have been developed. Then, the FE models have been compared to the EMA of the sub-groups of both test rigs obtaining a successful verification.

The comparison between the experimental and simulated FRFs has been based on the computation of the relative error between the correspondent eigenfrequencies. In all the comparisons, the models were always stiffer with respect to the real system principally due to material's data inhomogeneities, excessive simplification in the simulations, and stiffness of the elements adopted in the mesh. Then, the bending and axial test rigs have been adopted to test the TT2 and TT7 beams. For this purpose, the FE model of the test rig has been tuned to solely quantify the effect of the composite beam providing results according to the initial expectations.

In conclusion, the initial goal has been accomplished since both test rigs are able to excite the desired mode shapes in the desired frequency range. Moreover, the test benches allow to solely quantify the contribution of the composite beam and the boundary conditions. Then, it has been proved that shifting the length of the vertical beam of the bending test rig allows to tune the eigenfrequencies of the system to get a sufficient amount of results to investigate the damping of the specimens. On the other hand, in case the eigenfrequency of the tailplane is know from flight test, the length of the test rig can be tuned to replicate the same frequency of the system.

4.1 Bending (asymmetric) test rig

The comparisons related to the bending test rig were carried out with 1100 mm and 600 mm free length to prove the variability of the length to tune the eigenfrequencies of the system to obtain more data to investigate.

The bending test rig has been verified with a "Bottom to Top" approach. Starting from the vertical beam, the maximum error was 7.5%, whereas, considering the entire bending test rig, the error was 9.6%. Both results were below the acceptance threshold conventionally set to 10%, therefore the bending test rig was validated. Then, the test bench was validated also including the TT2 (full carbon beam). The entire system was compared to the analogue simulation, evidencing again an excessive stiffness of the model with respect to the reality. This was not caused only by the test rig itself since Scheffler [23], who realized the finite element model of TT2, figured out that the carbon's material data obtained from the data sheet of the manufacturer are stiffer with respect to the real behavior. Despite of this, the entire model has been approved since the relative errors of the three peaks considering the refined model are: 10.8%, 1.8% and 0.5%.

After the validation of the entire system, it has been used to test the TT2 and TT7 I-beams. According to the expectations, TT7 FRF always precedes the TT2 FRF since the full carbon beam is stiffer and lighter, which means that the eigenfrequencies are higher. The damping investigation has been carried out considering the influence of the boundary condition, the contribution of the I-beam, and the effect of the material on damping. The frequency range of interest is characterized by three peaks for both TT2 and TT7 FRFs. It came out that the 1st and 3rd peaks have almost at the same frequency for both beams because the effect of the composite beam on the test rig is almost negligible in terms of change of mass and stiffness. While the second peak is induced only by the composite beam since ω_n is characteristic of the I-beam and not of the test bench. Therefore, the comparison is done on this peak since its damping factor is generated mainly by the I-beam. The corresponding mode shape is the desired asymmetric configuration.

For 1100 mm, the 2nd peak of TT2 is at 103.6 Hz with ζ=0.777 %, while TT7 is at 88.1 Hz with ζ=1.085 %. While, for 600 mm, the 2nd peak of TT2 is at 94.1 Hz with ζ=1.942 %, while TT7 is at 70.1 Hz with ζ=4.862 %. The global damping factor of the 600 mm TT2 is 140% of the 1100 mm, while the damping factor of the 600 mm TT7 is 250% of the 1100 mm. Considering the same DUT, there is a limited difference between the damping factors of 1st peak considering the two lengths. While, in the 2nd peak the difference is relevant. This is induced by the increase of stress (and strain) in the central location of the composite beam with respect to the 1st peak. The deformation of the 600 mm respect to the 1100 mm could be exploited in the design of the tailplane inducing its deformation in a way that maximizes damping. This is even more evident in the TT7 where the increment is twice than in the TT2. Since the 2nd peak is not affected by the test rig, the relevant difference between the beams is given by the advantage of flax over carbon regarding damping. The 3rd peak is not included in this analysis because it is characterized by a relevant influence of the test rig, and for the 600 mm the deformed configuration is not the one of interest.

The global damping factors have been compared to the damping factors of the test rig. This revealed that the shorter test rig is stiffer and damps more. In the 1100 mm, the 1st peak of the test rig is slightly more damped than the 3rd; where ζ_1=0.181% and ζ_3=0.160%. But the global damping factor of TT2 has the opposite trend. This is caused by the contribution of the deformation of the I-beam which has a larger entity for the 3rd peak compared to the 1st. Regarding the 600 mm, the 3rd peak of the test rig is slightly more damped than the 1st. But this difference does not justify the discrepancy of the global damping factor of TT2. This is also induced by the deformation of the composite beam. Regarding TT7, oppositely to TT2, for 1100 mm the 1st peak is more damped than the 3rd, since the test rig has the opposite trend, it means that there is a contribution of the I-beam.

It has been tried to dynamically decouple the I-beam from the test rig by mean of dynamic sub-structuring to obtain a FRF directly comparable to the one obtained from the free-free impact test. The obtained result was not comparable to the free-free impact test of the TT2 beam. A possible remedy to this inconvenience would be to perform the experimental sub-structuring to obtain the admittance matrix directly from the experiments because the input data obtained from the normal mode also include the torsional modes and due to the difference of stiffness between the composite of the beam and the metal materials of the test rig, it results that only the beam is deformed.

Considering the next applications, it is recommended to test all the different composite beams in the complete length range from 1100 mm to 500 mm. This should help to identify a more detailed trend of the damping factor over the frequency. Before the realization of the tailplane, since the deformation of the beam is concentrated in the central part in proximity of the constraint, it would be useful to test mixed I-beams composed by flax in the center and carbon in the branches. Where, the carbon content provides high stiffness and the flax high damping. Moreover, by taking into account the contribution of the boundary condition and the stress of the I-beam, it should be possible to evaluate the strain of the composite beam over the length variation. Then, this could be applied to the tailplane where, by properly designing it, it would be possible to obtain the asymmetric mode shape deformation, but with a maximized damping factor.

4.2 Axial (symmetric) test rig

The axial test rig is included into the bending test rig; therefore, since the latter has been successfully approved, this assumption has been extended also to the axial one. In addition, the axial test rig can be schematized as a rigid mass mounted on the shaker (I-beam constraint sub-group); thus, due to this simplicity it does not worth to simulate it. Consequently, the axial test rig has been directly adopted to test the TT2 and TT7 I-beams.

Initially, the TT2 was tested and the measured FRF has been compared to the simulation. The entire model has been approved with a relative error corresponding to the unique peak of 9.8%. Then, TT2 and TT7 I-beams were compared considering the eigenfrequencies and the corresponding damping factors. Due to the transversal motion of the I-beam, the quality of the curves obtained from the axial tests is lower quality compared to the curves obtained from the bending tests. The frequency resolution has been tuned to smooth the curves. In conclusion, it has been decided to use the curve with 0.15625 Hz of resolution.

The experimental FRF of TT2 is characterized by a single peak located at 219.21875 Hz, while the peak of the simulation is located at 240.7 Hz. Therefore, also for the axial test rig, the model is stiffer with respect to the real system. In this case, due to the limited number of parts, contacts and phenomena inducing possible inhomogeneities, it is evident that the parameters of the datasheet of the carbon fiber set in the simulation are stiffer compared to the real material. According to the simulation, the mode shape corresponding to this frequency is the symmetric configuration of interest. Considering TT7, the peak is located at 178.4375 Hz. TT2 has ξ =0.785% while TT7 has ξ=1.105%. According to the expectations, the eigenfrequency of TT2 is higher that the eigenfrequency of TT7 since it is stiffer and lighter. On the contrary, TT7 has a higher damping factor compared to TT2 since it is mainly composed by flax which damps more than carbon.

Considering the next applications, it is recommended to test all the composite beams with the axial test rig to evaluate the damping factors and compare them with the bending test rig and the cantilever beam.

4.3 Overall conclusion

Due to the difference of the test rigs and of the deformation of the composite beam emerged that is not possible to hold an absolute comparison between the results of the two test benches. They can be used for relative comparison between different hybridized solutions. Anyway, by coincidence it came out that the damping factors of the 2nd peak of the 1100 mm bending test are close to the axial with different eigenfrequencies, while for the 600 mm they are completely different. In addition, the damping factors of the I-beam of the two test rigs were compared to the ones obtained by Scheffler [23] constraining the beam as cantilever. From the relative comparison it results that in all cases the damping factor increases over the frequency. By considering the length of 1100 mm and the axial, it comes out that there is almost a factor of 2 between the cantilever beam damping factors and the axial and bending 1100 mm tests. It looks like, since the actual constraint subdivides the I-beam in two parts, the cantilever beam is only one branch of the composite beam. While, by analyzing the 600 mm this does not stand anymore due to the increased strain of the composite beam.

5 References

[1] A. Datta, "Fundamental understanding, prediction and validation of rotor vibratory loads in steady-level flight," University of Mariland, College Park, 2004.

[2] A. S. M. J. S. Stupar, "Measurement and Analysis of Vibrations on the Helicopter Structure in Order to Detect Defects of Operating Elements," *Scientific Technical Review,* vol. 62, no. 1, pp. 58-63, 2012.

[3] G. J. Leishman, "Principles of helicopter aerodynamics with CD extra," Cambridge University press, 2006.

[4] R. P. S. P. F. Sheridan, "Interactional aerodynamics - a new challenge to helicopter technology," *Journal of the American Helicopter Society,* vol. 25, no. 1, pp. 3-21, 1980.

[5] L. G. M. H. J. John, "Increasing the damping properties of carbon laminates by flax fiber hybridization for rotorcraft applications," in *48th European Rotorcraft Forum*, Winterthur, Switzerland, 2022.

[6] A. K. e. a. editor, An Advanced Five-Bladed Bearingless Main Rotor Dynamics and Acoustics from Draft to Flight Test, 2018.

[7] J. X. L. M. B. W. G. Z. a. L. W. J. Yang, "Vibration and damping characteristics of hybrid carbon fiber composite pyramidal truss sandwich panels with viscoelastic layers," *Composite structures,* vol. 106, pp. 570-580, 2013.

[8] a. M. H. K. Strohmann, An Eco-Efficient Helicopter Tailplane Hybridized from Flax, Balsa and Carbon, 2019.

[9] A. R. a. P. Choi, "The Elements of Polymer Science and Engineering," *Biopolymers,* pp. chapter 13, pages 521–535. Woodhead Publishing, third edition, 2013.

[10] C. O. a. M. K. e. U. Kowarsch, "High order CFD-simulation of the rotor fuselage interaction," in *39th European Rotorcraft Forum*, 2013.

[11] M. K. a. E. K. U. Schaeferlein, ""Aeroelastic simulation of the tail shake phenomenon"," *Journal of the American Helicopter Society,* vol. 63, no. 3, pp. 1-17, 2018.

[12] Braun, "Development of antiresonance force isolators for helicopter vibration reduction," *Journal of the American Helicopter Society,* vol. 27, no. 4, pp. 37-44, 1982.

[13] T. R. M. E. S. P. G. U. a. M. H. e. M. Rinker, "Simulation of Rotor-Empennage Interactional Aerodynamics in Comparison to Experimental Data," 2019.

[14] T. R. M. E. S. P. G. U. M. H. M. Rinker, Simulation of Rotor-Empennage Interactional Aerodynamics in Comparison to Experimental Data, 2019.

[15] K. C. F. a. Lamb, "Experimental investigation of main rotor wake induced empennage vibratory airload for the RAH-66 Comanche helicopter," American Helicopter Society, 1993.

[16] A. E. L. D. H. K. L. S. R. E. E. B. M. B. M. Carus, "Wood-plastic composites (WPC) and natural fibre composites (NFC)," *Nova-Institute: Hürth, Germany ,* vol. 15, pp. 1-16, 2015.

[17] K. A. Henschel, "Biocomposites in Aviation Structures on the Example of Flax and its Hybrids," Technische Universität München, München, 2019.

[18] A. E. M. J. L. R. M. A. M. H. B. M. Ameur, "Damping Analysis of Unidirectional Carbon/Flax Hybrid Composites," *International Journal of Applied Mechanics,* vol. 10, no. 5, 2018.

[19] P. E. B. C. J. G. P. J. -A. E. M. F. Duc, "Damping of thermoset and thermoplastic flax fibre composites," *Composites Part A: Applied Science and Manufacturing,* vol. 64, pp. 115-123, September 2014.

[20] J. N. G. Fairlie, "Damping properties of flax/carbon hybrid expoxy/fibre-reinforced composites for automotive semi-structural applications," *Fibers,* vol. 8, no. 10, p. 64, 2020.

[21] W. Z. H. S. R. A. J. M. B. M. Assarar, "Evaluation of the damping of carbon-flax reinforced composites," *Composite Structures,* vol. 132, pp. 148-154, 2015.

[22] W. Z. R. A. H. K. J. M. B. M. Assarar, "Improving the damping properties of carbon fibre reinforced composites by interleaving flax and viscoelastic layers," *Composites Part B: Engineering,* vol. 152, pp. 248-255, 2018.

[23] B. Scheffler, *"Influences of hybrid flax and carbon ply structures on the dynamic behaviour of aerospace profiles, especially damping",* Munich: Masther Thesis, 2022.

[24] A. D. V. C. B. Y. R. R. P. G. V. Dries Peumans, "Accurate estimation of the non-parametric FRF of lightly-damped mechanical systems using arbitrary excitations," *Mechanical Systems and Signal Processing,* vol. 130, pp. 545-564, 2019.

[25] W. Z. H. S. R. A. J.-M. B. Mustapha Assarar, "Evaluation of the damping of hybrid carbon–flax reinforced composites," *Composite Structures,* vol. 132, pp. 148-154, 15 November 2015.

[26] S. M. a. T. L. A. Bismarck, "Plant Fibers as Reinforcement for Green Composites," 2005.

[27] H. L. Bos, "The potential of flax fibres as reinforcement for composite materials. PhD Thesis," Technische Universiteit Eindhoven, Eindhoven, 2004.

[28] N. C. a. K. J. L. Yan, "Flax fibre and its composites," *Composites Part B,* p. 195, 2014.

[29] C. Soutis, "Fibre reinforced composites in aircraft construction," *Progress in Aerospace,* 2005.

[30] R. R. Franck, "Bast and Other Plant Fibres," *Woodhead Publishing,* 2005.

[31] R. S. M. K. L. K. K. S. M. H. a. H.-J. E. R. Rinberg, "Anwendungspotenzial von naturbasierten hybriden Leichtbaustrukturen," *eutscher Luft- und Raumfahrtkongress,* 2016.

[32] S. Mahmoudi, A. Kervoelen, G. Robin, L. Duigou, E. Daya and J. Cadou, "Experimental and numerical investigation of the damping of flax–epoxy composite plates," *Composite Structures,* vol. 208, pp. 426-433, 2019.

[33] D.D.L.Chung, "Structural composite materials tailored for damping," *Journal of Alloys and Compounds,* vol. 355, no. 1-2, pp. 216-223, 2003.

[34] J. A.S.Hadi, "Measurement and theoretical modelling of the damping properties of a uni-directional glass/epoxy composite," *Composite Structures,* vol. 34, no. 4, pp. 381-385, April 1996.

[35] R. F. G. C. T. S. &. S. K. C. S. A. Suarez, "The influence of fiber length and fiber orientation on damping and stiffness of polymer composite materials," *Experimental Mechanics,* vol. 26, pp. 175-184, June 1986.

[36] K. J. &. B. R. M. Md Zillur Rahman, "Vibration damping of flax fibre-reinforced polypropylene composites," *Fibers and Polymers,* vol. 18, pp. 2187-2195, 2017.

[37] T. P. a. B. Bensaude-Vincent, "Materials Research Activities, Hystory of composites," History of recent science & technology, 2002.

[38] T. S. a. J. Takahashi, "Prediction of Energy Intensity of Carbon Fiber Reinforced Plastics for Mass-Produced Passenger Cars," in *9th Japan International SAMPE Symposium*, Japan, 2005.

[39] W. R. M. J. C. H. P. L. D. Sunter, "The manufacturing energy intensity of carbon fiber reinforced polymer composites and its effect on life cycle energy use for vehicle door lightweighting," in *20th International Conference on Composite Materials*, Copenhagen, Denmark, 2015.

[40] J. P. J. D. Nabi Saheb, "Natural fiber polymer composites: A review," *Advances in Polymer Technology,* vol. 18, no. 4, pp. 351-363, Winter 1999.

[41] J. I. I. V. Paul Wambua, "Natural fibres: can they replace glass in fibre reinforced plastics?," *Composites Science and Technology,* vol. 63, no. 9, pp. 1259-1264, July 2003.

[42] M. M. L. T. D. Amar K. Mohanty, Natural fibers, biopolymers, and biocomposites, CRC Press, 2005.

[43] M. G. A. E. T. M. L. K. L. Pickering, "A review of recent developments in natural fibre composites and their mechanical performance," *Composites Part A: Applied Science and Manufacturing,* vol. 83, pp. 98-112, April 2016.

[44] R. S. Alma Hodzic, Natural fibre composites, Woodhead Publishing , 2014.

[45] A. B. Karine Charlet, "Mechanical properties of interfaces within a flax bundle – Part I: Experimental analysis," *International Journal of Adhesion and Adhesives,* vol. 31, no. 8, pp. 875-881, December 2011.

[46] T. L. H. U. F. S. B. Wielage, "Processing of natural-fibre reinforced polymers and the resulting dynamic–mechanical properties," *Journal of Materials Processing Technology,* vol. 139, no. 1-3, pp. 140-146, 20 August 2003.

[47] V. K. M. S. k. R. Z. S. Prabhakaran, "Sound and Vibration Damping Properties of Flax Fiber Reinforced Composites," *Procedia Engineering,* vol. 97, pp. 573-581, 2014.

[48] P. E. B. J. -A. E. M. F. Duc, "The role of twist and crimp on the vibration behaviour of flax fibre composites," *Composites Science and Technology,* vol. 102, pp. 94-99, 6 October 2014.

[49] P. B. G. B. P. M. .. S. F. A. El-Hafidi, "Determination of dynamic properties of flax fibres reinforced laminate using vibration measurements," *Polymer Testing,* vol. 57, pp. 219-225, February 2017.

[50] P.-E. B. J.-A. E. M. Fabien Duc, "Dynamic mechanical properties of epoxy/flax fibre composites," *Journal of Reinforced Plastics and Composites,* vol. 33, no. 17, pp. 1625-1633, 2014.

[51] R. H. N. A. F. M. P. S. Marie-Joo Le Guen, "Tailoring the vibration damping behaviour of flax fibre-reinforced epoxy composite laminates via polyol additions," *Composites Part A: Applied Science and Manufacturing,* vol. 67, pp. 37-43, December 2014.

[52] R. H. N. A. F. M. P. S. M.-J. Le Guen, "Tailoring the vibration damping behaviour of flax fibre-reinforced epoxy composite laminates via polyols additions," *Composite Part A,* vol. 67, pp. 37-43, 2014.

[53] J. S. S. M. G. a. M. M. S. Nilmini P.J. Dissanayake, "Energy use in the production of flax fiber for the reinforcement of composites," *Journal of Natural Fibers,* vol. 6, no. 4, pp. 331-346, 2009.

[54] D. B. D. a. H. V. S. Gangarao, "Critical review of recent publications on use of natural composites in infrastructure," *Composites Part A,* vol. 43, pp. 1419-1429, 2012.

[55] H. L. Bo Madsen, "Guidelines for mechanical design with biocomposites: properties, weight and cost," *JEC Magazine,* vol. 37, 2007.

[56] M. F. Ashby, Materials and the Environment: an eco-informed material choice, Butterworth-Heinemann/Elsevier, 2nd edition, 2013.

[57] C. B. B. S. J. R. E. M.-R. B. W. Gregor Wernet, "The ecoinvent database version 3 (part I): overview and methodology," *The International Journal of Life Cycle Assessment,* vol. 21, no. 9, pp. 1218-1230, 2016.

[58] A. E. H. P. B. G. Garip Genc, "Comparison of the mechanical properties of flax and glass fiber composite materials," *Journal of Vibroengineering,* vol. 14, no. 2, pp. 572-581, 2012.

[59] M. K. D. L. Michael Karus, "Study On Markets and Prices for Natural Fibres (Germany and EU)," Technical Report March, nova Institute, Hürth, Germany, 2000.

[60] S. M. S. A. A. N. M. R. I. M. F. M. Alkbir, "Fibre properties and crashworthiness parameters of natural fibre-reinforced composite structure: a literature review," *Composite Structures,* vol. 148, pp. 59-73, 2016.

[61] R. E. S. R. C. B. M. W. K. K. James Meredith, "Natural fibre composite energy absorption structures," *Composites Science and Technology,* vol. 72, no. 2, pp. 211-217, 2012.

[62] J. T. S. D. T. V. C. S. F. T. L. C.-A. D. M. L. L. P. G. Fabrizio Sarasini, "Damage tolerance of carbon/flax hybrid composites subjected to low velocity impact," *Composites Part B: Engineering,* vol. 91, pp. 144-153, 2016.

[63] N. C. L. Yan, "Crashworthiness characteristics of flax fibre reinforced epoxy tubes for energy absorption application," *Materials and Design,* vol. 51, pp. 629-640, 2013.

[64] F. Vanfleteren, "Technical Data Sheet - FLAXPREG T-UD," Technical report, LINEO S.A.S., 2015.

[65] N. L. M. P. S. A. B. Karthik-Ram Ramakrishnan, "Experimental Characterisation of the Impact Resistance of Flax Fibre Reinforced Composite," in *ECCM17- 17th European Conference on Composite Materials*, Munich, Germany, 2016.

[66] M. C. T. T. H. F. T. Y. Lebaupin, "Effect of Stacking Sequence on Low Velocity Impact and Post-Impact Behavior of Flax/Polyamide 11 Composites," in *ECCM17 - 17th European Conference on Composite Materials*, Munich, Germany, 2016.

[67] D. E. O. B. A. T. I. U. Kling, "Future Aircraft Wing Structures Using Renewable Materials," in *Deutscher Luft- und Raumfahrtkongress 2015*, 2015.

[68] I. V. A. V. V. F. Bensadoun, "Are flax-epoxy composites tough? In ECCM17," in *17th European Conference on Composite Materials*, Munich, Germany, 2016.

[69] J. M. Berthelot, "Damping analysis of laminated beams and plates using the Ritz method," *Composite structures,* vol. 74, pp. 186-201, 2006.

[70] M. A. Y. S. A. E. M. J. M. Berthelot, "Damping analysis of composite materials and structures," *Composite Structures,* vol. 85, no. 3, pp. 189-204, 2008.

[71] R. H. N. A. F. G. W. E. M. P. S. M. J. Le Guen, "The damping-modulus relationship in carbon/flax fibre hybrid composites," *Composites Part B,* vol. 89, pp. 27-33, 2016.

[72] J. N. G. Fairlie, "Damping properties of flax/carbon hybrid epoxy/fibre-reinforced composites for automotive semi-structural applications," *Fibers,* vol. 8, no. 10, p. 64, 2020.

[73] A. E. M. J. L. R. M. A. M. H. B. M. Ameur, "Damping Analysis of Unidirectional Carbon/Flax Fiber Hybrid Composites," *International Journal of Applied Mechanics ,* vol. 10, no. 5, 2018.

[74] T. F. C. Berninger, *Experimental Vibrational Analysis - Version 0.9,* Munich: Chair of Applied Mechanics - TUM, 2019.

[75] N. A. E. Soren Linnet Gjelstrup, "What is Modal Analysis: The Ultimate Guide," DEWESoft, [Online]. Available: https://dewesoft.com/daq/what-is-modal-analysis. [Accessed 11 06 2022].

[76] D. J. Ewins, Modal Testing: Theory and Practice, Research Studies Press Letchworth , 1984, vol. 15.

[77] A. G. P. J. S. Bendat, Engineering Applications of Correlation and Spectral Analysis, New York: Wiley Interscience, 1980.

[78] P. V. S. V. P. Guillame, Frequency-Domain Maximum Likelihood Identification of Modal Parameters with Confidence Intervals, Leuven: Katholieke Universiteit, 1998, pp. 359-366.

[79] B. P. P. G. T. D. T. M. El-Kafafy, "Constrained maximum likelihood modal parameter identification applied to structural dynamics," *Mechanical Systems Signal Processing,* vol. 24, no. 3, pp. 573-595, 2010.

[80] R. W. B. D. L. B. Marco A. Peres, "Practical Aspects of Shaker Measurements for Modal Testing," in *ISMA* , Leuven, Belgium, 2010.

[81] "Frequently Asked Questions Modal Shakers and Related Topics," The Modal Shop Inc. - A PCB Group Company.

[82] "The Fundamentals of Modal Testing," Agilent Technology , 2000.

[83] J. S. E. B. J. S. C. Schedlinski, "Application of optical measurement techniques for experimental modal analyses of lightweight structures".

[84] X. D. H. R. G. W. Y. Hong, "Vibration and damping analysis of a composite blade," *Materials and Design,* vol. 34, pp. 98-105, 2012.

[85] H. S. W. P. D. W. J. V. J. De Visscher, "Identification of the Damping Properties of Orthotropic Composite Materials Using a Mixed Numerical Experimental Method," *Applied Composite Materials,* pp. 13-33, 1997.

[86] C. E. S. C. Bilal Sharqi, "Ground Vibration Testing on Very Flexible Aircraft," in *AIAA Scitech 2020 Forum*, Orlando, FL, 2020.

[87] M. A. D. S. M. Viscardi, "Design and testing of a prototype foam for lightweight technological applications," *International Journal of Mechanics,* vol. 10, 2016.

[88] S. V. R. H. M. H. S. P. Jalali, "Noise Effects on Modal Parameters Extraction of Horizontal Tailplane by Singular Value Decomposition Method Based on Output Only Modal Analysis," *Journal of Solid Mechanics,* vol. 11, no. 3, pp. 678-689, 2019.

[89] F.-A. R. Haddadpour H., "Evaluation of quasi-steady aerodynamic modeling for flutter prediction of aircraft wings in incompressible flow," *Thin-Walled Structures,* vol. 44, no. 9, pp. 931-936, 2006.

[90] O. A. N. K. A. Moosavi M. R., "Flutter of subsonic wing," *Thin-Walled Structures,* vol. 43, no. 4, pp. 617-627, 2005.

[91] M. S. A. R. E. R. E. R. Fotsing, "Lightweight damping of composite sandwich beams: Experimental analysis," *Journal of Composite Materials,* vol. 47, no. 12, pp. 1501-1511, 2012.

[92] Damping Technologies Inc. , *Characterization of the dynamic mechanical properties of materials using the vibrating beam technique,* 2007.

[93] R. A. E. C. E. Z. A. Pagani, "Static and dynamic testing of a full-composite VLA by using digital image correlation and output-only ground vibration testing," *Aerospace Science and Technology,* vol. 112, 2021.

[94] M. P. Y. G. M. B. Christopher Ciavarella, "An extensive helicopter ground vibration test: from pretest analysis to the study of non-linearities," in *44th European Rotorcraft Forum*, Delft, Netherlands, 2018.

[95] H. C. R. d. D. J. d. A. J. R. A. J. M. C. W. H. A. R. G. G. J. D. J. D. Bart Peeters, "Modern solutions for Ground Vibration Testing of large aircraft".

[96] R. W. B. Marco A. Peres, "Modal Testing Excitation Guidelines," The Modal Shop, Inc., Cincinnati, Ohio.

[97] A. E. M. M. K. D. O. F. T. M. P. M. G. G. Č. M. B. D. J. R. Tomaž Bregar, "pyFBS: A Python package for Frequency Based Substructuring," *The Journal of Open Source Software,* vol. 7, no. 69,3399, 2022.

[98] R. R.G.Ni, "A rational method for obtaining the dynamic mechanical properties of laminae for predicting the stiffness and damping of laminated plates and beams," *Composites,* vol. 15, no. 3, pp. 193-199, 1984.

[99] J. Y.M.Haddad, "On the trade-off between damping and stiffness in the design of discontinuous fibre-reinforced composites," *Composites Part B: Engineering,* vol. 34, no. 1, pp. 11-20, January 2003.

[100] M. J. a. M. Thariq, Sustainable Composited for Aerospace Applications, Woodhead Publishing, 2018.

[101] A. J. M. U. D. S.-W. Andrzej K. Błedzki, "Fibres and Textiles in Eastern Europe," *Biocomposites in the past and in the future,* vol. 96, no. 6B, pp. 15-22, 2012.

[102] "Biotex Flax 100 g/m2 2x2 Twill," Composites Evolution Ltd, 2018. [Online]. Available: https://compositesevolution.com/products/natural-fibre-prepregs/.

[103] "Bandhini Homewear," B. H. Design, [Online]. Available: http://bandhinihomeweardesign.blogspot.com/2012/06/more-factsabout-our-linens.html. [Accessed 24 10 2018].

[104] B. V. G. D. M. M. T. A. Treviso, "Damping in composite materials: Properties and models," *Composites Part B: Engineering,* vol. 78, pp. 144-152, 2015.

[105] Z. Y. Z. R. G. J. M. N. B. H. N. Dhakal, "Development of flaxcarbon fibre hybrid composites for enhanced properties," *Carbohydrate Polymers,* vol. 96, pp. 1-8, 2013.

[106] A. V. G. D. B. V. Fiore, "Mechanical behavior of carbon/flax hybrid composites for structural applications," *Journal of Composite Materials,* vol. 46, no. 17, pp. 2089-2096, 2012.

[107] A. A. C. U. J. Flynn, "Hybridized carbon and flax fiber composites for tailored performance," *Materials and Design,* vol. 102, pp. 21-29, 2016.

[108] W. Z. H. S. R. A. J. M. B. M. Assarar, "Evaluation of the damping of hybrid carbon-flax reinforced composites," *Composite Structures,* vol. 132, pp. 148-154, 2015.